DISSERTATION

A MONTHLY, TWO-SOIL-LAYER STATISTICAL-DYNAMICAL WATER BALANCE MODEL FOR HYDROECOLOGICALLY FOCUSED CLIMATE IMPACT ASSESSMENTS

Submitted by

John P. Kochendorfer

Department of Civil Engineering

In partial fulfillment of the requirements for the Degree of

Doctor of Philosophy

Colorado State University
Fort Collins, Colorado
Spring 2005

COLORADO STATE UNIVERSITY

March 29, 2005

WE HEREBY RECOMMEND THAT THE DISSERTATION PREPARED UNDER OUR SUPERVISION BY JOHN P. KOCHENDORFER TITLED "A MONTHLY, TWO-SOIL-LAYER STATISTICAL-DYNAMICAL WATER BALANCE MODEL FOR HYDROECOLOGICALLY FOCUSED CLIMATE IMPACT ASSESSMENTS" BE ACCEPTED AS FULFILLING IN PART REQUIREMENTS FOR THE DEGREE OF DOCTOR OF PHILOSOPHY.

Committee on Graduate Work

Dr. Dennis Ojima

Roger A Pielke Sr

Dr. Roger A. Pielke, Sr.

Jose D. Salas

Dr. Jose D. Salas

Freeman M Smith

Dr. Freeman Smith

Advisor : Dr. Jorge A. Ramírez

Sandra Woods

Department Head/Director

ABSTRACT OF DISSERTATION

A MONTHLY, TWO-SOIL-LAYER STATISTICAL-DYNAMICAL WATER BALANCE MODEL FOR HYDROECOLOGICALLY FOCUSED CLIMATE IMPACT ASSESSMENTS

An operational version of a statistical-dynamical water balance model is developed which is applicable to hydroecologically focused regional-scale climate impact assessments. Major improvements to the model include implementation at a monthly scale, addition of snow and frozen soil, division of vadose-zone soil into two layers, and a more realistic representation of vegetation. The latter is achieved by coupling the water balance model to the Shuttleworth-Wallace evapotranspiration model. The coupled model is applied to the central United States over a half-degree grid using vegetation, soil and climate data from the Vegetation Ecosystem Modeling and Analysis Project. After detailed review of the literature, careful estimation of the parameters of the evapotranspiration, soil-hydraulic and stochastic-precipitation sub-models is performed. An excellent match of modeled mean annual runoff to contours of streamflow is achieved with only minimal calibration of two evapotranspiration parameters. Model validity is further established through comparison of results for the mean and interannual variability of the water balance with observations of leaf area index (LAI), vegetation productivity and soil moisture.

Surprising little dependence of the percentage of total evapotranspiration that is bare-soil evaporation on climate and vegetation type is found, with most of the variation across the study area attributable to soil texture and the resultant differences in vegetation density. The implication is that the higher (lower) soil moisture content in humid (dry) climates is more-or-less offset by the greater (lower) vegetation density.

The partitioning of evapotranspiration in the model is highly dependent on vegetation density in the form of LAI. The spatial and interannual variation in LAI is captured in the model through application of the hypothesis that, in any year in which water is significantly limiting, vegetation will draw soil moisture down in the latter half of the growing season approximately to the point at which the vegetation just begins to experience water stress. This “LAI-maximization” hypothesis is supported through the analysis of observed soil moisture, soil-moisture retention data and water-stress studies in the plant physiology literature. Analysis of the sensitivity of model-maximized LAI to soil texture shows that the model is able to reproduce the inverse texture effect, which consists of the observation that natural vegetation in dry climates tends to be most productivity in sandy soils.

Comparison of model results to interpolated estimates of storm flow from USGS gauging stations shows that, for most combinations of climate and soil, the one-dimensional formulation of infiltration dynamics does a reasonable job of approximating the spatially complex process of surface runoff generation at the regional scale. However, overestimation of surface runoff in dry climates is substantial if subgrid variability in soil hydraulic properties is included. This may be a scale issue in that much surface runoff in dry climates never reaches a gauged stream channel. In contrast, subgrid variability of soil hydraulic properties appears to be much less important in humid climates. Rather, the model tends to *underestimate* surface runoff in those climates owing to the unaccounted-for connection of the vadose zone to shallow groundwater and the resulting Dunne (*i.e.*, saturation excess) runoff and enhancement of Hortonian runoff.

Although the model tends to underestimate the interannual variability in surface runoff and overestimate the interannual variability in base flow, it matches the overall structure in the observations. Specifically, it reproduces the linear decrease in the coefficients of variation of storm flow with the means, as well the peak in the coefficients of variation of base flow for means around one cm. The later is seen to be associated with a region of high interannual variability of precipitation over the central Great Plains. The model also reproduces the positive correlation between the skewness coefficients and the coefficients of variation in both storm flow and base flow. The tendency of the model to underestimate the interannual variability in storm flow is attributed to subgrid variability in precipitation and runoff processes, and to the spatiotemporal variability of antecedent soil moisture. The less severe overestimation of the interannual variability of base flow is attributed more to groundwater storage than to scale issues.

APPENDIX A: INTEGRATED HYDROLOGICAL/ECOLOGICAL/ECONOMIC MODELING FOR EXAMINING THE VULNERABILITY OF WATER RESOURCES TO CLIMATE CHANGE

A methodology for assessing regional-scale hydrologic vulnerability to climate variability that incorporates ecologic and economic factors is presented. A simple economic model of damages due to hydrologic drought and the decision to invest in "augmented" yield to mitigate these damages is coupled to a statistical-dynamical, soil-vegetation-climate model of the annual water balance. The coupling is through the cumulative distribution function (CDF) of annual basin yield as estimated by the model. Using Bayesian concepts for optimal decision-making under uncertainty, uncertainty in the yield CDF is propagated through the drought damage model to the hypothetical investment decision.

APPENDIX B: THE IMPACT OF LAND-ATMOSPHERE INTERACTIONS ON THE TEMPORAL VARIABILITY OF SOIL MOISTURE AT THE REGIONAL SCALE

This study examines the impact of the nonlinear dynamics of soil-moisture feedbacks to precipitation on the temporal variability of soil moisture at the regional scale. Our approach first formulates the large-scale soil-water balance as an ordinary differential equation and then recasts it as a stochastic differential equation by incorporating colored noise representing the high-frequency temporal variability and correlation of precipitation. The underlying model couples the atmospheric and surface-water balances and accounts for both *precipitation recycling* and *precipitation-efficiency feedbacks,* which arise from the surface energy balance. Based on the governing Fokker-Planck equation, we derive three different analytical solutions (corresponding to differing forms and combinations of feedbacks) for the steady-state probability density function of soil moisture. Using NCEP/NCAR reanalysis data, estimates of potential evapotranspiration, and long-term observations of precipitation, streamflow and soil moisture, the model is parameterized for a 5°×5° region encompassing the State of Illinois. We show that *precipitation-efficiency feedbacks* can be significant contributors to the variability of soil moisture at the regional scale. *Precipitation recycling*, on the

other hand, increases the variability by a negligible amount. For all feedback cases, the probability density function is unimodal and nearly symmetric. The analysis concludes with an examination of the dependence of the shape of the probability density functions on spatial scale. It is shown that the associated increases in either the correlation time scale or the variance of the noise will produce a bimodal distribution when *precipitation-efficiency* feedbacks are included. However, the magnitudes of the necessary increases are of an unrealistic magnitude.

John Paul Kochendorfer
Department of Civil Engineering
Colorado State University
Fort Collins, CO 80523-1372
Spring 2005

ACKNOWLEDGEMENTS

I would like to thank all those people whose support—material and immaterial—made this dissertation possible. In particular, my gratitude goes out to: my advisor, Jorge Ramírez, for his unfailing enthusiasm; Mike Hobbins, for help with the kriging of the storm statistics; Gene Gander, for finding the R-5 soil moisture data on his home PC when everyone else thought they were lost; my friends and officemates, for putting up with my idiosyncrasies, especially when the going got rough; and last, but not least, my parents for their financial and spiritual support.

The research was partially supported by the U.S. Department of Energy through a Graduate Fellowship for Global Change and the National Institute for Global Environmental Change (Cooperative Agreement No. DE-FC03-90ER61010).

> "....what a long, strange trip it's been."
>
> —*Truckin'* by the Grateful Dead

TABLE OF CONTENTS

TABLE OF CONTENTS
(continued)

LIST OF TABLES

LIST OF FIGURES

LIST OF FIGURES
(continued)

LIST OF FIGURES
(continued)

LIST OF FIGURES
(continued)

Figure **Page**

LIST OF FIGURES
(continued)

Figure **Page**

LIST OF FIGURES
(continued)

LIST OF FIGURES
(continued)

Figure **Page**

LIST OF FIGURES
(continued)

Chapter 1: Introduction

1.1. Motivation

Impact assessments performed at the regional scale are essential for understanding the implications of climate change and variability for the diversity of human and natural systems dependent on and integrated with the climate system. Regional-scale impact assessments can be designed for a variety of scientific and policy purposes, each of which can require modeling and data at different levels of scale, resolution and certainty. This dissertation is devoted to the development of a statistical-dynamical water balance model that is suited to addressing issues of scale, uncertainty and variability in hydroecologically focused climate impact assessments. In general, statistical-dynamical models use stochastic formulations of the temporal or spatial variability of parameters and state variables while still maintaining some representation of the physics of the system. Their nature makes them amenable to the quantification of variability and the propagation of uncertainty with a variety of analytical and numerical techniques such as derived distributions and Monte Carlo simulation. Part of that nature is also to encourage parsimonious use of parameters and driving variables. From an operational standpoint, this makes a statistical-dynamical model more likely to be applicable outside of regions where—and time frames when—there are detailed observations of the hydroclimatic environment. We are in particular interested in developing a water balance model that can be driven by large-scale spatial and temporal averages of rainfall, such as those produced by remote sensing and climate modeling.

The climate-soil-vegetation model of Eagleson (1978a-g) was used as the starting point for model development. The Eagleson model is a one-dimensional representation of the fluxes of water between the land surface and atmosphere. Through use of fundamental physical equations and a stochastic model of precipitation, Eagleson (1978b-e) derives expected annual values of those fluxes. He also shows how an analytical form for the frequency distribution of annual precipitation can be used with the water balance equation (which is composed of the equations for the expected values of the fluxes) to derive a frequency distribution of annual runoff (Eagleson 1978g). While the Eagleson model in its original (or near original) form has been used extensively to study the hydrologic coupling of climate, soil and vegetation (e.g., Eagleson 1978f; Eagleson 1982; Eagleson and Tellers 1982; Eagleson and Segarra 1985; Milly and Eagleson 1987; Salvucci and Entekhabi 1994b; and Marani et al. 1997), it is limited as an operational tool for climate impact assessment—although Valdes et al. (1994) have shown its potential in that regard. The principal goal of this dissertation is then to develop and evaluate an operational version of the Eagleson model. Major components of that effort were to apply the model on a monthly scale, include snow and frozen soil, divide the vadose zone into two soil layers, and improve the representation of vegetation in the model. Model formulation is detailed in Chapter 2.

Although completion of a rigorous climate impact assessment with the model is beyond the scope of this dissertation, a "toy" integrated assessment was performed with an early, annual version of the model. A paper presented at a meeting of the American Society of Civil Engineers is included as Appendix A. It outlines a derived-distribution methodology for assessing the economic or environmental impacts of the interannual variability of runoff and for quantifying the expected benefits of mitigation decisions. An important aspect of the methodology is the inclusion of uncertainty in the climate parameters. Using a value-of-information framework, it is shown that, in terms of improved decision-making, the expected benefits of including such uncertainties can be substantial.

1.2. Objectives

Within overall development and evaluation of an operational version of the Eagleson model, a number of more specific objectives and interests were pursued in this dissertation. These are discussed below.

1.2.1. *Application of the Model to the Central United States*

The model is applied to the area of the United States bounded on the East and West by 87.5° W and 105° W, and on the South and North by 32.5° N and 45° N. That area encompasses most of what is considered to be the semi-arid U.S. Great Plains plus more humid regions to the east. The predominant climatic feature of the Great Plains is a strong longitudinal gradient in annual precipitation superimposed on a latitudinal gradient in temperature. The study area also contains a wide range of soils and vegetation over which to validate model results.

Our desire was to apply the model at a resolution high enough to capture regional patterns in the interaction of climate, soil and vegetation, and concurrently, to gain an understanding of the relative importance of subgrid variability in model parameters and runoff processes across variations in those three factors. From a pragmatic standpoint, we were also interested in using existing spatial datasets to estimate parameter values and drive the model. The database of the Vegetation/Ecosystem Modeling and Analysis Project (VEMAP; Kittel et al. 1996), which covers the entire United States at a resolution of a half of a degree, meets many of the data needs of the model. Specifically, it contains monthly climate variables over the period 1895-1993, as well as information on soils and vegetation types. Considerable additional effort was required to translate soil textural information to values of the soil parameters, and to develop a half-degree dataset of the parameters of the stochastic precipitation model from observations of hourly precipitation. Estimation of parameter values is detailed in Chapter 3.

1.2.2. *Partitioning of Evapotranspiration*

One of the attractive features of the Eagleson model is that it partitions evapotranspiration into transpiration and bare-soil evaporation. That partitioning is significant for the soil-water balance because the dynamics of the two processes are very different (see Sections 2.3.5 and 2.3.7). Nevertheless, it is often lacking in many water balance models, particularly those designed for use in rainfall-runoff models. On the other hand, it is included in many so-called soil-vegetation-atmosphere transfer (SVAT) schemes, which are generally designed for use as the land surface component of climate models. However, such models apparently disagree widely as to the relative magnitude of each component. For example, a comparison study of 14 SVAT models (Mahfouf et al. 1996) involved application of each model to a soybean crop in southwestern France over the five months of the 1986 growing season. For the 13 models that include it, bare-soil evaporation as a percentage of total evapotranspiration ranged from 1.5% to 44%. In light of such results, one of the main objectives of this dissertation is to capture and assess the partitioning of evapotranspiration over the range of climate, soil and vegetation conditions found in the study area. Validation of that partitioning is done to the extent possible using existing observations of bare-soil evaporation in the literature, as well as through the calculation of water-use efficiencies from the model results for average annual transpiration and large-scale estimates of vegetation productivity (see Sections 5.4 and 5.5).

1.2.3. *Vegetation Density and Water-Balance Dynamics*

Beyond the partitioning of evapotranspiration, we are interested in general in the role of vegetation in the dynamics of the water balance. To model vegetation with greater realism and detail than contained in the original Eagleson model, the water balance model was coupled to the evapotranspiration model of Shuttleworth and Wallace (1985), which is a one-dimensional energy combination model that divides the land surface into a coupled, two-component system comprised of the soil surface and the vegetation canopy (see Section 2.4).

The principal measure of vegetation density in the Shuttleworth-Wallace (SW) model is green leaf area index (LAI), which measures the ratio of transpiring leaf surface to land surface. Long-term, large-scale estimates of LAI based on satellite observations have recently become available to the wider research community (e.g., Los et al. 2000; Buermann et al. 2002). While such estimates could be used to drive the SW model over the period of the observations, their usefulness outside that period may be limited, especially under scenarios of climate change in which vegetation density and speciation is likely to change. Furthermore, there is still a great deal of uncertainty in both the mean and interannual variability in satellite-based observations of LAI (see Section 3.3.2). A hypothesis to be tested in this dissertation is that the mean peak in green LAI and its interannual variability can be captured by a simple modeling rule in which the peak of a fixed-shape envelope of LAI is maximized annually under the constraints of available soil moisture (see Sections 4.4, 5.2 and 6.3). In order to assess the significance of maximizing LAI on an annual basis, we also hold LAI fixed at the average maximized values (see Section 7.2). Finally, we consider the control that soil texture exerts on vegetation productivity (in the form of peak green LAI) through the water balance by examining whether the so-called inverse texture effect (Noy-Meier 1973) is observable in model results (see Sections 5.2 and 7.3).

1.2.4. *Seasonality of Soil Moisture*

Application and testing of the above LAI maximization hypothesis requires accurate modeling of the seasonal dynamics of soil moisture. In the central United States, late fall through early spring is typically a period of soil moisture recharge, followed by depletion over the growing season. We validate soil-moisture results by comparison with long-term observations at four sites within the study area spanning a range of climatic conditions (see Section 5.6). Using site-specific information on vegetation and soils, we evaluate the extent to which such factors are the source of modeling uncertainty and subgrid variability in soil moisture. For the most humid site, we also look at the potential effect of a shallow water table on vadose-zone moisture and the overall water balance.

1.2.5. *Partitioning of Precipitation into Surface Runoff and Infiltration*

An additional aspect of the Eagleson model critical to accurately capturing the water balance is the partitioning of precipitation at the land surface into surface runoff and infiltration (Eagleson 1978e). While this is also typically a strength of parameter-intensive rainfall-runoff models, it is absent in many simpler water-balance models and SVAT schemes, particularly those that operate at longer time steps. Surface runoff can not only be a significant part of total runoff but can also influence vegetation dynamics, as it is water unavailable for transpiration. In our model, we use Eagleson's (1978e) original formulation of infiltration dynamics, which captures only Hortonian (*i.e.*, infiltration-excess) runoff. While Eagleson (1978f) and others (Marani et al 1997; Salvucci and Entekhabi 1994b) have examined the sensitivity of that formulation to the climate and soil parameters in the model, there has been no rigorous effort to compare model predictions with observations. Doing so across the wide-ranging soils and climates of the study area is a major objective of this dissertation (see Section 5.7). Specifically, we developed a data set of storm-flow and base-flow statistics by application of a hydrograph separation methodology to daily streamflow data from 932 USGS stream gauges located across the study area. Comparison of interpolated values to model results provides a basis for assessing the ability of the one-dimensional model to approximate the spatially complex process of surface-runoff generation. In particular, we evaluate the significance of uncertainty and subgrid variability in soil hydraulic properties through an analysis of the sensitivity of surface runoff to scaled soil parameters (see Section 7.4).

1.2.6. *Interannual Variability of the Water Balance*

Because vulnerabilities to climate change and variability are typically associated with extremes in the hydrologic cycle, it is crucial for any model used for climate impact assessment to be able to capture the interannual variability of the water balance. We focus the analysis on precipitation and runoff, the two components of the water balance for which there are the most widespread and longest-term measurements. The interannual variability in the VEMAP precipitation data is compared to the interannual variability implied by the stochastic precipitation model (see Section 6.2). We then consider what the differences imply about the sources of the interannual variability of precipitation. The interannual variability in modeled surface runoff and groundwater recharge is compared to the interannual variability in storm flow and base flow in the above noted streamflow observations (see Section 6.4). By examining the structure in the coefficients of variation and skewness in the model results and observations, we quantify the significance of subgrid processes to the interannual variability of storm flow, and groundwater storage to the interannual variability of base flow.

1.3. Stochastic Soil Moisture Approaches to the Temporal Variability of the Water Balance

The expected-value approach of Eagleson is only one statistical-dynamical methodology for capturing the impact of the high-frequency variability of precipitation on the water balance, albeit a particularly powerful one for the objectives of this dissertation. Nonetheless, it is not without its weaknesses, the most fundamental of which is that deriving the expected values of the water balance fluxes requires lumping soil moisture—the main controlling variable—into a “temporal average of the spatial average” (Eagleson 1978a). We partially address the spatiotemporal variability of soil moisture in our version of the model by using three values of soil moisture that vary according to a monthly time step (see Section 2.2). An alternative is to keep the formulation of the fluxes simple enough that soil moisture can be treated as a stochastic variable. Two approaches that do so in a similar manner but at different spatial scales are discussed below.

One of the issues encountered in scaling a point model such as the Eagleson model up to regional scales is the potential for feedbacks from the land surface to the atmosphere. As soil moisture can be viewed as the principal mediator of those feedbacks, a stochastic soil moisture formulation of the coupled land-atmosphere water balance is one means of evaluating the impact of the feedbacks on the overall temporal variability of the water balance. As an ancillary project to the main work of this dissertation, such a formulation was developed and used to study the regional-scale temporal variability of soil moisture over an area encompassing the State of Illinois. A paper published in the Journal of Hydrometeorology is attached as Appendix B.

A significant feature of the generic, spatially dimensionless soil-water-balance equation is that it applies at all scales (providing that the control volume is properly defined.) The challenge for specific implementations is formulating each flux in a manner appropriate to the scale and the problem being studied. In the case of statistical-dynamical approaches, the stochastic formulation of precipitation is the most critically scale-dependent flux. In the paper in Appendix B, precipitation is treated as a continuous soil-moisture-dependent process modulated by colored noise. The formulation of precipitation and the other fluxes allows the water balance equation to be written as a stochastic differential equation (SDE) that has a probability density function of soil moisture as a steady-state solution.

Rodriguez-Iturbe et al (1991) were the first to apply an SDE-based approach to the large-scale coupled land-atmosphere water balance. More recently, Rodriguez-Iturbe and coworkers (*e.g.,* Rodriguez-Iturbe et al. 1999; Laio et al. 2001a) have applied the same approach to the soil water balance at a point. Their work is of particular interest to this dissertation for two reasons. The first is that it also models the arrival of precipitation events as a Poisson process, and therefore possesses a conceptually similar stochastic forcing as the Eagleson model. The second is it that it models the probabilistic behavior of moisture stress in vegetation (*e.g.*, Ridolfi et al. 2000; Fernandez-Illescas et al. 2001; Porporato et al 2001). A key assumption of the stochastically stationary form of their model is that water stress is principally an inter-storm phenomenon. In contrast, in applying the water-limited LAI-maximization hypothesis in our monthly version of the Eagleson model, we have assumed that water stress is principally a seasonal phenomenon. While our results support seasonal water stress being the dominant control on vegetation density, it is likely that inter-storm stress also plays a role, especially with regard to the fitness and dominance of individual species (*e.g.,* Laio et al. 2001b). We examine the seasonal and interannual variation in soil moisture across the study area, and its implications for the likelihood of water stress, in observations and model results in Sections 4.4, 5.6, and 6.3.

Chapter 2: Model Formulation

2.1. Overview of the Original Eagleson Model and Its Solution

Eagleson's statistical-dynamic water balance model (Eagleson 1978a-g) is a one-dimensional representation of soil moisture dynamics as forced by a stochastic climate. More specifically, atmospheric supply of moisture, *i.e.*, precipitation, is modeled as rectangular pulses that arrive according to a Poisson process (see Figure 2.1). A single interstorm/storm event is completely described by the time between storms, t_b, the storm duration, t_r, and the storm intensity, i. The storm depth, h $(= it_r)$, is also an important characteristic. t_b, t_r and i are assumed to be independent and well approximated by exponential distributions. h is taken to be gamma-distributed for the sake of analytical tractability, despite the assumption being inconsistent with the previous assumptions. The atmospheric demand for moisture is modeled more simply as a constant rate of potential evaporation, e_p. In Eagleson's original annual version, climate is taken as stationary throughout a "rainy season" in which all precipitation falls as rain.

Soil moisture dynamics at the land surface are captured using a modified version of Phillip's (1969) approximate analytical solution to the concentration-dependent diffusion equation (*i.e.*, the Richards equation). Soil hydraulic properties are based on the Brooks and Corey (1966) model. Using a derived-distribution approach, the one-dimensional physical model is combined with the probability distributions of the stochastic precipitation model to arrive at expected values of single storm and interstorm fluxes of infiltration, bare soil evaporation and surface retention evaporation. These values are then aggregated to annual values by multiplying by the expected number of storms over the length of the rainy season. Transpiration during interstorm periods is linearly superimposed on the dynamics of bare soil evaporation and assumed to take place at a constant fraction Mk_v of e_p, where M is the fractional vegetation coverage, and k_v is the vegetal transpiration efficiency. Similarly, recharge to groundwater is modeled as steady-state gravity drainage less hydrostatic capillary rise from a fixed water table. Assuming no change in soil moisture storage, the mean annual soil-water balance can be written as

$$E[I_A(s,\text{climate},\text{soil})] = E[E_{TA}(s,\text{climate},\text{soil},\text{vegetation})] + E[R_{gA}(s,\text{climate},\text{soil})] \quad (2.1)$$

where

$E[I_A]$ the expected value of annual infiltration (cm);

$E[E_{TA}]$ the expected value of annual evapotranspiration from soil (cm);

$E[R_{gA}]$ the expected value of annual recharge to groundwater (cm).

Each term in (2.1) has an analytical form and is dependent on soil moisture as defined by relative soil saturation, s, and on a relatively small number of climate, soil and vegetation parameters. s varies between zero and one and is given by

$$s = \frac{\theta_t - \theta_r}{n_t - \theta_r} \quad (2.2)$$

where

θ_t total volumetric soil water content;

θ_r residual volumetric soil water content;

n_t total porosity.

The numerator in (2.2) equals the effective volumetric soil water content, θ, and the denominator equals the effective porosity, n.

Although the dependence on soil moisture of all three terms in (2.1) is represented by the same letter s, in actuality different values of s at different points in time and in the soil column control the given fluxes. Namely, infiltration is dependent on s at the beginning of storms, while the bare soil evaporation component of evapotranspiration depends on the s at the beginning of interstorm periods. While these two fluxes are primarily dependent on s in the upper part of the soil column, recharge to groundwater is controlled by s at the bottom of the soil column. The analytical solution of all three fluxes requires an assumption of initially uniform soil moisture in a semi-infinite soil column. In order to solve (2.1), Eagleson (1978a) uses a single value, s_o, which the author defines to be the "temporal average of the spatial average" and which Salvucci and Entekhabi

(1994a) show to be more precisely associated with the "equivalent steady-state moisture profile." With that simplification, (2.1) can be solved numerically for s_o. Eagleson surmises that the use of a single value of s tends to overestimate surface runoff as a result of s_o being an overestimate of the mean pre-storm soil moisture.

2.2. Overview of the New Monthly, Two-Soil-Layer Version of the Eagleson Model

One advantage of the annual formulation of Eagleson's model—and its assumption of a uniform, steady-state value of soil moisture—is that it obviates the need to consider storage and the depth of the dynamic layer of the soil. However, as an operational tool for climate impact assessment, the annual version is significantly limited. In order to have a model that captures the seasonal dynamics and depth-dependence of soil moisture, a monthly, two-soil-layer version was developed for this dissertation.

The development of the present version of the model involved a process of application of Eagleson's original model and successively more complicated versions to several locations across the study area with long-term records of soil moisture. Additional insight was drawn from comparisons made by Salvucci and Entekhabi (1994a,b) between solutions of Eagleson's model and numerical simulations with the finite difference model of Milly (1982), which is based on the same soil physics. The first important conclusion resulting from those analyses is that the steady-state solution of soil moisture from Eagleson's model can be a substantial overestimate of the actual temporal mean in the root zone, with the difference being greater for drier climates. This is explainable by the fact that the actual mean is less than the post-storm soil moisture, which controls bare soil evaporation. Closure of the water balance can only be achieved by a higher value of s_o, which serves both to decrease infiltration and to increase groundwater runoff and bare soil evaporation. The resulting overestimate in surface runoff is in addition to that which Eagleson realized would occur with the temporal mean. An additional observation from the work of Salvucci and Entekhabi (1994a,b) is that the mean soil moisture profile is nearly identically to the mean pre-storm profile. This is the consequence of the fact that the majority of the redistribution of soil moisture after a storm occurs within a few days of the storm. As seen below, an assumption that the mean pre-storm soil moisture is equal to the temporal mean is used in the solution of the model.

The version of the model developed for this dissertation is illustrated schematically in Figure 2.2. The soil column has been divided into root (upper) and recharge (deep) zones, with mean monthly values of soil moisture of s_u and s_d, respectively. s_d is assumed to be uniform with depth and to vary slowly on a seasonal cycle. As noted above, the highly dynamic nature of the root zone requires consideration of not only the temporal mean value of soil moisture in that zone but also the mean values prior to storm and interstorm periods. Eagleson's (1978c) analytical solution of the Richards equation uses the assumption of initially uniform soil moisture in a semi-infinite soil column. As long as the bottom of the root zone is deeper than the average penetration depth of the wetting and drying fronts during storm and interstorm periods, respectively, the semi-infinite assumption is reasonably satisfied. However, the presence of wetting and drying fronts implies non-uniform initial conditions. During periods of soil moisture recharge, the temporal mean of soil moisture generally decreases with depth, and the assumption of a uniform initial profile will tend to underestimate surface runoff. In contrast, during periods of soil moisture depletion, soil moisture generally increases with depth, and the assumption leads to overestimating runoff. More significant, however, is the pronounced wetting front that is usually present at the end of storms. The estimation of a mean penetration depth for the wetting front, z_p—over which infiltration is averaged to obtain s_p, the mean post-storm soil moisture—is described in Section 2.3.

Another major difference of the present version of the model is that bare soil evaporation and transpiration are treated as coupled processes above the soil surface. Vegetation is conceptualized as being distributed evenly across the land, with bare soil interspersed between individual plants or small clumps of plants—as opposed to non-interacting fractions of the land surface. As a result, available energy is relatively homogeneously distributed across the land surface at the scale of the stand, such that one can define a point near the canopy top where there is a combined flow of latent and sensible heat from the two surfaces. We thus make use of the quantity e_{ps}, which is the rate of potential bare soil evaporation in the presence of the given density of vegetation, in contrast to Eagleson's use of e_p, which is that in the absence of vegetation (*i.e.*, $M=0$).

Likewise, we define e_{pv} as the potential rate of transpiration from the given density of vegetation, as opposed to Eagleson's definition as the rate for a closed canopy (*i.e.*, $M=1$). To estimate both potential rates, we use a two-component evaporation model (Shuttleworth and Wallace 1985) in which leaf area index (LAI) is the principal measure of vegetation density. In order to simplify use of the separate rates, we assume that surface retention of precipitation occurs significantly only on vegetation in the form of interception. In contrast, Eagleson treats surface retention as occurring at the same depth over both vegetation and bare soil.

A final difference is that the present formulation does no account for interaction with the groundwater table. Although it would be easy enough to include capillary rise from a fixed water table in the manner of Eagleson (1978c), the need to determine a temporally and spatially representative water table depth at the regional scale introduces additional difficulties. In regions where the water table is largely below the recharge zone, we might assume that is in unconsolidated parent material with low capillarity. In regions where the water table is frequently in the recharge zone or higher, the model will underestimate s_u and, consequently, evapotranspiration and surface runoff. Surface runoff will also be underestimated by virtue of the fact that, as in Eagleson's (1978e) original formulation, it is modeled as occurring only by the Hortonian (*i.e.*, infiltration excess) mechanism. In general, the one-dimensional form of the model is a significant limitation to the modeling of runoff processes.

Following Eagleson, we write equations for the soil water balance in terms of expected values of the relevant fluxes. Crucial additions are snow storage at the surface and moisture storage in both soil layers. The water balance of the snowpack during month i is given by

$$\Delta S_i = f_{s_i} E[P_i] - E[W_i] \tag{2.3}$$

where

ΔS_i	change in water equivalent of the snowpack (cm);
P_i	precipitation (cm);
f_{si}	fraction of precipitation which is snow;

W_i	water equivalent of the snowmelt (cm).

The water balance in the root zone during month *i* is defined by

$$n_u z_u \Delta s_{u_i} = E[I_i(s_{u_i})] - E[E_{v_i}(s_{u_i})] - E[E_{s_i}(s_{p_i})] - E[Q_{ud_i}(s_{u_i}, s_{d_i})] \tag{2.4}$$

where

n_u	effective porosity of the root zone;
z_u	depth of the root zone (cm);
Δs_{ui}	change in soil saturation in the root zone;
I_i	infiltration (cm);
E_{vi}	vegetal transpiration (cm);
E_{si}	evaporation from bare soil (cm);
Q_{udi}	flow from the root zone to the recharge zone (cm).

The water balance in the recharge zone is

$$n_d z_d \Delta s_{d_i} = E[Q_{ud_i}(s_{u_i}, s_{d_i})] - E[R_{g_i}(s_d)] \tag{2.5}$$

where

n_d	effective porosity of the recharge zone;
z_d	thickness of the recharge zone (cm);
Δs_{di}	change in soil saturation in the recharge zone;
R_{gi}	gravity drainage from the bottom of the recharge zone (cm).

2.3. Expected Values of Water Balance Fluxes

In this section, the equations that govern the expected values of the fluxes in and out of the two soil layers are presented. The focus is on equations unique to the present version of the model. Accordingly, the reader is referred to Eagleson (1978a-e) for detailed derivations of equations that are similar to or unchanged from the original model. The flux calculations use six evapotranspiration parameters, five precipitation parameters

Table 2.1. Parameters of the water balance model.

SYMBOL	DESCRIPTION	UNITS
evapotranspiration:		
e_{ps}	mean rate of potential bare-soil evaporation	cm/day
e_{pv}	mean rate of potential transpiration	cm/day
e_{hv}	mean rate of evaporation from vegetal interception	cm/day
h_v	vegetal interception capacity	cm
Ψ_{uc}	critical root-zone soil matric potential	cm
Ψ_{lc}	critical leaf water potential (equivalent to the wilting point matric potential in the root zone)	cm
precipitation:		
m_{tr}	mean storm duration	days
m_{tb}	mean duration of interstorm periods	days
m_i	mean storm intensity	cm/day
m_h	mean storm depth	cm
κ	parameter of the gamma distribution of storm depth	dimensionless
soil:		
K_s	saturated hydraulic conductivity	cm/day
Ψ_s	bubbling matric potential	cm
m	pore size distribution index	dimensionless
n	effective porosity	dimensionless
z	thickness of soil layer	cm
other:		
τ	length of the month	days
T	mean air temperature	°C

and five soil parameters for each soil layer. In addition, air temperature is used in the modeling of snow accumulation and melt and soil freezing. Model parameters are summarized in Table 2.1 and will be used in the remainder of the dissertation without definition. As in Section 2.2, the subscripts u and d on the soil parameters refer to values for the root and recharge zones, respectively. For the sake of notational parsimony, flux rates and soil moisture will not be indexed by month. Likewise, all climate parameters have monthly varying values but will not be indexed. On the other hand, all soil parameters are assumed temporally invariant.

2.3.1. *Snow Accumulation and Melt*

For most of the study region, snow is a relatively small component of annual precipitation totals. In consideration of that fact, we model snow accumulation and melt more simply and deterministically than we do rainfall. Specifically, we use a temperature index methodology. During months in which the mean temperature is below -4 °C, all precipitation during the month is assumed to be snow. When the mean temperature is above 6 °C, all precipitation is taken to be rain. Between the two temperatures, precipitation is linearly fractionated between snow and rain such that

$$f_s = \begin{cases} 1, & T \leq -4\,^{\circ}C \\ (6-T)/10, & -4\,^{\circ}C < T < 6\,^{\circ}C \\ 0, & T \geq 4\,^{\circ}C \end{cases} \tag{2.6}$$

Snowmelt is assumed to occur whenever T is above -4 °C. The rate of snowmelt is taken to be 0.5 cm per °C above that temperature and to occur for a maximum of three consecutive days. All of the snow that falls in a given month is made available for melt in that month. Thus,

$$E[W] = \begin{cases} 0, & T \leq -4\,^{\circ}C \\ \min\{S + f_s\, E[P], 1.5(4+T)\}, & T > -4\,^{\circ}C \end{cases} \tag{2.7}$$

where S is the water equivalent of the snowpack at the beginning of the month (cm).

2.3.2. *Groundwater Recharge*

As in Eagleson (1978c), percolation to groundwater is modeled as steady-state gravity flow. Unlike Eagleson, we do not account for capillary rise from the groundwater table. Thus groundwater recharge is simply equal to the hydraulic conductivity in the recharge zone. Brooks and Corey (1966) formulate the dependency of the unsaturated hydraulic conductivity on s as

$$K(s) = K_s s^c \tag{2.8}$$

where c is the pore disconnectedness index, which the authors show to be related to the pore size distribution index by

$$c = \frac{2+3m}{m} \tag{2.9}$$

The expected value of recharge to groundwater in the given month is thus

$$E[R_g] = \tau K_{sd} s_d^{c_d} \tag{2.10}$$

2.3.3. *Flow between Soil Layers*

Darcy's Law for unsaturated flow governs the moisture flux between the root zone and the recharge zone:

$$Q(s) = K(s)\left({d\Psi(s)}/{dz} + 1 \right) \tag{2.11}$$

where

$Q(s)$	vertical flow (cm/day);
$d\Psi(s)/dz$	matric potential gradient (cm/cm).

Matric potential, Ψ, is taken as positive (*i.e.*, the deficit below atmospheric pressure). Positive Q thus represents flow from the root zone to the recharge zone, while negative Q represents flow in the other direction. Brooks and Corey (1966) formulate the dependency of the matric potential on s as

$$\Psi(s) = \Psi_s s^{-1/m} \tag{2.12}$$

Ideally, we would use in (2.11) the values of $K(s)$ and $d\Psi(s)/dz$ at the interface of the two soil layers. However, because the interface is actually an ill-defined transition zone, we use the mean value of s in each layer. The hydraulic conductivity is then estimated as the geometric mean of $K_u(s_u)$ and $K_d(s_d)$. For estimation of the gradient of the matric potential, we take $\Psi_u(s_u)$ and $\Psi_d(s_d)$ to be separated by a distance of $\frac{1}{2}(z_u + z_d)$. For the expected value of flow between soil layers during the given month, this gives

$$E[Q_{ud}] = \tau \frac{(K_{su} K_{sd} s_u^{c_u} s_d^{c_d})^{1/2}}{2} \left[\frac{2\left(\Psi_{sd} s_d^{-1/m_d} - \Psi_{su} s_u^{-1/m_u} \right)}{z_u + z_d} + 1 \right] \tag{2.13}$$

2.3.4. *Infiltration and Surface Runoff*

Figure 2.3 illustrates how surface runoff from a single rectangular pulse of rainfall is modeled. $f_i(t)$ is the infiltration capacity and is based on Philip's approximate analytical solution of the Richards equation (Eagleson 1978c):

$$f_i(t) = \tfrac{1}{2} S_i t^{-1/2} + \tfrac{1}{2} A_o \qquad (2.14)$$

where

$$A_o = \tfrac{1}{2} K_{su}\left(1 + s_u^{\,c_u}\right) \qquad (2.15)$$

and S_i is the effective infiltration sorptivity (cm/day$^{1/2}$) over the range of s_u to one for the relative soil saturation. Salvucci and Entekhabi (1994a) argue that Eagleson's (1978c) equation for S_i does not account for the infinite diffusivity that develops at $s = 1$. In their use of the model, they include a modification to S_i suggested by Philip (1958) that gives

$$S_i = \left[2 n_u K_{su} \Psi_{su} (1 - s_u) \left(1 + \frac{10(1 - s_u)\phi_i(s_u, m_u)}{3 m_u \pi} \right) \right]^{1/2} \qquad (2.16)$$

where $\phi_i(s_u,m_u)$ is the dimensionless effective infiltration diffusivity, for which Eagleson (1982) uses the approximation,

$$\phi_i(s_u, m_u) = \left[\tfrac{5}{3} + \left(\tfrac{1}{m_u} + 2 \right) (1 - s_u)^{1.425 - 0.0375\left(\frac{1}{m_u} + 2\right)} \right]^{-1} \qquad (2.17)$$

The soil surface becomes saturated and runoff begins when the infiltration capacity falls below the intensity of the storm, i. The time at which this occurs, t_p, is referred to as the *ponding time* and is typically estimated using the time compression approximation (TCA) (Salvucci and Entekhabi 1994a). As shown in Figure 3, the TCA consists of shifting the infiltration capacity curve to the right by an amount t_s, such that the area beneath the shifted curve from t_s to t_p is equal to it_p, the depth of infiltrated rainfall at t_p. Once runoff begins at t_p, rainfall excess, R^*_{sj}, is generated by the given storm (indexed as j) from that point until the storm ends at t_r. In applying the TCA, Eagleson (1978e) approximates R^*_{sj} as the difference between $i(t_p - t_r)$ and the area beneath the initial infiltration capacity curve, $f_i(t)$, from t_p to t_r. We believe it is more accurate to use the area beneath the shifted capacity curve, $f_i(t - t_s)$, as shown in Figure 2.3. R^*_{sj} is then given by

$$R^*_{sj} = \int_{t_o}^{t_r} \left(i - \tfrac{1}{2} S_i (t - t_s)^{\frac{1}{2}} - A_o \right) dt \tag{2.18}$$

Eagleson (1978e) shows that, under the assumption that $i >> A_o$,

$$t_p \cong \frac{S_i^2}{2(i - A_o)^2} \tag{2.19}$$

It can also be shown that the TCA leads to

$$t_s \cong \tfrac{1}{2} t_p \tag{2.20}$$

With the above two approximations, (2.18) evaluates to

$$R^*_{sj}(i, t_r, s_u) \cong \left[i - \tfrac{1}{2} K_{su} \left(1 + s_u^{c_u} \right) \right] t_r - S_i t_r^{\frac{1}{2}} \tag{2.21}$$

where (2.15) has been substituted.

Through approximate integration of the joint probability distribution of i and t_r (which under the assumption of the independence of i and t_r is simply the product of the two exponential distributions) over the domain of R^*_{sj}, Eagleson (1978e) derives a probability distribution for R^*_{sj}, which, in the absence of capillary rise, has as its mean

$$E[R^*_{sj}] = m_i m_{tr} e^{-2\sigma - A_o/m_i} \Gamma(\sigma + 1) \sigma^{-\sigma} \tag{2.22}$$

where

σ capillary infiltration parameter (dimensionless);

$\Gamma(\sim)$ gamma function.

σ is defined by

$$\sigma = \frac{1}{2}\left(\frac{S_i^{\,2}}{m_{tr} m_i^{\,2}}\right)^{1/3} \tag{2.23}$$

(2.22) and (2.23) are unaffected by the difference between our and Eagleson's calculation of R^*_{sj} because one of the approximations employed by Eagleson involves dropping the second term of (2.21), which is the term in our equation different (by a factor of $2^{1/2}$) from that of Eagleson's.

In Figure 2.3 and in the derivation of (2.22), it is assumed that the time it takes to fill surface retention is negligible. In order to account for the volumetric effect of surface retention, Eagleson (1978e) takes the expected value of surface runoff to be the difference between (2.22) and the expected value of evaporation from surface retention. Tellers and Eagleson (1980) observe that this counts surface retention against only storms producing runoff. They propose setting the rainfall excess equal to surface runoff and subtracting surface retention from infiltration. Doing that and using a set of relationships that stem from the assumption of the independence of i, t_r and t_b:

$$m_h = m_i \, m_{tr} \tag{2.24}$$

$$m_v = \frac{\tau}{m_{tr} + m_{tb}} \tag{2.25}$$

$$E[P] = m_v \, m_h \tag{2.26}$$

where m_v is the mean number of storms in the given month, we can use (2.22) to write a surface runoff ratio for rainfall:

$$\frac{E[R_s]}{(1 - f_s)\, E[P]} = e^{-2\sigma - A_0/m_i}\,\Gamma(\sigma + 1)\sigma^{-\sigma}, \; f_s < 1 \tag{2.27}$$

where R_s is total surface runoff from rainfall for the given month (cm).

The $1\text{-}f_s$ factor has been applied in (2.27) under the simplifying assumption that, in months with both snow and rainfall, the two types of precipitation occur in separate periods, with the length of the snow period given by $f_s\,\tau$. Furthermore, rain-on-snow events at the transition from a snow to a rain period are not explicitly considered. We do, however, consider the general possibility of surface runoff from snowmelt by applying the dynamic model for rain depicted in Figure 2.3. The total snowmelt for the month is assumed to occur in a single pulse with duration up to 3 days. (2.7) then leads to

$$i_w = 0.5(T+4) \tag{2.28}$$

$$t_{rw} = \min\left\{E[W]/i_w\,,3\right\} \tag{2.29}$$

where i_w and t_{rw} are the intensity (cm/day) and duration (days) of the snowmelt pulse, respectively. The expected depth of runoff from the pulse is given by (2.21):

$$E[R_w] = R^*_{s\,j}(i_w, t_{rw}, s_u) \tag{2.30}$$

A consideration for both snowmelt and rainfall is whether infiltration occurs into frozen soil. A temperature index approach is taken here as well, such that whenever the sum of the mean temperatures of the given month and the previous month is below 0°C, the following correction factor devised by Rawls and Brakensiek (1985) is applied to the hydraulic conductivity of the root zone soil:

$$FSC = \begin{cases} 2.0 - 1.9\dfrac{s_u}{s_{33}}, & s_u < s_{33} \\ 0.1, & s_u \geq s_{33} \end{cases} \tag{2.31}$$

where s_{33} is the effective soil saturation in the root zone at a matric potential of 33 kPa (=337 cm), as determined by (2.12).

Subtracting snowmelt and rainfall runoff, along with interception loss, from the inputs to infiltration gives the expected value of infiltration during the given month as

$$E[I] = (1 - f_s)E[P] + E[W] - E[R_s] - E[R_w] - E[E_{hv}] \tag{2.32}$$

where E_{hv} is evaporation from vegetal interception. An equation for $E[E_{hv}]$ is presented in the next section.

The final quantity that must be estimated for our model of infiltration dynamics is the mean penetration depth of wetting fronts, over which the expected value of infiltration will be distributed. Eagleson (1978c) approximates mean penetration depths based on the sum of a diffusive component and a gravity drainage component. The diffusive component is taken from the analytical solution of the Richards equation, with the standard assumptions of constant diffusivity, D, initially uniform soil moisture, θ_i, and a different, but constant soil moisture at the surface, θ_o (Eagleson 1970). That solution is

$$\frac{\theta - \theta_o}{\theta_i - \theta_o} = erf\left[\frac{z}{2(Dt)^{1/2}}\right] \tag{2.33}$$

For the purposes of estimating how deep the water table must be for the assumption of a semi-infinite soil column to be satisfied, Eagleson sets the argument of the error function in (2.33) equal to two. At that value, the error function evaluates to 0.995, meaning that, at the corresponding depth z, θ is only slightly perturbed away from θ_i and towards θ_o. In the case of infiltration, a penetration depth so estimated would be at the asymptotic tail of the wetting front and typically on the order of the root zone depth or greater. In order to provide a penetration depth more suitable to our purposes, we set the argument of the error function equal to one, at which the error function evaluates to 0.84. We thus rewrite Eagleson's equation for the penetration depth as:

$$z_p = 2(D_i m_{tr})^{1/2} + \frac{m_{t_r} K_{su}}{n_u} \tag{2.34}$$

where D_i is the effective infiltration diffusivity (cm^2/day), which Eagleson (1978c) derives as

$$D_i = \frac{5 K_{su} \Psi_{su} \phi_i (s_u, m_u)}{3 m_u n_u} \tag{2.35}$$

With a value for z_p determined, the mean post-storm relative soil saturation is calculated as

$$s_{p_i} = s_{u_i} + \frac{E[I_i]}{n_u z_{p_i}} \tag{2.36}$$

2.3.5. *Evaporation from Bare Soil*

As illustrated in Figure 2.4, the rate of exfiltration by bare-soil evaporation is estimated in a manner analogous to the infiltration rate. The analog to rainfall with constant intensity is a constant rate of potential evaporation, e_{ps}. Initially evaporation proceeds at e_{ps}. This is typically referred to as *stage-one* evaporation. At time t_p, the maximum rate at which the soil can deliver moisture (i.e., the exfiltration capacity), $f_e(t)$, drops below e_{ps}. Beyond t_p, evaporation proceeds at the rate determined by $f_e(t)$ and is referred to as *stage-two* evaporation. At time t_e, $f_e(t)$ reaches zero and bare-soil evaporation ceases. The process can be cut short at any point by the end of the interstorm period defined by t_b. In the manner of the infiltration process, t_p is estimated using the TCA via a time shift in $f_e(t)$ of t_s. Following Eagleson (1978d), we derive an expected value for bare soil evaporation during the j^{th} interstorm period by integrating the product of the volume of the bare soil evaporation and the probability distribution of t_b over the three domains of t_b (i.e., $t_b \le t_p$, $t_p < t_b \le t_e$ and $t_e < t_b$):

$$\begin{aligned} E[E_{sj}] = {} & \int_0^{t_p} e_{ps}\, t_b\, f_{T_b}(t_b)\, dt_b + \int_{t_p}^{t_e} \left(e_{ps}\, t_p + \int_{t_p}^{t_b} f_e(t - t_s)\, dt \right) f_{T_b}(t_b)\, dt_b \\ & + \int_{t_e}^{\infty} \left(e_{ps}\, t_p + \int_{t_p}^{t_e} f_e(t - t_s)\, dt \right) f_{T_b}(t_b)\, dt_b \end{aligned} \tag{2.37}$$

The exponential distribution of t_b is

$$f_{T_b}(t_b) = \frac{e^{-\frac{t_b}{m_{tb}}}}{m_{tb}} \tag{2.38}$$

The formulation of (2.37) is greatly simplified by the fact that we do not include an initial period of evaporation from surface retention, as does Eagleson (1978d).

Based on an exact solution of the differential equation for the analogous problem of heat conduction in solids (Carslaw and Jaeger 1959), Eagleson (1978c) presents an equation for the exfiltration capacity, under the absence of gravity and with the root sink being evenly distributed over the root zone:

$$f_e(t) = \tfrac{1}{2} S_e t^{-\frac{1}{2}} - (2e_v / z_u)(D_e t / \pi)^{\frac{1}{2}} \tag{2.39}$$

where

S_e exfiltration sorptivity (cm/day$^{1/2}$);

e_v mean rate of transpiration (cm/day);

D_e effective exfiltration diffusivity (cm^2/day).

Entekhabi and Eagleson (1989) derive the exfiltration sorptivity as

$$S_e = 2 s_p^{\frac{1}{2m_u}+2} \left[\frac{8 n_u m_u K_{su} \Psi_{su}}{3(1+3m_u)(1+4m_u)} \right]^{\frac{1}{2}} \tag{2.40}$$

The effective exfiltration diffusivity is related to the exfiltration sorptivity by (Eagleson 1978c)

$$D_e = \pi \left(\frac{S_e}{2 n_u s_d} \right)^2 \tag{2.41}$$

Eagleson (1978c) states that the first term of (2.39) is about two orders of magnitude greater than the second for typical parameter values. However, the second term grows with t (as the first term decreases) and can be comparable in size to the first term when $t \geq m_{tb}$. After dropping the second term, Eagleson (1978c) goes on to include a negative e_v term. This implicitly assumes that the vegetation extracts moisture at the surface, as opposed to evenly throughout the root zone. More realistic than either assumption is one of extraction from the root zone in proportion to the density of root mass. In Section 3.3.3, we estimate root zone depths based on the fit of observations of root density to an exponential curve (Jackson et al. 1996). Carslaw and Jaeger (1959) also present a solution for the heat-conduction problem with a sink of exponentially distributed intensity. Using that solution, we formulate the exfiltration capacity function as

$$f_e(t) = \tfrac{1}{2} S_e t^{-\frac{1}{2}} - e_v \{1 - e^{\alpha^2 D_e t} erfc\,[(\alpha^2 D_e t)^{\frac{1}{2}}]\} \tag{2.42}$$

where α is the decay constant for the root density. In Section 3.3.3, we take the depth of the root zone to be that which contains 95% of the root mass. Under that assumption, it can be shown that

$$\alpha = -\frac{\ln[0.05]}{z_u} \tag{2.43}$$

We note that neither (2.42) nor Eagleson's (1978c) final formulation of the exfiltration capacity function includes a gravity-drainage component (which would be included in a complete solution of the problem.) Eagleson (1978c) neglects gravity drainage based on its relative size. We can further argue for neglecting it for our two-soil-layer version of the model by recognizing that, as the soil in the root zone dries down, the potential gradient between it and the recharge zone becomes increasingly negative, thereby offsetting the gravity flow between the two layers to the eventual point of creating a net flow upwards. Neglecting this upwards flow in the latter part of interstorm periods offsets neglecting the net flow down at the beginning of interstorm periods.

Even with its neglect of the flow between the root and recharge zones, (2.42) is of a form that does not allow for analytical evaluation of (2.37). However, (2.39) does lead to an analytical solution. We use that knowledge, plus the fact that the second term of (2.42) is generally greater than the second term of (2.39) but less than e_v, to approximate the second term of (2.42) with a weighted sum of the second term of (2.39) and e_v:

$$f_e(t) \cong \tfrac{1}{2} S_e t^{-\frac{1}{2}} - (1-w)\,e_v - w\,(2e_v/z_u)(D_e\, t/\pi)^{\frac{1}{2}} \tag{2.44}$$

where w is the weight. We solve for w, by setting (2.42) and (2.44) equal at $t = m_{tb}$. Along with (2.43), this leads to

$$w = \frac{e^{x} erfc[x^{1/2}]}{1 + \dfrac{2x^{1/2}}{\sqrt{\pi}\ln[0.05]}} \tag{2.45}$$

where

$$x = \frac{\ln^{2}[0.05] D_{e} m_{tb}}{z_{u}^{2}} \tag{2.46}$$

In Figure 2.4, w is plotted as a function of x. A minimum of 0.685 is reached at x=1.10. w subsequently increases, reaching one again at x = 3.88. At greater values of x, (2.42) is greater than (2.39) when $t = m_{tb}$. Consequently, w is held at one when x exceeds 3.88. Such cases are rare because they generally involve large values of both D_e and m_{tb} (because D_e is an increasing function of s, large values of m_{tb} imply relatively small values of D_e for a given soil.)

With (2.44) as the exfiltration capacity curve and (2.41) substituted in, (2.37) evaluates to

$$\begin{aligned} E[E_{sj}] = {} & m_{tb} e_{ps} + \tfrac{1}{2} S_{e} (\pi m_{tb})^{1/2} \left(1 - \frac{w e_{v} m_{tb}}{n_{u} z_{u} s_{p}}\right) \left\{ erf\left[\left(\frac{t_{e} - t_{s}}{m_{tb}}\right)^{1/2}\right] - erf\left[\left(\frac{t_{p} - t_{s}}{m_{tb}}\right)^{1/2}\right]\right\} e^{-\frac{t_{s}}{m_{tb}}} \\ & - m_{tb} \left\{ e_{ps} + e_{v} \left[1 - w + \frac{w S_{e}}{n_{u} z_{u} s_{p}} (t_{p} - t_{s})^{1/2}\right]\right\} e^{-\frac{t_{p}}{m_{tb}}} + m_{tb} e_{v} \left\{1 - w + \frac{w S_{e}}{n_{u} z_{u} s_{p}} (t_{e} - t_{s})^{1/2}\right\} e^{-\frac{t_{e}}{m_{tb}}} \end{aligned} \tag{2.47}$$

From the TCA,

$$t_{p} = \frac{1}{e_{ps}} \left\{ S_{e} (t_{p} - t_{s})^{1/2} - \frac{2 w e_{v} S_{e}}{3 n_{u} z_{u} s_{p}} (t_{p} - t_{s})^{3/2} - (1 - w) e_{v} (t_{p} - t_{s}) \right\} \tag{2.48}$$

where

$$t_p - t_s = \left\{ \frac{\left[\left(e_{ps} + (1-w)e_v\right)^2 + \frac{2w\, e_v S_e^{\;2}}{n_u z_u s_p} \right]^{1/2} - e_{ps} - (1-w)e_v}{\frac{2w\, e_v S_e}{n_u z_u s_p}} \right\}^2 \qquad (2.49)$$

t_p substituted back into (2.49) yields t_s. Setting $f_e(t_e\text{-}t_s)$ equal to zero gives

$$t_e = t_s + \left\{ \frac{\left[(1-w)^2 e_v^{\;2} + \frac{2w\, e_v S_e^{\;2}}{n_u z_u s_p} \right]^{1/2} - (1-w)e_v}{\frac{2w\, e_v S_e}{n_u z_u s_p}} \right\}^2 \qquad (2.50)$$

The expected value of total evaporation from bare soil during the given month is simply the product of (2.47) and the mean number of interstorm periods:

$$E[E_s] = (1 - f_s) m_v E[E_{sj}] \qquad (2.51)$$

where we have again applied the assumption of the separation of snow and rain periods within the month. We further assume that in months when the soil is frozen, evaporation is zero regardless of the fractionation of precipitation between snow and rain.

2.3.6. *Evaporation from Vegetal Interception*

Eagleson (1978d) derives the expected value of evaporation from surface retention by integrating the product of the volume of evaporation from surface retention and the joint probability distribution of h and t_b over two domains of h ($0 < h < h_v$ and $h \geq h_v$) and two of t_b ($0 < t_b < h/e_{hv}$ and $t_b \geq h/e_{hv}$). Allowing for our assumption that all surface retention is vegetal interception, the result is

$$E\left[E_{hj}\right]=m_{tb}e_{hv}\left\{1-\left(1-\frac{\gamma\left[\kappa,\lambda h_v\right]}{\Gamma\left[\kappa\right]}\right)e^{-\frac{h_v}{m_{tb}e_{hv}}}-\frac{\gamma\left[\kappa,\lambda h_v+{}^{h_v}\!/\!_{m_{tb}e_{hv}}\right]}{\Gamma\left[\kappa\right]}\left(1+\frac{{}^{h_v}\!/\!_{m_{tb}e_{hv}}}{\lambda h_v}\right)^{-\kappa}\right\} \tag{2.52}$$

where λ (= κ/m_h) is a parameter of the gamma distribution of h, and $\gamma[\sim]$ is the incomplete gamma function. For typical climates and values of h_v, most storms will fill the interception capacity and most interstorm periods will last long enough to evaporate all of the interception, such that (2.52) will not be much less than h_v. The expected value of total evaporation from interception for the given month is the expectation for a single interstorm period times the expected number of interstorm periods:

$$E[E_{hv}]=\left(1-f_s\right)m_v E[E_{hj}] \tag{2.53}$$

Although sublimation from intercepted snow can be significant, particularly from the canopy of conifer forests, we take no account of it. Likewise, sublimation from the snowpack is not considered. Rather, all snowfall contributes to the snowpack at the soil surface and subsequently infiltrates into the soil or runs off during snowmelt. For estimation of the interception capacity of the canopy for rainfall, we assume that it is proportional to the area of all vegetation surfaces, such that

$$h_v = 0.02\,L_T \tag{2.54}$$

where L_T is the total leaf area index. The factor of 0.02 is primarily based on a compendium of literature values of h_v presented by Rutter (1975), with consideration of the potential for additional *intra*-storm evaporation from interception.

2.3.7. *Transpiration*

Transpiration is assumed to take place at the potential rate e_{pv} unless the vegetation is under moisture stress. To estimate the reduction of transpiration due to moisture stress, we employ a framework outlined by Eagleson (1978e), but ultimately not employed in his model in favor of the assumption that vegetation is unstressed in the mean state of the water balance. The framework—often attributed to Cowan (1965), following the work of Gardner (1960) and van den Honert (1948)—treats the soil-vegetation component of the soil-vegetation-atmosphere continuum as an analog of Ohm's Law of electricity. More specifically, the flow of liquid water between the pore spaces in the soil and the cell walls of the internal pore spaces of the leaves is assumed proportional to the potential difference and inversely proportional to the resistance to flow between the two points. Thus we can write

$$Q_{sl} = \frac{\Psi_l - \Psi_u(s_u)}{R_s(s_u) + R_v} \qquad (2.55)$$

where

Q_{sl}	flow between soil and leaves (cm/day);
Ψ_l	potential of liquid water in the leaves of the plant (cm);
R_s	resistance to water flow in the soil (days);
R_v	resistance to water flow in the vegetation (days).

The soil resistance is a function of the hydraulic conductivity of soil, and so both it and the soil matric potential are highly nonlinear functions of soil moisture. In contrast, the plant resistance is often taken to be constant for vegetation at a given state of growth.

Assuming for unstressed vegetation that the flow of water through the vegetation is in equilibrium with the rate of transpiration, we can solve for Ψ_l using (2.55) to get

$$\Psi_l = \Psi_u(s_u) + \left(R_s(s_u) + R_v\right)\breve{e}_{pv} \qquad (2.56)$$

where $\breve{e}_{pv}$ is the instantaneous rate of potential transpiration. (2.56) is assumed to hold as long Ψ_l is below a critical value, Ψ_{lc}. When $\breve{e}_{pv}$ and s_u are such that (2.56) requires that $\Psi_l > \Psi_{lc}$, the leaf stomata will begin to close, thereby reducing the rate of transpiration and maintaining Ψ_l at Ψ_{lc}. Under the condition of drying soil and increasing soil potential, (2.55) indicates that transpiration will decrease until $\Psi_u = \Psi_{lc}$, at which point all stomata are fully closed and transpiration ceases. It is for this reason that Ψ_{lc} is often equated with the soil matric potential at the "permanent wilting point." Because s_u controls the water balance in the root zone, we are interested in s_{uc}, the value of s_u at the point that $\Psi_l = \Psi_{lc}$. Before applying (2.56) to the task, we recognize two features of the problem. First, for typical root densities, R_s is not significant relative to R_v until Ψ_u is well above Ψ_{uc} (*i.e.*, the value of Ψ_u at s_{uc}) (Newman 1969). Second, $\breve{e}_{pv}$ is used in (2.56) because of the large diurnal variation in potential transpiration; when $s_{uc} = s_c$, Ψ_l will reach Ψ_{lc} only at the daily peak in $\breve{e}_{pv}$. Following Cowan's (1965) assumption of sinusoidal variation in $\breve{e}_{pv}$ during daylight, it can be shown that the peak value of $\breve{e}_{pv}$ is

$$\breve{e}_{pvp} = \frac{2e_{pv}}{t_d} \tag{2.57}$$

where t_d is the length of daylight (days). Substituting (2.57) into (2.56) and neglecting R_s gives us an equation for Ψ_{uc}:

$$\Psi_{uc} = \Psi_{lc} - 2e_{pv}\,R_v/t_d \tag{2.58}$$

Values of resistances for individual plants are found throughout the literature in a variety of units. Converting those values to values of R_v for stands of vegetation requires knowledge or assumptions about leaf, stem and root densities. In general, the greater the vegetation density the lower is the resistance. At the same time, increasing vegetation density increases the transpiratory demand. Furthermore, the climatic factors that determine the potential rate of transpiration are also major determinants of the speciation and morphology of the vegetation. Rather than try to capture the complex interactions that go into determining R_v, we assume that the second term of (2.58) is relatively invariant within given climatic regions and/or vegetation classes at the time of the year when water stress is most likely to occur. That assumption allows us to assign directly values of Ψ_{uc}, for which there are numerous observations in the literature. Assuming fixed values of Ψ_{uc} is fairly common in the modeling of evapotranspiration (Guswa et al. 2002). Also typical is to assume that the rate of evapotranspiration or transpiration decreases linearly with soil moisture between s_{uc} and the wilting point. That assumption gives

$$e_v = \begin{cases} e_{pv}, & s_u \geq s_{uc} \\ \dfrac{s_u - s_w}{s_{uc} - s_w} e_{pv}, & s_w < s_u < s_{uc} \\ 0, & s_u \leq s_w \end{cases} \tag{2.59}$$

where s_w is the relative soil saturation at the permanent wilting point.

In order to estimate the expected value of total transpiration for the given month, we assume that transpiration does not take place until all intercepted precipitation is evaporated following the termination of a storm:

$$E[E_v] = (1 - f_s)(m_{tb} - m_{th}) m_v \, e_v \tag{2.60}$$

where m_{th} is the mean time (days) it takes for interception to evaporate and is given by

$$m_{th} = \frac{E[E_{hj}]}{e_{hv}} \tag{2.61}$$

2.4. Potential Rates of Evaporation and Transpiration

The coupling of transpiration and bare soil evaporation above the soil surface is captured through application of the Shuttleworth-Wallace (SW) model of evapotranspiration from sparse crops (Shuttleworth and Wallace 1985). The SW model is a one-dimensional energy combination model, similar in form to the better-known Penman-Monteith (PM) model (Monteith 1965). Like the PM model, the SW model employs the concept of aerodynamic and surface resistances, but, unlike the "big leaf" of the PM model, the SW model divides the land surface into a coupled, two-component system comprised of the soil surface and the vegetation canopy (see Figure 2.5). The coupling occurs principally through the division of available energy between the two surfaces and the combination of the sensible and latent heat fluxes from the two surfaces at a hypothetical point of "mean canopy flow." With estimation of the vapor pressure deficit at that point, the PM equation can be applied to each flux separately. The potential rates of bare soil evaporation and transpiration are thus given by

$$e_{ps} = \frac{f_c}{\lambda} \frac{\Delta A_s + \rho c_p D_o / r_{as}}{\Delta + \gamma\left(1 + r_{ss}/r_{as}\right)} \tag{2.62}$$

$$e_{pv} = \frac{f_c}{\lambda} \frac{\Delta\left(A - A_s\right) + \rho c_p D_o / r_{ac}}{\Delta + \gamma\left(1 + r_{sc}/r_{ac}\right)} \tag{2.63}$$

where

f_c	factor for the conversion of mm/s to cm/day (=8640);
λ	latent heat of vaporization (J/kg).
A	available energy over the entire land surface ($\mathrm{Wm^{-2}}$);
A_s	available energy at the soil surface ($\mathrm{Wm^{-2}}$);
ρ	density of air ($\mathrm{kgm^{-3}}$);
c_p	specific heat at constant pressure ($\mathrm{Jkg^{-1}{}^\circ C^{-1}}$);
D_o	vapor pressure deficit at height of mean canopy flow (mb);
Δ	gradient of saturated vapor pressure deficit with temperature ($\mathrm{mb^\circ C^{-1}}$);
γ	psychrometric constant ($\mathrm{mb^\circ C^{-1}}$);
r_{as}	aerodynamic resistance between the soil and mean canopy flow ($\mathrm{sm^{-1}}$);
r_{ac}	bulk leaf-boundary-layer resistance of the canopy ($\mathrm{sm^{-1}}$);
r_{sc}	bulk stomatal resistance of the unstressed canopy ($\mathrm{sm^{-1}}$);
r_{ss}	resistance at the soil surface during stage-one evaporation ($\mathrm{sm^{-1}}$).

We can also approximate the rate of evaporation from vegetal interception with

$$e_{hv} = e_{pv}\Big|_{r_{sc} = 0} \tag{2.64}$$

In the same manner that the PM equation is derived (*i.e.*, by substituting the resistance-based flux equations for sensible and latent heat into the energy balance equation), Shuttleworth and Wallace (1985) show that

$$D_o = D + \left[\Delta A - (\Delta + \gamma)\lambda E\right] r_{aa} / \rho c_p \tag{2.65}$$

where

D	vapor pressure deficit at the reference height (mb);
r_{aa}	aerodynamic resistance between the height of mean canopy flow and the reference height (sm^{-1});
λE	latent heat flux (Wm^{-2}).

The presence of the λE term in (2.65) means that a rigorous solution of (2.62)-(2.64) requires simultaneous solution of actual evapotranspiration. To avoid a large number of iterations of the model and to preserve our treatment of the potential rates as external drivers of the water balance, we exploit the knowledge that, due the relative size of r_{aa}, D_o does not deviate much from D. We thereby first approximate λE in each month using the water balance model and $D_o = D$ in (2.62) and (2.63). These values are then substituted into (2.65) to obtain approximations of D_o. Such an approach is consistent with the limited representativeness of observed values of D; the meteorological stations where humidity measurements are made are often well removed from the dominant vegetation of the region. In addition, we are using averages of D over the entire month, whereas the most appropriate values would be the averages over just the periods in which bare-soil evaporation and transpiration actually occur at their respective potential rates. D tends to be lower at those times because they immediately follow rainstorms, and because there is a negative feedback of humidity to potential evapotranspiration.

Potentially related to the issue of the value of D is the use of r_{ss} in (2.62). If (2.62) were used to estimate the rate of stage-two evaporation, r_{ss} would be the resistance to vapor flow between the point in the subsurface where the soil air is saturated and the surface. As such, it would need in some way to be modeled as an increasing function of the drying process (*e.g.*, Camillo and Gurney 1986; Choudhury and Monteith 1988; Stannard 1993). Although an implicit or explicit assumption of most formulations of *potential* evaporation is that the soil column is moist enough that the air at the soil surface is saturated (*i.e.*, r_{ss}=0), we (via unpublished analysis), along with others (*e.g.*, Sellers et al 1992; Camillo and Gurney 1986), have found that a significant non-zero value of r_{ss} is needed to predict accurately evaporation from even well watered soils. This may be a case of imprecision in the rubric of potential evaporation as applied to pre-stage-two evaporation (*e.g.*, van Bavel and Hillel 1976, Brutsaert and Chen 1995) or simple modeling error—such as that induced by use of the monthly average of D. It may also represent actual resistances imposed by soil crusting or the mulching effect of plant litter. Bond and Willis (1969), for example, found that moderate amounts of straw (as low as 560 kg/ha) significantly reduced stage-one evaporation from experimental soil columns. Although use of a non-zero r_{ss} for stage-one evaporation will necessarily be imprecise, we include small (relative to those representative of mid-to-late stage-two evaporation), fixed values in the calculation of e_{ps}.

The available energy terms in (2.62), (2.63) and (2.64) are composed of net incoming radiation and energy horizontally advected to the region by the wind, less heat conduction into the subsurface soil and chemical and physical energy stored by the vegetation and near-surface soil. Energy advection and storage are typically insignificant at the monthly and regional scales. Ignoring those quantities gives

$$A = R_n - G \tag{2.66}$$

$$A_s = R_{ns} - G \tag{2.67}$$

where

R_n net radiation over the entire land surface (W/m^2);
R_{ns} net radiation at the soil surface (W/m^2);
G net heat conduction into the soil (W/m^2).

While the annual average of G is assumed zero, it tends to be substantially positive in the late spring/early summer and substantially negative in the late fall/early winter for mid-to-high latitude regions with large annual temperature variations. Based on an equation derived by Sellers (1965), we approximate the annual cycle in G as

$$G = \frac{T_{max} - T_{min}}{2} \left(\frac{2\pi C}{365} \right)^{\frac{1}{2}} \sin \left[\frac{2\pi (J - 105)}{365} + \frac{\pi}{4} \right] \tag{2.68}$$

where

T_{max} maximum monthly mean air temperature (°C);

T_{min} minimum monthly mean air temperature (°C);

C product of the heat capacity and the thermal conductivity of the soil ($W^2\, m^{-4}\, {}^{\circ}C^{-2}$ day);

J Julian day of the middle of the month.

C is dependent on both the texture and moisture content of the soil. Based on graphical data presented by Sellers (1965), $C^{1/2}$ ranges from about 3 $Wm^{-2}\,{}^{\circ}C^{-1}$ day$^{1/2}$ for dry clay to about 10 $Wm^{-2}\,{}^{\circ}C^{-1}$ day$^{1/2}$ for saturated sand. Setting the quantity under the square root in (2.68) equal to one will thus provide a rough approximation of G for typical soil conditions.

The net incoming radiation, R_n, is equal to absorbed incoming shortwave radiation less net outgoing longwave radiation:

$$R_n = S_r(1 - \alpha) - L_n \tag{2.69}$$

where

α surface albedo;

S_r incoming shortwave radiation;

L_n net outgoing longwave radiation.

If (2.69) is negative, an inversion correction factor of 0.5 is applied. R_{ns} is estimated from R_n using a Beer's Law relationship:

$$R_{ns} = R_n \exp(-\mu L_T) \tag{2.70}$$

where

μ extinction coefficient (dimensionless);

L_T total leaf area index of standing vegetation.

L_T is the sum of the leaf area index of transpiring green vegetation, L_G, and that of non-transpiring components of the canopy, L_D:

$$L_T = L_G + L_D \tag{2.71}$$

To estimate L_D, we assume that it consists of (1) a persistent part—mainly live and dead woody stems and other supporting tissue, but also (especially in grasslands and wetlands) some standing-dead herbaceous matter that takes a long time to decay or to be eaten, and (2) senescent and dead leaves after peak greenness is reached. The first component is taken as a fixed fraction of peak green LAI. For the second, we borrow the assumption by Sellers et al. (1996) that the decrease in LAI caused by dead and dying leaves remains for one month (before the leaves fall off or are eaten.) The formulation for L_D can then be written as

$$L_{D_i} = \begin{cases} f_p\, L_{Gp}, & L_{G_i} \geq L_{G_{i-1}} \\ f_p\, L_{Gp} + (L_{G_{i-1}} - L_{G_i}), & L_{G_i} < L_{G_{i-1}} \end{cases} \tag{2.72}$$

where

f_p ratio of persistent non-transpiring LAI to peak green LAI;

L_{Gp} peak green LAI;

L_{Gi} green LAI during month *i*.

Shuttleworth and Wallace (1985) estimate the two aerodynamic resistances in (2.62), (2.63) and (2.65) as linear combinations of the values for bare soil (*i.e.*, $L_T = 0$) and a closed canopy (*i.e.*, $L_T \geq 4$):

$$r_{aa} = \begin{cases} \frac{1}{4} L_T\, r_{aa}(4) + \frac{1}{4}(4 - L_T)\, r_{aa}(0), & 0 \leq L_T \leq 4 \\ r_{aa}(4), & L_T > 4 \end{cases} \tag{2.73}$$

$$r_{as} = \begin{cases} \frac{1}{4} L_T\, r_{as}(4) + \frac{1}{4}(4 - L_T)\, r_{as}(0), & 0 \leq L_T \leq 4 \\ r_{as}(4), & L_T > 4 \end{cases} \tag{2.74}$$

The authors derive the closed canopy aerodynamic resistances by assuming neutral stability, such that, above the canopy, the eddy diffusion coefficient increases in proportion to the product of the friction velocity and the height above the zero plane displacement, while below the canopy, it increases exponentially with height. They integrate the corresponding equations, first from the soil surface to the height of mean canopy flow and then from the height of mean canopy flow to the reference height, to obtain

$$r_{as}(4) = \frac{\ln[(x-d)/z_o]}{k^2 u} \frac{h_c}{n_e(h_c - d)} \{\exp n_e - \exp[n_e\{1-(d+z_o)/h_c\}]\} \tag{2.75}$$

$$r_{aa}(4) = \frac{\ln[(x-d)/z_o]}{k^2 u} \left\{ \ln[(x-d)/(h_c - d)] + \frac{h_c}{n_e(h_c - d)} (\exp[n_e\{1-(d+z_o)/h_c\}]-1) \right\} \tag{2.76}$$

where

x	reference height above the canopy for meteorological measurements (m);
d	zero plane displacement of the closed canopy (m);
z_o	roughness length of the closed canopy (m);
k	von Karman's constant (dimensionless);
u	wind speed at the reference height (m/s);
h_c	canopy height (m);
n_e	eddy diffusion decay constant for the closed canopy (dimensionless).

The height of mean canopy flow is taken as $d + z_o$. The zero plane displacement and roughness length are assumed to be a fixed fraction of the canopy height:

$$d = 0.63 h_c \tag{2.77}$$

$$z_o = 0.13 h_c \tag{2.78}$$

The bare soil aerodynamic resistances are estimated by splitting the total bare soil aerodynamic resistance (*i.e.*, that between the soil surface and reference height) at the height of mean canopy flow:

$$r_{aa}(0) = \ln^2[x/z_{os}]/k^2u - r_{as}(0) \tag{2.79}$$

$$r_{as}(0) = \ln[x/z_{os}]\ln[(d+z_o)/z_{os}]/k^2u \tag{2.80}$$

where z_{os} is the roughness length of the bare soil, typically assumed to be 0.01 m.

Finally, the bulk resistances in (2.62) and (2.63) must also be integrations over the whole canopy. Stomatal resistance generally decreases with increasing shortwave irradiance and, therefore, increases with depth into the canopy. Woodward (1987) proposes the following hyperbolic relationship:

$$r_s = r_{s_{min}} + \frac{b}{S_r} \tag{2.81}$$

where

r_s stomatal resistance (sm^{-1});

r_{smin} minimum stomatal resistance (sm^{-1});

b sensitivity of stomatal resistance to irradiance ($\mathrm{sm}^{-1}\mathrm{Wm}^{-2}$).

The author gives a value of 29500 $\mathrm{sm}^{-1}\mathrm{Wm}^{-2}$ for b. By conceptualizing differential horizontal layers of the canopy as resistances in parallel, we can integrate the inverse of (2.81) over the canopy to obtain the inverse of the bulk stomatal resistance (*i.e.*, the canopy conductance.) If we apply Beer's Law to the extinction of S_r through the canopy and assume that transpiring and non-transpiring LAI are distributed vertically in proportion to one other, we can perform the integration over L_G as

$$r_{sc}^{-1} = \int_0^{L_G} \left(r_{s_{min}} + \frac{b}{S_r} e^{\frac{\mu L_T}{L_G} l_G} \right)^{-1} dl_G \tag{2.82}$$

which evaluates to

$$r_{sc} = \frac{r_{s_{min}}}{L_G}\left(1 + \frac{\ln\left[r_{s_{min}} + b/S_r\right] - \ln\left[r_{s_{min}} + (b/S_r)\, e^{\mu L_T}\right]}{\mu L_T}\right)^{-1} \tag{2.83}$$

A similar approach can be applied to the increase of leaf-boundary-layer resistance as the windspeed decreases with depth in the canopy. Choudhry and Monteith (1988) combine assumptions of (1) an exponential decrease in windspeed with height, and (2) proportionality of leaf-boundary-layer resistance to the inverse of the square root of windspeed, to obtain

$$r_{ac} = \frac{1}{L_G}\left\{\frac{0.02}{n_w}\left(\frac{u_c}{w_l}\right)^{1/2}\left(1 - \exp\left[-\frac{n_w}{2}\right]\right)\right\}^{-1} \tag{2.84}$$

where

n_w wind speed decay constant (dimensionless);

u_c wind speed at the canopy height (m/s);

w_l average leaf width (m).

For the windspeed decay constant, we use an empirical dependency on LAI developed by Lafleur and Rouse (1990) from evapotranspiration measurements in a subarctic wetland:

$$n_w = 2.6\, L_T^{\;0.36} \tag{2.85}$$

Although (2.85) may not be representative of other biomes, r_{ac} is generally small relative to r_{sc} and therefore does not have to be estimated with great accuracy.

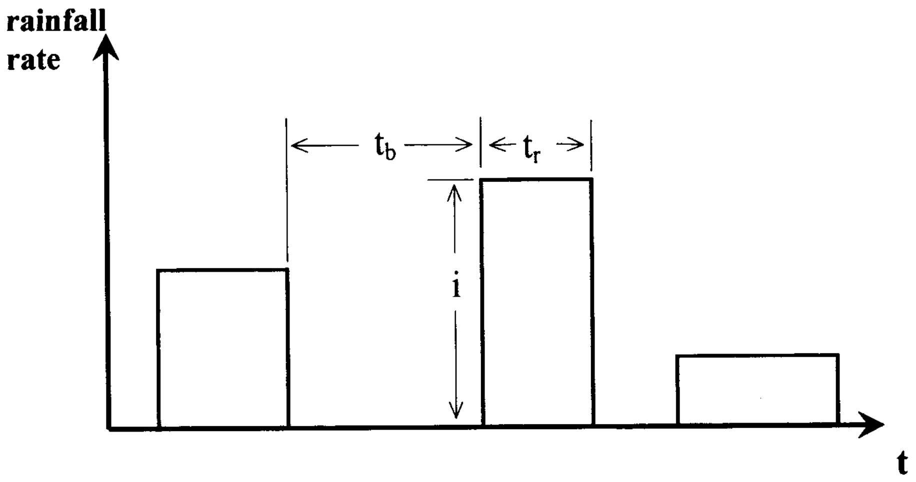

Figure 2.1. Rectangular pulse model of precipitation.

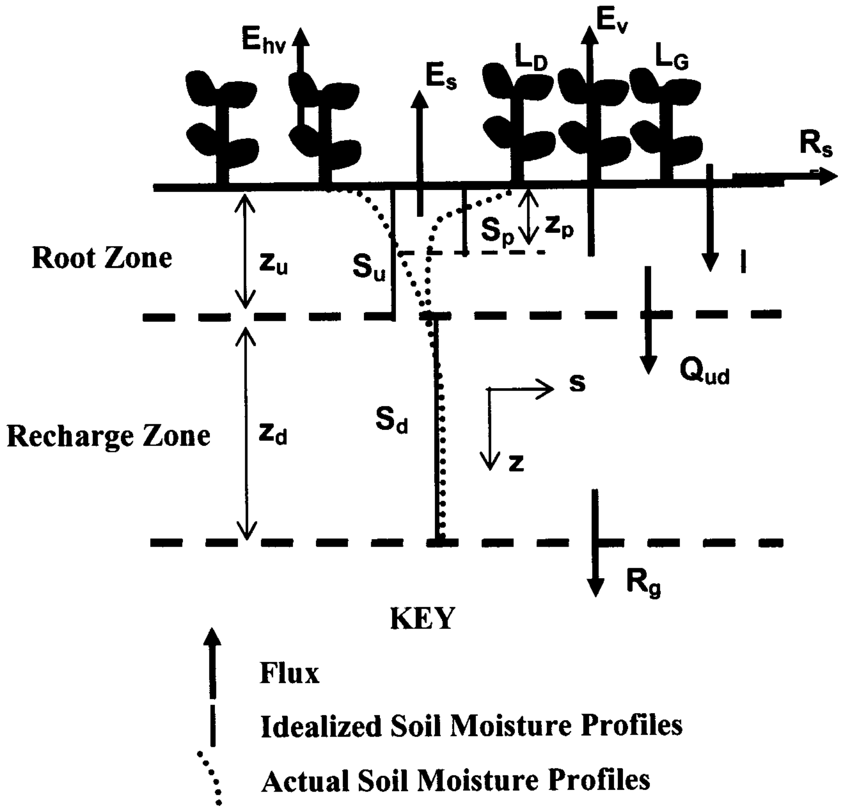

Figure 2.2. The new monthly, two-soil-layer version of the Eagleson model.

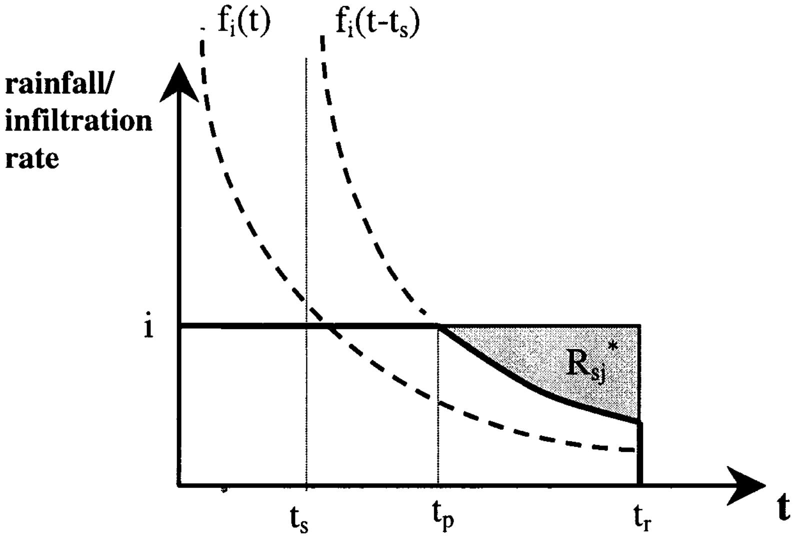

Figure 2.3. Model of the dynamics of infiltration

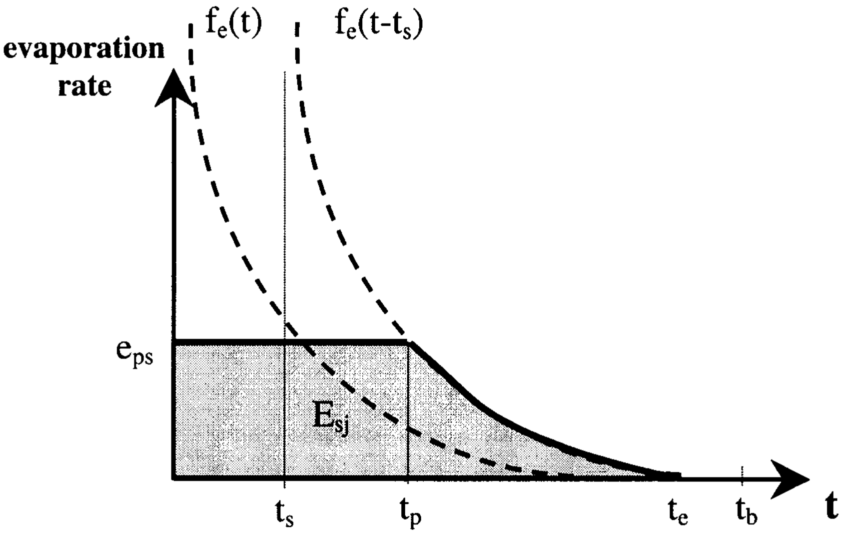

Figure 2.4. Model of the dynamics of bare-soil evaporation.

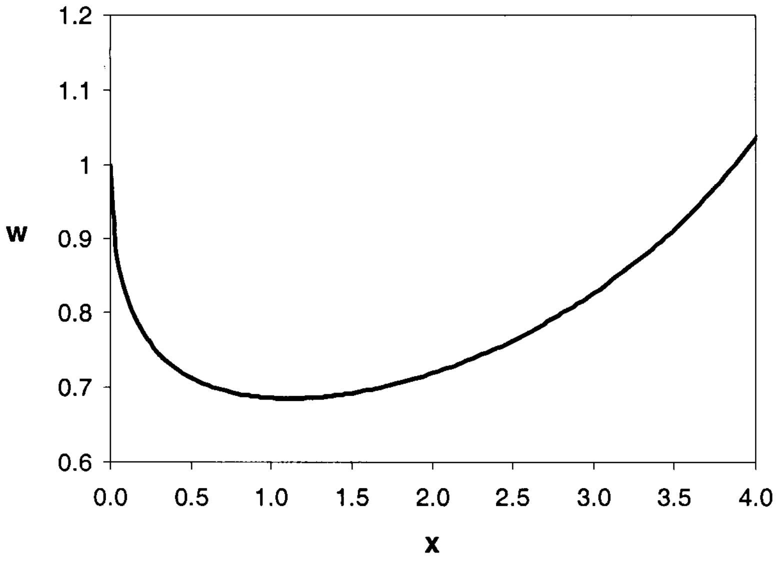

Figure 2.5. Weighting factor applied to the two versions of the seconf term of the exfiltration capacity curve.

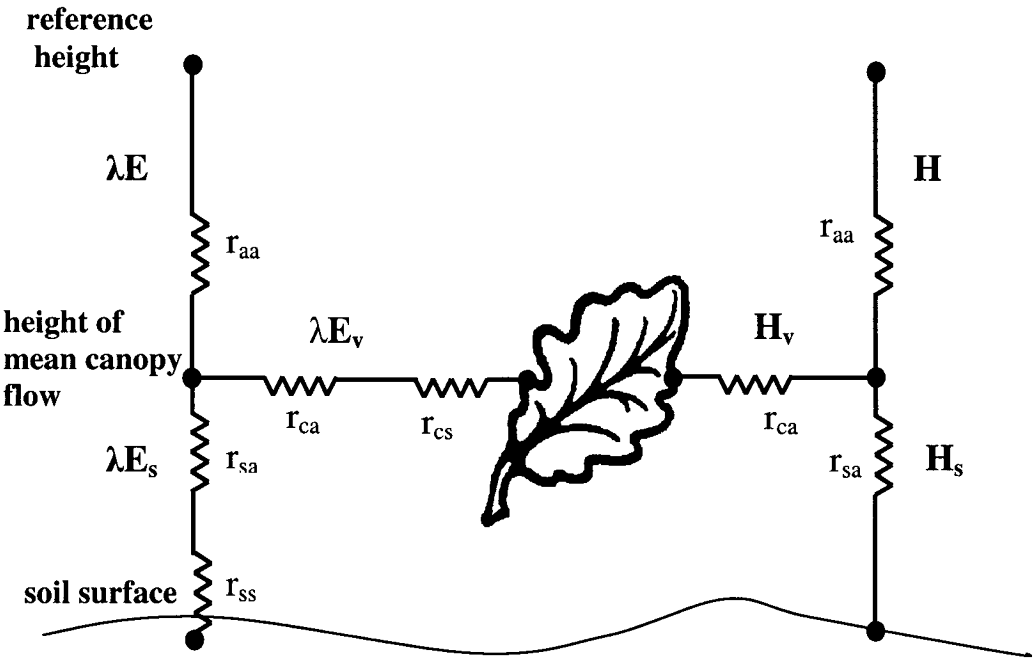

Figure 2.6. The Shuttleworth-Wallace evapotranspiration model. Adapted from Shuttleworth and Wallace (1985).

Chapter 3: Estimation of Parameter Values

3.1. Soil Hydraulic Parameters

The VEMAP soils data (Kittel et al. 1996) were drawn from a 10-km gridded database developed by the USEPA (Kern 1995), which is in turn based on the State Soil Geographic Database (STATSGO; USDA 1994) of the US Department of Agriculture Soil Conservation Service. The dataset contains 18 parameters for 0-50 cm and 50-150 cm layers and up to four “modes” within each 0.5-degree grid cell. Grid-cell averages (weighted by modal area) are also provided. Further details of the development of the VEMAP soils database can be found in Kittel et al. (1995) and Rosenbloom and Kittel (1996). The VEMAP variables most useful to estimation of the Brooks-Corey parameters are bulk density and texture (*i.e.*, percentages of sand, silt and clay). Bulk density can readily be converted to total porosity with the standard assumption of a mineral density of 2.65 g/cm^3:

$$n_t = 1 - \rho_b / 2.65 \tag{3.1}$$

where ρ_b is the soil bulk density (g/cm^3). The grid-cell averages of total porosity, percent sand and percent clay for each layer are plotted over the study area in Figure 3.1. We note that, within each of the depicted classes, large block of contiguous cells possess identical values. This is surprising given that the cell values are averages derived from a much higher resolution dataset. It may be an outcome of the original values being inferred from texture class, as opposed to actual measurements, which are not contained in STATSGO in a consistent manner.

We made a qualitative comparison of the values in Figure 3.1 to maps of the same quantities (http://www.essc.psu.edu/soil_info/index.cgi?soil_data&conus&data_cov) produced from CONUS-SOIL (Miller and White, 1998), a 1-km soils database also derived from STATSGO. Although the two datasets appear to be reasonably in accord, the higher resolution maps make clear the high degree of variability that can be found within a 0.5-degree grid cell. Figure 3.2 depicts the USDA soil textural classes in which the sand and clay percentages in Figure 3.1 fall. Comparison to a map of "dominant" soil textures in the STATSGO map units (http://www.essc.psu.edu/soil_info/index.cgi?soil_data&conus&data_cov) produced from CONUS-SOIL shows significant differences. For example, the largest textural class over the study area in the CONUS-SOIL map is silt loam. Most of the corresponding cells in Figure 3.2a are designated as either loam or silty clay loam. However, many of the sand and clay percentages for those cells fall on or near the boundary with the silt loam texture on the USDA texture triangle. All things considered, we have reason to assume a significant amount of uncertainty and subgrid variability in the VEMAP soils data.

Over the years, numerous studies have quantified the relationship between soil texture and soil hydraulic properties. In particular, Rawls, Brakensiek and co-authors (*e.g.*, McCuen et al. 1981, Rawls et al. 1982, Rawls and Brakensiek 1982, Rawls and Brakensiek 1985) have focused on the Brooks-Corey parameters. Their most comprehensive database was compiled from 26 sources in the literature and contains water-retention-vs.-matric-potential data for 1323 soils from 32 states (Rawls et al. 1982). They optimized the fit of (2.2) and (2.12) to all the data with five or more observations and kept those with a s-vs.-Ψ correlation coefficient significant at the 95% level. Table 3.1 lists by USDA textural class the values that the authors report for the arithmetic means of total porosity and residual water content, the geometric mean of the effective saturated matric potential and the geometric mean of the pore size distribution index. We use the geometric means of the latter two parameters because Brakensiek et al. (1981) found that, for most textural classes, those parameters better fit a lognormal than a normal distribution.

One option for estimating θ_r, Ψ_s and m would be to use the textural classification in Figure 3.2 to assign the corresponding values in Table 3.1. Given the issue noted above concerning sand and clay percentages falling near or at textural class boundaries, we sought a method that would take into account variations within a textural class. Results of Rawls and Brakensiek (1982) indicate that some of the very large within-class variation of water retention characteristics can be explained by differences in actual percentages of sand and clay, as well as bulk density and organic matter content. Their study involved multivariate linear regression of those four variables against water content held at various matric potentials. Rawls et al. (1983) fit the Brooks-Corey parameters to water retention curves obtained from the resulting regression equations. They plot the parameters on the USDA soil texture triangle for a soil organic matter content of 0.5% and a range of porosities, from a base value to a 30 percent increase. Using the same results, Rawls and Brankensiek (1985) develop a set of quadratic regression equations with percent sand, percent clay and porosity as the independent variables. It would seem that the regression equations of Rawls and Brankensiek (1985) would make the most of the information content of the VEMAP soils data. However, comparison of the plots in Rawls et al. (1983) with the values in Table 3.1 reveals significant discrepancies. Given that the latter values are based on direct fits to real moisture retention curves from a larger set of observations, we rely on them rather than the Rawls and Brakensiek (1985) regression equations.

To capture within-class variation that is due to differences in grain size distribution, we adopt the approach used by Cosby et al. (1984) to investigate the relationship between soil texture and the parameters of the Campbell (1974) equation for the soil moisture retention curve. [Like (2.12), the Campbell equation is a power law, but unlike (2.12), uses saturation measured relative to total porosity rather than effective porosity. Consequently, only a coefficient and an exponent need to be fit to empirical data.] Because the largest source of their soil-moisture-retention data (which is used in common with Rawls et al. (1982)) identifies only the textural class of each soil sample, they assign values of percent sand, silt and clay to the midpoint of each class on the USDA texture triangle and perform linear regressions of those values against means of the hydraulic parameters within each textural class. Their midpoint percentages of sand and clay are listed in Table 3.1. Because there are only 11 USDA textural classes, nonlinear regression would not be warranted. In addition, the linearity assumption means the grid-cell averages of percent sand and clay will give the grid-cell averages of the Brooks-Corey parameters. Presented in Table 3.2 are the results of multivariate linear regression of the percentages in Table 3.1 against the adjacent parameter means. For Ψ_s and m, both the R^2 values and the much greater significance of one independent variable over the other are similar to the results obtained by Cosby et al. (1984) for the analogous

Campbell parameters. Although either the intercept or one of the coefficients in each regression is not significant at the standard 95% level, we included all of them in the equations used to estimate parameter values.

The results from application of the equations, with a lower limit of 0.12 placed on *m*, to the VEMAP average percent sand and clay data over the study area are depicted in Figure 3.3. Regardless of the actual depths of the root and recharge zones, the 0-50 cm parameter values are used for the former zone, and the 50-150 cm values are used for the latter. Using (2.2) and (2.12), we translated the Brooks-Corey parameters to two other common measures of the water retention characteristics of soil: the field capacity—which per convention was calculated as the water content at 0.33 bar (340 cm), and the permanent wilting point—calculated as the moisture content at 15 bar (15,300 cm). Their values are depicted in Figure 3.4 along with their difference, which is typically referred to as the available water content.

In addition to water retention data, Rawls et al. (1982) also performed a literature search for unsaturated hydraulic conductivity data. By "visual analysis" of those data, they developed a "representative" curve of percent saturation vs. hydraulic conductivity for each USDA textural class. Presumably such a qualitative approach was taken because of the enormous variability in hydraulic conductivity typically found within and across textural classes. The across-textural-class variability is illustrated by the values of saturated hydraulic conductivity listed in Table 3.2, which Rawls et al. (1982) obtained from the endpoints of their curves. Comparison with saturated hydraulic conductivities from Cosby et al. (1984)—which are geometric means from the same soil samples used in their Campbell-parameter estimation—shows good agreement with the first five, coarser textural classes. However, for the remaining classes, which contain significant amounts of clay, the Rawls et al. (1982) values are smaller by factors of around 4-6 for five of the six, and smaller by around a factor of 20 for sandy clay. Unfortunately, it is also in those ranges of clay content that most of the VEMAP data fall. Clearly, a great deal of uncertainty is associated with estimation of saturated hydraulic conductivity from textural information only.

An alternative to purely empirical correlations between soil texture and saturated hydraulic conductivity is some sort of theoretical relationship based on the water-retention characteristics of the soil. Rawls et al. (1982) tested an equation derived by Brutsaert (1967), who substituted (2.13) into a permeability model developed by Childs and Collis-George (1950). That equation is

$$K_s = a\left(\frac{n_t - \theta_r}{\Psi_s}\right)^2 \frac{m^2}{(m+1)(m+2)} \tag{3.2}$$

The constant a incorporates gravity and various fluid constants and, according to Brutsaert (1967), should have a value of 270 cm^3/s when K_s is in cm/s. Rawls et al. (1982) found that, with their geometric means of Ψ_s and m, (3.2) overestimated their observation-based values of K_s by an order of magnitude. A value for a of 21 cm^3/s gave the best least-squares fit between log-transformed values of K_s ($R^2 = 0.92$). Ahuja et al. (1989) were able to obtain good results with another empirically fitted, theoretically based equation in the form of a generalized Kozeny-Carman relationship:

$$K_s = B\phi_e^{\eta} \tag{3.3}$$

where φ_e is effective porosity defined as total porosity less water held at 33 kPa. For the constants B and η, they obtained values of 1058 cm/hr and 3.4, respectively, by a log-log regression fit of (3.3) to 297 measurements from 8 different soils ($R^2 = 0\ .71$). We estimated φ_e for the textural classes in Table 3.1 using (2.2) and (2.12) with the adjacent Brooks-Corey parameter values. The results of the subsequent application of (3.3) are higher than both the values of Cosby et al. (1984) and those of Rawls et al. (1982) for the first five classes, but in-between for the crucial high-clay-content soils (see Table 3.1). The variability in that range of K_s, both within and across soil series, is particularly evident in the plot of φ_e-vs.-K_s observations in Ahuja et al. (1989), which shows K_s values over four orders of magnitude for φ_e values between 0.05 and 0.1. In the end, we choose to use (3.2) calibrated to the geometric means of the two studies. In addition to resulting in the water balance model generating a realistic amount of surface runoff, that equation requires only calibration of a single parameter and is directly dependent on the Brooks-Corey parameters. The best log-transformed match between the observed geometric means and the calculated values is with a equal to 35 cm^3/s ($R^2 = 0.93$). Shown in Figure

3.5 are the results of application of the equation (with a lower limit of 5.0 cm/day placed on K_s) to the total porosities in Figure 3.1 and the Brooks-Corey parameter values in Figure 3.2. The issue of uncertainty and variability in saturated hydraulic conductivity is further explored in Section 7.4 in the form of a sensitivity analysis.

3.2. Storm Statistics

We derived monthly values for the statistics of the Poisson rectangular-pulse precipitation model from hourly observations of precipitation as compiled by the National Climatic Data Center (NCDC) and made available on CD-ROM by EarthInfo, Inc. (EarthInfo 1999). Those observations were taken by recording rain gauges located at National Weather Service, Federal Aviation Administration, and Cooperative Observer stations. Thousands of these stations began making observations in and soon after 1948 and continue through the present. The 50-year period from 1949 to 1998 was selected for parameterization of the precipitation model. Stations in the NCDC database were included in the analysis if they have records for at least 40 of the 50 years and have no more than 20% missing data for the available years. Within an area extending 2.5° latitude and longitude beyond the boundaries of the study area, 706 stations met these criteria (see Figure 3.6).

For calculation of monthly statistics at each of the 706 stations, we loosely followed the methodology outlined by Hawk and Eagleson (1992). A key difference is in our treatment of missing data. Rather than filling in missing hourly values with the climatological mean in the manner of Hawk and Eagleson (1992), we simply ignored the given storm/interstorm period. Provided that missing values occur randomly throughout the record—as opposed to, for example, more often during the most intense storms—the storm statistics will be unbiased by our method. A second difference is in the assignment of an interstorm period (*i.e.*, t_b) to a given month. Rather than assigning it to the month in which the subsequent storm begins, we assign it to the month in which the middle of the interstorm period falls.

Another important decision needs to be made with regards to defining a storm. Because individual periods of continuous precipitation tend to be clustered within a given storm, we do not want to define an "independent" storm as just any set of consecutive hours of recorded precipitation. Rather, we need to select a minimum number of precipitation-free hours that must separate precipitation events in order for those events to be considered parts of independent storms. To make this choice, Hawk and Eagleson (1992) employ the method of Restrepo-Posada and Eagleson (1982), which uses the assumption that t_b is exponentially distributed. A key feature of the exponential distribution is that its mean and standard deviation are equal. The process is then one of finding the minimum time between storms, t_{bmin}, that most closely produces that property for the given month. More specifically, when t_{bmin} is too low, the distribution is biased low and the mean is less than the standard deviation. As t_{bmin} is raised, and lower values of t_b are eliminated, the mean and standard deviation will converge. In actuality, however, the use of t_{bmin} produces a truncated distribution (Restrepo-Posada and Eagleson 1982). If the distribution is also exponential, it can be shown that the mean will be greater than the standard deviation. A distribution more fundamental to a Poisson process is the Poisson distribution itself, which gives the probability of a specific number of events occurring over a specific period of time. The distribution possesses the property that its mean and variance are equal. We thus selected a value of t_{bmin} for a given month at a given station based on the convergence of the mean and variance of the number of storms in all months in which there are no missing data. Despite the theory, we found that for many months, particularly at stations in the southern and central areas of the study area, complete convergence occurred at very large (>24 hours) values of t_{bmin}. This may be the result of the fact that in those areas both the Gulf of Mexico and the Pacific Ocean are significant sources of moisture. In this case, modeling storm arrivals with a compound Poison distribution might provide a better fit. Nonetheless, the water balance model is not suited to the additional complexity. In the end, in order not to lump together convective storms that may be generated on a diurnal cycle, we limited t_{bmin} to be no greater than 18 hours.

With a Poisson arrival process approximated, m_{tb}, m_{tr}, m_i and m_h were set equal to the respective sample means. The method of moments was likewise applied to the estimation of κ, such that, under the assumption of h being gamma-distributed,

$$\kappa = \left(m_h / S_h\right)^2 \tag{3.4}$$

where S_h is the sample standard deviation of h. Once the storm statistics were determined for each month at each of the 706 stations, the next step was to interpolate them to the half-degree grid of the study area. Ordinary kriging—detailed descriptions of which can be found elsewhere (*e.g.*, Kitanidis 1993)—was selected *a priori* as the preferred method. Prior to performing the kriging, continental-scale trends in the statistics were removed by means of a quadratic regression on longitude and latitude, thereby leaving a set of residuals to be interpolated. The key feature of kriging is its use of models of spatial covariance termed "semivariograms." From amongst five of the more common semivariogram functions, one was selected for each statistic in each month based on the best least-squares fit to the data. Based on the typical semivariogram range and the density of stations, up to 12 of the nearest stations within 300 km were used in the interpolation at each grid cell. The final step was the application of the quadratic regression equations to the interpolated residuals. The results for January and July are presented in Figures 3.7-3.12.

A key assumption of the stochastic precipitation model is the independence of storm duration and intensity. To test this assumption, we calculated Kendall's correlation coefficient, τ_k, in each month. τ_k is a nonparametric, rank-based measure and therefore well suited to the extreme values that exponential distributions are prone to produce. The reader is referred to Hirsch et al. (1993) for a description of the procedure involved in its calculation. Values of τ_k interpolated to the study grid from the precipitation stations are shown in Figure 3.13 for January and July. The vast majority of station values that contributed to grid-cell values outside the range -0.1 to 0.1 are significant at the 95% level, while inside that range, most are not significant. The trend in all months is for significantly negative correlation in winter for the west and central-north of the study area, transitioning to small negative correlation, with pockets of insignificant and small positive correlation over the entire region in summer. Large negative correlation is thus primarily a phenomenon of the very low winter precipitation of the drier half of the study area. Much of it is in fact spuriously due to the precision with which precipitation depths are recorded. Specifically, at many stations for much of the record, depths are recorded in tenths of inches; so a trace amount of precipitation that falls within an hour will have a calculated intensity of 0.1 in/hr, which is not unusually low for snowfall. Such observations bias the joint distribution of intensity and duration to short duration, high intensity events. Compounding the problem—and making application of correlation tests appropriate to censored data difficult—is the fact that the precision in the NCDC database for many stations switches between hundredths and tenths of inches at various points in the record. Nevertheless, there is clearly a real tendency for storm duration to be negatively correlated to intensity, meaning that the assumption of independence results in overestimating the probability of long duration, high intensity storms. The degree to which this translates to (2.27) overestimating surface runoff is not easily quantified.

Before using (2.27), we want at a minimum to ensure that (2.26) holds. Because in general $m_{tb} >> m_{tr}$, this will be the case as long as h and t_b are independent. Application of the Kendall procedure to those parameters produced values of τ_k significant at the 95 percent level for only 14 percent of the 8472 station-month pairs. Significant values were scattered roughly evenly across months and stations, with 93 percent positive. Attributing the significantly negative values of τ_k to the five percent background rate of false positives, we conclude that there is a tendency for slightly positive correlation between h and t_b. A positive correlation implies that when storms are more numerous, their depths are lower (and vice versa), thereby resulting in (2.26) being an overestimate of mean monthly precipitation.

We can also test (2.26) by comparison with the monthly precipitation values in the VEMAP database. Those data were derived using the Parameter-elevation Regressions on Independent Slopes Model (PRISM; Daly1994) for the period 1895-1993 from monthly observations from many of the same stations used in the derivation of the storm statistics. Presented in Figures 3.14-3.16 are the mean PRISM values for the months of January and July and for the entire year over the period 1949-1993. Also plotted are the percentages by which mean precipitation calculated with (2.26) and the interpolated values of m_{tb}, m_{tr} and m_h differs from the corresponding PRISM values. The great majority of Poisson model values are within +/-15% of the PRISM values. The differences are about equally divided between positive and negative, indicating that there are greater sources of error than the slight positive correlation between h and t_b. The largest differences are primarily in January and in the western half of the study area.

Therefore, the precision issue may be a source of error here as well. In general, snowfall is a notoriously difficult quantity to measure accurately. Measurement error, however, is not restricted to stations with low winter precipitation. This became apparent when we compared the hourly observations (from which the Poisson statistics are derived) with monthly observations (from which the PRISM data are derived) at stations all across the study area. The completeness of the records is often very different. For months where both records are complete, we frequently found hourly totals differing from the monthly value by 20 percent or more. Some of the error in the Poisson model is certainly also due to sampling and interpolation error, particularly where the station density is low (e.g., central South Dakota and central Kansas) and where topography has a strong control on precipitation (*e.g.*, over the Black Hills and along the Rocky Mountain Front Range). Under the assumption that the PRISM values are better estimates of mean monthly precipitation, they are used for $E[P]$ in (2.7), (2.27) and (2.32).

3.3. Evapotranspiration Model Inputs and Parameters

3.3.1. *Climate Variables*

In addition to precipitation, monthly climate variables drawn from the VEMAP database consist of incoming solar radiation, air temperature and water vapor pressure. A discussion of the derivation of those data can be found in Kittel et al. (1995) and Rosenbloom and Kittel (1996). Four variables necessary for implementation of the Shuttleworth-Wallace model not included in the VEMAP database are net long-wave radiation, surface albedo, air pressure and monthly windspeed (the last being provided only as a seasonal climatology.) Net long-wave radiation was estimated from cloudiness, surface temperature and humidity using a methodology outlined by Sellers (1965). Cloudiness was estimated as a linear function of the ratio of solar radiation incident at the surface to that incident at the top of the atmosphere, with the slope and intercept visually calibrated to maps of a climatology of observed percent sunshine (Baldwin 1973). Surface albedo was taken from a gridded, monthly climatology created by Hobbins (2000) based on Gutman (1988). Surface air pressure and surface windspeed data were drawn from monthly values produced by the NOAA-CIRES Center for the Diagnosis of Climate (http://www.cdc.noaa.gov/cdc/reanalysis/) from results of the NCEP/NCAR reanalysis project (Kalnay et al. 1996). The data were bi-linearly interpolated to the 0.5-degree VEMAP grid from the 2.5-degree reanalysis grid via Delauney triangulation (*e.g.*, Petrie 1991). Air pressures were first converted to sea level and then brought back to the elevation of each grid cell after interpolation. The interpolated values of windspeed were extrapolated down from a reference height of 10 m to the canopy heights under an assumption of neutral stability and a logarithmic wind profile. The remaining, water-vapor-related variables (*i.e.*, D, Δ, γ and λ) were calculated from vapor pressure, air temperature and air pressure using standard formulas presented by Shuttleworth (1993).

3.3.2. *Green Leaf Area Index*

As elaborated in Chapter 2, LAI is the principal measure of vegetation density in the formulation of evapotranspiration and thus controls much of the model parameterization. Over the past couple of decades, a great deal of research has been devoted to estimating LAI and other vegetation parameters from remotely sensed data. A particularly useful data stream has proven to be the normalized difference vegetation index (NDVI) as derived from near-infrared and visible land-surface reflectance measured by Advanced Very High Resolution Radiometers (AVHRR) aboard NOAA satellites (Asrar et al. 1984). NDVI is closely related to the fraction of photosynthetically active radiation (FPAR) absorbed by the vegetation (Sellers 1985).

Understanding of the relationship between NDVI and LAI has matured to the point that two recent efforts have succeeded in producing gridded, multiyear global datasets of LAI at resolutions appropriate to large-scale hydrometeorological modeling. Los et al. (2000) applied an updated version of a sequence of corrections, collectively referred to as FASIR (Sellers et al.1996b), to monthly 1°-by-1° NDVI data from the Global Inventory Monitoring and Modelling System (GIMMS) for the period 1982-90. The FASIR methodology addresses sensor degradation, volcanic aerosols, cloud contamination, short-term atmospheric effects, solar zenith angle variations and missing data. The FASIR-corrected NDVI was then converted to green LAI, via FPAR, with a set of empirically based relationships whose form and parameter values are dependent on the land-cover classification of Sellers et al. (1996b). Los et al. (2000) evaluate the interannual variability of their LAI dataset by comparison with variations in precipitation and air temperature over regions of Western Europe, Brazil and the Sahel. Through use of principal component analysis, they conclude that the observed variability in climate is consistent with the response of vegetal transpiration and growth implied by aggregated LAI values for the three regions.

Buermann et al. (2002) developed the second multiyear global dataset of LAI from NDVI data as produced by the NOAA/NASA Pathfinder AVHRR Land (PAL) program. Those data were kept at their 8-km grid-cell resolution and corrected for a suite of factors similar to those addressed by the FASIR corrections (Myneni et al. 1998). The corrected NDVI data were aggregated to monthly values and converted to FPAR and green LAI for the period July 1981 to September 1994 with an algorithm based on a land-cover classification and the three-dimensional radiative transfer model of Myneni et al. (1997). Buermann et al. (2002) find good agreement between their NDVI-based LAI and field measurements from land-atmosphere field campaigns at three sites in North America. Of particular relevance to the study area of this dissertation is the Kansas grassland site of the First International Field Experiment (FIFE). Buermann et al. (2002) compare the distribution of field-measured LAI from the FIFE site with the distribution of a similar number of their LAI values for the same year and month, but from across a wider region of the Midwestern United States. The standard deviations of the two distributions are similar, while the mean of the satellite-derived distribution is about 50 percent higher. Like Los et al. (2000), Buermann et al. (2002) validate the interannual variability of their LAI data through correlation to precipitation and temperature anomalies over several dispersed regions of the globe. The authors also make direct comparison between monthly time series of their LAI data and that of Los et al. (2000) for four continental-scale biomes. The data of Los et al. (2000) are higher for all four biomes. The greatest differences, at factors of more than two, are for the grasslands of the Midwestern United States and Southern Africa. Buermann et al. (2002) assess the interannual variability in the paired time series as "qualitatively similar." For the grassland biomes, that comparison appears to translate to anomalies generally of the same sign but larger by a factor up to four for the time series from Los et al. (2000).

The differences in the datasets of Los et al. (2000) and Buermann et al. (2002) reveal the high degree of uncertainty still associated with NDVI-based estimates of LAI. Nonetheless, they are the best option for the scale of our study area. The analysis of Buermann et al. (2002) suggests that, at least for the grasslands in the study area, their data are more representative. Our own comparison with site-specific LAI data (Richie et al. 1976,;Knight 1973; Hazlett 1992; and Scurlock et al. 2001) from within the study area agrees with their assessment. Coincidently, the dataset of Buerman et al. (2002) is also the only of the two currently available to the public at a resolution at least as high as the 0.5° VEMAP grid. From a 0.5° version of the dataset posted by the authors at http://cybele.bu.edu, we calculated monthly averages of green LAI over the study area for the period July 1981- June 1991. Figure 3.17 shows the peak average LAI and the month in which it occurs. It should be noted that since the data were acquired in the spring of 2002, the authors have posted a newer version on their website. Our comparison of that version with the original data showed significantly higher (by up to a factor of three for grasslands) averages of peak LAI over the study area. The authors in fact believe that their latest data in general overestimate LAI (Myneni 2003, personal communication). In that light and in consideration of the evidence for the representativeness of the original data presented in Buermann et al. (2002), we elected to continue to use their original data. As explained in greater detail in Section 4.1.3, the LAI observations are used only to provide a fixed-shape envelope of green LAI, which is maximized under the constraints of available soil moisture.

3.3.3. *Parameter Values Specific to Vegetation Class*

The SW evapotranspiration model was developed for a simple, monoculture crop canopy. Its use for grasslands is a natural extension. However, there is a great deal of uncertainty in its application to more complex canopies such as those of forests, woodlands and savanna. Nonetheless, we believe it is of a general enough nature that effective parameter values can be estimated for all classes of vegetation.

Version 2 of the VEMAP vegetation classification scheme consists of 22 natively occurring vegetation classes, 11 of which are found in the study area of this dissertation. An agricultural "mask", which identifies cells as consisting of few, around half and nearly all crops, was also created for the VEMAP project. In the model parameterization, we took those cells east of the 100th meridian that are nearly all cropped as such, while the remaining cells are taken to be the native vegetation class. We also changed the native vegetation class for a number of cells in order to isolate individual vegetation classes to climatically similar regions. Specifically, 11 cells of temperate deciduous savanna in Texas and New Mexico was re-designated as warm temperate/subtropical mixed savanna, while in southern Missouri the reverse change was made to two cells. In Wisconsin, we changed three cells of temperate continental coniferous forest to cool temperate mixed forest. The resulting distribution of vegetation classes within the study area is illustrated in Figure 3.18.

Parameters values specific to each of the 12 vegetation classes in the study area are listed in Table 3.3. All of the parameters were defined in Chapter 2. Sources for parameter values are identified in the table and include other modeling studies, field studies and literature surveys. The precision applied to estimating a parameter value was a function of the availability, range and uncertainty of values in the literature, as well as of the sensitivity of model results to the given parameter. Many values, such as canopy height and leaf width, are only order of magnitude estimates. Careful consideration was given to the monthly timescale at which the model is implemented, especially with regard to r_{smin}, the minimal stomatal resistance. In selecting parameter values, we also considered the degree to which vegetation classes other than the designated one are present. For example, much of the area designated as wetland and temperate deciduous savanna is cultivated cropland. Significant calibration was performed for the values of only two parameters, r_{smin} and r_{ss}, the soil-surface resistance. The calibration process consisted mainly of visually matching modeled mean annual runoff to contours of observed streamflow. Additional consideration was given to the partitioning of evapotranspiration into transpiration and bare-soil evaporation. All parameters values were kept well within their predetermined range of uncertainty, and their original rank by vegetation class was preserved. In initially estimating values of r_{ss}, we took the view that they are mainly due to the litter layer.

As the main determinant of the absolute amount of water available for transpiration, root zone depth is one of the more important parameters in soil-vegetation-atmosphere transfer schemes (Mahfouf et al. 1996; Jackson et al. 2000). The distribution of roots below a given stand of vegetation is a complex function of plant speciation and phenology, chemical and physical properties of the soil, and climate. Many of those factors converge to produce similar root distributions within a given biome (Schenk and Jackson 2002). Jackson et al. (1996) compiled a database of 250 root studies, which they grouped into 11 biomes. They fit the exponential equation of Gale and Grigal (1987) to plots of cumulative root fraction vs. soil depth within each biome. We used the resulting decay constants to calculate root zone depth as the depth that contains 95% of the root biomass. Because temperate savanna and wetlands are not amongst the biome classes used by Jackson et al. (1996), we selected values intermediate between grasses and forests. Likewise, the root zone depth of conifer woodland was taken as intermediary between that of savanna and forest. Evapotranspiration estimates are much less sensitive to the depth of the recharge zone, which mainly controls the phase and amplitude of the annual cycle in groundwater recharge. A recharge zone of about twice the depth of the root zone gave seasonality in groundwater recharge (and hence base flow) consistent with the observed seasonality in streamflow across the study area (Geraghty et al. 1973). Accordingly, values for z_d of 100, 150 and 200 cm were assigned to vegetation classes based on the closest match to twice the corresponding value of z_u.

Table 3.1. Values of Soil Hydraulic Properties from the Literature

USDA Textural Class	Midpoint on USDA Triangle (Cosby et al.1984)		Observed Brooks-Corey Parameters (Rawls et al. 1982)				Observed K_s (cm/day)			Calculated K_s (cm/day)	
			Arithmetic Mean		Geometric Mean		Rawls et al. (1982)	Cosby et al. (1984)	Geo-metric mean	eqtn. (3) B=1058 η=3.4	eqtn. (1) a=35
	% Sand	% Clay	n_t	θ_r	Ψ_s (cm)	m					
sand	92	3	0.437	0.020	7.26	0.592	504	421	461	704	847
loamy sand	82	6	0.437	0.035	8.69	0.474	147	121	133	401	399
sandy loam	58	10	0.453	0.041	14.7	0.322	62	45	53	154	81
loam	43	18	0.463	0.027	11.2	0.220	32	29	30	53	83
silt loam	17	13	0.501	0.015	20.8	0.211	16	24	20	50	27
sandy clay loam	58	27	0.398	0.068	28.1	0.250	10	38	20	17	9.3
clay loam	32	34	0.464	0.075	25.9	0.194	5.5	21	11	16	9.8
silty clay loam	10	34	0.471	0.040	32.6	0.151	3.6	18	8.0	7.3	4.9
sandy clay	52	42	0.430	0.109	29.2	0.168	2.9	62	13	2.9	4.1
silty clay	6	47	0.479	0.056	34.2	0.127	2.2	12	5.0	3.4	3.1
clay	22	58	0.475	0.090	37.3	0.131	1.4	8.4	3.5	2.1	2.3

Table 3.2. Results of Multivariate Linear Regression of Brooks-Corey Parameters

Parameter	Intercept	Coefficients		R^2	P-values		
		% Sand	% Clay		Intercept	% Sand	% Clay
θ_r	-0.0295	0.00067	0.00201	0.831	0.1120	0.0120	0.0003
Ψ_s	14.6	-0.0934	0.454	0.893	0.0144	0.1508	0.0012
m	0.202	0.00329	-0.00318	0.868	0.0238	0.0066	0.0564

Table 3.3. Parameter Values Specific to Vegetation Class

Vegetation Class	z_u (cm)	z_d (cm)	r_{ss} (sm^{-1})	r_{smin} (sm^{-1})	h_c (m)	w_l (m)	f_d	μ	n_e	Ψ_{uc} (10^3 cm)	Ψ_{lc} (10^3 cm)
temperate continental coniferous forest	120	200	150	600	10	0.001	0.2	0.50	4.0	3	15
cool temperate mixed forest	100	200	250	500	10	0.04	0.2	0.60	4.0	2	15
warm temperate/ subtropical mixed forest	100	200	225	500	10	0.04	0.2	0.60	4.0	2	15
temperate deciduous forest	90	200	200	400	10	0.08	0.2	0.60	4.0	2	15
temperate conifer xeromorphic woodland	90	200	150	600	7	0.001	0.2	0.50	4.0	5	20
temperate deciduous savanna	70	150	175	400	4	0.02	0.2	0.50	3.0	5	20
warm temperate/ subtropical mixed savanna	70	150	75	425	3	0.02	0.2	0.45	2.5	8	20
C3 grasses	50	100	125	250	0.5	0.01	0.3	0.45	2.0	10	25
C4 grasses	50	100	100	400	0.5	0.01	0.3	0.45	2.0	10	25
subtropical arid shrubs	130	200	50	400	1	0.01	0.2	0.50	2.0	15	30
wetlands	70	150	75	350	1	0.02	0.2	0.60	3.0	5	15
crops	70	150	100	325	1	0.02	0.1	0.65	2.5	5	15
references	1		2,3,4	5,6,7, 8,9,10	11,12	11	2,12,13	10,14 15,16	10,15 16,17	18,19,20,21,22,23, 24,25,26,27,28,29	

Table 3.3: (cont.)

references: 1. Jackson et al. (1996), 2. Sellers et al. (1992), 3. Camillo and Gurney (1986), 4. Bond and Willis (1969), 5. Korner et al. (1979), 6. Woodward (1987), 7. Running and Hunt (1993), 8. Rutter (1975), 9. Nielson (1995), 10. Jarvis et al. (1976), 11. Sellers et al. (1996), 12. Dickinson et al. (1993), 13. Hazlett (1992), 14. Ross (1975), 15. Denmead (1976), 16. Ripley and Redmann (1976), 17. Rauner (1976), 18. Cowan and Milthorpe (1968), 19. Newman (1969), 20. Hellkvist et al. (1973), 21. Richter (1976), 22. Gardner and Ehlig (1963), 23. Gardner (1960), 24. Sala et al. (1981), 25. Boyer (1971), 26. Denmead and Shaw (1962), 27. Gollan et al. (1986), 28. Federer (1979), 29. Havraneck and Benecke (1978).

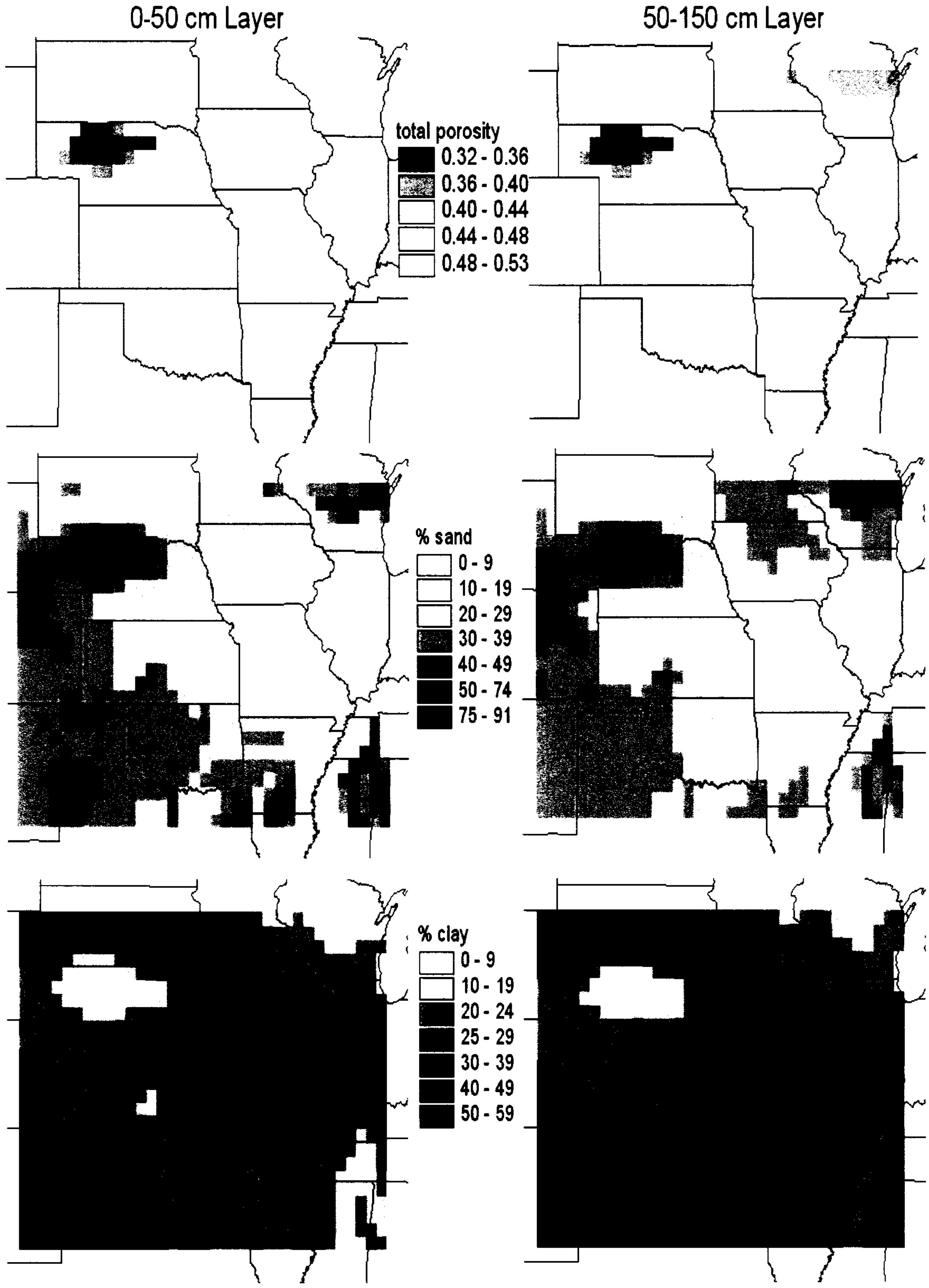

Figure 3.1. Grid-cell averages of total porosity, percent sand and percent clay from VEMAP soils database.

Figure 3.2. USDA textural classes based on sand and clay percentages in Figure 3.1.

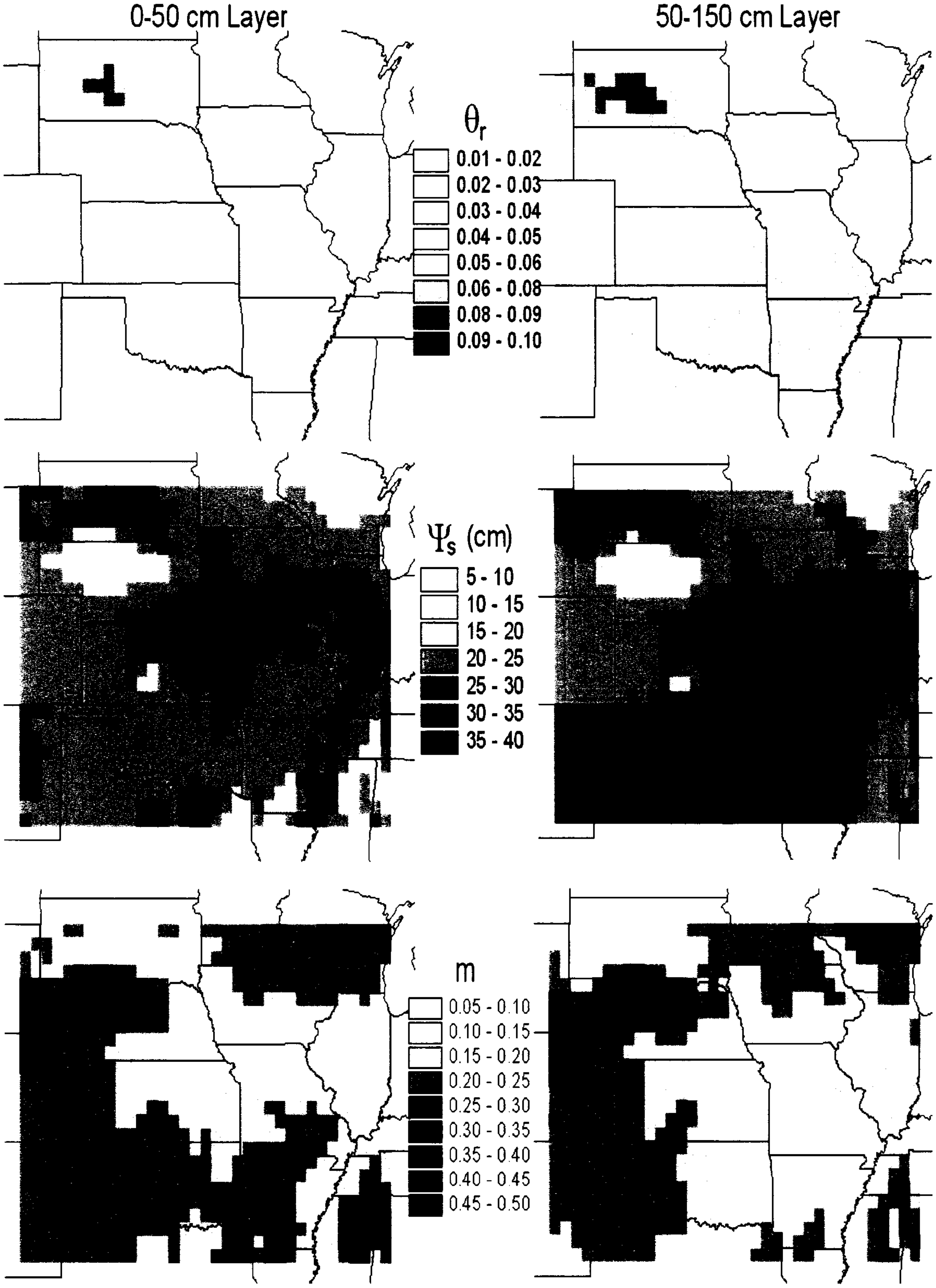

Figure 3.3. Brooks-Corey parameters as calculated with regression results from Table 3.1 and percentages of sand and clay in Figure 3.1.

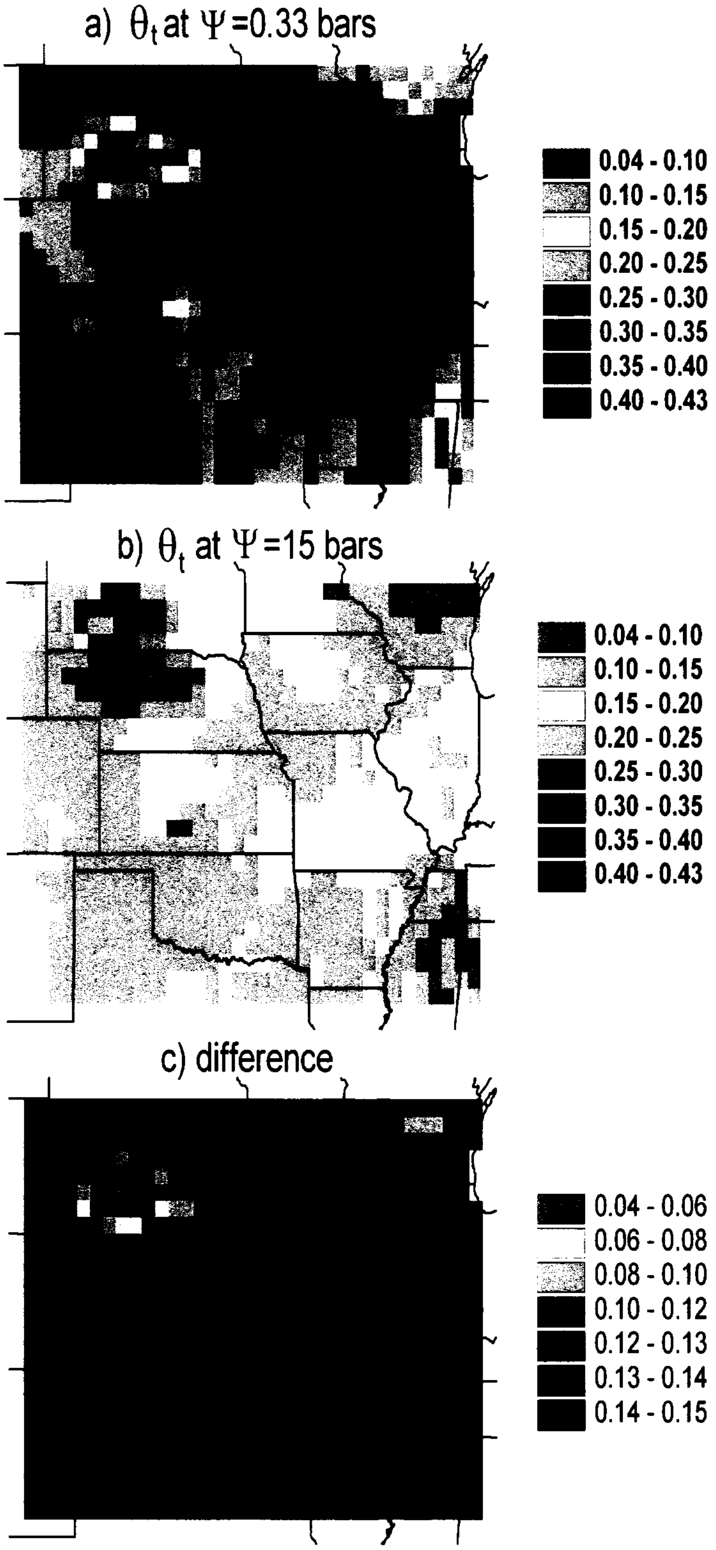

Figure 3.4. Soil moisture content at a matric potential of (a) 0.33 bars (i.e., field capacity), (b) 15 bars (i.e., permanent wilting point); and (c) the difference (i.e., available water capacity).

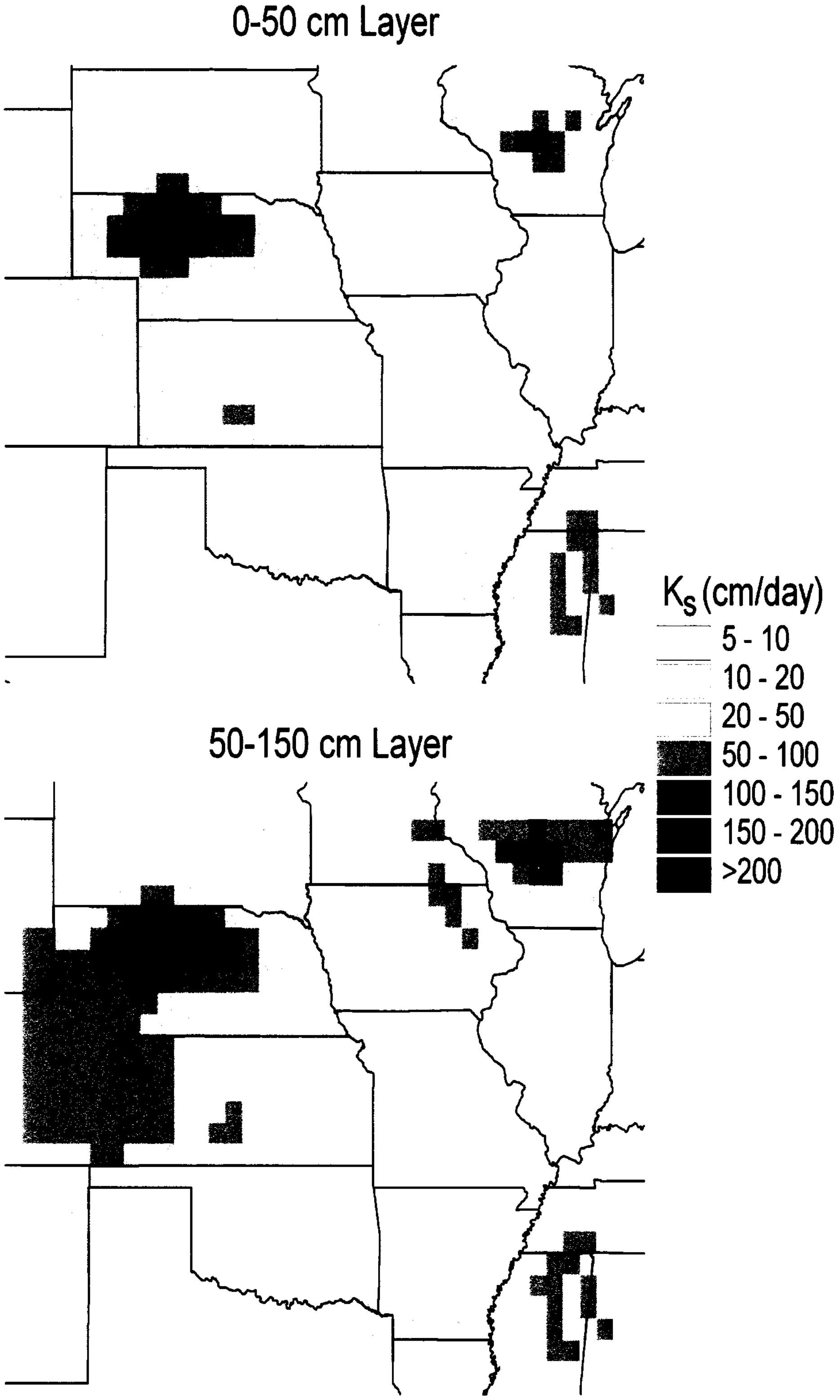

Figure 3.5. Saturated hydraulic conductivity as calculated with (3.2), a = 35 cm3/s and the Brooks-Corey parameters in Figure 3.2.

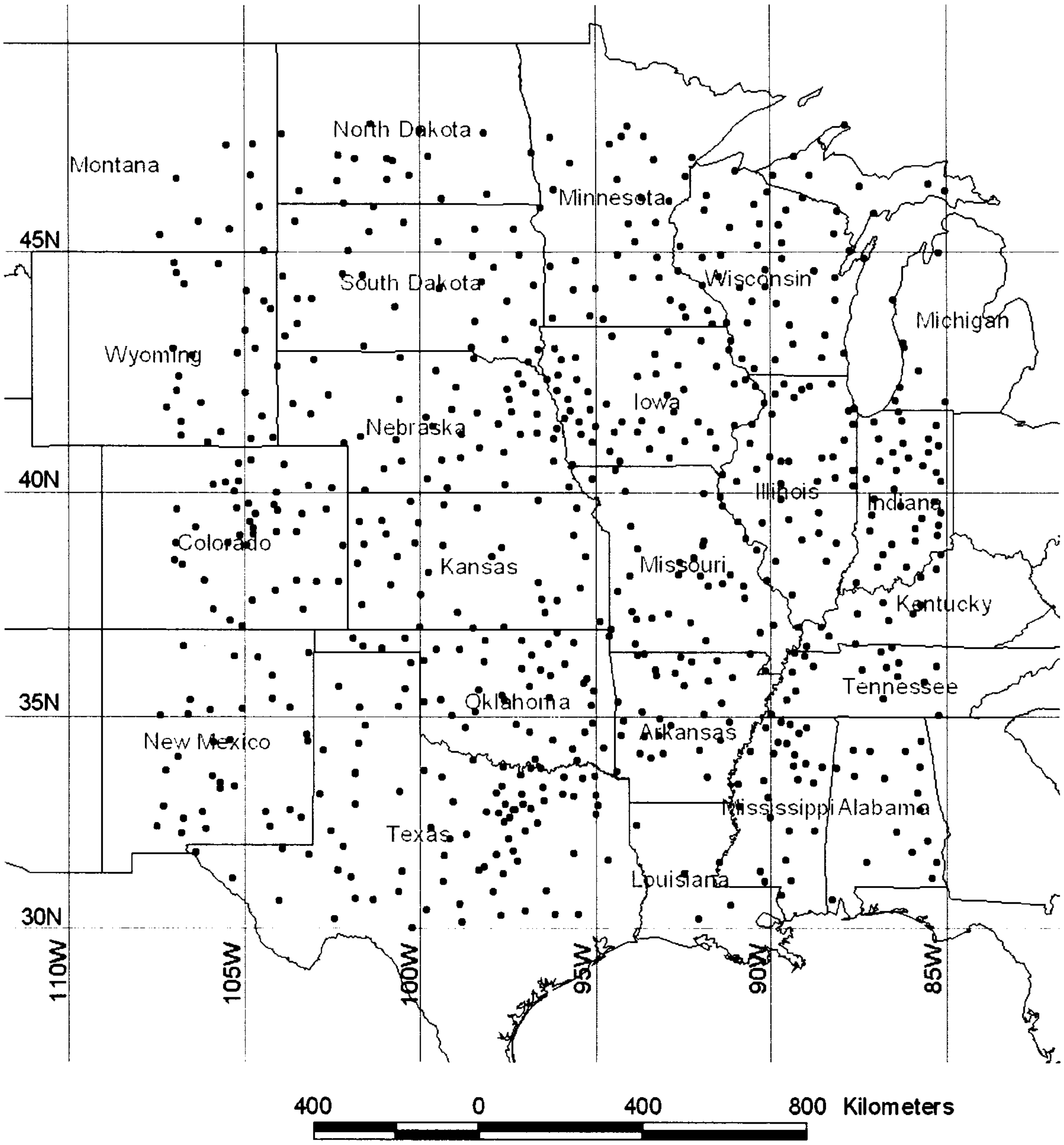

Figure 3.6. Locations of the 706 hourly precipitation observation stations used in the calculation and interpolation of storm statistics.

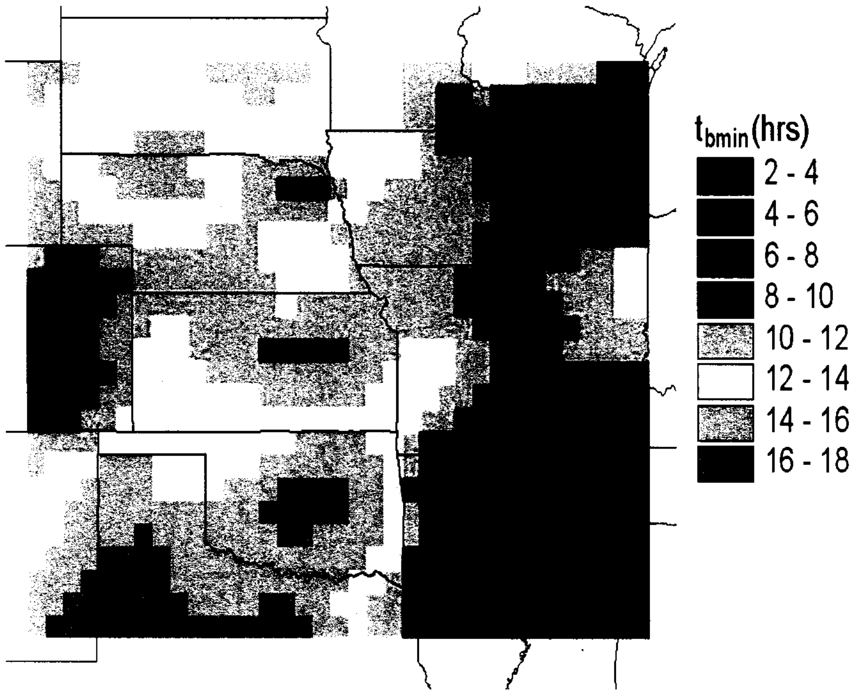

a) January

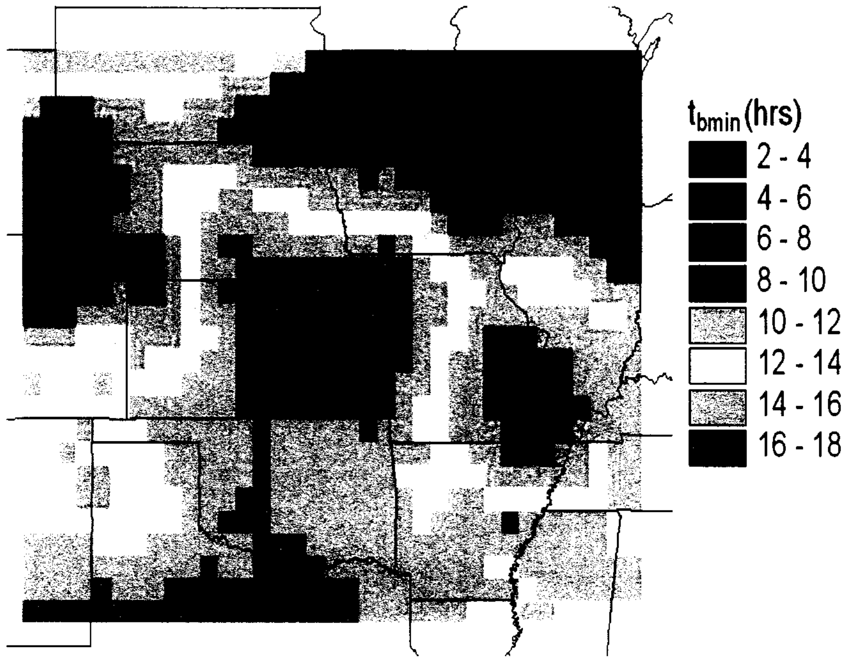

b) July

Figure 3.7. Minimum time between storms (hrs) necessary for defining independent storms: (a) January and (b) July.

a) January

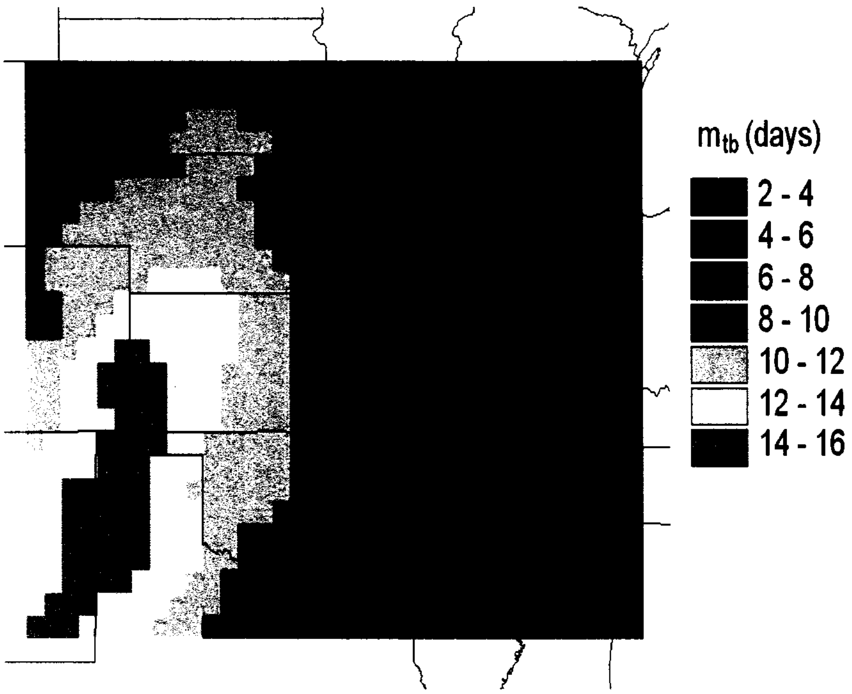

b) July

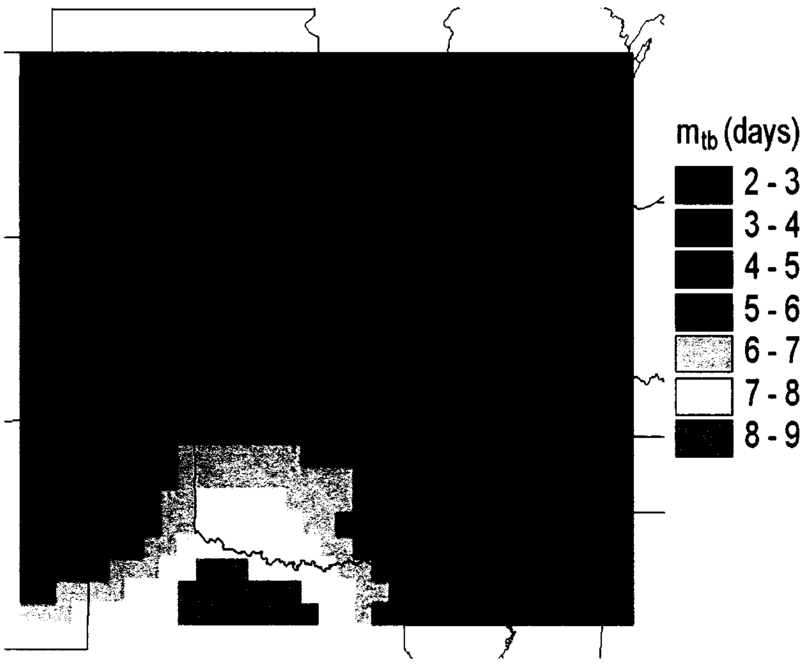

Figure 3.8. Mean time between storms (days): (a) January and (b) July.

a) January

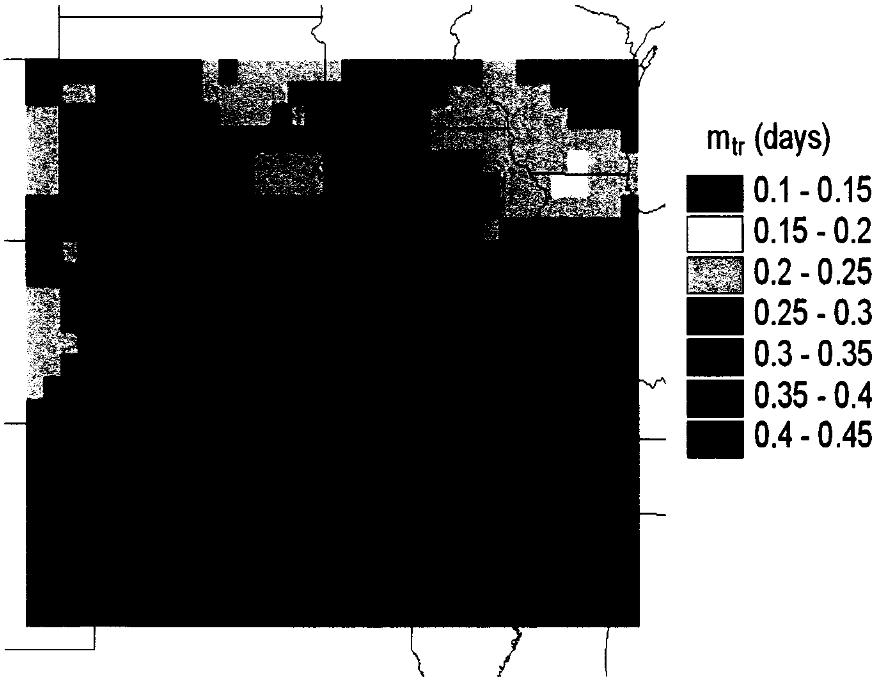

b) July

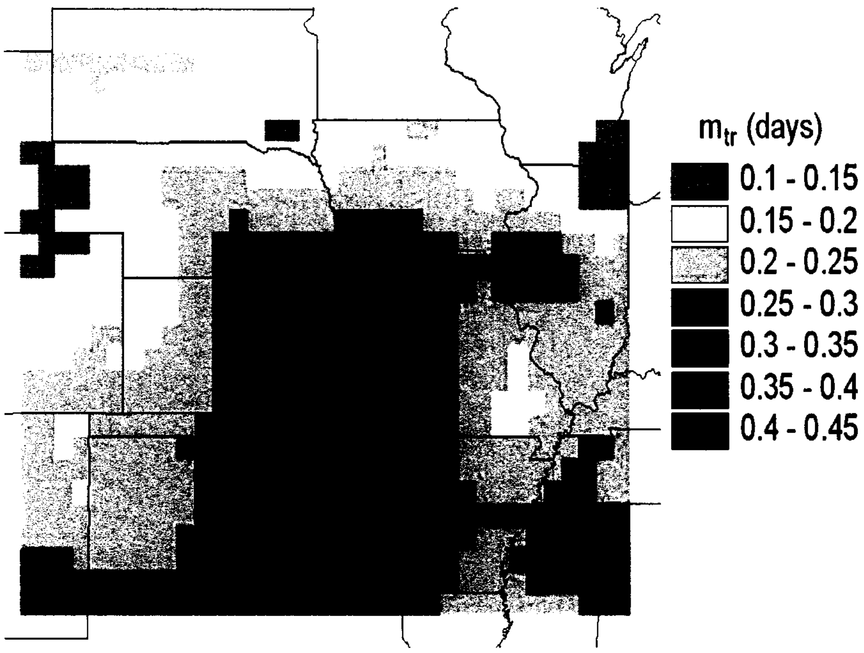

Figure 3.9. Mean storm duration (days): (a) January and (b) July.

a) January

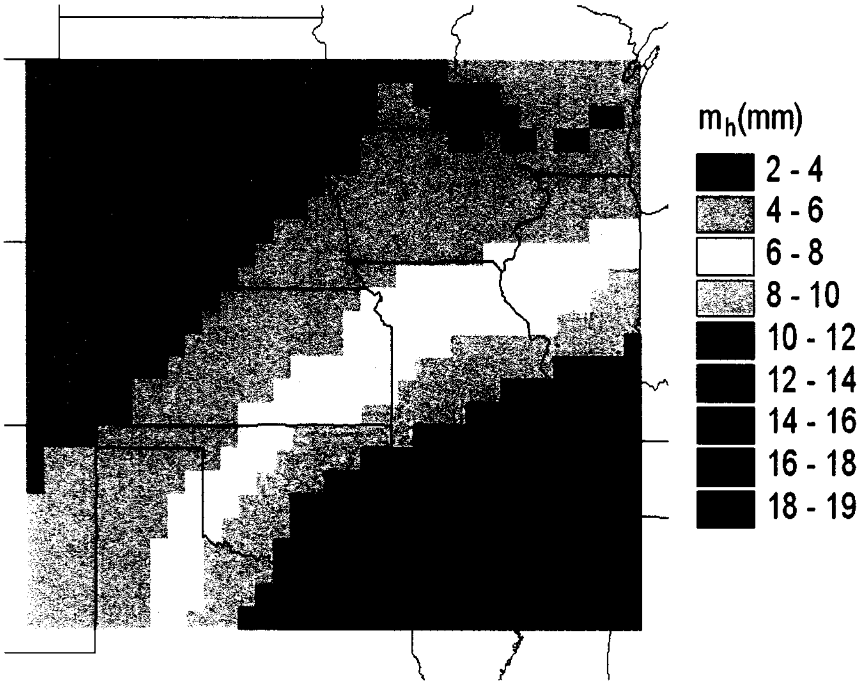

b) July

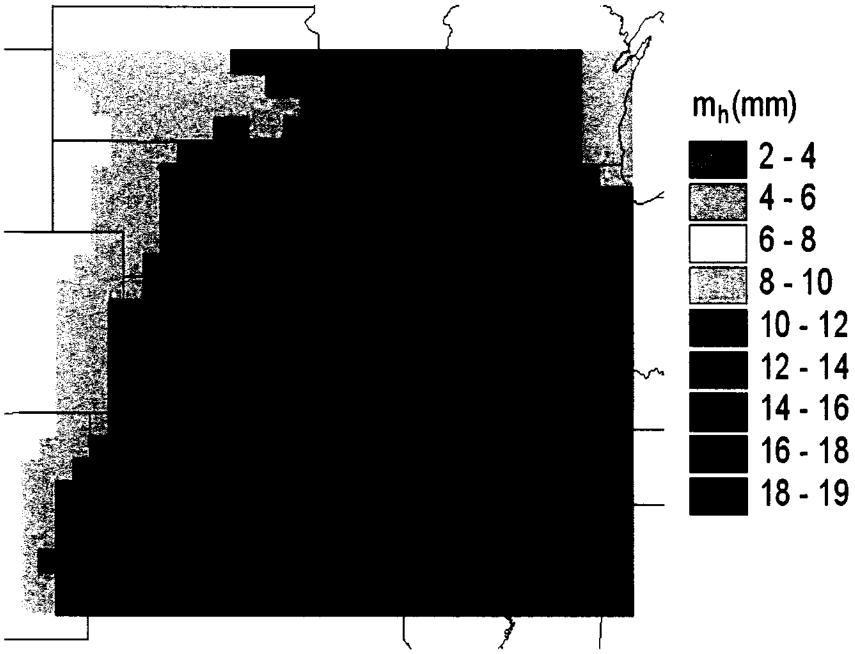

Figure 3.10. Mean storm depth (mm): (a) January and (b) July.

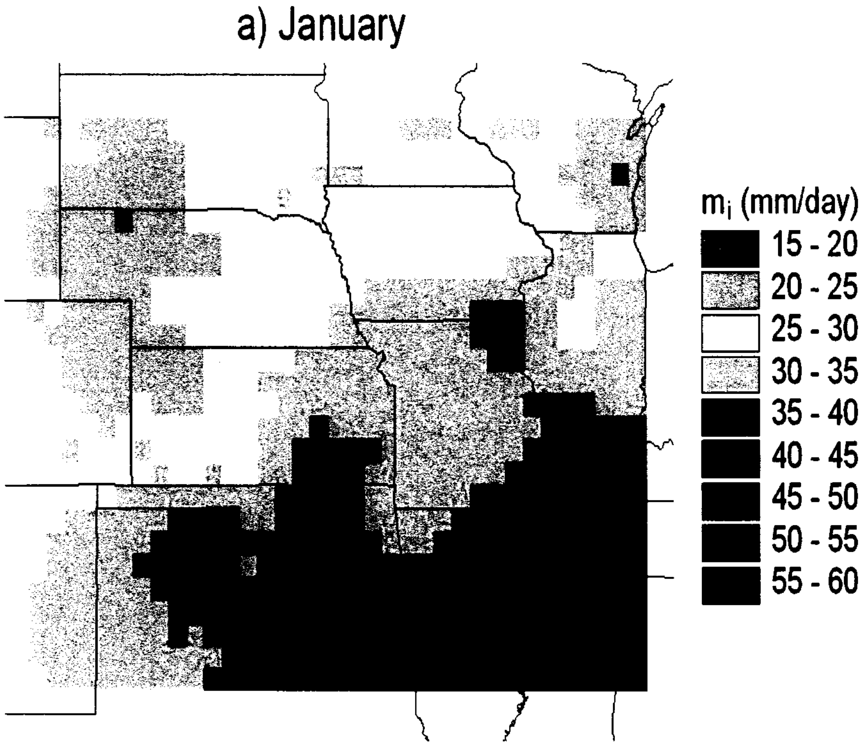

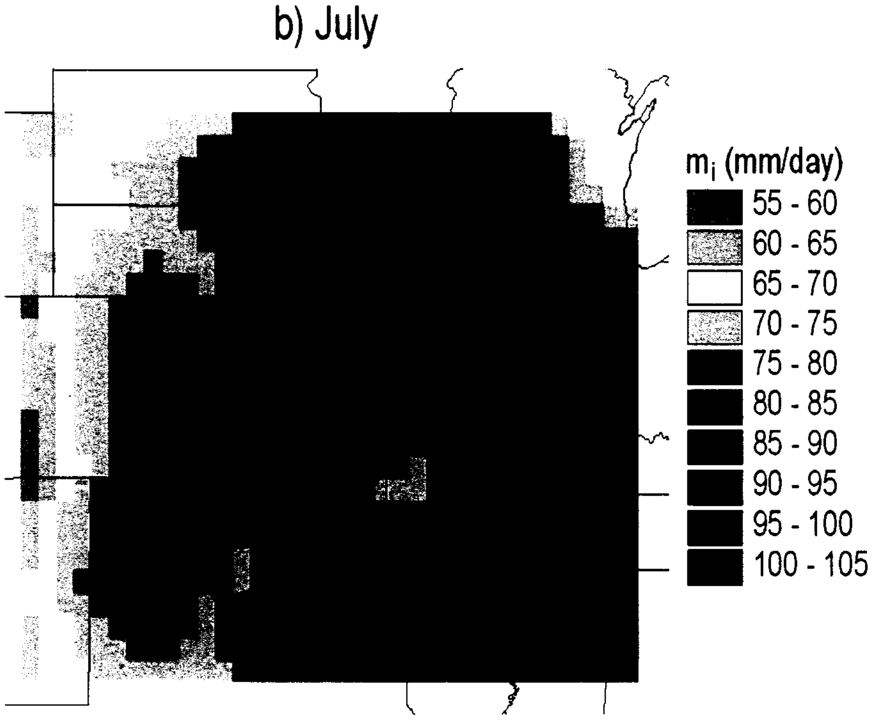

Figure 3.11. Mean storm intensity (mm/day): (a) January and (b) July.

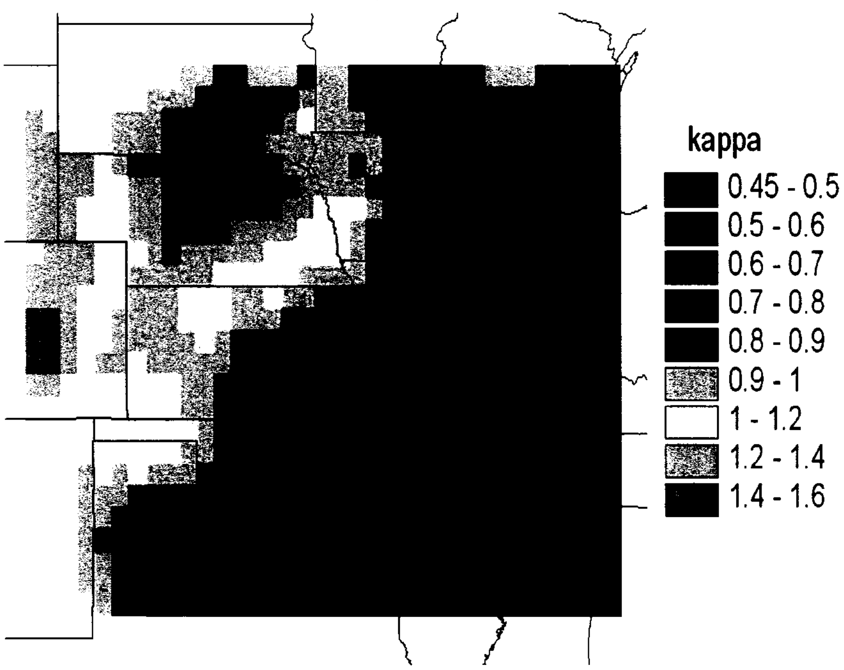
a) January

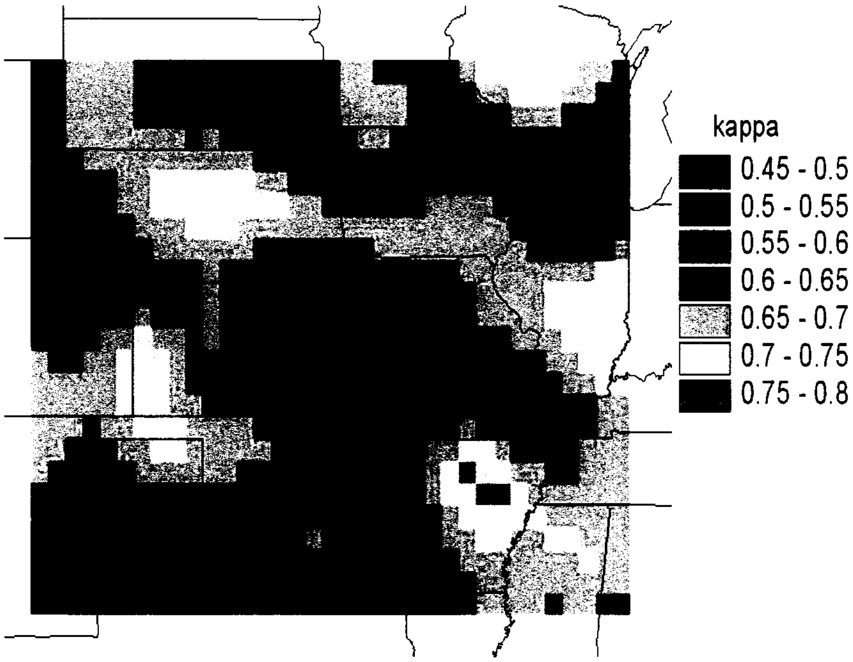
b) July

Figure 3.12. κ parameter of gamma distribution of storm depth: (a) January and (b) July.

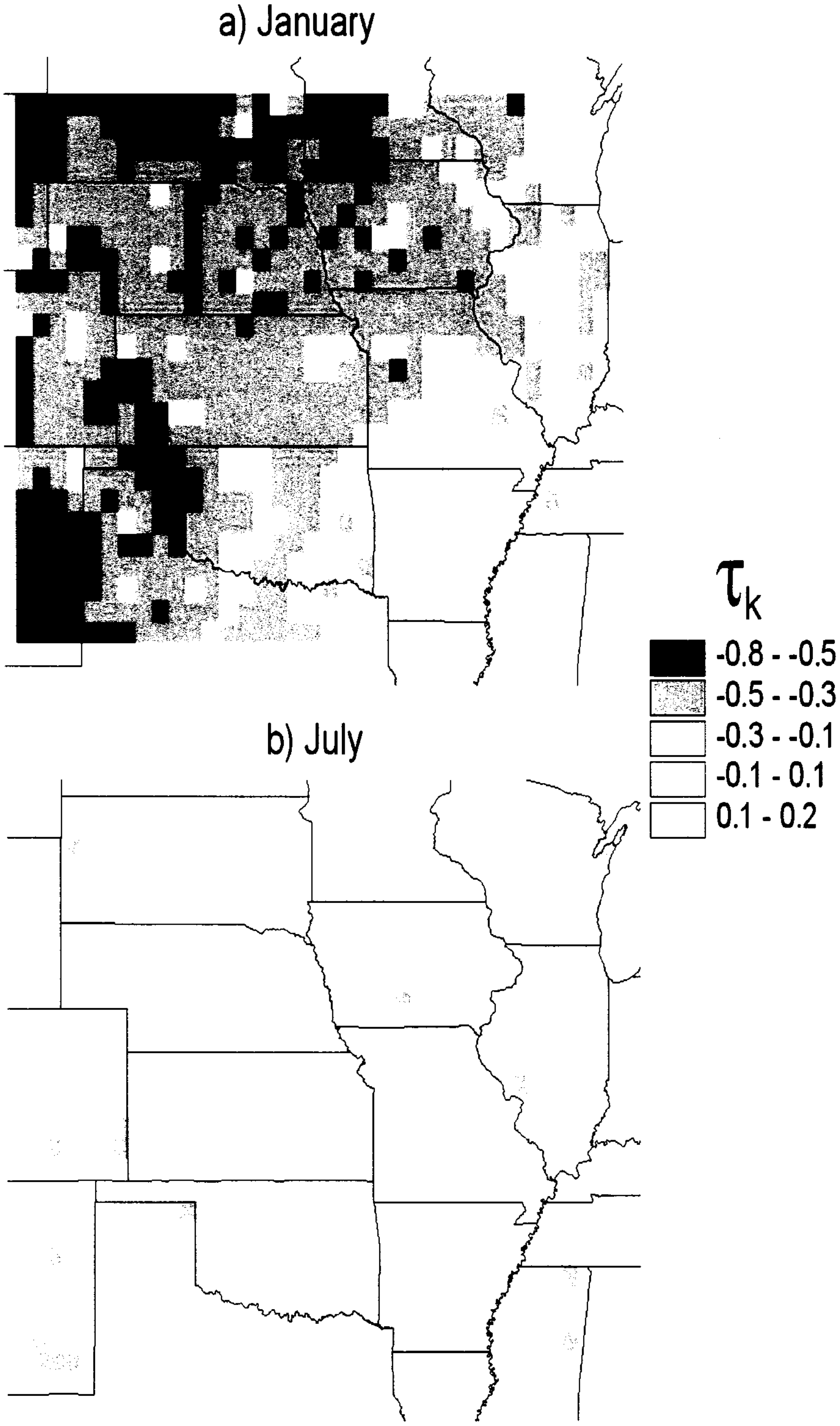

Figure 3.13. Correlation between storm duration and intensity as measured by Kendall's coefficient, τ_k: (a) January and (b) July.

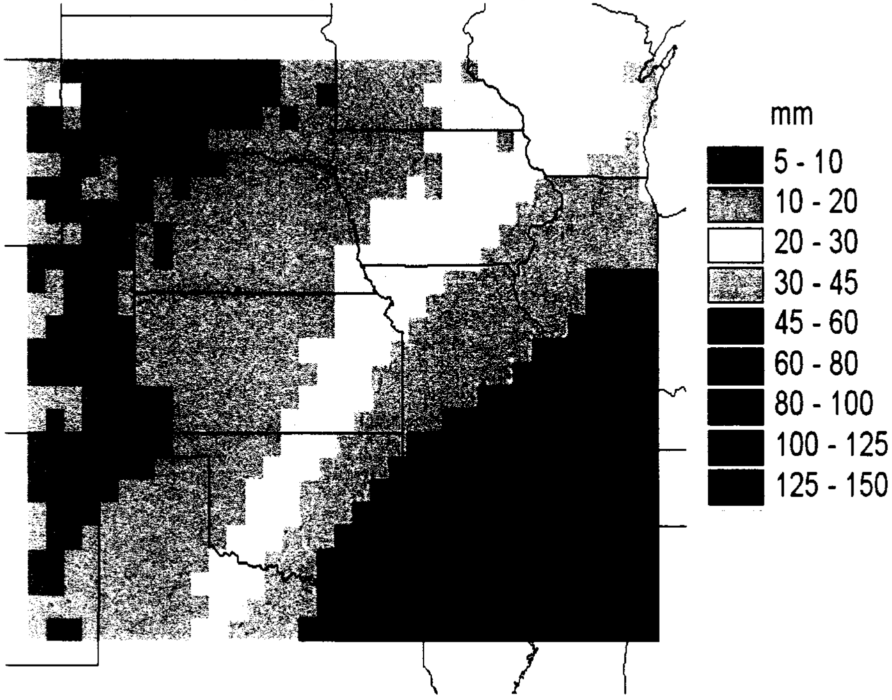

a) PRISM precipitation -January mean

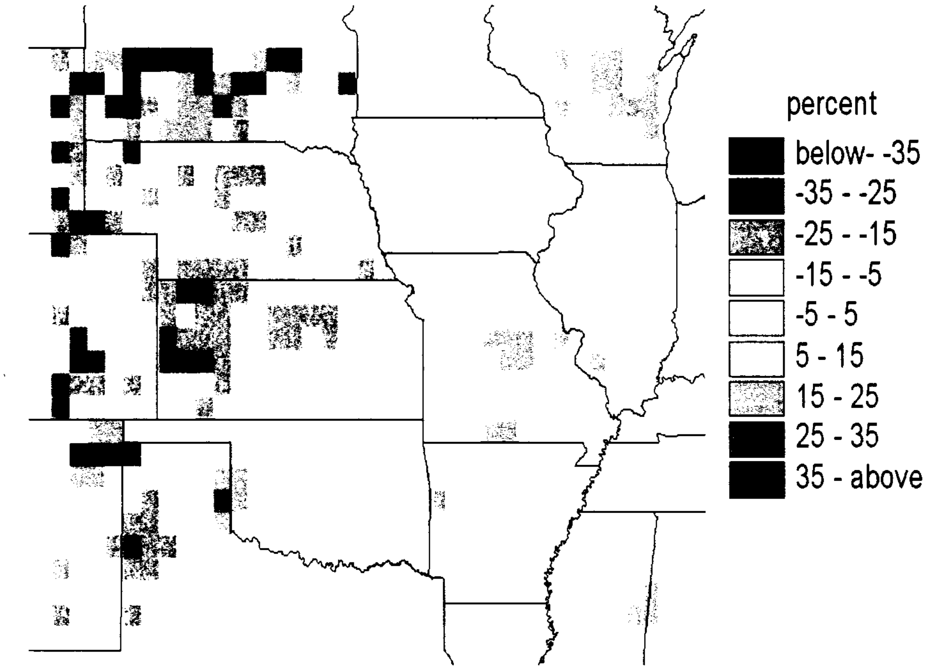

b) Poisson model difference

Figure 3.14. (a) mean January precipitation (1949-1993) from the VEMAP/PRISM database, and (b) the percent by which mean precipitation calculated with (2.24) and the corresponding storm statistics in Figures 3.6-3.8 differs from the PRISM means

a) PRISM precipitation - July mean

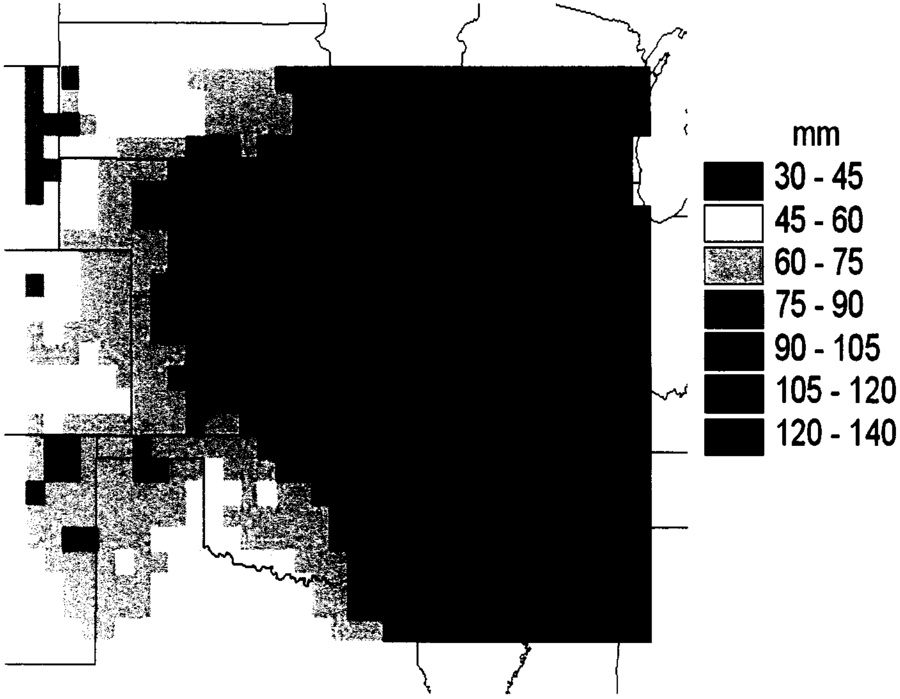

b) Poisson model difference

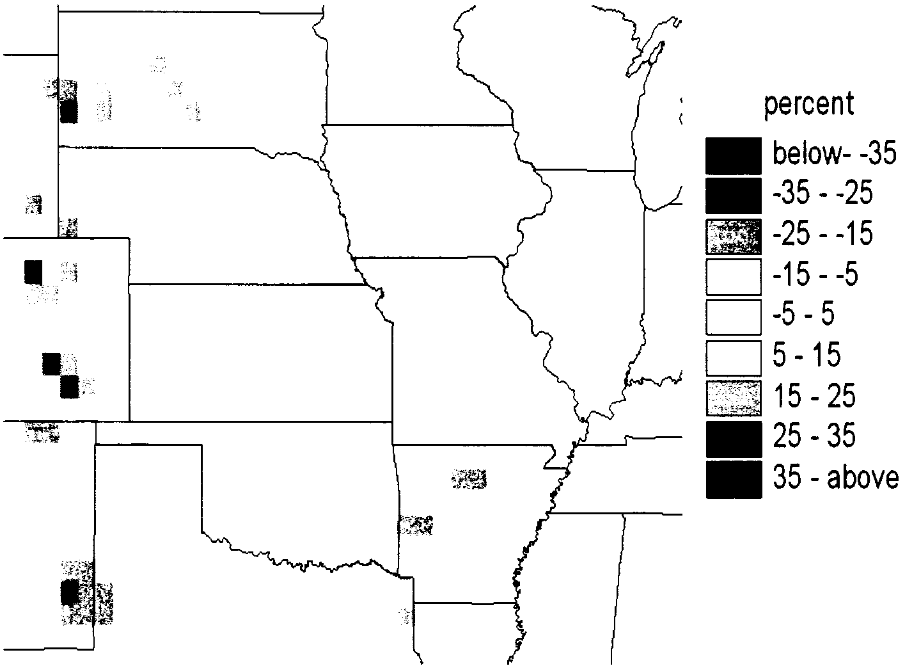

Figure 3.15. (a) mean July precipitation (1949-1993) from the VEMAP/PRISM database and (b) the percent by which mean precipitation calculated with (2.24) and the corresponding storm statistics in Figures 3.6-3.8 differs from the PRISM means.

a) PRISM precipitation - annual mean

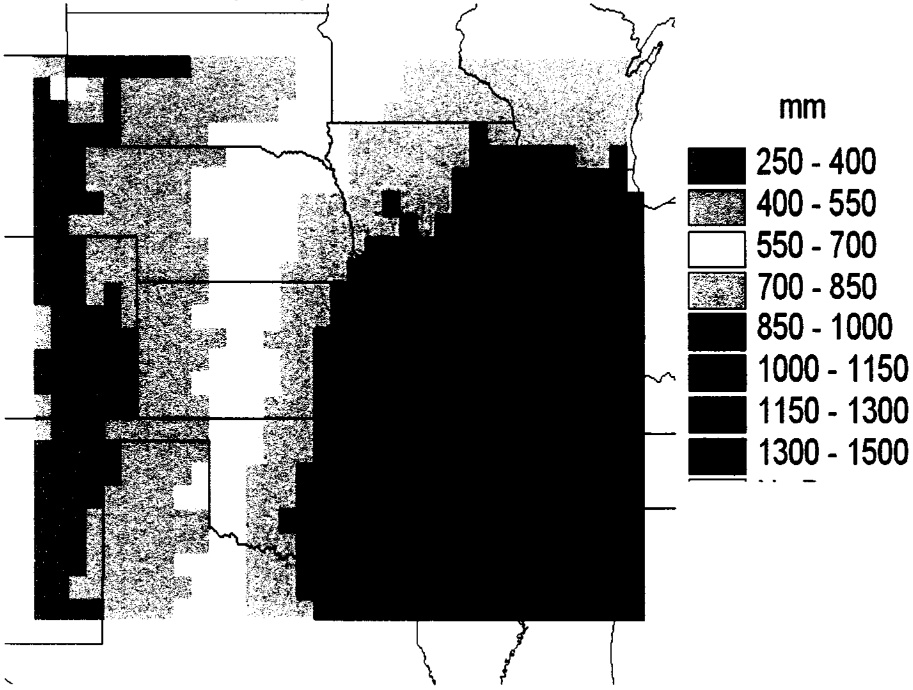

b) Poisson model difference

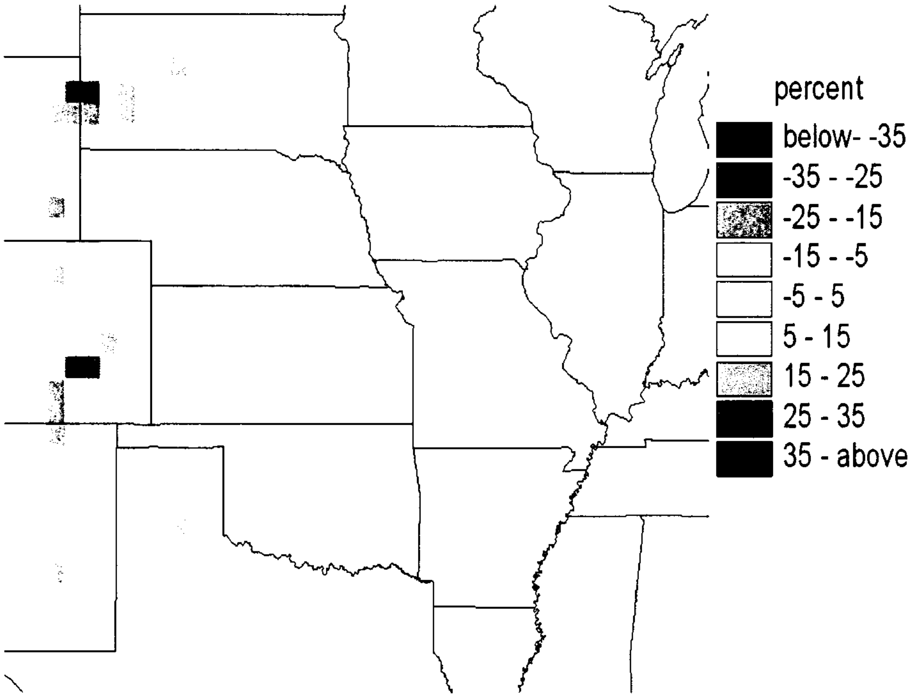

Figure 3.16. (a) mean annual precipitation (1949-1993) from the VEMAP/PRISM database and (b) the percent by which mean precipitation calculated with (2.24) and the corresponding storm statistics for each month of the year differs from the PRISM means.

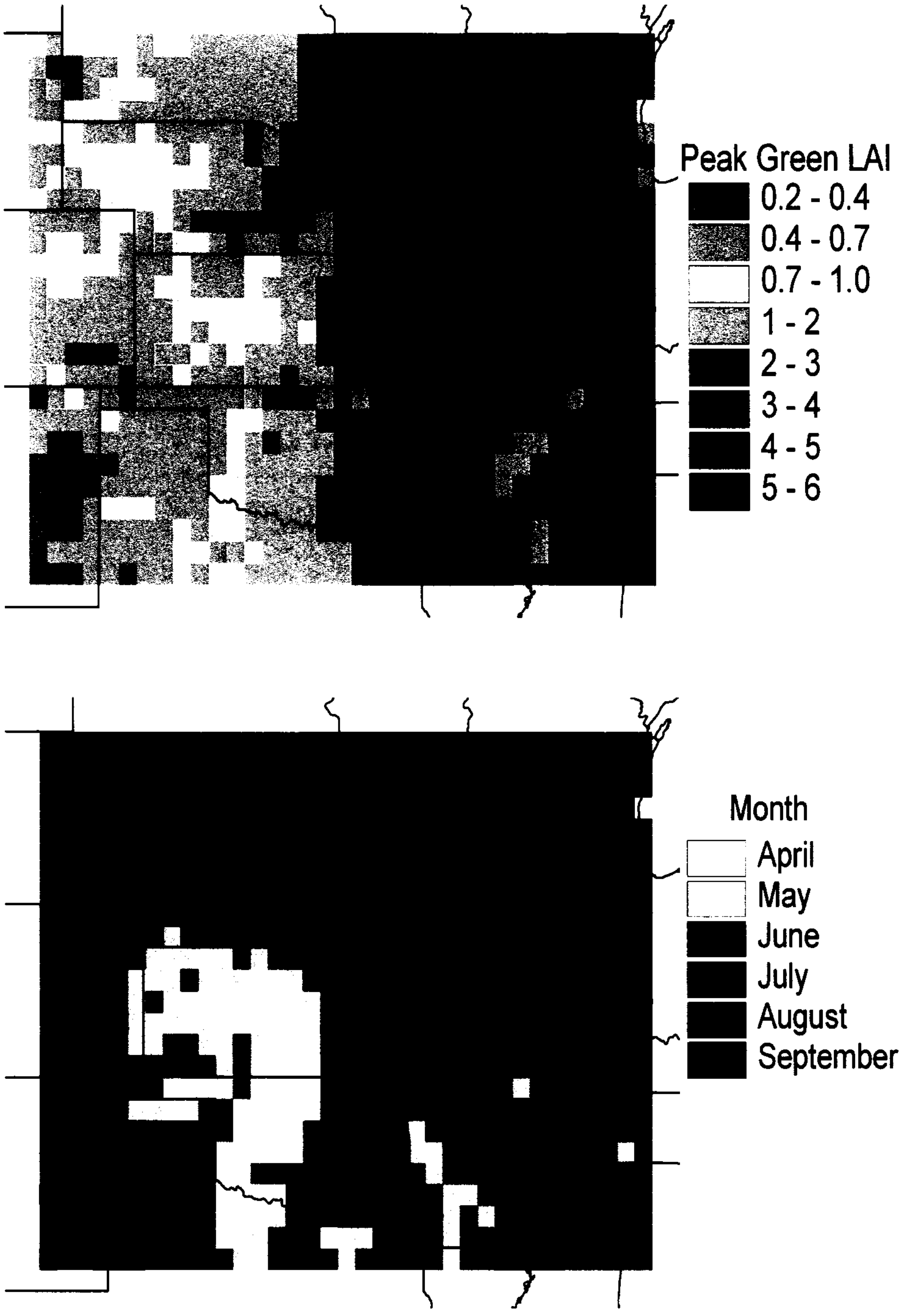

Figure 3.17. Peak monthly average green LAI (July 1981- June 1991) and the month in which it occurs. From the dataset of Buermann et al. (2002).

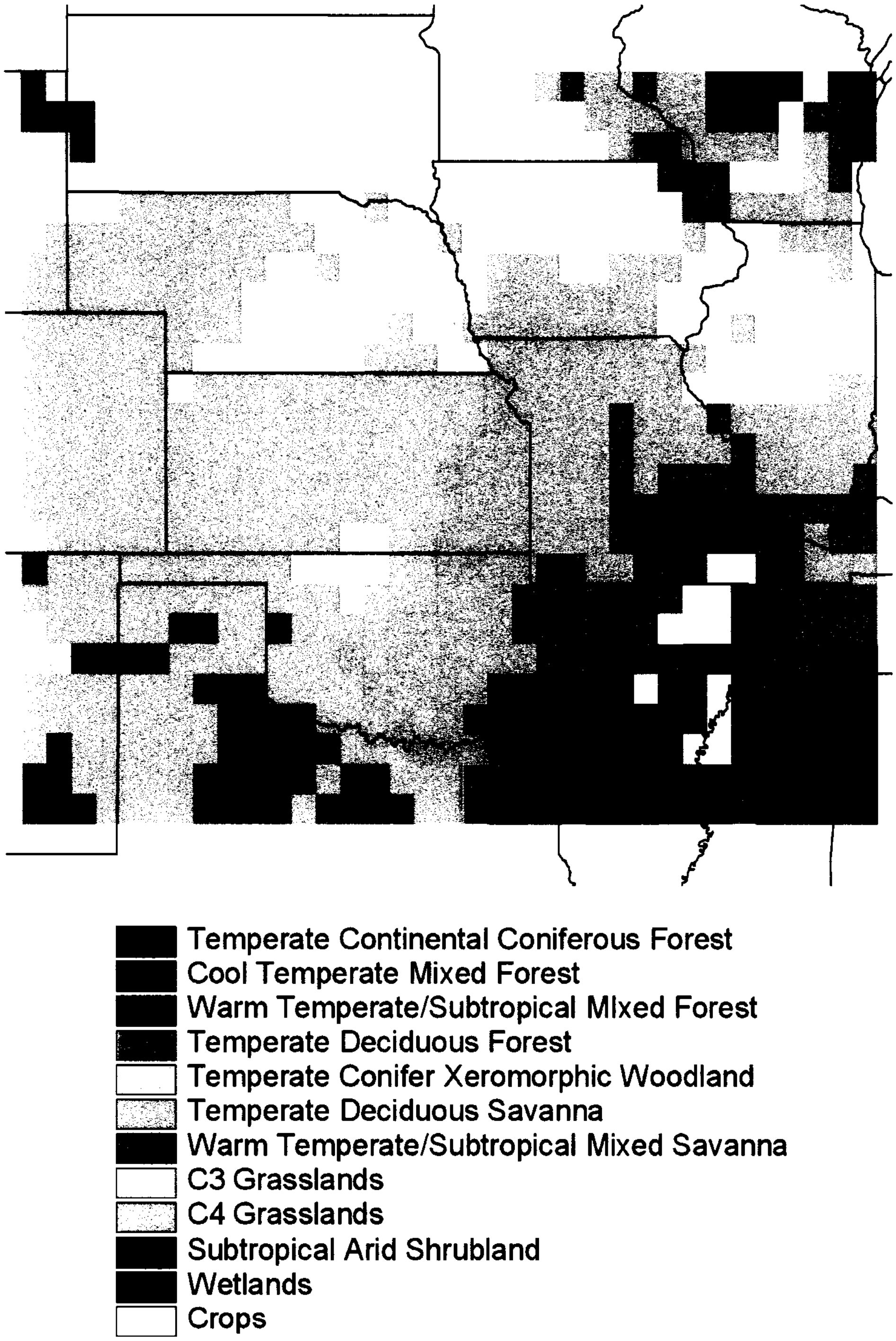

Figure 3.18. The modified VEMAP version 2 vegetation classification.

Chapter 4: Methodology for Capturing Interannual Variability

4.1. Introduction

As noted in the Section 2.1, expected annual values of the water balance fluxes in the original Eagleson model are found by numerically solving for s_o, the value of s that closes the water balance. Our monthly, two-layer version can be solved in a similar manner. The task is of course much more complex, given values for s must be found and the water balance closed for two soil layers in each of twelve different months. A solution scheme was developed to do just that using mean monthly values of the climate variables, storm statistics and green LAI. In each month, values of s_u and s_d are found such that the changes in storage from the beginning to the end of the month (based on an assumption of linear change in soil moisture across the month) are equal to the net of the fluxes in and out of the two soil layers. The annual water balance is closed by solving for values of s_u and s_d for January which are returned for the subsequent January through solution of the intervening monthly water balances. Another implementation of the model was developed which is driven by a time series of monthly climate variables. In that version, the same procedure is used to solve s_u and s_d in each month. This second version can be used to estimate both the long-term mean of the water balance and its interannual variability. For this reason, as well as issues of nonlinearity discussed in the following sections, the time-series version was the one used to calibrate the model and generate results. We continue to use expected value notation; however, it should be noted that expected values are being calculated for specific months of specific years and that long-term averages presented in the remaining chapters are averages of those expected values.

4.2. Recharge-Zone Soil Moisture and Groundwater Runoff

The monthly expected values of the water balance fluxes as obtained by solution of the annual water balance will not equal their long-term means. This is mainly because the formulation of the expected values of the fluxes do not account for the stochastic nature of soil moisture—the main controlling variable. The more nonlinear the relationship between s and the fluxes, the worse the approximation of using the mean of s becomes. The most nonlinear relationship exists for groundwater runoff. To wit, a range of 0.12 to 0.50 for m (see Figure 3.2) corresponds to a range for the exponent c in (2.9) of 7 to 20 (see (2.10)). Therefore, using the mean value s_d in (2.9) has the potential to underestimate the long-term mean of groundwater runoff significantly. We suggest that soil moisture in the recharge zone is persistent enough that application of (2.9) in a given month will provide an adequate estimate of groundwater runoff for that specific month, and that our main concern should be with the interannual variability of s_d. Therefore, use of the time-series version of the model, which resolves the interannual variability of s_d, should provide a better estimate of the long-term mean water balance. In fact, comparison of results between that version and the expected-value-solution version showed the latter to produce substantially lower mean groundwater runoff for much of the study area.

4.3. Root-Zone Soil Moisture, Precipitation and Surface Runoff

Due to the nonlinearities involved, the use of a mean value of s will also underestimate surface runoff (see Section 2.3.4). Again we suggest that our greatest concern is with the interannual variability of soil moisture. In this case, the interannual variability of s_u is directly dependent on the interannual variability of precipitation and subsequent infiltration. In his derived-distribution approach to modeling interannual variability, Eagleson (1978e) substitutes annual values of P for $E[P]$ in his annual water balance equation. Similarly, in our time-series implementation we use actual monthly values of P for $E[P]$ in (2.3), (2.25) and (2.30).

When substituting values of P for $E[P]$, Eagleson (1978e) assumes that the parameters of the Poisson precipitation model remain unchanged. However, a given value of P that is larger (smaller) than $E[P]$ increases the likelihood of greater (fewer) than the mean number of storms for that month, as well the likelihood for deeper (shallower) storms than the mean depth. By applying Bayes' Theorem to the Poisson stochastic precipitation model, Salvucci and Song (2000) derive probability distributions for the number of storms and the mean storm depth over a given period conditioned on the actual precipitation for that period. Using our notation, their equation for the conditional mean number of storms can be written as

$$m_v\big|_P = \frac{\displaystyle\sum_{n=1}^{\infty} \frac{m_v^{\,n}}{(n-1)!} \frac{(m_v \kappa P / E[P])^{n\kappa - 1}}{\Gamma[n\kappa]}}{\displaystyle\sum_{n=1}^{\infty} \frac{m_v^{\,n}}{n!} \frac{(m_v \kappa P / E[P])^{n\kappa - 1}}{\Gamma[n\kappa]}} \tag{4.1}$$

As discussed in Section 3.2, we use values of *E[P]* as determined by a long-term mean of *P*, as opposed to (2.24). As explained by Salvucci and Song (2000), the conditional distribution of the number of storms remains Poissonian because the conditioning process does not add correlation between interarrival times. Assuming that storm depth and interarrival times are independent (a tendency for only slight positive correlation was found in Section 3.2), the mean of the conditional distribution of storm depths is given by

$$m_h\big|_P = \frac{m_v}{m_v\big|_P} \frac{P}{E[P]} m_h \tag{4.2}$$

Unlike the Poisson distribution for the number of storms, the form of the gamma distribution of storm depths does not remain unchanged by the conditioning process. The conditional distribution as derived by Salvucci and Song (2000) contains infinite series of similar form to those in (4.1). Deriving an expected value for surface retention evaporation from that distribution would be analytically intractable. However, because surface retention evaporation is a relatively small component of the water balance and is subject to errors greater than the small differences in the form of the distribution of storm depths, using an assumption of a gamma distribution (with parameters $m_h|_P$ and κ) and the resulting equation (2.40) will provide adequate estimates of the expected value of surface retention.

More important is the task of translating the conditional probability distribution of storm depth into conditional probability distributions of storm duration and intensity, as required by the methodology used to derive an expected value of surface runoff. The assumption there is that storm duration and intensity are exponentially distributed. As noted in Section 2.1, that assumption is inconsistent with gamma-distributed storm depths. Likewise, it is inconsistent with the conditional distribution of storm depth. Without proof, we assume that the conditional distributions of storm intensity and duration maintain both exponential distributions and independence, and therefore we can substitute the conditional means for the unconditional ones in (2.22). Following (2.23), we write

$$m_h\big|_P = m_i\big|_P \, m_{tr}\big|_P \tag{4.3}$$

The independence of i and t_r also means that the ratio of their conditional means to their means will be identical. Using that fact, dividing (4.3) by (2.23) and substituting in (4.2) leads to

$$\frac{m_i\big|_P}{m_i} = \frac{m_{tr}\big|_P}{m_{tr}} = \left(\frac{m_v}{m_v\big|_P}\frac{P}{E[P]}\right)^{\frac{1}{2}} \tag{4.4}$$

If we also maintain the assumption of the independence of storm duration and the time between storms, we can, in the manner of (2.24), write

$$m_v\big|_P = \frac{\tau}{m_{tr}\big|_P + m_{tb}\big|_P} \tag{4.5}$$

Solving for $m_{tb}|_P$ and substituting in (4.4) gives

$$m_{tb}\big|_P = \frac{\tau}{m_v\big|_P} - m_{tr}\left(\frac{m_v}{m_v\big|_P}\frac{P}{E[P]}\right)^{\frac{1}{2}} \tag{4.6}$$

The process of running the time-series version of the model is now one of substituting the conditional values of m_v, m_h, m_i and m_{tb} for their unconditioned values in the expected value formulations of the water balance fluxes, along with the actual monthly values of P for $E[P]$. As do Salvucci and Song (2000) for the two locations to which they apply their equations, we found that across our study area most of the increase or decrease in precipitation over the mean translates to changes in the expected value of storm depth. Specifically, $m_v|_P/m_v$ generally falls around 0.8 and 1.2 when the actual monthly precipitation is respectively one half and twice the mean. Comparison of a model run using the conditional means with a run using the unconditional ones showed relative increases in mean annual surface runoff being significant only in the southwest of the study area. However, the interannual variability of surface runoff increases substantially across the entire study area.

4.4. Leaf Area Index and Transpiration

A final important source of nonlinearities in the interannual variability of the water balance is the variation in vegetation density, which is measured in the model by green LAI. For a means of capturing the interannual variability of LAI, we turn to the discipline of biogeography, which has long concerned itself with predicting the type and density of vegetation that will establish itself in a given climate. While the earliest studies focused on the easily observable quantities of precipitation and temperature (*e.g.*, Holdridge 1947), more recent studies have looked more directly at the role of the water balance. For example, Stephenson (1990) correlated North American plant formations with actual evapotranspiration and its deficit below potential evapotranspiration. Others have taken a more process-based modeling approach. In particular, one of the biogeochemistry and two of the biogeography models in the VEMAP (VEMAP members 1995)—BIOME-BGC (Running and Hunt 1993), DOLY (Woodward et al. 1995) and MAPSS (Nielson 1995)—treat LAI as a dependent variable which is maximized under the constraints of available water and energy.

In order to capture the interannual variability in potential and actual evapotranspiration that is due to variation in vegetation density, we use the idea of a water-limited maximization of LAI. Although the above-mentioned models apply the concept only to the mean water balance, we believe that it has applicability on a year-to-year basis. Specifically, we propose that in any given year, the green LAI of the canopy is just large enough, within certain bounds, to utilize soil moisture down to a physiologically determined minimum, which occurs in the latter half of the growing season. In order to capture the constraints of leaf phenology, we use a fixed-shape envelope of green LAI, which is scaled in every month by the same factor. That envelope is determined by the long-term mean estimates of green LAI derived from the NDVI by Buerman et al. (2002), as discussed in Section 3.3.2. Maximizing LAI on a yearly basis is somewhat teleological in that the peak LAI generally pre-dates the minimum in soil moisture; in years with a wet late growing season, a higher peak is reached in anticipation of the greater availability of soil moisture, while in dry years, a lower peak is reached in anticipation of the drought. We address those implications by proposing that, under the constraints of the fixed shape of the LAI envelope, increases or decreases in LAI in the first half of the growing season serve as proxies for changes in the latter half that would occur with a more fluid and realistic variation in LAI over the growing season. Furthermore, we constrain the minimum and maximum factor by which the LAI envelope is scaled to, respectively, 50% and 150% of the average. Those percentages are primarily based on the mapping of the interannual variation of grassland productivity over the U.S. Great Plains by Sala et al. (1988). We also place an absolute lower and upper limit on peak green LAI of 0.2 and 6.0 for all vegetation classes. The upper limit is the same one applied by Buermann et al. (2002) in their conversion of the NDVI to LAI. An upper limit is necessary because for a closed canopy, light *inter alia* is the main limiting factor.

Choice of a soil-moisture minimum that is used to maximize LAI is our remaining concern. In both BIOME-BGC and MAPPS, the maximization of LAI is constrained by the wilting-point matric potential, while DOLY allows for the complete utilization of precipitation by the vegetation. We suggest that such constraints will overestimate transpiration. Rather, we hypothesize that the point to which soil moisture is drawn down in a water-limited system is on average somewhat above the wilting point and that the critical soil-moisture potential, Ψ_{uc}, which was defined in Section 2.3.6 as the potential which initiates stomatal closure at the daily peak in transpiratory demand, approximates that point well. While a detailed theory as to the ecophysiological mechanism involved in a soil-moisture minimum at Ψ_{uc} is beyond the scope of this dissertation, it makes sense from a general adaptation standpoint that vegetation would leave some reserve of soil moisture to reduce the risk of leaf abscission during a late-growing-season drought. Furthermore, the need for stomatal closure represents a strong signal to a plant that the wilting point is close at hand.

In Section 5.6, we compare modeled mean monthly soil moisture with multi-year observations at four sites across the study area. Here we look at the interannual variability in the observations at the three driest sites and assess the extent to which it conforms to the hypothesis of an annual soil-moisture minimum at $\Psi_{uc.}$ The first two sites are USDA grassland research locations: the Central Plains Experimental Range (CPER) in northeast

Colorado and R-5 experimental watershed in central Oklahoma. Details of the collection of the soil moisture data are discussed in Section 5.6. In Figure 4.1, monthly root-zone volumetric moisture content over the observation periods are plotted for a clay-loam slope and a sandy-loam slope at the CPER, and for the entire R-5 watershed, which is composed of silt loam soils. Indeed, we see that in all three plots soil moisture reaches a minimum over a relatively narrow range in the latter half of the growing season. That range is about 0.13 to 0.14 for the clay-loam slope and 0.09 to 0.10 for the sandy-loam slope at the CPER. For the considerably more humid R-5 watershed, the range is wider at about 0.10 to 0.15. Soil moisture retention data collected at both sites is plotted in Figure 4.2. Although the CPER data are for soils collected elsewhere at the site, they were matched to the slope soils based on sand and clay percentages.

For all three of the above cases, comparison of the soil moisture data with the soil moisture retention data shows that in each year soil moisture in the root zone is drawn down to or near 15 bars of matric potential. While measurement error is significant in *in situ* soil moisture data and in any form of matric potential data, we can still say with confidence that in all three cases soil moisture is always drawn to some point along the flat part of the soil moisture retention curve above about 5 bars. That part of the curve is typically associated with water held to the soil particles by adsorption (Jury et al. 1991). The above analysis was the primary basis for setting the value of Ψ_{uc} to 10,000 cm (9.8 bars) in the model parameterization (see Table 3.3). That that value is also very near the matric potential at which stomatal closure is initiated at the daily peak in transpiratory demand is suggested by the work of Sala et al. (1981), who made leaf water potential and conductance measurements of *Bouteloua gracilis*—the dominant species in the shortgrass steppe and a major species in the mixed grasses of the R-5 watershed—during an artificially extended period of soil moisture dry-down at the CPER.

In Section 5.6, we also compare model results to soil moisture measurements from the USDA's W-2 experimental watershed in southwestern Iowa. Western Iowa is located on the eastern edge of the Great Plains, where according to model results, potential evapotranspiration is just balanced by precipitation on an annual average basis (see Figure 5.9c). Vegetation on the W-2 watershed is a rain-fed corn crop managed under conventional tillage, and soil texture is silty clay loam/silt loam. Average monthly volumetric soil moisture in the root zone is plotted in Figure 4.3 for the 23 years of observations. The annual minimum in soil moisture is clearly more variable for this semi-humid location than for the two semi-arid grassland locations. Nonetheless, there is a global minimum in the range of 0.15 to 0.17 that is reached in about 25% of the years. We suggest that it is only in those years that crop growth is substantially water-limited and that in other years the crop is at or near maximum productivity. Although we do not have a full soil-moisture retention curve for the soils in the watershed, Chung et al. (1999) report values of water content at 1/3 and 15 bars which are nearly identical to the values for the silt loam soils at the R-5 watershed. Assuming Figure 4.2b is also representative of the W-2 soils puts Ψ_{uc} at about 5 bars.

Denmead and Shaw (1962) measured transpiration rates from corn plants in containers over a range of soil moisture states and potential transpiration conditions. They found that the soil matric potential at which the actual transpiration rate was reduced below the potential rate (as defined by the maximum rate) varied from 0.3 bar at a potential rate of 6.4 mm/day to 6 bars at a potential rate of 1.4 mm/day. Such a dependency on the potential rate supports the resistance model outlined in Section 2.3.7. Nonetheless, in that section we suggested that under field conditions, typical vegetation density and transpiratory demand would combine to give a fairly constant value of $\Psi_{uc.}$ In Chapter 5, we see that modeled transpiration in the Corn Belt in July averages 2 to 3 mm/day (see Figure 5.7b). At 2 mm/day of transpitory demand, Denmead and Shaw (1962) saw a reduction in transpiration beginning at about 3 bars of soil matric potential. Gollan et al. (1986) found the leaf conductance of potted wheat and sunflower plants was reduced at nearly the same matric potential. The preceding evidence from the literature suggests that a Ψ_{uc} of 5 bars (5000 cm) slightly overestimates the matric potential at which most annual crops are water stressed. Nonetheless, we choose to use the observed minimum because reproducing that is our main concern. Furthermore, the results of Denmead and Shaw (1962) and Gollan et al. (1986) show transpiration to be about 80% of demand at 5 bars. Given that crops are typically maintained at a higher density than natural vegetation through fertilization and other management, it makes sense that the average soil moisture minimum in water-limited years might be below the point of stress.

Although we do not have soil moisture observations for trees (i.e., the other major plant form in the study area), Federer's (1979) study of a hardwood forest in New Hampshire shows birch and maple trees undergoing a reduction in transpiration at a soil matric potential of about 2 bars. Havraneck and Benecke (1978) found a similar value for conifer seedlings. Other values of Ψ_{uc} in Table 3.3 are essentially rough interpolations and extrapolations of the values for grasses, crops and trees based on the estimated composition of annual crops, herbaceous perennials and woody species present for the vegetation class. We also assumed some correlation to Ψ_{lc}, for which there are many more observations in the literature. In the end, it appears that the difference between the water content at Ψ_{uc} and at the wilting-point matric potential (*i.e.*, Ψ_{lc}) is not all that great for most vegetation (see Figure 4.4)—showing just how adept plants are at extracting available soil water. The greatest differences are for forests on medium textured and finer soils. For a difference of 0.05 and a one-meter depth of the root zone, the corresponding 5 cm of water represents 10-15% of typical modeled annual transpiration (see Figure 5.11c)—not a trivial percentage, but also probably not the greatest source of uncertainty in modeled transpiration.

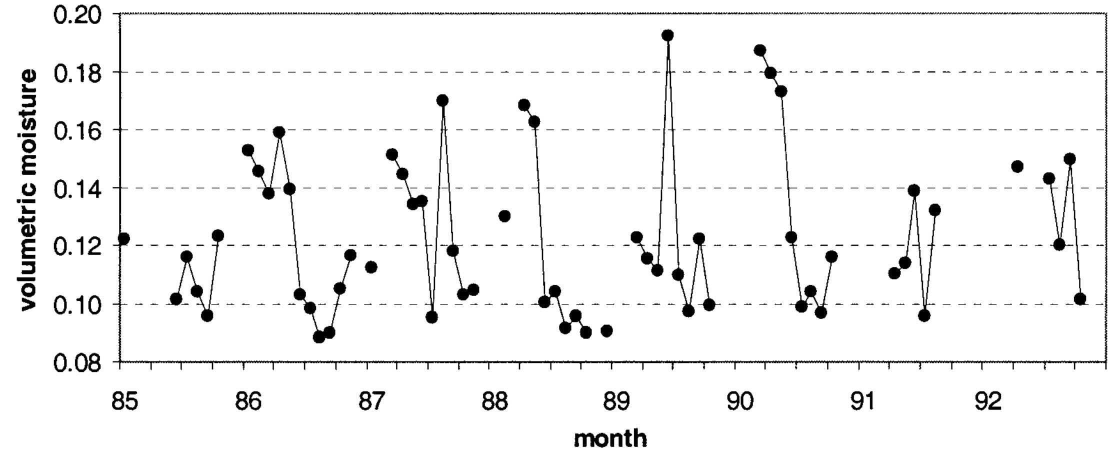
(a) CPER sandy loam slope

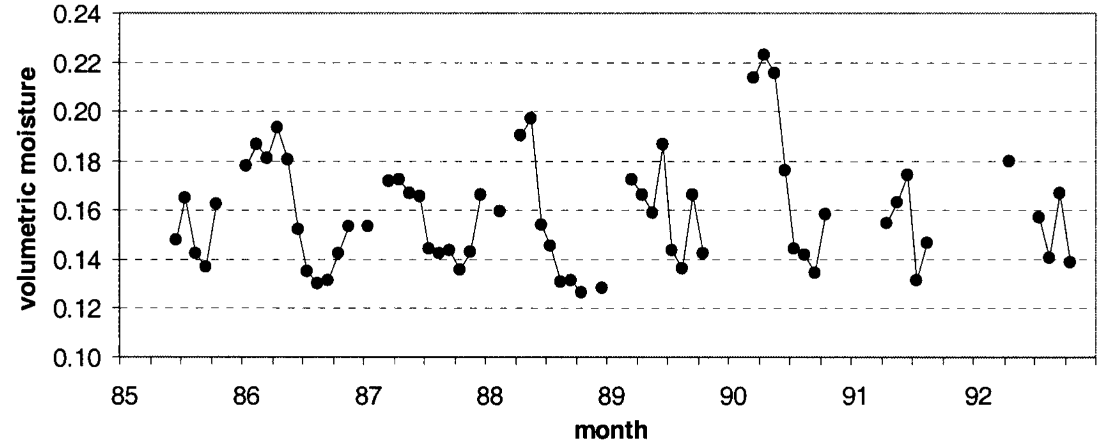
(b) CPER clay loam slope

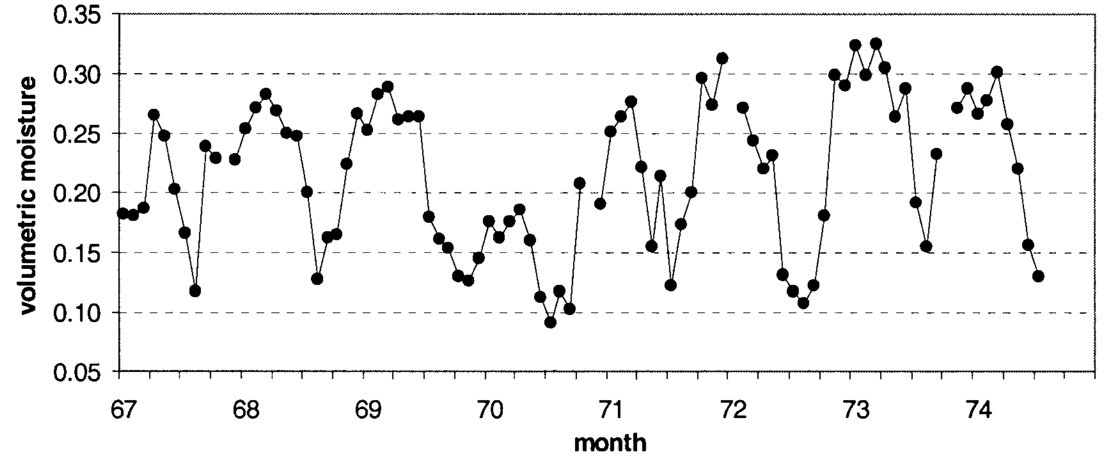
(c) R-5 watershed

Figure 4.1. Monthly observed volumetric water content in the root zone: (a) along a sandy loam slope at the Central Plains Experimental Range (CPER) in northeast Colorado, (b) along a clay loam slope at the CPER, and (c) at the R-5 watershed in Central Oklahoma. See Section 5.6 for details on the sites and soil moisture sampling.

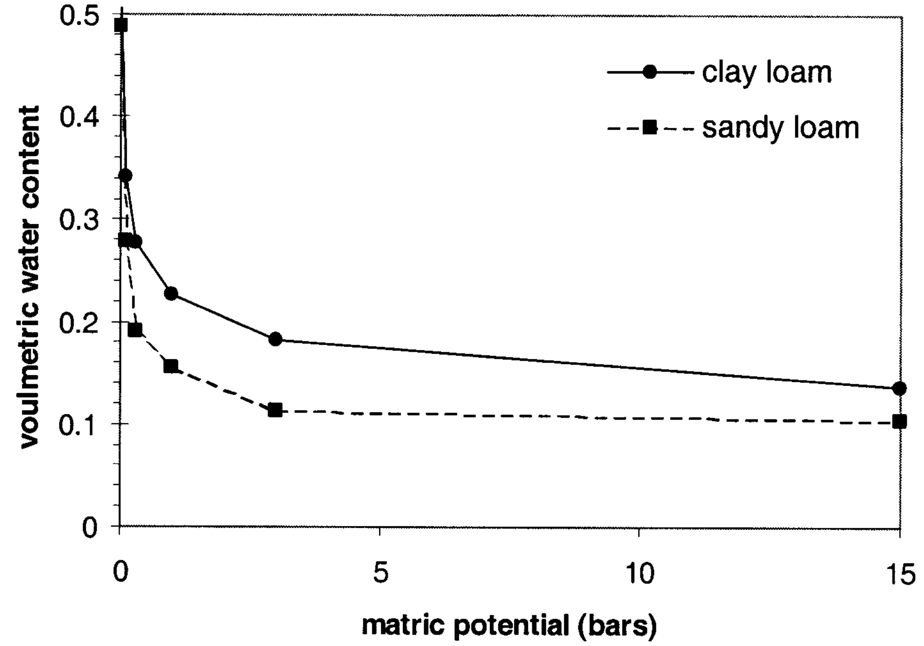

(a) CPER

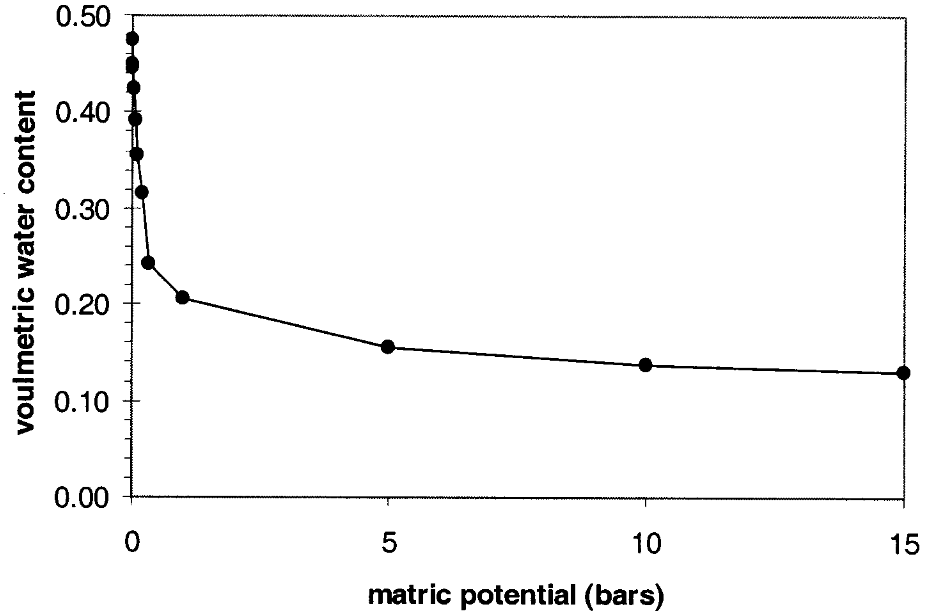

(b) R-5 watershed

Figure 4.2. Soil moisture retention in soils at (a) the CPER (Van Haveren and Galbraith 1971) and (b) the R-5 watershed (Luxmoore and Sharma 1980).

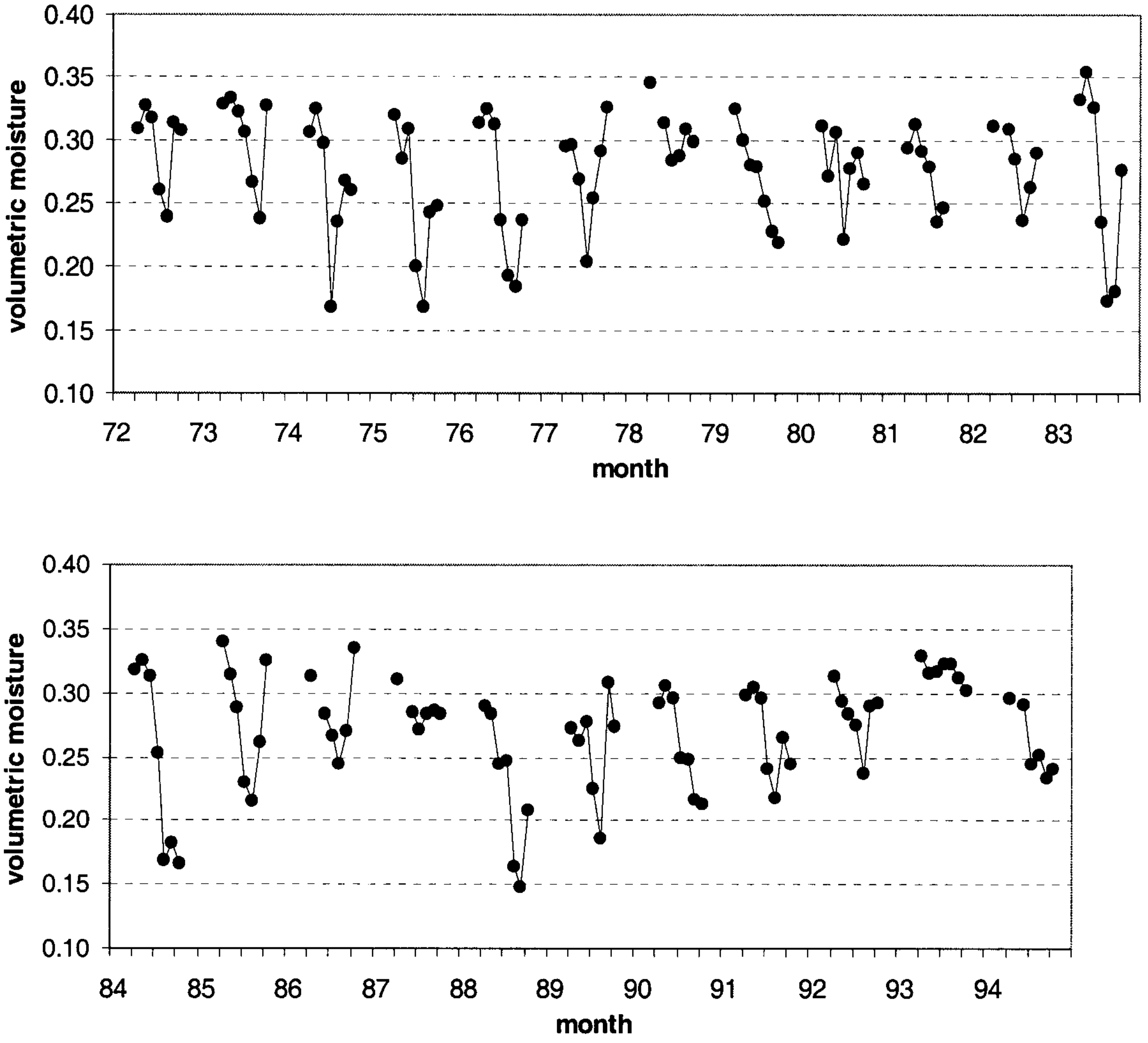

Figure 4.3. Monthly observed volumetric water content in the root zone at the W-2 watershed in southwestern Iowa. See Section 5.6 for details on the site and soil moisture sampling.

a) θ_t at Ψ_{uc}

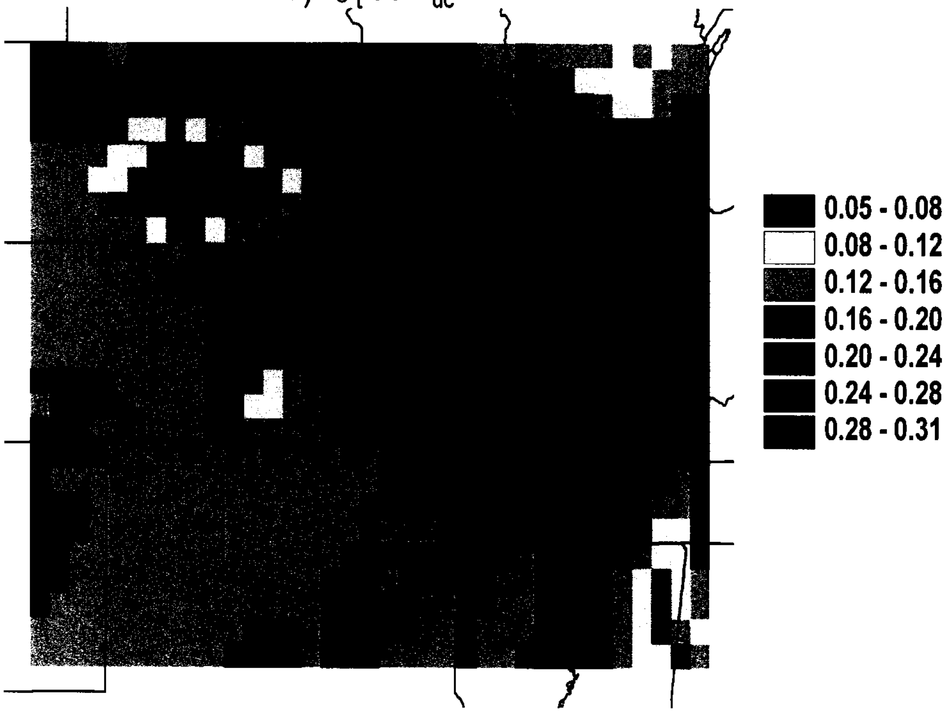

b) difference with θ_t at Ψ_{lc}

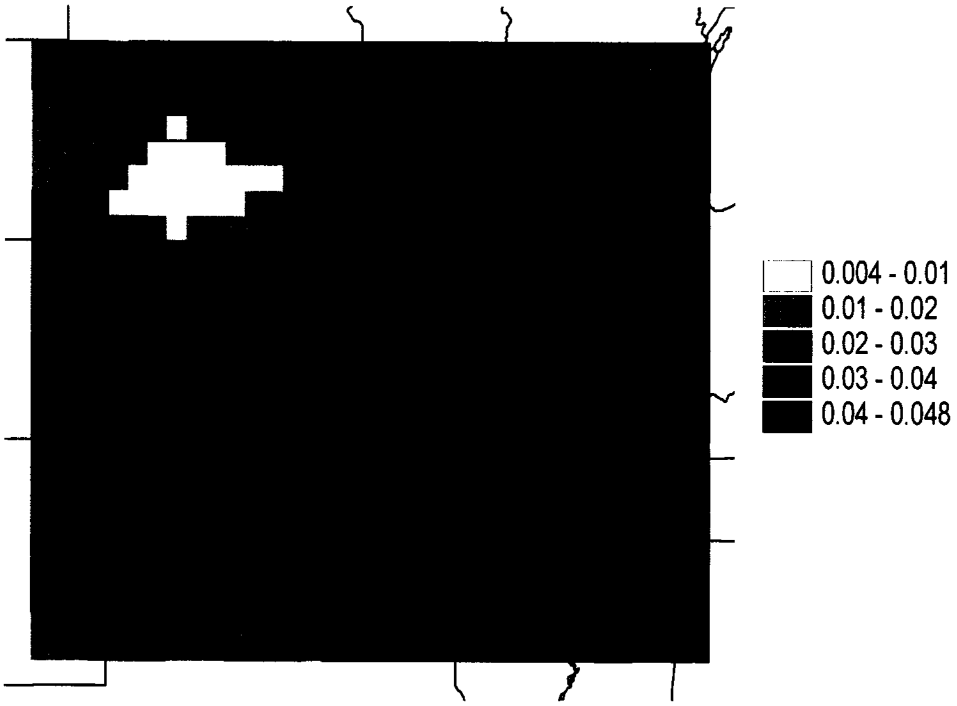

Figure 4.4. (a) volumetric water content in the root zone at the critical soil matric potential and (b) its difference with the water content at the vegetation-specific wilting point.

Chapter 5: Results for the Mean Water Balance

5.1. Overview

As discussed in Section 3.3.3, we calibrated values of two of the parameters of the evapotranspiration model by vegetation class via a visual fit of modeled mean annual runoff to contours of observed streamflow. The resulting degree of correspondence between the model results and the contours is examined in Section 5.7. Because the streamflow contours were developed as an average for the period 1951-1980 (Gebert et al., 1987), we use that 30-yr period as our base modeling period for the calculation of the mean water balance. No separate validation period is examined. Rather, the validity of the model is established through the realism with which it reproduces not only runoff but also all other components of the water balance. Those components consist of green LAI, bare-soil evaporation, transpiration and soil moisture. Each is examined in detail in the following sections. Because soil moisture controls all the major water balance fluxes, it is arguably the most important variable to model accurately, and therefore particular attention is paid to validating that component—especially with regard to seasonality. In the final section, in which we look at mean annual runoff, the breakdown of total runoff into surface runoff and groundwater runoff is also examined.

5.2. Maximized Leaf Area Index and Above-Ground Net Primary Productivity

Figure 5.1a depicts the 30-year averages of peak green LAI maximized on a year-to-year basis as described in Section 4.4. Those averages as a fraction of the 10-year averages of Buerman et al. (2002) (see Figure 3.15) are shown in Figure 5.1b. In Figure 5.2, the two sets of numbers are plotted against each other for each of the 872 grid cells of the study area. The degree of correlation (R^2=0.80) in the power regression indicates that the maximized LAI preserves the general climatic trend of increasing LAI with increasing humidity. As indicated by the plot and Figure 5.2b, the tendency is for the maximized LAI to be higher in the drier regions and the unaltered observations to be higher in the wetter regions. As a whole, the maximized LAI, with a mean of 2.79 and standard deviation of 1.61, tends to be slightly larger and slightly less variable than the unaltered observations, which possess a mean of 2.66 and a standard deviation of 1.78. A comparison of mean annual precipitation over the study area for the 30-yr modeling period with that for the 11-yr period of NDVI-based observations of green LAI showed that the two means are within 10% of each other for the majority of grid cells. The most distinct exception is the part of the study area encompassing New Mexico, Texas and Oklahoma, where precipitation over the 11-yr period runs as much as 40% greater than over the 30-yr period. This is in contrast to the smaller unaltered LAI observations over most of the same region. Furthermore, no significant correlation was found between the differences in precipitation and the differences in LAI for the study area as a whole.

Given the uncertainties in the NDVI-based observations discussed in Section 3.3.2, we cannot assume that the unaltered observations are a more accurate representation of actual LAI. Using ground-based observations and productivity data, we examine below the likely accuracy of the maximized LAI as compared to the unaltered observations. Our primary interest is with the water-limited grassland systems of the western half of the study area.

Because of the labor-intensive nature of data collection, ground-based observations of LAI are sparse and tend to be limited in temporal and spatial extent. Scurlock et al. (2001) compiled a global dataset of field-measured LAI as reported by numerous researchers. Several sites contained in that dataset are located within the study area of this dissertation. For the most part, those sites are in grid cells where there is generally good agreement between the maximized LAI and the unaltered NDVI-based observations of peak green LAI. Taken together with their limited spatial and temporal extent, the values reported at nearly all the sites are uncertain and varied enough that both the maximized LAI and the unaltered observations can be assessed comparable to the field measurements.

As seen in Figure 5.12b, the maximized LAI is greater than the unaltered observations over most of the grassland region. The area of greatest disagreement is centered midway along the border between Nebraska and Oklahoma. The dataset of Scurlock et al. (2001) contains LAI measurements at two sites within this area. They are cited as unpublished data from field sites of the USDOE's ARM/CART program. The first is an LAI of 7.5 for a 1997-1998 harvest of a wheat crop located at 36.75° N 97.08° W. For the corresponding grid cell, which is parameterized as C_4 grasses, the maximized LAI is 5.9, indicating that for most years the upper bound of 6.0 is reached. In contrast, the unaltered observed peak in green LAI is only 2.1. The second site is located in the adjacent grid cell to the east at 36.85° N 96.68° W. The vegetation there is reported as grass, with two undated LAI measurements of 5.4 and 5.8. For the grid cell, the maximized LAI is 2.1, and the unaltered observation is 1.9. We suspect that the field measurements are biased towards the high side, but nonetheless, they suggest a region of higher productivity. Also indicative of the potential for higher productivity is the fact that, according to the vegetation classification (see Figure 3.18), a group of seven cells just to the west of the field measurements are mostly in crops. Located at the southern end of the area of higher maximized LAI, at 35.15° N 97.75° W, is the USDA's R-5 experimental watershed, which is one of the sites used in model development and to validate soil moisture (see Section 5.6). For this grassland catchment, two hydrologic modeling studies were found that use field-based estimates of peak green LAI of 2.5 (Ritchie et al., 1976) and 3.2 (Luxmoore and Sharma, 1980). For the corresponding grid cell, the model-maximized LAI is 2.1, and the unaltered satellite-based observation is 1.1—further evidence that the latter underestimates peak green LAI in this area of the grasslands.

Given the paucity of field-measured LAI, we turn to another measure of vegetation density, aboveground net primary production (ANPP). Zheng et al. (2003a) integrated 15 studies containing mostly empirical estimates of net primary productivity (NPP) for a variety of terrestrial biomes across the globe. The end product of that effort is a half-degree gridded dataset of ANPP and total NPP (TNPP) (Zheng et al 2003b). Of relevance to this dissertation, estimates of grassland productivity are provided over most of the Great Plains of the United States. The sources of those data are three studies using grassland productivity data from the USDA Natural Resource Conservation Service (NRCS). Tieszen et al. (1997) correlated potential rangeland production estimates with NDVI data from 1989 to 1993 to estimate ANPP at a one-kilometer resolution for 13 major grassland seasonal land cover classes. Figure 5.3a depicts the portion of their data, as aggregated to a half degree by Zheng et al. (2003a), which overlaps with the study area of this dissertation. The second study using the USDA productivity data is that of Sala et al. (1988), who grouped the data for 9498 sites into Major Land Resource Areas (MLRA) within each state. As resampled to the half-degree grid by Zheng et al. (2003a), ANPP for the 60 of the MLRA groupings that fall within the study area are depicted in Figure 5.3b. Figure 5.4 compares the ANPP estimates of Sala et al. (1988) with those of Tieszen et al. (1997) for the 51 grid cells at which the two datasets overlap.

The maximized peak-green LAI values for those cells designated as grassland in the model parameterization are plotted against the corresponding Tieszen-et-al. (1997) estimates of ANPP in Figure 5.5a. The unaltered observations of peak-green LAI are plotted against the ANPP estimates in Figure 5.5b. Based on a power curve fit, the ANPP data is substantially more correlated to the maximized LAI (R^2=0.59) than to the unaltered observations (R^2=0.42). We note that both the LAI observations and the ANPP estimates are derived from the NDVI data—albeit in very different ways. For this reason, the higher correlation between LAI and ANPP brought about by the maximization is a particularly strong endorsement of that process. In Figure 5.6, the two sets of LAI estimates are also compared to the purely ground-observation-based ANPP data of Sala et al. (1988). By a similar margin, the maximized LAI are more correlated (R^2=0.52) than are the unaltered observations (R^2=0.36).

As seen in Figure 5.1b, the most distinct exceptions to the trend in the grasslands region of a maximized LAI larger than the unaltered observations are the high-clay-content regions around south-central South Dakota and east-central Texas (see Figures 3.1 and 3.2). The region in South Dakota is the largest and is within two Major Land Resource Areas designated as the Northern and Southern Rolling Pierre Shale Plains. In contrast to that region, where the grid cells contain the highest percentages of clay within the larger study area, the Sand Hills region of Nebraska just to the South is the locus of the highest percentages of sand. Over the entire Sand Hills region the maximized LAI is larger than the observations, with the ratio greater than two for a few of the cells. The contrast in maximized LAI between the two regions is reflected in the Tieszen et al. (1997) ANPP data in Figure 5.3a; in the Pierre Shale Plains, ANPP generally falls in the range of 60 to 110 g/cm^2, while in the Sand Hills, it generally falls in the range of 120 to 170 g/cm^2. The maximized LAIs in the corresponding grid cells range from 0.7 to 0.9 and 1.3 to 1.9, respectively—the same approximate one-to-two ratio as ANPP. In contrast, the unaltered observations of peak green LAI (see Figure 3.17) are actually higher over the

Pierre Shale Plains than over the Sand Hills. That the model reproduces the higher productivity of the Sand Hills suggests that it is able to capture the so-called "inverse texture effect." As first elucidated by Noy-Meier (1973), the inverse texture effect explains the observation that, in dry climates, soils of high permeability tend to be more productive than soils of low permeability, despite the higher water holding capacity of the latter. This is primarily because low-permeability soils hold the water nearer the surface—rather than allowing it to drain deeper—where it is readily lost to bare-soil evaporation. The ability of the model to capture the inverse texture effect is evaluated more rigorously in the form of a sensitivity analysis in Section 7.3. In Section 5.4, we examine in more detail how the factors affecting bare-soil evaporation manifest themselves in the model results.

We cannot compare the maximized LAI against the unaltered observations without addressing the impact of land use. Grazing is the predominate land use in the grasslands region. The significance of grazing intensity can be seen in comparison of the R-5 catchment, which was moderately grazed, with the adjacent R-7 catchment, which has similar soils but was intensely grazed. As a result of the overgrazing and subsequent erosion, the vegetation cover was significantly smaller over the R-7 catchment; Ritchie et al. (1976) indicate a peak green LAI value of 0.5 for the R-7 catchment, and Luxmoore and Sharma (1980) report a value of 0.75. The maximized LAI may thus be more representative of a "potential" LAI, which would be achieved in the absence of overgrazing, fire, infestation, disease or other significant disturbances. At least some of the difference between the maximized LAI and the unaltered observations over the grasslands is then attributable to one or more of those disturbances, grazing being the most likely culprit.

Second in importance in the grasslands to grazing is crop production. While only a handful of cells within the grassland region are designated as crops in the model parameterization, crops are raised throughout. For example, the April and May peak in green LAI over much of the central and southern grasslands (see Figure 3.17) is an indication of the prevalence of winter wheat there. Because it occurs when transpirational demand is still relatively low, the early peak in fact allows for the relatively high maximized LAI in this region. The maximized LAI may thus be more representative of wheat than the more predominate grasslands. In contrast to an early peak in green LAI, management factors, such as fertilizer application and irrigation, likely play a role in the maximized LAI underestimating the actual grid-cell averages. In fact, many of small clusters of cells over the grassland region where the maximized LAI is less than the unaltered observations correspond to areas of high levels of irrigation. These areas include the plains along the Front Range of the Rocky Mountains and around the Black Hills, and the Platte River valley in southern Nebraska (USGS 1993). Other areas of intense irrigation appear as just localized reductions in the generally positive difference between the maximized LAI and the unaltered observations. As seen in Figure 5.1b, these areas include a few cells in the southwest corners of Kansas and the Texas panhandle.

5.3. Potential Evapotranspiration

Results from application of the Shuttle-Wallace model to the calculation of potential rates of bare-soil evaporation and transpiration are depicted in Figure 5.7 for the months of January and July and for the sum of all months. As with actual fluxes defined in Chapter 2, the potential quantities are calculated as expected values, which in analogy to (2.51) and (2.60), can be written as

$$E[E_{ps}] = (1 - f_s) m_v m_{tb} \, e_{ps} \tag{5.1}$$

$$E[E_{pv}] = (1 - f_s) m_v \left(m_{tb} - m_{th}\right) e_{pv} \tag{5.2}$$

where $E[E_{ps}]$ and $E[E_{pv}]$ are, respectively, the expected values of potential bare-soil evaporation and potential transpiration in a given month. Values in Figure 5.7 are averages over the base 30-year period. As seen in Figure 5.7a, the month of January is dominated by potential bare-soil evaporation. Over most of the northern half of the study area, average January values of $E[E_{ps}]$ are less 0.1 cm due to mean temperatures below -4° C and a resultant value of f_s of one in nearly all of the 30 years. The results for July in Figure 5.7b are indicative of the growing season; the distribution of potential transpiration mirrors the distribution of peak green LAI in Figure 5.1a. Potential bare-soil evaporation acts as a complement to potential transpiration, being higher in areas of lower LAI. Because evapotranspiration takes place predominantly in the growing season, similar patterns of potential evapotranspiration are seen for the annual totals in Figure 5.7c.

Expected values of evaporation from vegetal interception for January, July and the entire year are depicted in Figure 5.8. As those quantities are principally a function of total LAI, they also follow the distribution of peak green LAI. We add vegetal interception to the potential quantities to obtain a definition of total potential evapotranspiration:

$$E[E_{pt}] = E[E_{ps}] + E[E_{pv}] + E[E_{hv}] \tag{5.3}$$

Figure 5.9 shows the distribution of average total potential evapotranspiration for January, July and the entire year. Also plotted in Figure 5.9 are the differences between average precipitation and average potential evapotranspiration. A positive value indicates that the atmospheric supply of moisture is sufficient to meet the atmospheric demand over the given period and is typically referred to as a precipitation surplus. In contrast, a negative value means the atmospheric demand is greater than supply and is referred to as a precipitation deficit. We see that, with the exception of the southwest corner of the study area, winter is a period of soil moisture recharge, while summer is one of depletion over the entire study area. The fact that there is minimal pre-growing-season recharge of soil moisture in the southwest corner is reflected in the very low peak green LAI in Figure 5.1a. On an annual basis, the line where precipitation equals potential evapotranspiration divides the region approximately in half vertically. That demarcation is of interest because it is what separates a semi-humid (wet) from a semi-arid (dry) climate in the climate classification scheme of Thornthwaite (1948).

While Thornthwaite (1948) introduced the concept of potential evapotranspiration, Penman's (1956) definition as "the amount of water transpired...by a short green crop, completely shading the ground, of uniform height and never short of water" has become more of a recognized standard. In contrast, Shuttleworth (1993) refers to the same quantity as "reference crop evaporation," while defining potential evaporation as that from "an idealized, extensive free water surface." He quantifies the reference crop as "an idealized grass crop with a fixed crop height of 0.12 m, an albedo of 0.23 and a surface resistance of 69 sm^{-1}." He further translates the crop height to an aerodynamic resistance of

$$r_a = 208/u_2 \tag{5.4}$$

where u_2 is the windspeed (m/s) at two meters. The above assumptions allow us to use the PM equation to calculate the reference crop evaporation rate as

$$e_{rc} = \frac{f_c}{\lambda} \frac{\Delta A + \rho c_p D u_2/208}{\Delta + \gamma(1 + u_2/3.01)} \tag{5.5}$$

where the notation is the same as for (2.62)-(2.63). For the purpose of comparison to our SW-based definition of potential evapotranspiration, monthly values of e_{rc} were calculated using the same climatic inputs as used in the SW model. Ten-meter winds were extrapolated down to 2 meters using the same roughness length, 0.015 m, assumed by Shuttleworth (1993) in the derivation of (5.5). Figure 5.10 shows the results of application of (5.5) at the monthly scale as aggregated to annual totals. The range of the resulting reference-crop evaporation rates is somewhat narrower than the range of SW-based potential rates, with former generally exceeding the latter in the humid half of the study area, and the latter exceeding the former in the drier half. The implication is that the combined soil and vegetation resistances in the SW calculations are smaller than the fixed surface resistance in the PM calculations for the drier half of the study area, and larger for the humid half. Because the portion of total potential evapotranspiration in the SW calculations that is bare-soil potential evaporation increases with increasing aridity, the larger combined surface resistances in the drier half are consistent with the observation of Penman (1948) that evaporation from well-watered bare soil exceeds that from well-watered grass under the same climatic conditions. In fact, the differences between the two sets of potential evapotranspiration calculations in the least vegetated parts of the study area are comparable to the approximate 15% average difference between his two sets of evaporation measurements.

5.4. Actual Bare-Soil Evaporation and Vegetal Transpiration

The average modeled values of bare-soil evaporation and transpiration for January, July and the entire year are plotted in Figures 5.11. Figure 5.12 depicts total evapotranspiration (which includes evaporation from vegetal interception) and the percentage of total evapotranspiration that is bare-soil evaporation. Over the northern part of the study area, no evapotranspiration takes place during January as a result of the potential values being zero or the soil being frozen. Over most of the remainder of the region, bare-soil evaporation is the dominant component of total evapotranspiration during January. In July, when green LAI is at or near its peak, bare-soil evaporation falls in the range of 10% to 30% of total evapotranspiration for the majority of the cells, with the percentages tending to the low side in the drier half of the study area. On an annual basis, bare-soil evaporation comprises between 30% and 60% of total evapotranspiration for nearly all the cells. The distribution of percentages shows surprisingly little correlation to vegetation class or climate. This suggests that the generally lower vegetation cover and lower soil-surface resistances in the drier half of the study area are more-or-less offset by the drier soil.

In contrast to vegetation class and climate, the influences of soil texture are clear in Figures 5.11 and 5.12. The differences in LAI resulting from the differences in soil texture between the Pierre Shale Plains and the Sand Hills manifest themselves as, respectively, regionally higher and lower percentages of bare-soil evaporation. In the humid half of the study area, the highest percentages of bare-soil evaporation (i.e., those in excess of 60%) are associated with the high-clay soils of the lower Mississippi River valley and Northeast Texas (see Figures 3.1 and 3.2). The proximate cause of these higher percentages is also the greater potential bare-soil evaporation (see Figure 5.7) that results from the regionally lower LAI (see Figure 5.1a). This might suggest that the inverse texture effect is also in operation here. However, the available water capacity of the corresponding cells is actually lower than in the surrounding cells (see Figure 3.4). Furthermore, if we look at bare-soil evaporation as a percentage of potential bare-soil evaporation (Figure 5.13), we see that the percentages are slightly higher than the surrounding cells in the high clay areas of the humid half, while slightly lower in the Pierre Shale Plains. This suggests that the lower diffusivity of the soils has a greater offsetting effect to the higher moisture content in the Pierre Shale Plains than in the humid regions. The difference has mainly to do with the degree to which bare-soil evaporation is soil controlled. In the humid half of the study area, at least 60% of the potential demand is met for nearly all the cells on an annual basis (Figure 5.13c). The 60% isoline corresponds nearly perfectly with the isoline of equal precipitation and potential evapotranspiration (See Figure 5.9c). Therefore, if we take that percentage as the division between primarily soil-controlled and primarily climate-controlled bare soil evaporation, those two descriptors then become synonymous with dry and humid climates, respectively. 60% on annual basis roughly corresponds to 90% for March (Figure 5.13a)—in other words, near complete satisfaction of demand in that month. As a final point in the examination of Figure 5.13, we note the regionally lower percentages associated with high sand-content soils of south-central Wisconsin. One might suspect the inverse texture effect at the opposite end of the spectrum of soil texture. However, neither the maximized peak green LAI (see Figure 5.1a) nor the unaltered observations (see Figure 3.17) show this region to be one of regionally higher LAI. This is simply because water is not substantially limiting in this region, as indicated by the relative high values of LAI. The same argument can be made against the potential for the inverse texture effect across the entire humid half of the study area.

Although relatively new isotopic methods (*e.g.*, Ehleringer and Dawson 1992) hold promise, separate observation of bare-soil evaporation and transpiration has historically been difficult. Therefore, there are not many data that can be used to validate the relative composition of total evapotranspiration in the model results. Rutter (1975) cites several water and energy balance studies in suggesting that bare-soil evaporation is 10-12% of annual evapotranspiration in forests and about 10% for crops in summer. Those percentages are considerably lower than the modeled percentages for the corresponding vegetation classes in Figures 5.12b and 5.12c. In comparison to the crop percentage, Villalobos and Fereres (1990) measured bare-soil evaporation to be 20 to 27% of total evapotranspiration from irrigated corn, cotton and sunflower in July and August in Southern Spain using microlysimeters. The dominant class for crops in Figure 5.12b is 20-30%. Without citation or indication whether it is on a seasonal or annual basis, Kramer (1983) states that, "it has been estimated that evaporation from soil under forests, meadows and cultivated crops is approximately 10, 25 and 45% of the total water loss, respectively." If the 45% figure for crops is for the growing season, it more-or-less agrees with data that he presents from Peter and Russell (1959), who, by covering the ground of a corn plot in Illinois, measured transpiration to be 45 to 51% of total evapotranspiration during three summers. In contrast to the above low figures for forests, Kramer (1983) presents data from Hoover (1944) for a forested watershed in North Carolina that shows bare-soil evaporation to be 44% of total evapotranspiration over a two-year period. The two dominant classes in Figure 5.12c form a range of 30 to 50% for all vegetation types. Based on the above discussion, we conclude that the modeled percentages of bare-soil evaporation fall roughly in the middle of the wide range of values reported in the literature.

5.5. Total Net Primary Productivity and Water Use Efficiency

We can further attempt to validate the magnitude and distribution of modeled transpiration through the calculation of water-use efficiency (WUE), which—by the definition (among many) that we will use—measures total plant production per amount of water transpired. Because the figures for the partitioning of evapotranspiration cited in the last section apply to well-watered crops and forests, the grassland productivity data in the NPP database of Zheng et al (2003a) (see Section 5.2) are particularly useful in this regard. In that database, the ANPP data of Sala et al. (1988) is converted to TNPP using a linear regression equation. That equation was developed from a third NPP dataset for the U.S. Great Plains, in which ANPP estimates were in turn calculated using a linear regression equation that relates annual mean precipitation to ANPP and that was developed using the ANPP data of Sala et al. (1988). The below-ground NPP (BNPP) in the third data set was estimated from an empirically based equation developed by Gill et al. (2002) that is dependent on ANPP, mean annual temperature and root turner over rate. The BNPP estimates added to the ANPP values provided estimates of TNPP. Zheng et al. (2003a) report that Tieszen et al. (1997) calculated BNPP using "an algorithm" derived by Gill et al. (2002), which presumably is the same equation applied in the third data set. Figure 5.14 depicts the TNPP estimates based on Sala et al. (1988) and those from Tieszen et al. (1997) that fall within the study area. In Figure 5.15, the two sets of estimates are compared for the 51 grid cells at which they overlap. Despite their apparent common basis, the TNPP estimates do not agree as well as do the ANPP estimates (see Figure 5.4), with the TNPP estimates from Tieszen et al. (1997) averaging about 75% of those based on Sala et al. (1988).

We re-ran the model for the base 30-year period with all the cells for which the native vegetation is C_3 or C_4 grassland parameterized as such. Cells in which the native vegetation is either one of the two savanna classes were also parameterized as C_4 grassland. By dividing TNPP values by the corresponding values of annual transpiration in cm and multiplying by 0.1, we arrived at WUE in units of g-C/kg-H_2O. The results using the two sets of TNPP estimates are plotted in Figure 5.16. For the C_4 grasslands, the pattern is one of increasing WUE as one moves out from the southwest, that is in the direction of increasing humidity. This is consistent with the physiology behind WUE: using a resistance model of the diffusion of CO_2 and water vapor across stomata, Kramer (1983) shows that WUE is inversely proportional to the difference in the vapor pressure of water inside and outside the leave. As an approximation of the latter over the growing season, we averaged the observed vapor pressure deficits for June, July and August for each grid cell. In Figure 5.17, the inverses of those averages are plotted against the corresponding values of C_4 WUE for both sets of TNPP estimates. The degree of correlation with the larger dataset suggests that variation in humidity explains a substantial amount of the variation in WUE over the C_4 grasslands.

Despite the clear climatic dependence of WUE, generalized values for specific species or classes of vegetation can be found scattered throughout the plant physiology literature. Based on a number of sources, Larcher (1980) presents single values and ranges of values of "transpiration ratios" categorized by life form, photosynthetic pathway and species. For C_3 grains and C_4 plants, the author lists ranges of 500-650 and 220-350 "liters of transpired water per kg of dry matter produced," respectively. Using a conversion factor of 0.45 g-C per g-dry matter (Zheng 2003a), those ranges correspond to WUEs of 0.69-0.90 and 1.3-2.0 g-C/kg-H_2O, respectively. Although the focus of the WUE values presented by Larcher (1980) is more on cultivated crops than on pasture grasses, we might assume that the WUEs of C_3 grasses fall somewhere in the former range and those of C_4 grasses fall in the latter range. The relative productivity of C_3 and

C_4 grasses across the western half of the Great Plains varies along a primarily north-to-south gradient, such that, for those cells in the study area designated as C_4 grassland, the relative productivity of C_4 species ranges from near 100% in central Texas to around 50% in the northern Nebraska, while for the C_3-grassland cells, it varies from 50% in northern Nebraska to 20% in central South Dakota (Epstein et al. 1997a). If we approximate the average relative productivity of C_4 grasses to be 35% in the C_3 cells of the study area and 75% in the C_4 cells, then we expect WUEs to fall in the range of 0.90 to 1.29 g-C/kg-H_2O for the C_3 grasslands and in the range of 1.15 to 1.73 g-C/kg-H_2O for the C_4 grasslands. For the WUEs calculated with the TNPP estimates of Tiezsen et al. (1997), the mean and standard deviation is 1.06 and 0.25, respectively, for the C_3 grasslands and 0.86 and .31, respectively, for the C_4 grasslands. For the WUEs based on the TNPP estimates of Sala et al. (1988), the C_3 grasslands produced a mean of 1.31 and standard deviation of 0.21, while the C_4 grasslands produced a mean of 1.18 and a standard deviation of 0.24. Both sets of TNPP estimates produced lower WUEs for the C_4 grasslands despite their higher stomatal resistance in the model parameterization. We might take those results as an indication that the model overestimates transpiration for C_4 grasslands. Equally plausible, however, is that the ranges of WUE reported by Larcher (1980) are more representative of humid climates, especially because they are crop-based values. In fact, the calculated WUEs for C_4 grid cells that are on the more humid side of the grasslands region mostly fall within the expected range of 1.15 to 1.73 g-C/kg-H_2O (see Figure 5.16).

The database of Zheng et al (2003b) also contains TNPP estimates for crops in the state of Iowa. Prince et al. (2001)—on whose study those estimates are based—made use of county-level, harvest-yield data collected by the USDA National Agricultural Statistics Service (NASS) from 1982 to 1996. They converted harvest yield to TNPP using harvest indices and shoot-to-root biomass ratios. The resulting TNPP data, as resampled by Zheng et al (2003a) to their half-degree grid, are plotted in Figure 5.18a. Figure 5.18b shows WUEs calculated with mean annual transpiration from a model run with all cells in Iowa parameterized as crops. The mean and standard deviation of those values are 1.78 g-C/kg-H_2O and 0.28 g-C/kg-H_2O, respectively. The only C_4 crop included in the study of Prince et al. (2001) was corn, which is the most commonly grown crop in the state. Larcher (1980) lists transpiration ratios for two species of corn that translate to WUEs of

1.3 and 1.7 g-C/kg-H_2O. The next most cultivated crop in Iowa is soybean. The transpiration ratio range given by Larcher (1980) for C_3 legumes translates to a WUE range of 0.56-0.64 g-C/kg-H_2O. According to data collected by the NASS (http://www.nass.usda.gov/ia/), over the last three decades, the acreage of soybeans in Iowa has steadily increased from about 20% to about 40% of total sown acreage, while corn has held steady at about 50%. Thus, even accounting for the higher percentages and productivity of corn, the modeled WUEs for crops over the high productivity areas of Iowa appear to be too large, suggesting that transpiration has been underestimated there. In comparison, the TNPP estimates in the database of Zheng et al (2003b) for grasslands over Iowa (which are from the third dataset mentioned in Section 5.2) run about 60% to 100% of the crop estimates, with the greatest difference where crops are most productive. Therefore, while modeled transpiration may underestimate that for the most productive crop fields, it may still be representative of the transpiration from the mixture of crops and other vegetation classes typically found in the grid cells parameterized as crops.

5.6. Soil Moisture

We identified four sets of long-term records of observed soil moisture encompassing a range of climatic conditions across the study area. At each of the sampling sites, we first averaged the soil moisture data vertically within the root and recharge zones as defined by the model parameterization for the corresponding grid cell. The values for each layer on the given sampling dates were then aggregated to a time series of monthly values, which were in turn averaged by month over the entire record to obtain estimates of the climatological means. More specific information about each of the four datasets and their use in this dissertation follows in order of increasing humidity.

The first soil-moisture dataset comes from the Central Plains Experimental Range (CPER) in north-central Colorado. Singh et al (1998) collected the data in order to study the long-term dynamics and spatial variation of soil moisture across soil textures and slope positions in this USDA-ARS shortgrass-steppe research site. Measurements were made by neutron probe from 30 to 90 cm of depth at 15 cm intervals. Over the period 1985-1992, data were collected about every two weeks in the growing season and less often during the remainder of the year. For the site with the finest texture (clay loam) and the site with the coarsest texture (sandy loam), we averaged the soil moisture data across the three slope positions (upland, midslope and lowland). We did not include data for November through February because measurements were made in those months during three or fewer of the eight years of the study.

The location of the second set of soil moisture data is the R-5 experimental watershed near Chickasha, Oklahoma. This moderately grazed, 24.7-acre watershed is covered by mixed, native grasses and was maintained by the USDA-ARS as part of the Southern Great Plains Research Watershed (USDA-ARS 1983). Loague (1992) provides graphical and tabular summary of soil moisture data collected within the watershed over two multi-year periods. Data were collected initially at four locations from November of 1966 to March of 1972. Measurements at 34 locations began in January of 1971 and continued through June of 1974. In both sampling periods, measurements were made by gravimetric method at six inches and by neutron probe below at six-inch intervals to a depth of 48 in. Measurement frequency was as high as four times per month, with the frequency generally lower outside the growing season. Monthly averages of the two datasets during the 15 months of overlap are nearly identical, and so we combined both datasets to obtain a single record of monthly, watershed-average soil moisture for the period November 1966 to June 1974.

The third set of soil moisture data comes from two cropped watersheds near Treynor, Iowa. The 83- and 107-acre watersheds are designated W-2 and W-3, respectively, and are also part of the network of USDA-ARS experimental watersheds. Along with analysis of the temporal variability of the soil moisture data, Entin (1998) gives details of its collection by neutron-probe and gravimetric techniques at three locations within each watershed. At each location, measurements were taken at three-inch intervals to a depth of 102 in. The data-collection effort lasted from 1972 until 1994, with observations averaging about twice a month from April through November. The spatiotemporal averages in the two watersheds are nearly identical, and so we choose to use only the data from W-2, which had been managed under conventional contour plowing many years prior to and throughout the period of soil-moisture measurement—in contrast to W-3, which, at the time measurements began, had just been converted from pasture to a ridge-till system (Chung et al. 1999). Those data, as well as the fourth dataset, were downloaded from the Global Soil Moisture Data Bank (Robock et al. 2000).

The fourth and final set of soil moisture data is from the Illinois Climate Network (ICN), which is operated by the Illinois State Water Survey (Hollinger and Isard 1994). The soil-moisture stations of the ICN consist of 17 grass-covered sites scattered throughout Illinois. Sixteen sites are located in the silt loam and silty clay loam soils that dominate the state. Two of those 16 sites, Bondville and Champaign, are within a few miles of each other. The soil at the Champaign site has undergone significant disturbance (Hollinger 2003, personal communication), and so we used only the Bondville site, leaving a total of 15 sites for our analysis. Measurement at the 15 sites began as early as 1981 and continues through the present. We use the data from 1983 (the first year of collection at all 15 sites) through 2001 (the last year available from the Global Soil Moisture Data Bank.) Observations are made by neutron probe at 20-cm intervals to a depth of 200 cm, with measurement frequency averaging about twice monthly during the growing season and once a month during the remainder of the year. All but the southern tip of Illinois is parameterized in the model as either crops or temperate savanna (see Figure 3.18), and so we used the 0-70 cm sampling depths to calculate root-zone soil moisture and the 70-200 cm sampling depths to calculate recharge-zone soil moisture. The turf grasses at the ICN sites likely have shallower rooting depths, among other differences in hydroclimatic properties.

The observations of mean volumetric soil moisture over the given periods of record are plotted on top of model results in Figure 5.19 for March (with the exception of the Treynor, IA site, for which April is plotted due to the lack of March measurements) and August in the root zone, and in Figure 5.20 for April and September in the recharge zone. Those months are the respective months in which modeled soil moisture most frequently reaches its annual maximum and minimum in each of the soil layers. Based on those plots, large-scale, climatic trends in moisture content appear to be captured by the model. The influence of soil texture is seen throughout the study area, mostly noticeably in the differences in moisture content between the Sand Hills and the Pierre Shale Plains. In the CPER observations, the significance of subgrid variability in soil texture is seen in the higher moisture retention of the clay-loam soil in comparison to the sandy-loam soil (where the latter has been plotted above the former).

Over Illinois, there is no clear spatial structure to either observed or modeled soil moisture. Apparently, the slight north-to-south increase in annual precipitation over Illinois (see Figure 3.16a) is more-or-less offset by the north-to-south increase in potential evapotranspiration (see Figure 5.9c). The means and standard deviations of observed soil moisture in Illinois are compared to the modeled means and standard deviations of the corresponding 15 grid cells in Table 5.1. Using the t-test for unequal variances, there is no significant difference at the 95% confidence level between the observed and modeled root-zone means for both March and August. However, the observed means in the recharge zone are significantly greater than the modeled means for both April and September. According to data from the Illinois State Climatologist's office (http://www.sws.uiuc.edu/atmos/statecli/Climate_change/iltrends.htm), annual average precipitation over the State was 99.3 cm for the 1983-2001 period, and 95.1 cm for the 1951-1980 period. Therefore, a small amount of the greater observed soil moisture can be attributed to a slightly wetter climate. In addition, because the turf grasses likely have a shallow rooting depth and are mowed, evapotranspiration may be reduced from that which would occur under the vegetation classes assumed in the model. Perhaps most significant is the fact that there is interaction with groundwater at many of the ICN sites (Hollinger 2003, personal communication). While there is no quantitative information available on water-table depths at the ICN sites, the ISWS maintains monitoring wells in shallow groundwater at 18 other locations across the state. Yeh et al. (1998) used water-level data from those wells, along with the ICN soil-moisture data, in the computation of a monthly soil-water balance for the state. They calculated statewide monthly average groundwater levels for 1983 to 1994 that ranged from 2.7 meters below the surface in March-April to 3.8 meters in September-October. To what extent those averages are representative of the water tables at the ICN sites is moot. Nevertheless, a month-by-month, site-by-site examination of the ICN soil-moisture data reveals that at many of the sites there is indication that the lowest sampling depth (*i.e.*, 190-200 cm) is frequently at or near saturation during wetter years. A method for inclusion of capillary rise is evaluated below.

In order to examine differences in the observations and model results in more detail, monthly mean values are plotted in Figure 5.21 for the three sites outside of Illinois and one of the Illinois sites. The clay-loam slope at the CPER site was selected because it most closely matches the soil of the corresponding model grid cell. Overall, there is good qualitative agreement in the phases and amplitudes of the annual variation in soil moisture between the observations and model results. The magnitude of modeled soil moisture, on the other hand, varies noticeably from the observations in one or both of the soil layers at each site. The degree to which differences between site-specific and model precipitation amounts, vegetation density and soil hydraulic properties are likely to be the sources of soil-moisture discrepancies at each of the four validation sites is discussed below. Preliminary to that discussion, Table 5.2 provides a comparison between the model parameterization and more site-specific estimates of peak green LAI and soil hydraulic properties, where available.

As seen in Figure 5.21a, the model overestimates mean volumetric soil moisture by up to five percent in both the root and recharge zones at the CPER clay loam site. In the root zone, the model shows greater fall-to-spring recharge followed by greater soil moisture depletion during the growing season. The amplitudes in the recharge zone, on the other hand, are both slight and nearly perfectly matched in size. As listed in Table 5.2, both peak green LAI and the soil moisture retention characteristics are very similar between the CPER site and the corresponding grid-cell parameter values. Therefore, on the basis of that information, we cannot attribute the differences between model and observed soil moisture to differences in soil tightness or vegetation density. The mean annual precipitation over the 30-year model run for the corresponding grid cell is 33.2 cm—only slightly less than the 35.2 cm reported by Singh et al (1998) for the period of their soil moisture observations. For the period from October to March, the authors note average precipitation of 8.7 cm, while the 30-year model average is 7.9 cm. Therefore, the greater soil moisture content in the model results does not appear to be due to precipitation differences. Rather, we suggest that at least some of the disagreement may be due to the redistribution of precipitation—in the form of surface runoff or blown snow, or both. Even though particle-size data presented by Singh et al. (1998) show no trend across the clay-loam slope, their soil-moisture data clearly show a moister environment in the lowland position. As seen in Figure 5.22, the average soil moisture in the lowland position nearly matches the modeled values. The differences in the slope positions might be even greater if it were not for the fact that the dominant grasses at the site appear to have responded to the greater availability of soil moisture in the lowland position with greater growth; Singh et al. (1998) list total vegetation cover as 42.2%, 49.2% and 55.4% for the upland, midslope and lowland positions, respectively.

The higher seasonal recharge in the model results at the CPER site could also be attributed to the fact that the model does not allow for sublimation from snow and assumes evaporation from soil moisture is zero during the months of January and February as a result of the soil being frozen. While those assumptions may be tenable in the more humid parts of the study area, they may lead to a significant overestimate of snowmelt recharge in the arid, high plains along the western edge of the study area. Van Haveren and Striffler (1976) summarize the results of a study (Van Haveren 1974) in which soil moisture was monitored over the period of soil moisture recharge from 1970 to 1971 at 60 locations across the CPER representing various combinations of grazing intensity, slope and wind exposure. Average soil-moisture recharge across all locations from October through April was 4.1 cm. Average precipitation measured at shielded gauges over the same period was 10.5 cm, which is very near the climatological mean. Seasonal recharge in the model amounts to 4.9 cm; and so based on a single observational period, the model appears to have overestimated seasonal recharge by about 20 % in the CPER grid cell—enough to explain only one to two percentage points in the difference between modeled and observed volumetric soil moisture.

More telling in the results of Van Haveren (1974) is the fact that the ratio of recharge to precipitation at each of the 60 sites ranged from -38% to 129%, with the negative numbers resulting from soil moisture depletion. Analysis of variance tests showed that higher levels of recharge were most strongly correlated with leeward slopes. Weaker associations of higher recharge rates with swale positions and light grazing intensity were also found. Those results, along with visual observations of snowpack distribution, lead Van Haveren and Striffler (1976) to conclude that blowing snow is the major source of variability in winter recharge in the shortgrass steppe. We thus conclude that the soil moisture observations of Singh et al. (1998), as averaged across the clay-loam slope, show slightly drier conditions than do model results because the winter snowpack and subsequent recharge is lower than the regional average due to the redistribution of snow or greater than average sublimation, or both.

Turning attention to the Chickasha, Oklahoma site, we see in Figure 5.21b that there is fairly good agreement in the root zone. In the recharge zone, modeled soil moisture is both greater and much steadier across the year than are the observations. The average annual precipitation in the 30-yr modeling period is 78.9 cm, as compared to an average of 75.9 cm measured by an on-site rain gauge over the 8-yr observation period. Therefore precipitation differences account for only a small amount of the soil moisture differences between the two periods. Part of the greater seasonal variability in the recharge-zone observations is due to the fact that we have observations only down to 120 cm, whereas the recharge-zone is modeled as reaching to 150 cm. Furthermore, substantial seasonal variation in moisture content is observable at all the sampling depths, suggesting that the actual root zone depth is deeper than the 50 cm in the model parameterization for grasses—a strong plausibility given that the watershed is located towards the humid side of the grasslands region and that the vegetation is comprised of mid-to-tall grasses, as well as short grasses. We re-ran the model for the R-5-containing grid cell with the root zone depth changed from 50 to 100 cm. Only minor changes in monthly average soil moisture resulted. The most significant change is that the greater storage in the root zone allowed for an increase in average peak green LAI from 2.1 to 2.8, which is right between the two site-specific numbers (see Table 5.2). A net increase in annual average evapotranspiration from 72.2 to 74.8 cm breaks down as follows: an increase in surface retention evaporation from 2.2 to 2.9 cm; an increase in transpiration from 37.7 to 44.4 cm; and a decrease in bare soil evaporation from 32.3 to 26.5 cm. The corresponding decrease in total runoff is from 6.4 to 3.8 cm. Clearly, accurate estimation of the depth of the root zone is important—but perhaps not as much as one might expect.

Rather than differences in precipitation or the definition of the depth of the root zone, it is more likely the fact that the soil parameters in the model imply a somewhat tighter soil than the actual soil (see Table 5.2) that accounts for the greater magnitudes of modeled over observed soil moisture for the R-5 watershed. The exception to that comparison occurs in the root zone in the first four months of the year. We suggest that the lower modeled soil moisture here is at least partly due to the April peak in green LAI discussed in Section 5.2.1. We thus re-ran the model for the R-5 grid cell with two other changes in parameter values: (1) the soil hydraulic parameters were adjusted to match soil-retention and saturated hydraulic conductivity data for the R-5 watershed provided by Luxmoore and Sharma (1980), and (2) the envelope of green LAI was changed to match that used by Ritchie et al. (1976)—which has a peak in June/July—in their modeling of evapotranspiration from the R-5 watershed for the year 1972. Modeled soil moisture for the revised parameter values is compared to the observations in Figure 5.23. Owing to the adjustment in soil parameters, there is a better match. The reduction of the field capacity in the root zone, however, keeps modeled spring soil moisture below observed. The change in the timing of peak green LAI results in a small-but-noticeable increase in spring soil moisture relative to that for the adjustment in soil parameters only. In terms of the overall water balance, the fact that the new green-LAI envelope is significantly narrower than the original appears to be more important; annual-average transpiration decreases by 13 cm, while bare-soil evaporation increases by 14 cm.

As with the first two sites, we see in Figure 5.21c that, for the Treynor, IA site, modeled soil moisture overestimates the observations. As with the R-5 watershed—but even more so, site-specific soil information for the W-2 watershed indicates soil that is significantly looser than the model parameterization (see Table 5.2). We re-ran the model for the corresponding grid cell using soil parameters derived from that information as follows: the regression equations developed in Section 3.1 were used to estimate K_s and n_r from sand and clay percentages, while the observed field capacity and wilting point were used to fit values of Ψ_s and m. Again, the results in Figure 5.24 show better agreement between modeled and observed soil moisture. However, modeled soil moisture now underestimates the observations in the recharge zone and in the root zone outside of spring. The biggest difference is in the August minimum in the root zone. In most years, the maximum peak green LAI of six is reached. This implies that either that maximum is too high or the critical soil moisture, s_{uc}, is too low. Regards the latter possibility, we note that the site-specific sand and clay percentages reported by Chung et al. (1999) produce values of Ψ_s and m (when used in the regression equations of Section 3.1) that are much closer to the original model parameterization than are the values derived from the field capacity and wilting point reported by the same authors. Thus, there is considerable uncertainty associated with the site-specific soil-parameter values.

At the Bondville, IL site, the last of the four soil-moisture validation sites in Figure 5.22, there is excellent agreement between observed and modeled soil moisture in the root zone and significantly higher observed values in the recharge zone. The latter comparison follows the statewide trend noted above. It was suggested there that interaction with the water table might be the most significant factor. As a first-order assessment of the potential importance of groundwater at the site, we examine the impact of a water table at a constant depth of two meters, which is both the bottom of the recharge zone in the model parameterization and the maximum sampling depth in the ISWS observations. To estimate capillary rise into the recharge zone, we employ the equation derived by Eagleson (1978c) based on Gardner's (1958) approximate analytical solution to the Richards equation for hydrostatic equilibrium:

$$w = K_{sd}\left(1+\frac{3}{2(m_d c_d - 1)}\right)\left(\frac{\Psi_s}{Z}\right)^{m_d c_d} \tag{5.6}$$

where

w	capillary rise from the water table (cm/day);
Z	depth to water table (cm).

The above equation was derived under the assumption of a dry surface and uniform soil properties down to the water table. For the soil parameter values, we have used those of the recharge zone, which, as discussed in Chapter 3, are derived from the average soil texture of the 50-150 cm depth in the VEMAP soils database.

As shown in Figure 5.26, inclusion of the water table increased the soil moisture content of the recharge zone by up to four percentage points. Clearly, the statewide discrepancy between observed and modeled soil moisture in the recharge zone is at least partially due to the lack of a groundwater component in the model. In the root zone, the increase is not as great, with the most noticeable difference being in the latter part of the growing season, which is when flow between the soil layers is from the recharge to root zone. A net decrease in average annual recharge to groundwater of 2.0 cm (from 19.6 to

17.6 cm) is balanced by increases in bare-soil evaporation, transpiration and surface runoff of 0.8 cm, 1.0 cm and 0.2 cm, respectively. The increase in transpiration is associated with an increase in average peak green LAI from 4.6 to 5.0. Therefore, the tendency of the model-maximized LAI to be lower than the unaltered observations over much of the wetter half of the study region (see Figure 4.2b) may also be at least partially explained by the lack of interaction with the water table.

5.7. Annual Runoff

The contours of annual streamflow used to calibrate the model were developed by Gebert et al. (1987) for the conterminous United States using streamflow data from 5,951 gauging stations. Those contours are overlain on modeled annual runoff in Figure 5.26. An excellent match to overall regional trends was obtained. The model even does a reasonable job of capturing the higher runoff over the topographically complex Black Hills and Ozark Mountains based on climate alone. Nonetheless, for a number of individual cells and small clusters of cells with runoff greater than two inches, differences between the contours and model results are as high as about +/-50 %. In addition, on a relative basis, the model substantially overestimates runoff over most of the driest part of the study area, *i.e.*, New Mexico and the Texas and Oklahoma panhandles. As shown below, this appears to be an overestimate in surface runoff. Many reasons could be cited for the differences between observed and modeled runoff. Some of the most significant not associated with measurement and interpolation error in the contours, nor with error in the water balance model, have to do with the fact that runoff calculated from streamflow may not necessarily be representative of actual hill-slope runoff. This may be the result of factors such as: manmade diversions; aquifers crossing watershed boundaries; evaporation and infiltration of runoff in depressions and stream channels; and long-term storage in groundwater and surface water.

Modeled average annual runoff is broken down into to surface and groundwater runoff in Figure 5.27. Comparison with Figure 3.2 shows the clear influence of soil texture on the partitioning of runoff. The extremes are evident in the northwest corner of the study area, where in the Sand Hills region all runoff is in the form of groundwater recharge, and in the Pierre Shale Plains, where runoff is almost exclusively surface runoff. Strong regional-scale dependence of surface runoff on soil texture is also visible in the southeast corner of the study area, where soil texture in the root zone varies from sandy loam in the Southern Coastal Plain MLRA to silty clay loam in the Mississippi River valley. The former soils generate less than 0.5 cm of surface runoff, while the latter generate surface runoff in the range of 20 to 30 cm.

In order to validate modeled surface runoff, we applied the hydrograph separation methodology of Woodruff and Hewlett (1970) to daily streamflow data from USGS stream gauges (http://nwis.waterdata.usgs.gov/usa/nwis/discharge). The methodology divides streamflow into a storm-flow component, which we equate with modeled surface runoff, and a base-flow component, which we equate with modeled groundwater recharge. Gauged watersheds were selected with drainage areas in the range of 50 to 1000 square miles (as compared to an average grid-cell size of about 930 mi^2). The number of watersheds was further reduced to those with at least 20 complete years of data. An exception was made for the Pierre Shale Plains region where all watersheds had fewer complete years. Five watersheds in this region, with 10 to 18 complete years of data, were added. In addition, the period of record was not limited to the 30-year modeling period. The earliest included year is 1901, although the vast majority of stations began recording in the 1930's or later. The last record year included is 2002. The average number of complete years is 44. Ideally, we would not use data from watersheds with any significant natural or manmade surface impoundments or diversions. As this information is not readily available, we attempted to eliminate such watersheds on the basis of anomalies in calculated surface runoff. We also used stream names and hydrologic unit codes to eliminate nested watersheds. In the end, 932 watersheds were included in the analysis. The associated gauging stations lie within the study area or within two degrees east, north and south of the study area. Watersheds to the west of the study area were not included because the majority falls within the Rocky Mountains.

Annual-average storm flow at the 932 gauging stations was interpolated to the half-degree grid of the study area using the inverse-distance-squared method (*e.g.*, Petrie 1991). Ideally, we would interpolate from the geographic center of the watershed; however, those locations are not reported by the USGS. Because the maximum watershed area is 1000 square miles, the geographic center may be one or two cells removed from the gauging station. Nonetheless, the interpolation methodology should be adequate for identifying regional patterns in storm flow. The results of the interpolation are depicting in Figure 5.28 along with the location of the gauging stations. In comparison to modeled surface runoff, observed storm flow shows a much less pronounced dependence on soil texture. Rather, the distribution follows more of climatic pattern of increasing with precipitation.

We make quantitative comparison of observed storm flow with modeled surface runoff in two ways. First, we plot log transforms of the two quantities against each other for each of the 872 grid cells of the study area in Figure 5.29. A linear regression reflects that the model mostly just captures the large-scale trend of increasing surface runoff with increasing humidity. In order to evaluate errors in modeled surface runoff in terms of their significance to the overall water balance, surface runoff ratios (which are defined as surface runoff divided by precipitation) and their difference with the observed surface runoff ratios are plotted in Figure 5.30. Two overlapping patterns are evident; there is a tendency for modeled runoff to be greater than observed both where total runoff is less than about 10 cm and over soils of lower permeability (silty clay loam and tighter soils). In soils of higher permeability (loam and looser soils), there is a tendency for the model to underestimate surface runoff where it is not negligible. The dependency of the errors in surface runoff ratios on saturated hydraulic conductivity is illustrated in Figure 5.31. That modeled surface runoff underestimates observed storm flow in the most humid part of the study area is consistent with the absence in the model of saturation-excess runoff. For the study area as a whole, subgrid variability in soil hydraulic properties is a potential reason for the model underestimating infiltration-excess runoff. That possibility is examined in Section 7.4. A related scaling issue is the fact that surface runoff may infiltrate downslope of the point where it was generated or upstream of a gauged stream channel. The resulting discrepancy between gauged storm flow and point-generated surface runoff is generally most significant in dry regions. As discussed in Section 3.2, the assumed independence of storm intensity and duration is a potential cause of the model overestimating point-generated surface runoff. Because surface runoff in the driest third of the study area is generally only generated during the most intense storms, the neglected negative correlation between the two storm parameters (see Figure 3.13) may also be a significant source of modeled surface runoff overestimating observed storm flow in the region. For the study area as a whole, we suspect that soil parameter uncertainty and the lack of additional runoff mechanisms in the model are the greatest source of error in modeled surface runoff. Under that heading, we include the impact that land use has on soil hydraulic properties and runoff processes.

The most pronounced exception to the pattern of the model underestimating surface runoff in the humid southeast corner of the study area is in the lower Mississippi River Valley. Two unique factors may be at play here; the extremely flat terrain and numerous wetlands may result in the hydrograph separation methodology underestimating surface runoff, while at the same time the artificial drainage structures that are a necessary part of growing crops in the region may have resulted in significant reduction of surface runoff from conditions of natural drainage. Nevertheless, there is still a real tendency for the model to overestimate surface runoff over soils of low permeability, one that is also evident over the clay soils of the Pierre Shale Plains and over the silty clay soils of northeast Texas. The soils of those two regions fall into the Vertisol soil order, which is defined by the formation of wide and deep surface cracks as a result of the high clay content. The model does not capture the consequent infiltration by "macropore" flow. In addition, the fact that the model-maximized LAI underestimates the observations in the above noted areas (see Figure 5.1) suggests that the soil parameter values overestimate the tightness of the associated soils.

Table 5.1: Comparison of modeled and observed soil moisture in Illinois (percent by volume).

parameter	root zone		recharge zone	
	March	August	April	Sept.
modeled:				
mean	37.5	25.0	34.6	30.4
stan. dev.	1.2	1.1	1.6	1.4
observed:				
mean	38.4	26.6	38.4	35.6
stan. dev.	2.0	3.8	3.6	2.9

Table 5.2: Comparison of model parameter values with site-specific information on soils and peak green LAI

site	soil zone	site-specific/ model	peak green LAI	% sand	% clay	texture class	Ks (cm/dy)	θ_t at 1/3 bar	θ_t at 15 bar	site-specific references
CPER, CO clay loam slope	root	site-specific	0.4-0.6	50	35	clay loam	20-50	0.27	0.13	Singh et al. (1998), Van Haveren and Galbraith (1971), Smith (1971), Rauzi and Smith (1973), Knight (1973), Hazlett (1992)
		model	0.7	41	25	loam	24	0.25	0.12	
	recharge	site-specific		39	30	clay loam	n.a.	0.27	0.14	
		model		43	24	loam	27	0.24	0.12	
Chickasha, OK R-5 watershed	root	site-specific	2.5, 3.2	n.a.	n.a.	silt loam	73	0.24	0.13	Luxmoore and Sharma (1980) Ritchie et al. (1976)
		model	2.1	34	24	loam	21	0.25	0.13	
	recharge	site-specific		n.a.	n.a.	n.a.	4	0.27	0.16	
		model		28	35	clay loam	6.8	0.29	0.17	
Treynor, IA W-2 watershed	root	site-specific	n.a.	4	27	silty clay loam/silt loam	n.a.	0.25	0.13	Chung et al. (1999)
		model	4.3	7	29	silty clay loam	6.6	0.37	0.23	
	recharge	site-specific		6	22	silt loam	n.a.	0.27	0.11	
		model		9	29	silty clay loam	6.5	0.35	0.22	
Bondville, IL ICN site	root	site-specific	n.a.	n.a.	n.a.	silt loam	n.a.	n.a.	n.a.	Hollinger and Isard (1994)
		model	4.6	14	27	silty clay loam/silt loam	10	0.33	0.20	
	recharge	site-specific		n.a.	n.a.	silt loam	n.a.	n.a.	n.a.	
		model		19	30	silty clay loam	7.6	0.30	0.18	

a) maximized peak green LAI

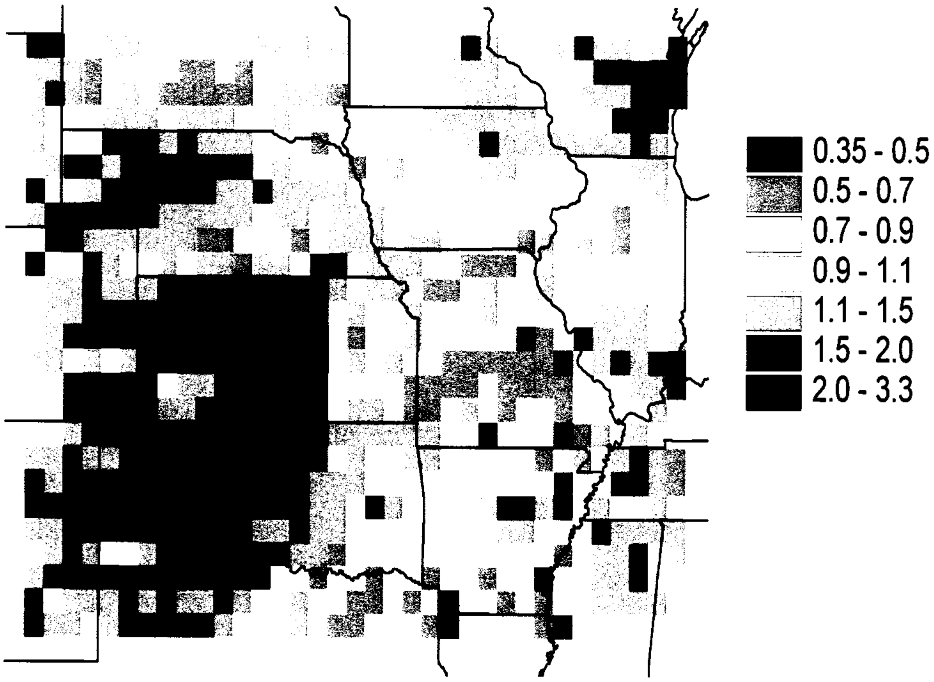

b) ratio to unaltered observations

Figure 5.1. (a) Average peak in model-maximized green LAI (1951-1980), and (b) its ratio to the average NDVI-based estimates (1981-1991) of Buerman et al. (2002).

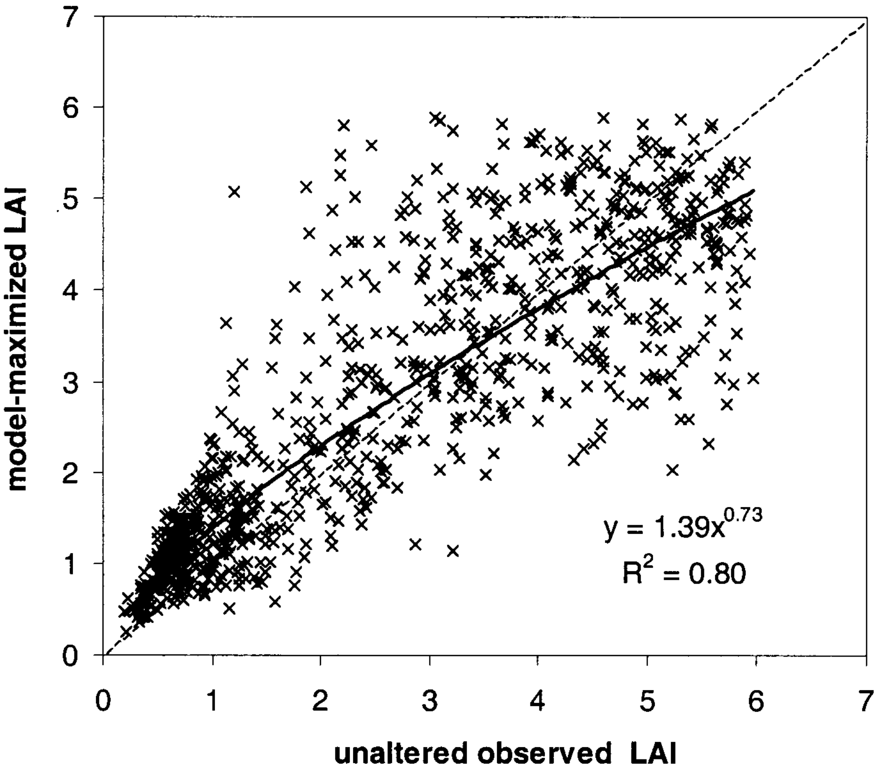

Figure 5.2 Average of the model-maximized peak in green LAI versus the average peak in the Buerman-et-al. (2002) NDVI-based observations for each of 872 grid cells

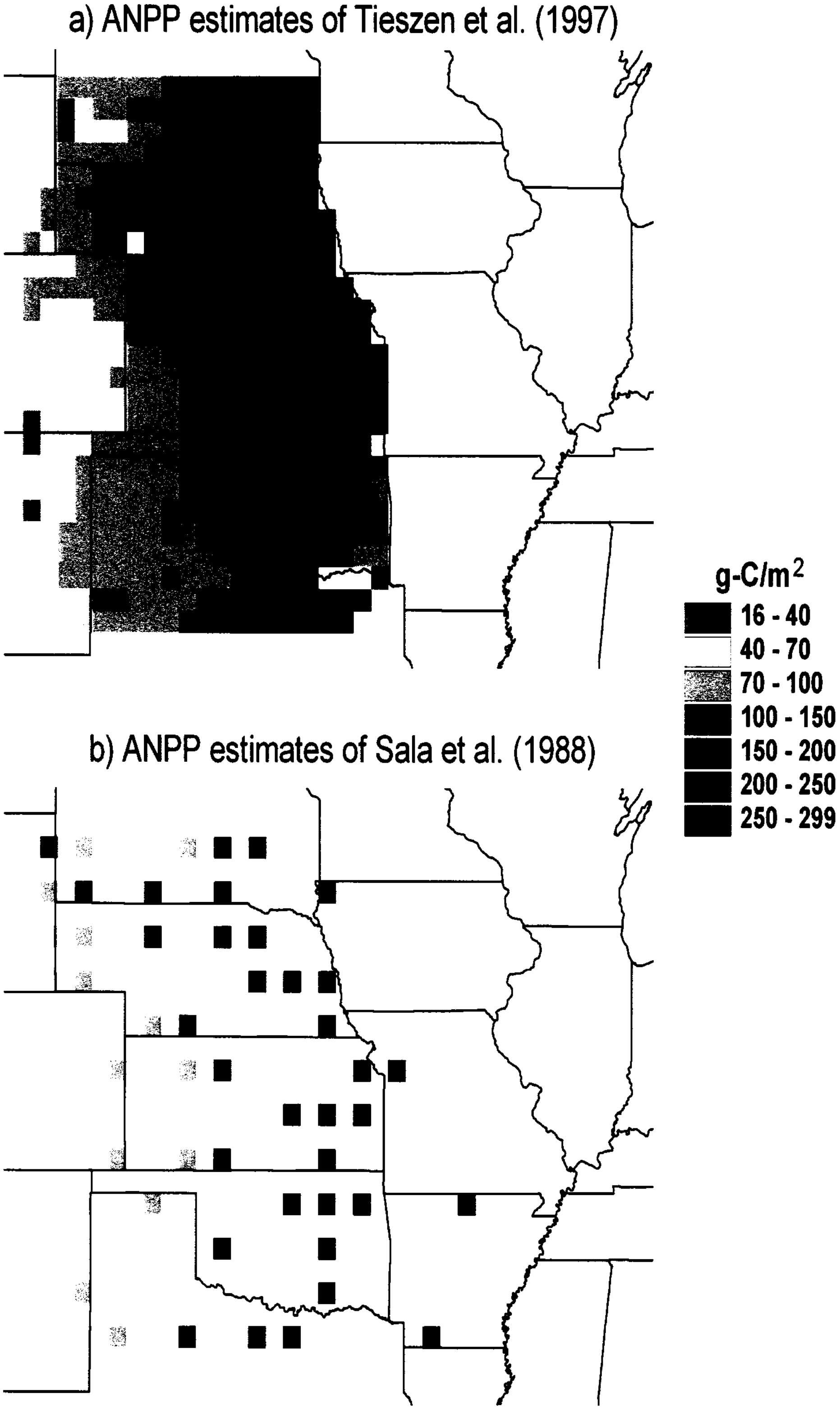

Figure 5.3. Aboveground net primary productivity (ANPP) estimates from the dataset of Zheng et al (2003b), as drawn from: (a) Tieszen et al. (1997) and (b) Sala et al. (1988).

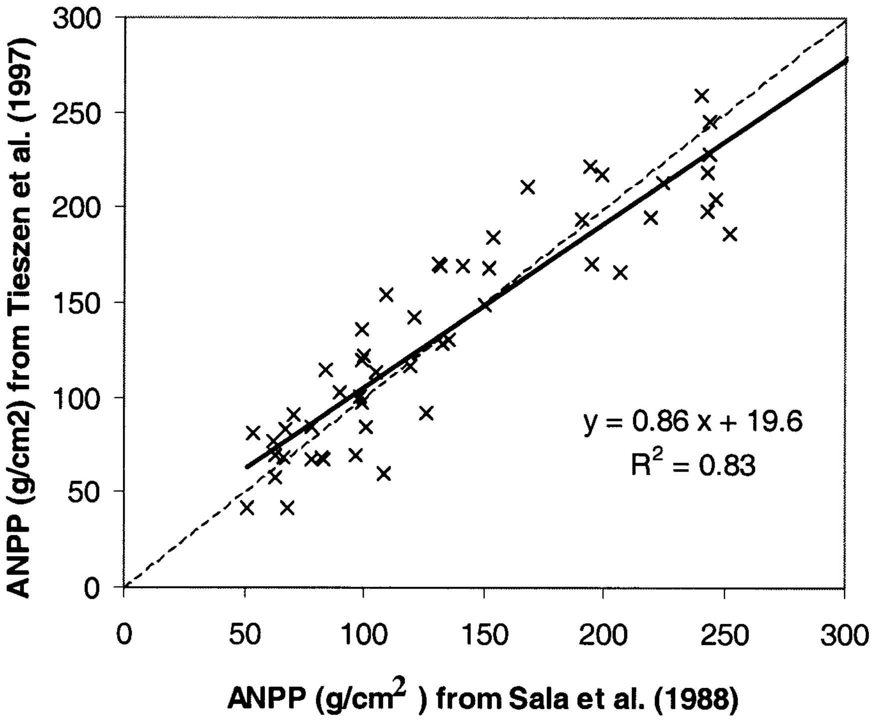

Figure 5.4. Comparison of the ANPP estimates of Sala et al. (1988) with those of Tieszen et al. (1997) for 51 grid cells at which they overlap.

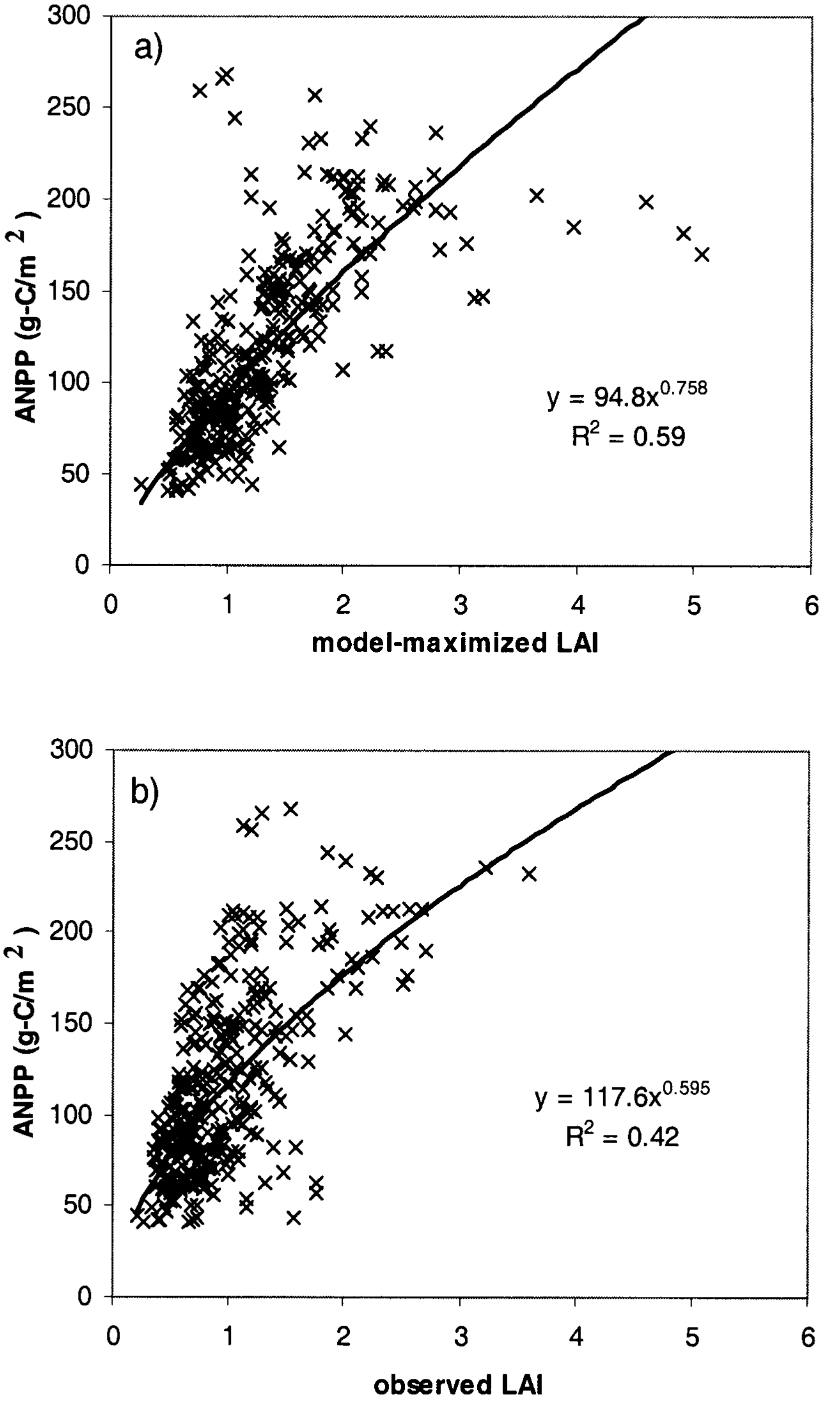

Figure 5.5. Comparison of the estimates of ANPP from Tieszen et al. (1997) with: (a) modeled-maximized peak green LAI, and (b) unaltered satellite-based observations of peak green LAI (Buerman et al., 2002).

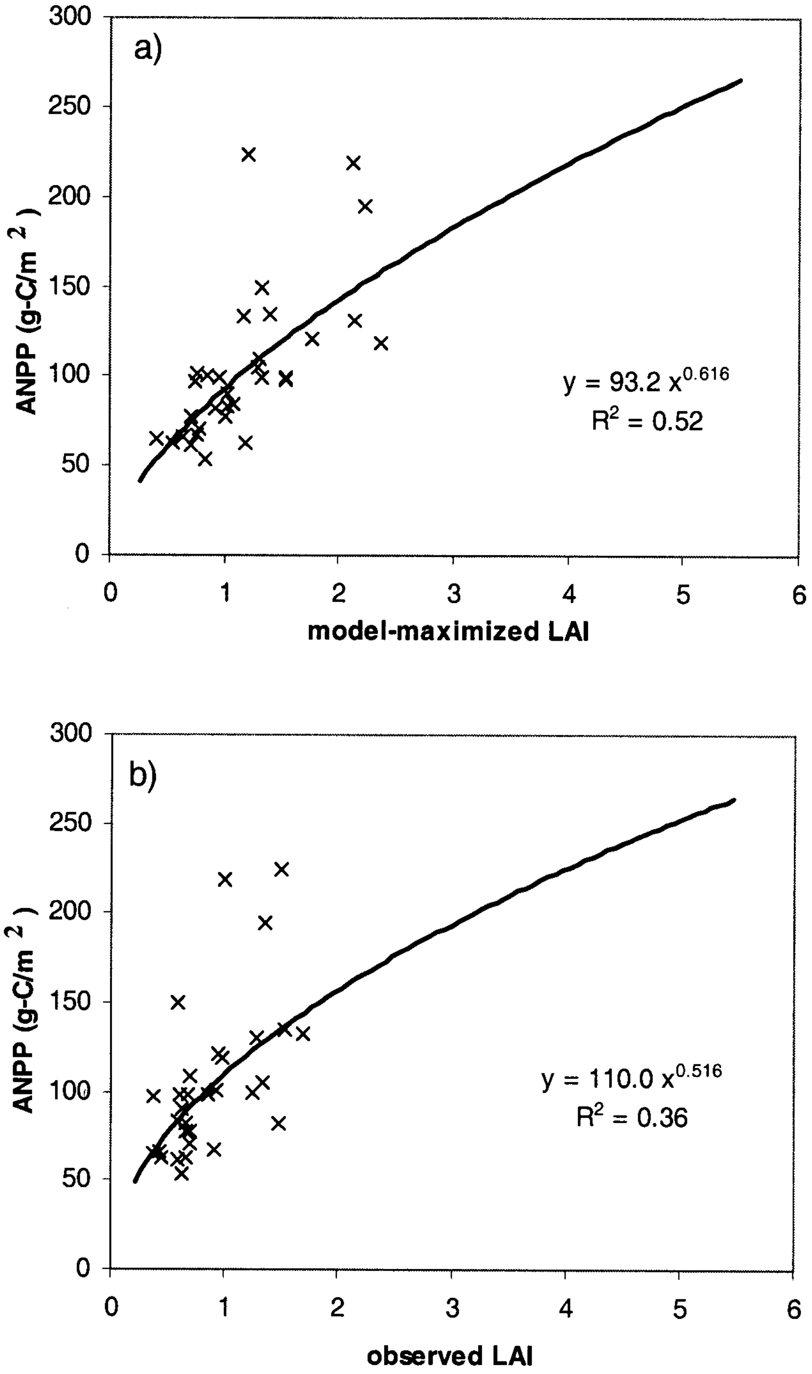

Figure 5.6. Comparison of the estimates of ANPP from Sala et al. (1988) with: (a) modeled-maximized LAI, and (b) unaltered satellite-based observations of LAI (Buerman et al., 2002).

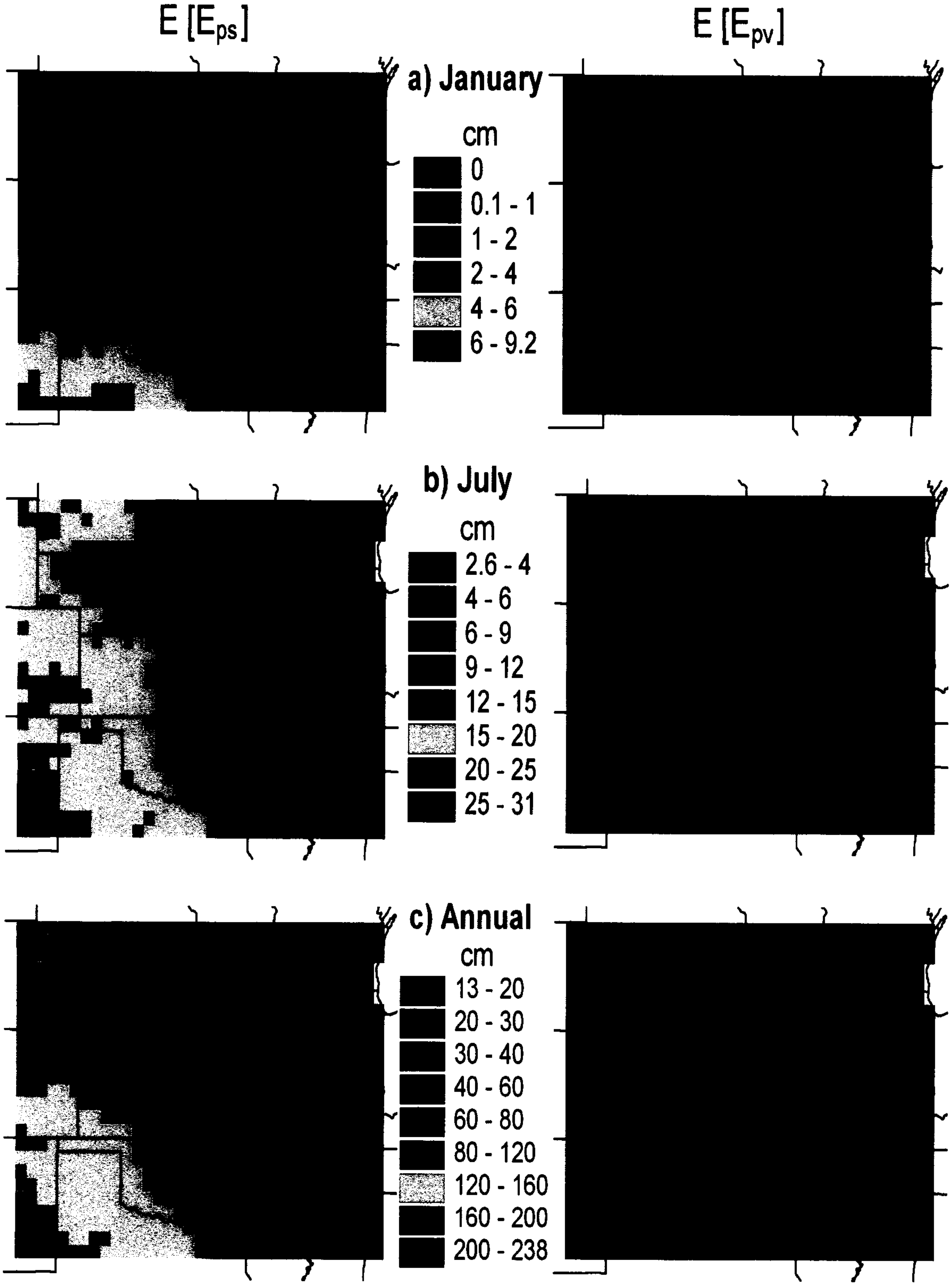

Figure 5.7. Average potential bare-soil evaporation and potential transpiration (1951-1980): (a) January, (b) July, and (c) annual.

E [E_{hv}]

a) January

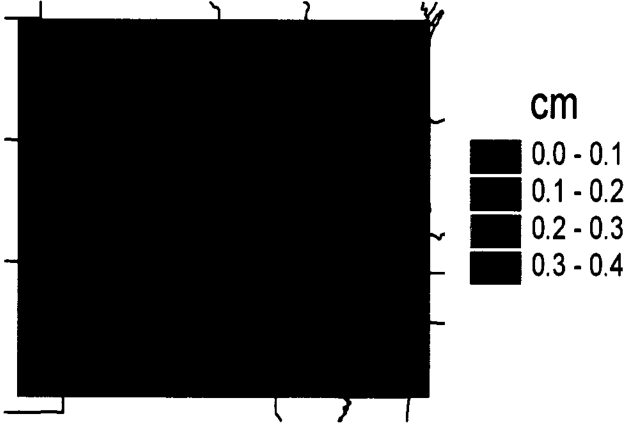

b) July

c) Annual

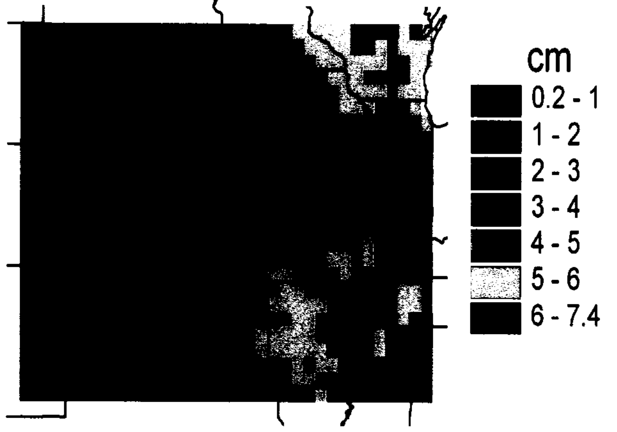

Figure 5.8. Average evaporation from vegetal interception (1951-1980): (a) January, (b) July and (c) annual.

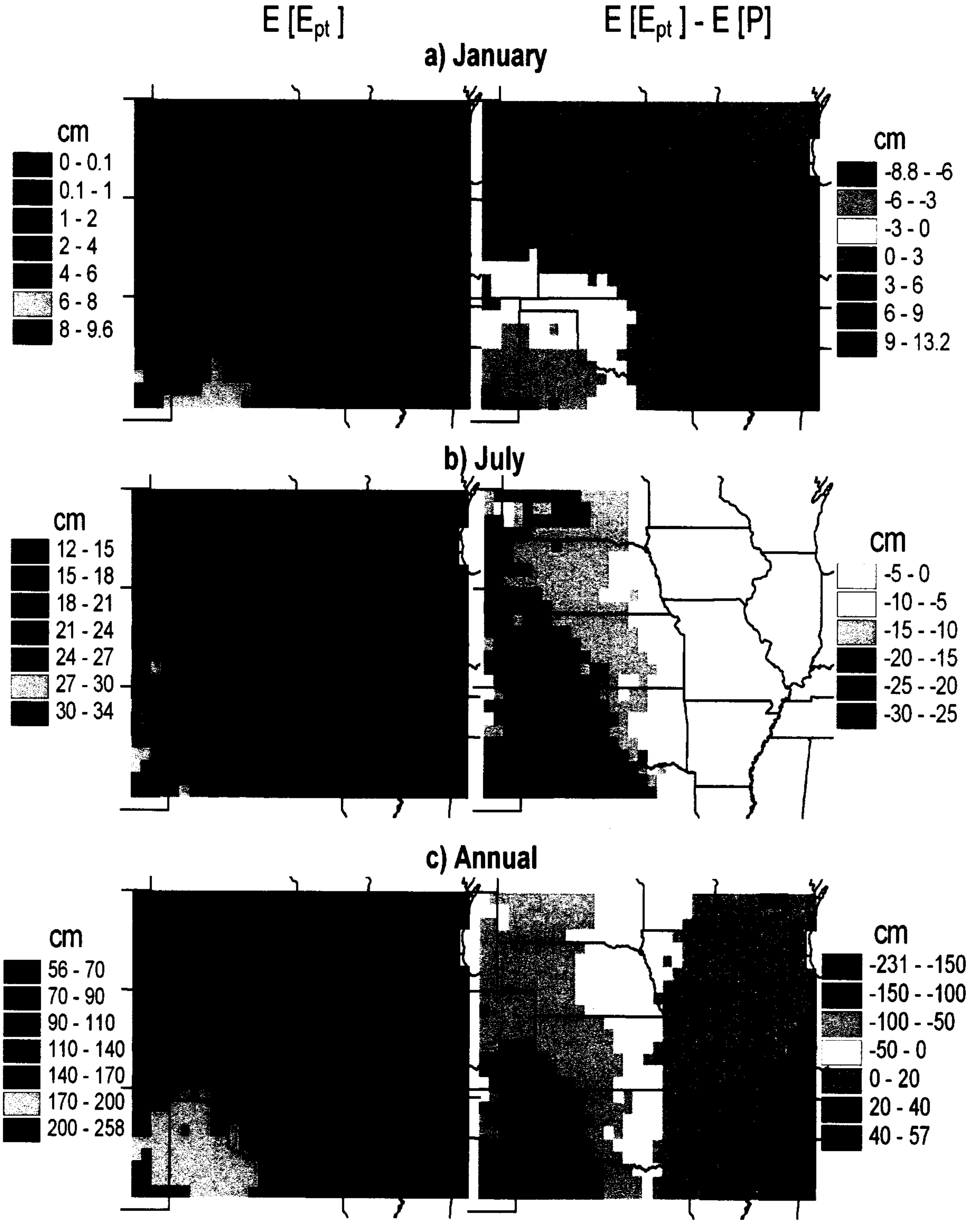

Figure 5.9. Average total potential evapotranspiration and difference with average precipitation (1951-1980): (a) January, (b) July and (c) annual.

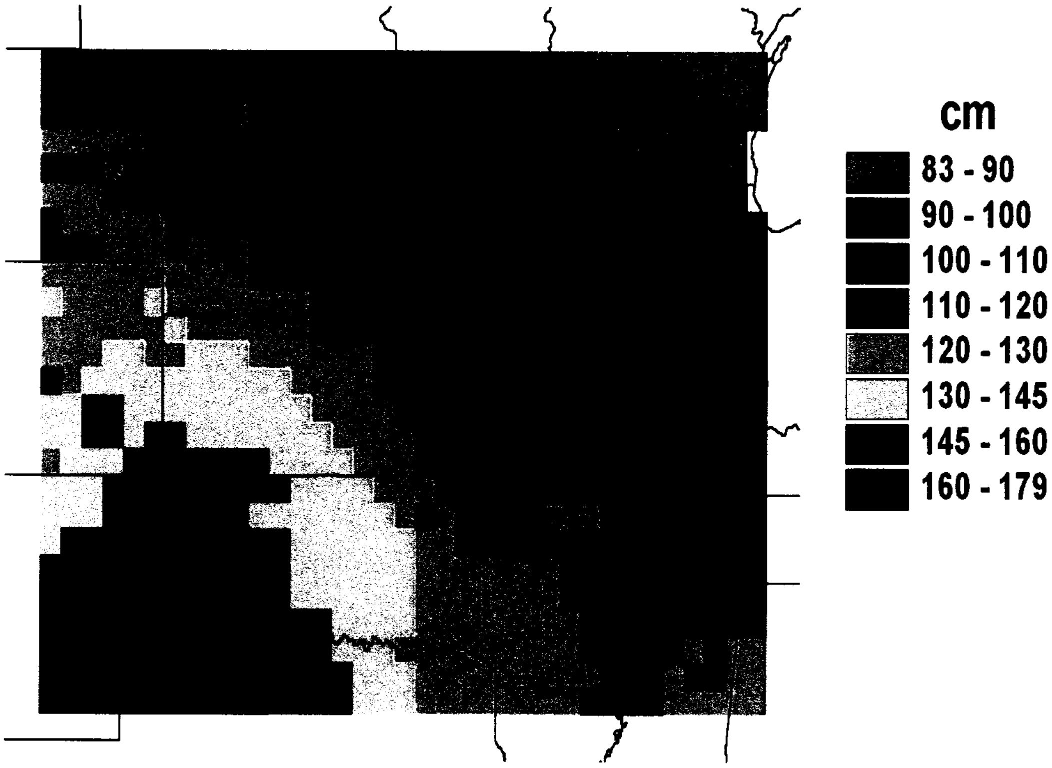

Figure 5.10. Annual reference crop evaporation (1951-1980) based on Shuttleworth (1993).

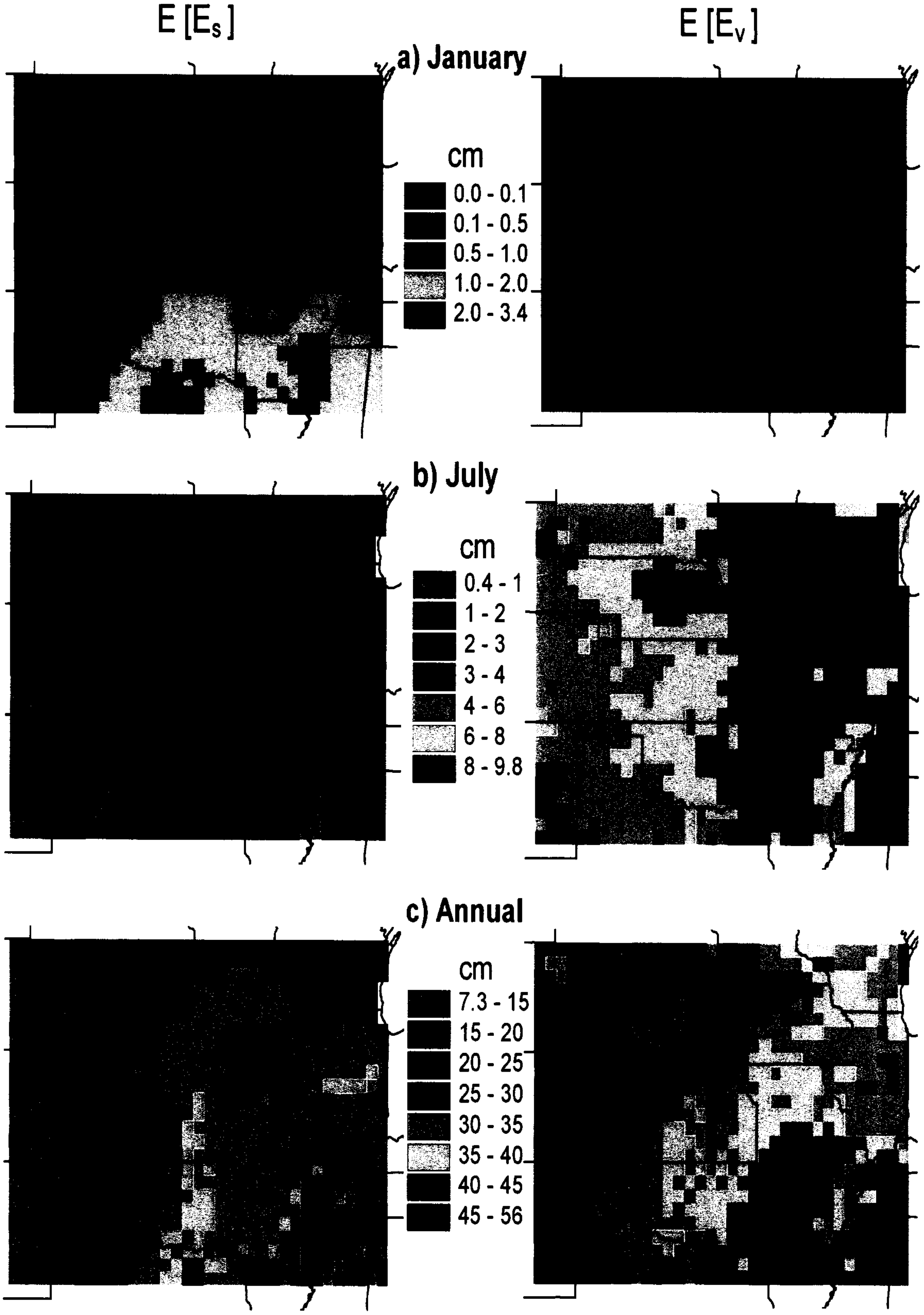

Figure 5.11. Average bare-soil evaporation and transpiration (1951-1980): (a) January, (b) July and (c) annual.

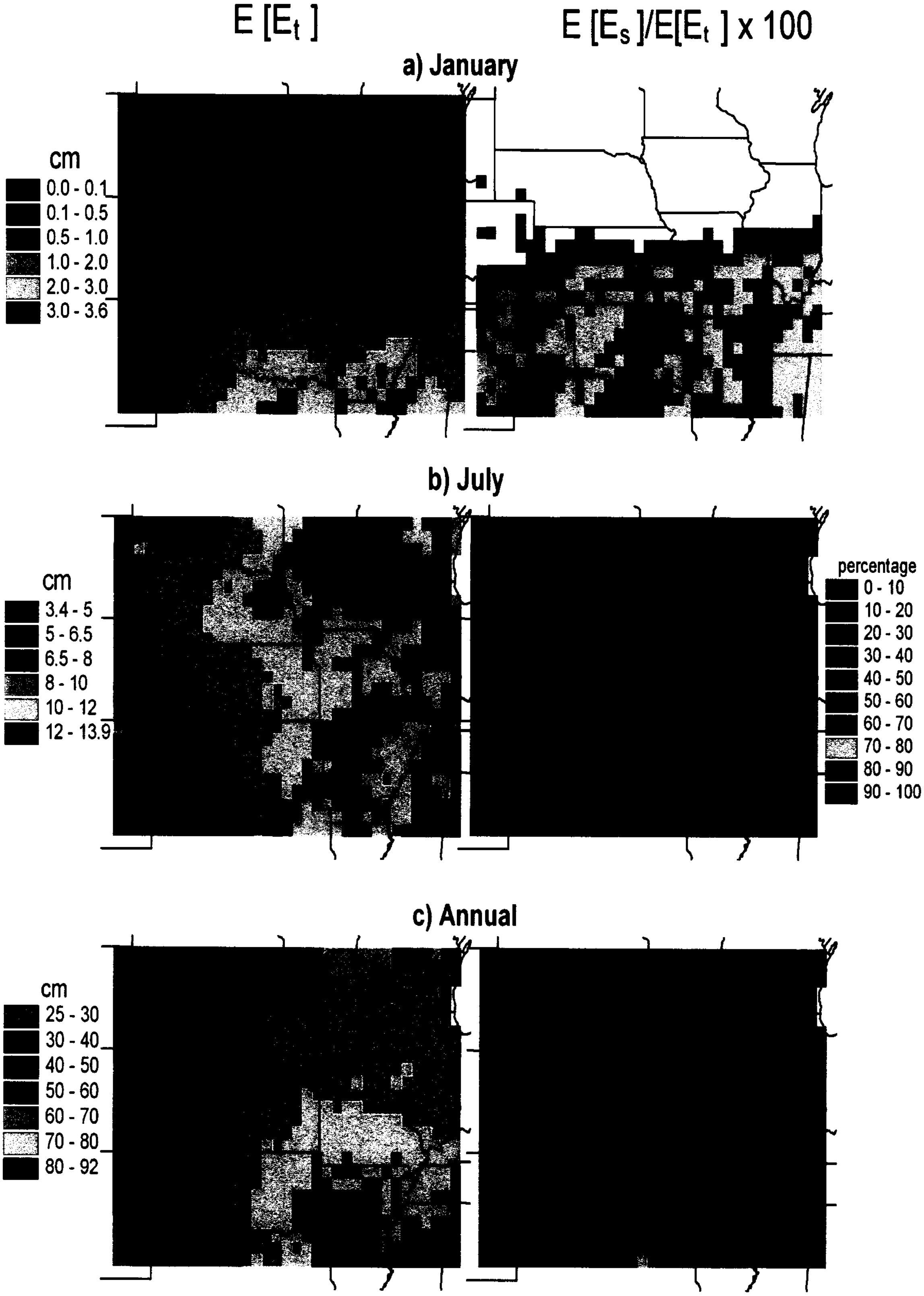

Figure 5.12. Average total evapotranspiration and bare-soil evaporation as a percentage of total evapotranspiration (1951-1980): (a) January, (b) July and (c) annual.

$E[E_s]/E[E_{ps}] \times 100$

a) March

b) August

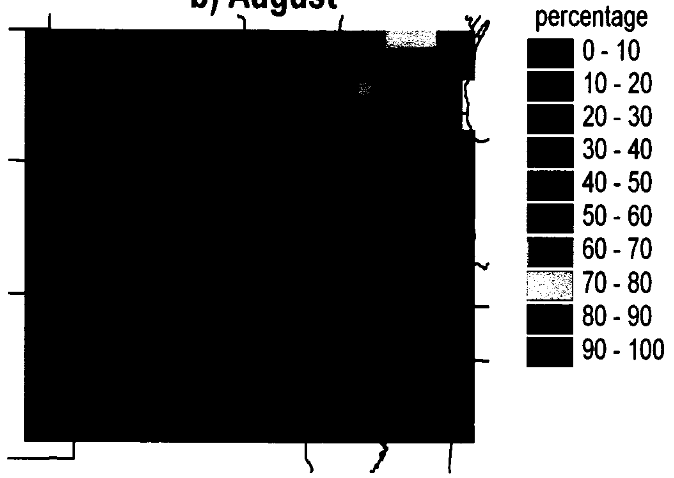

c) Annual

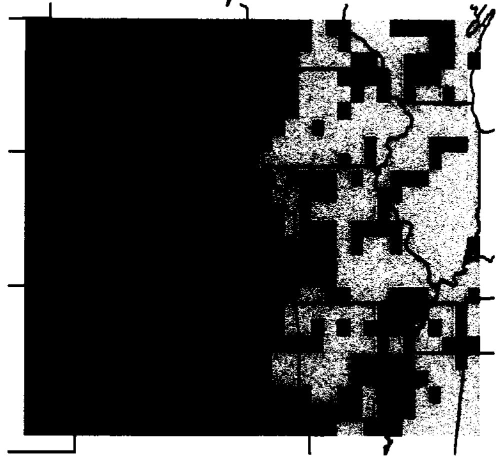

Figure 5.13. Average bare-soil evaporation as a percentage of bare-soil potential evaporation (1951-1980): (a) March, (b) August and (c) annual.

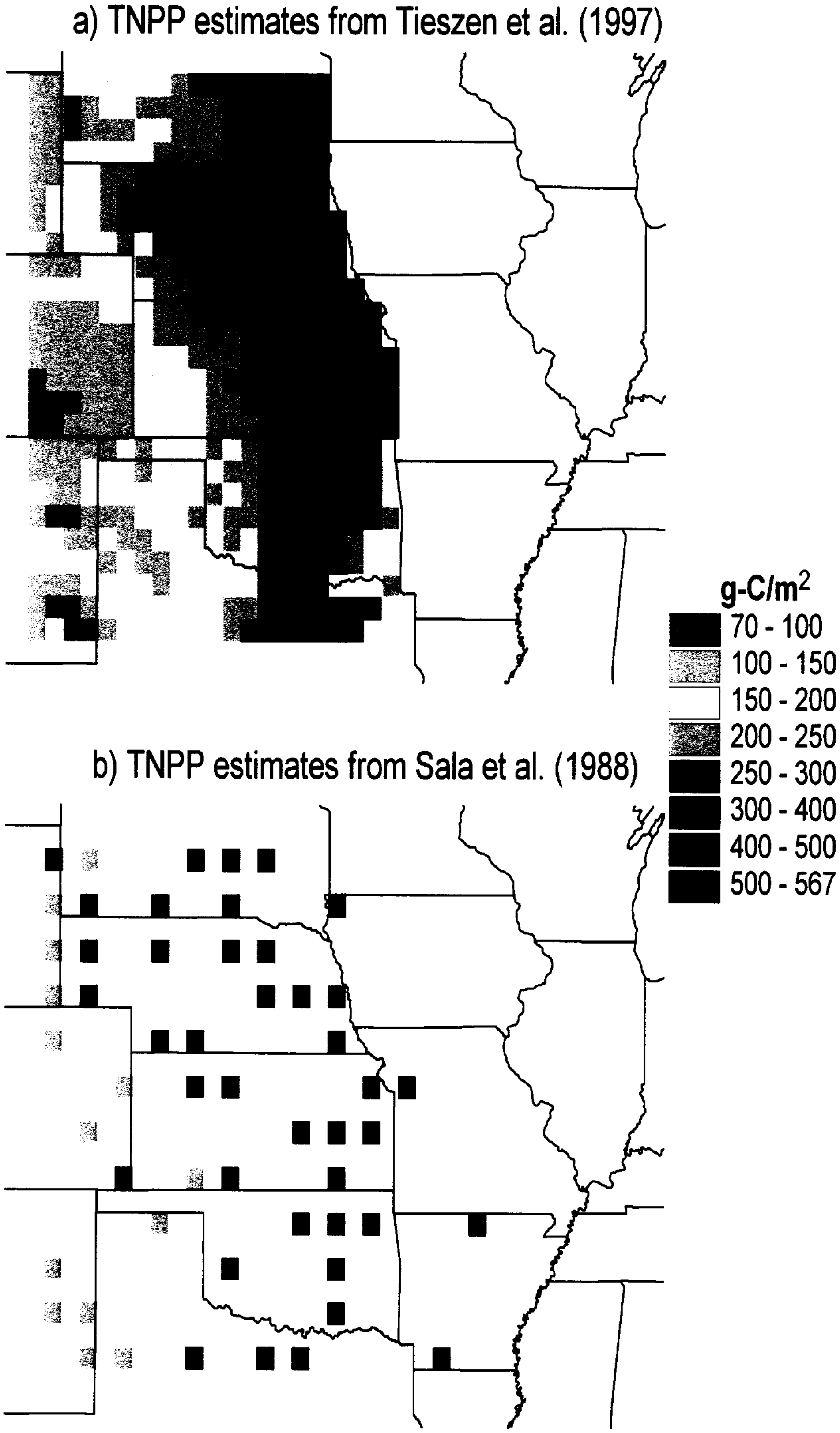

Figure 5.14. Total net primary productivity (TNPP) estimates from the dataset of Zheng et al (2003b), as drawn from: (a) Tieszen et al. (1997) and (b) Sala et al. (1988).

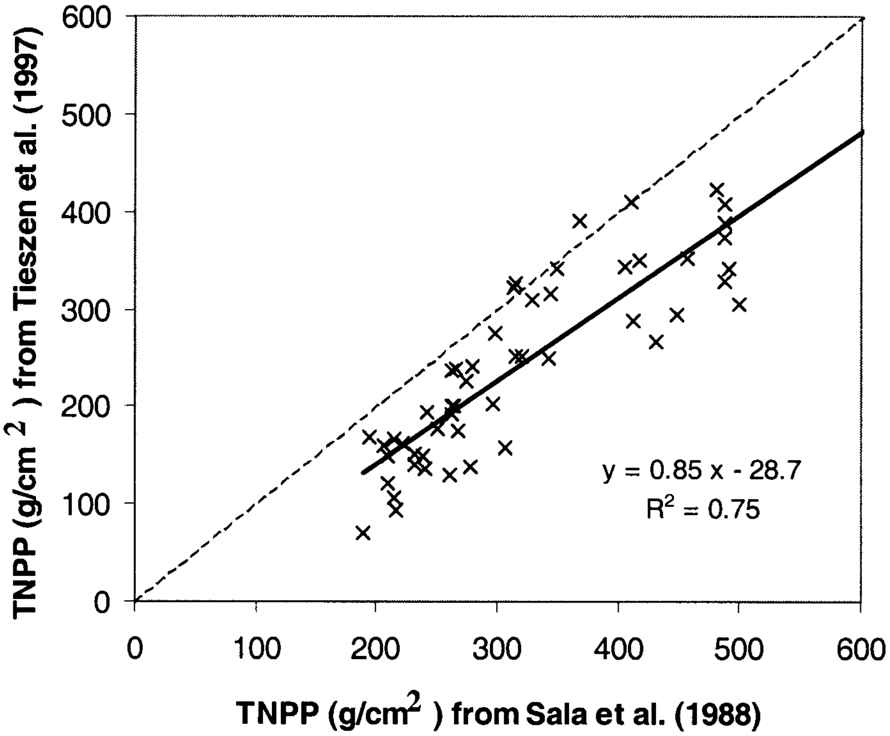

Figure 5.15. Comparison of the TNPP estimates based on Sala et al. (1988) with those from Tieszen et al. (1997) for 51 grid cells at which they overlap.

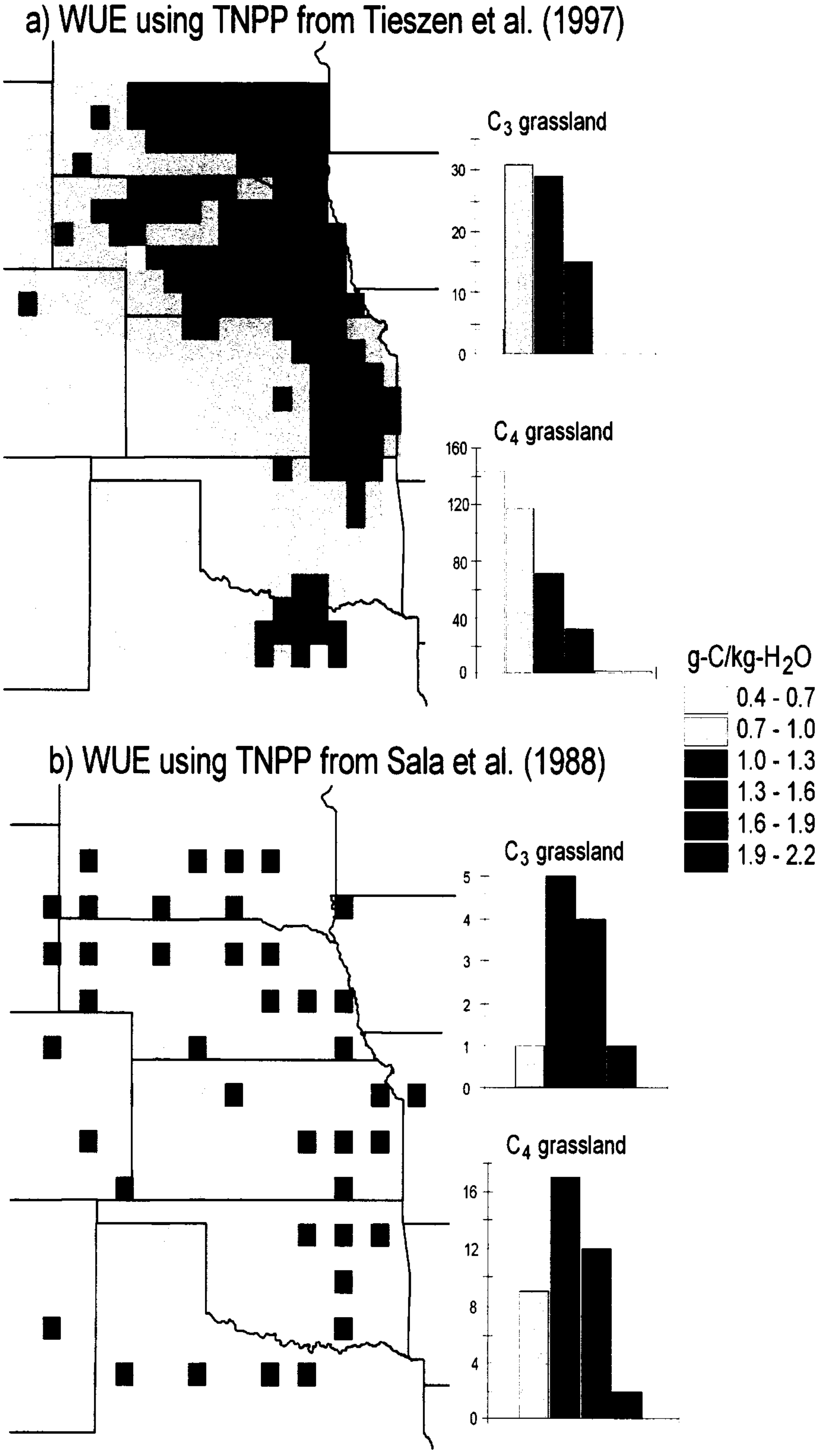

Figure 5.16. Water-use efficiencies (WUE) for grasslands calculated using modeled transpiration and TNPP estimates from Zheng et al (2003b), as drawn from:
(a) Tieszen et al. (1997) and (b) Sala et al. (1988).

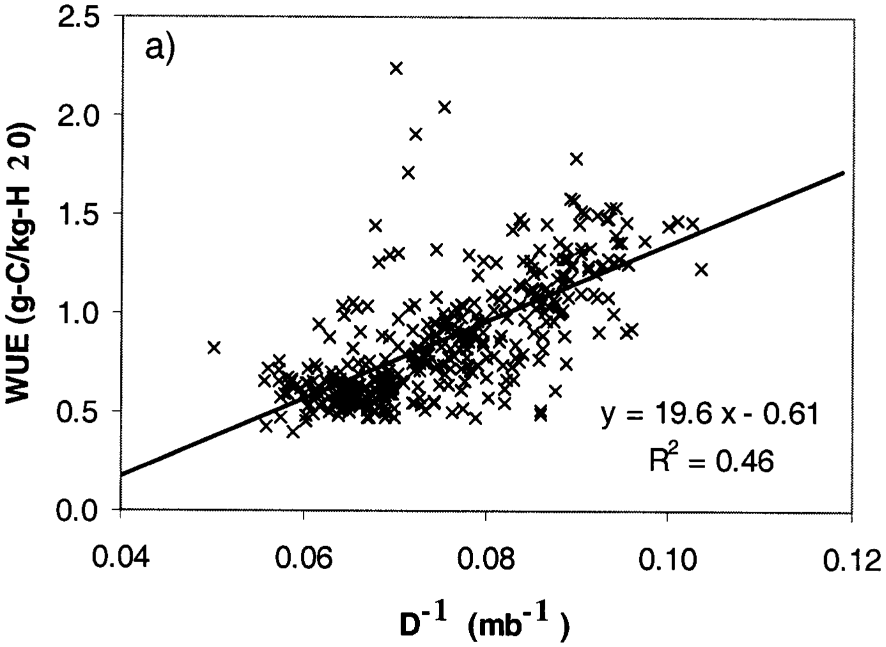

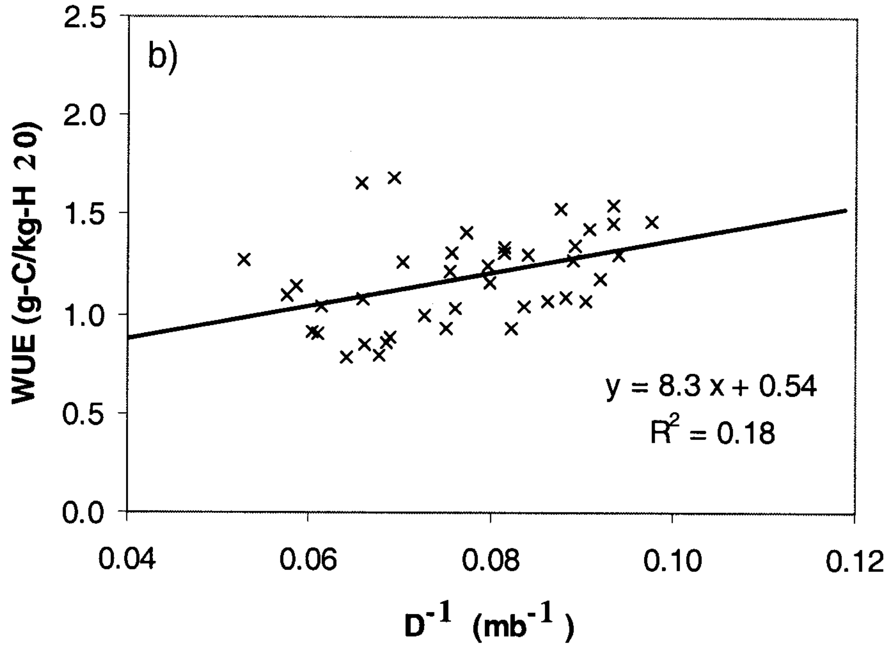

Figure 5.17. Inverse of the June-August average vapor pressure deficit vs. Water-use efficiencies (WUE) for C4 grasslands, as calculated using modeled transpiration and TNPP estimates from Zheng et al (2003b), as drawn from: (a) Tieszen et al. (1997) and (b) Sala et al. (1988).

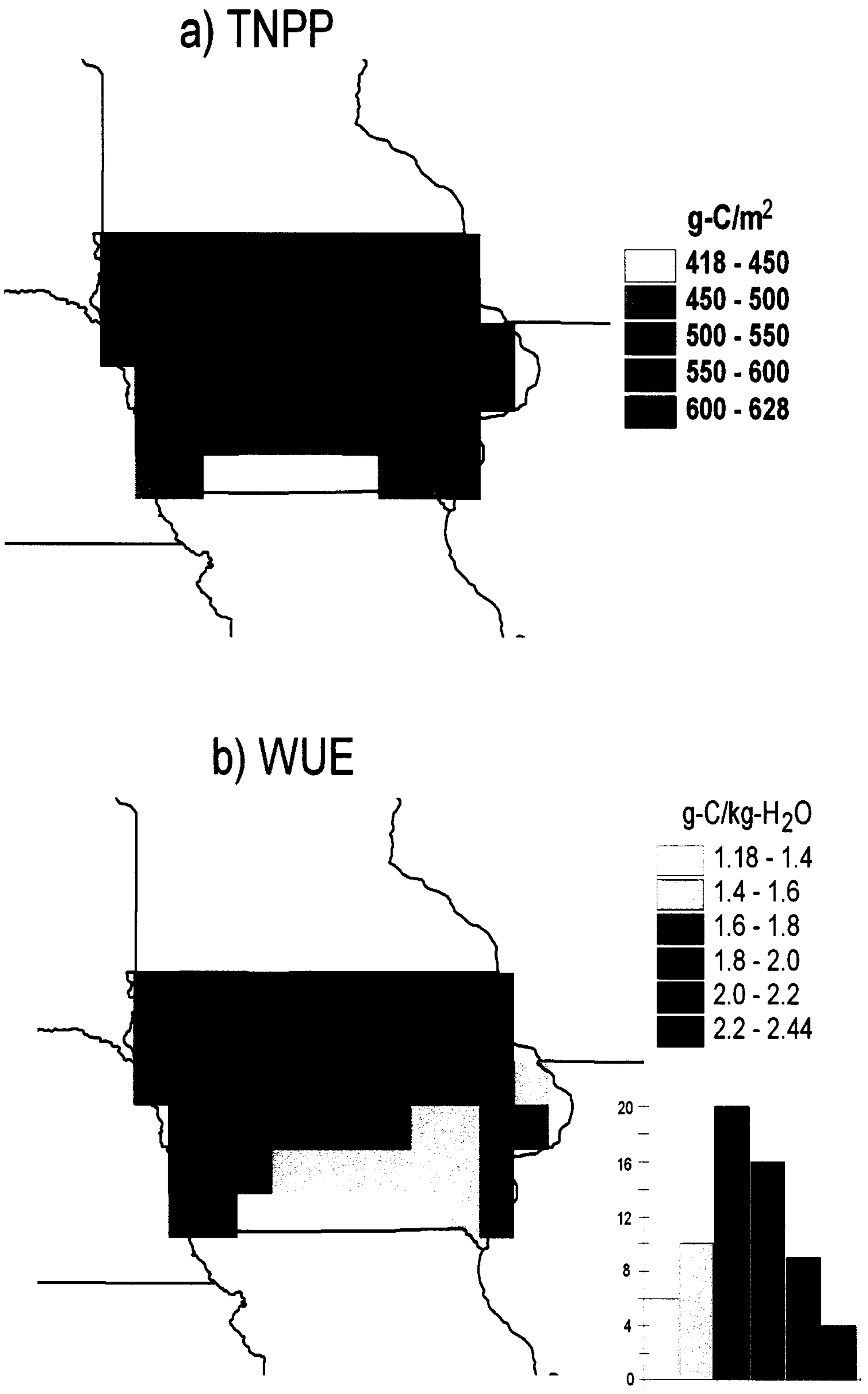

Figure 5.18. (a) Total net primary productivity (TNPP) estimates for crops in Iowa from the dataset of Zheng et al (2003b), as drawn from Prince et al. (2001), and (b) Water-use efficiencies (WUE) as calculated using modeled transpiration and the TNPP estimates.

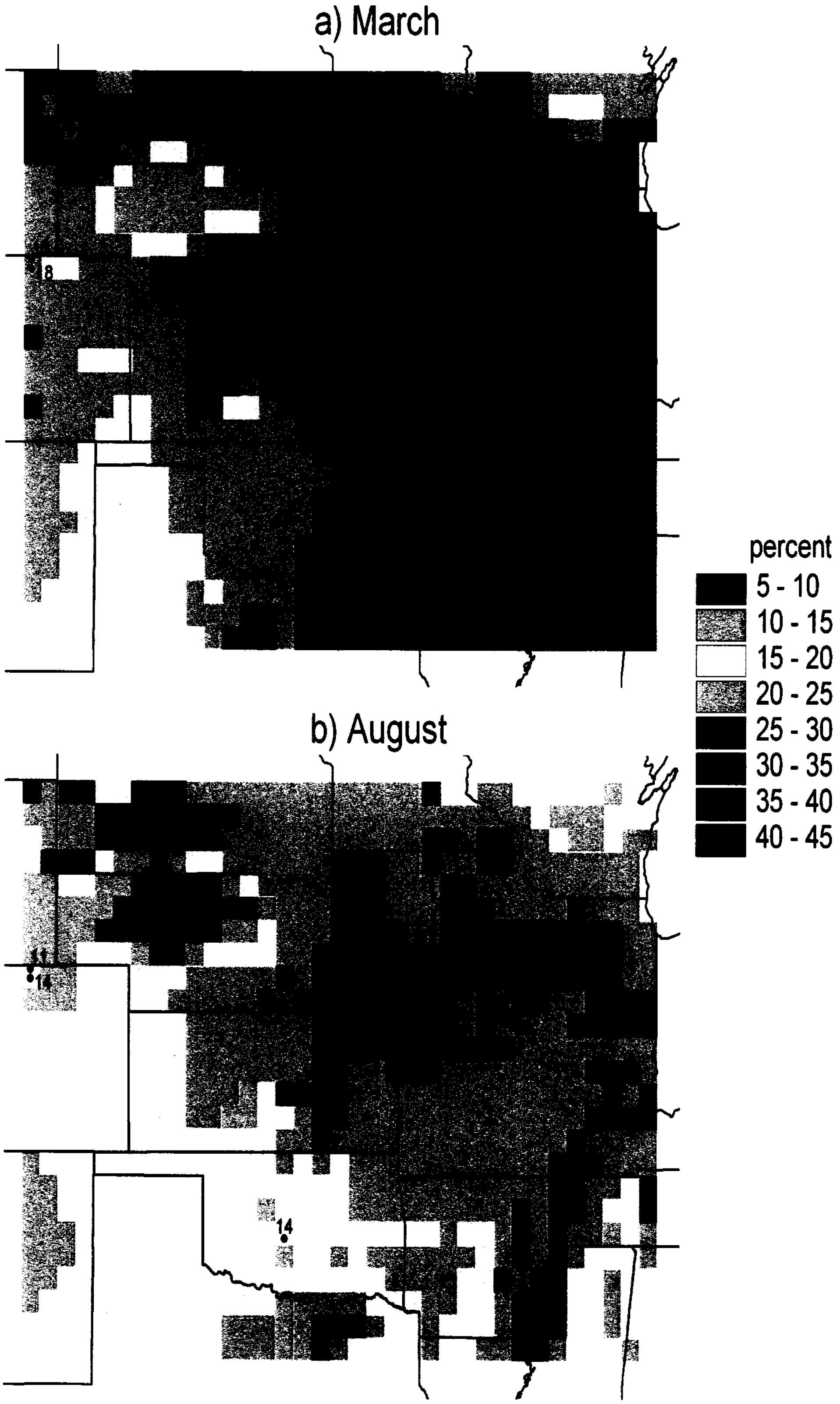

Figure 5.19. Comparison of modeled and observed volumetric soil moisture in the root zone: (a) March and (b) August.

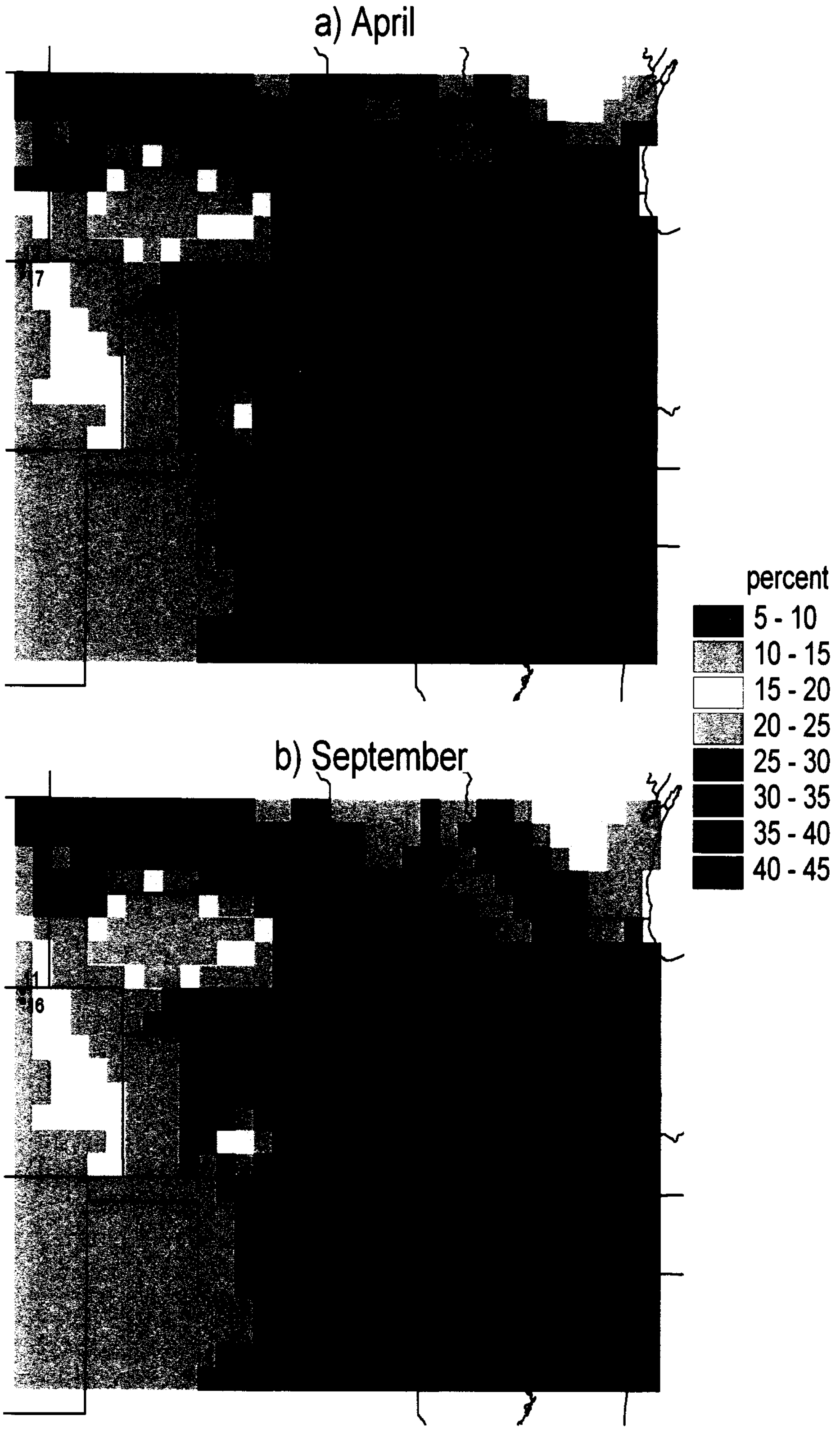

Figure 5.20. Comparison of modeled and observed volumetric soil moisture in the recharge zone: (a) April and (b) September.

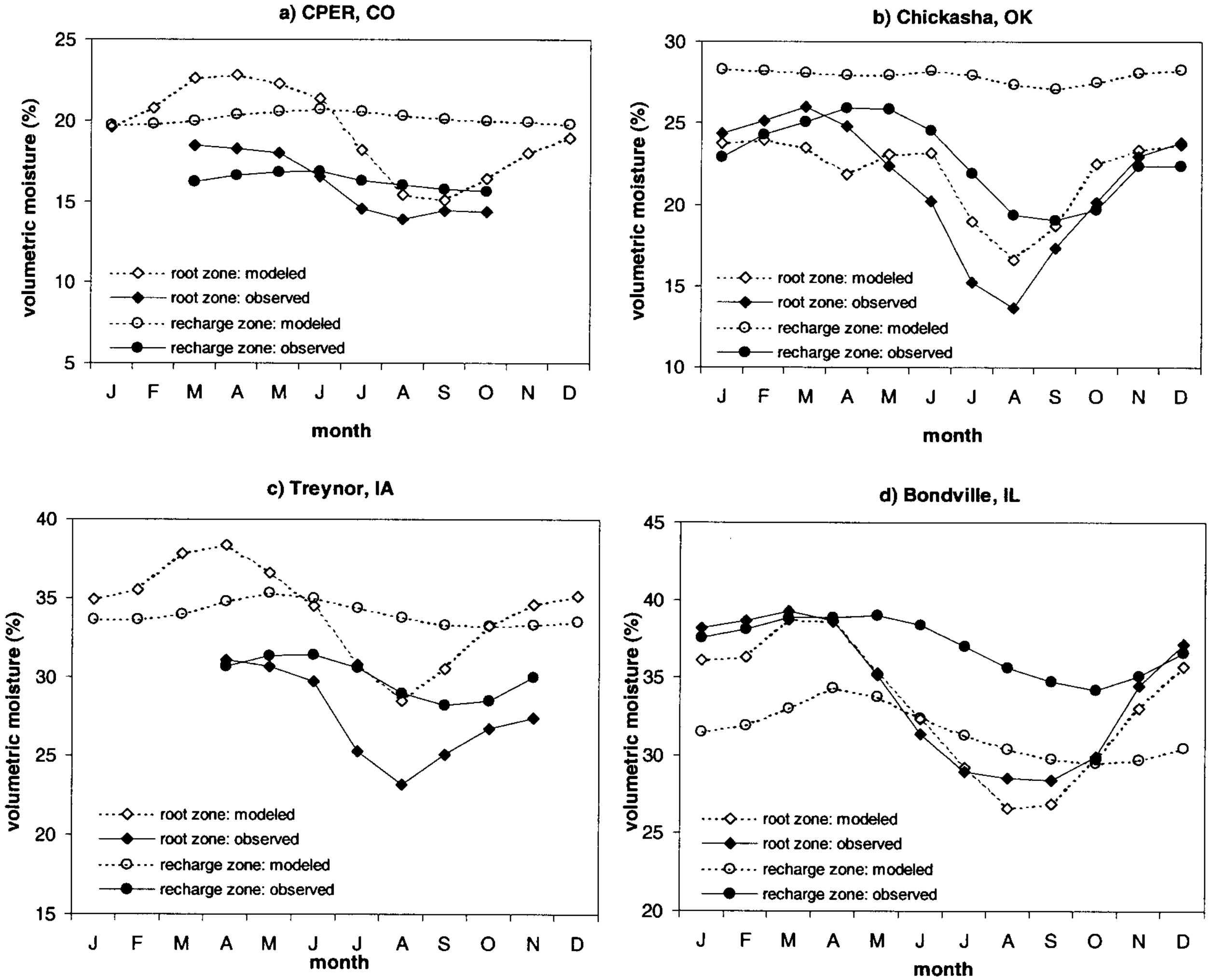

Figure 5.21. Comparison of modeled and observed soil moisture at four validation sites: (a) clay-loam slope at the Central Plains Experimental Range in Colorado, (b) the R-5 watershed at the USDA-ARS site near Chickasha, Oklahoma, c) the W-2 watershed at the USDA-ARS site near Treynor, Iowa, and (d) the Bondville, Illinois site of the Illinois Climatology Network.

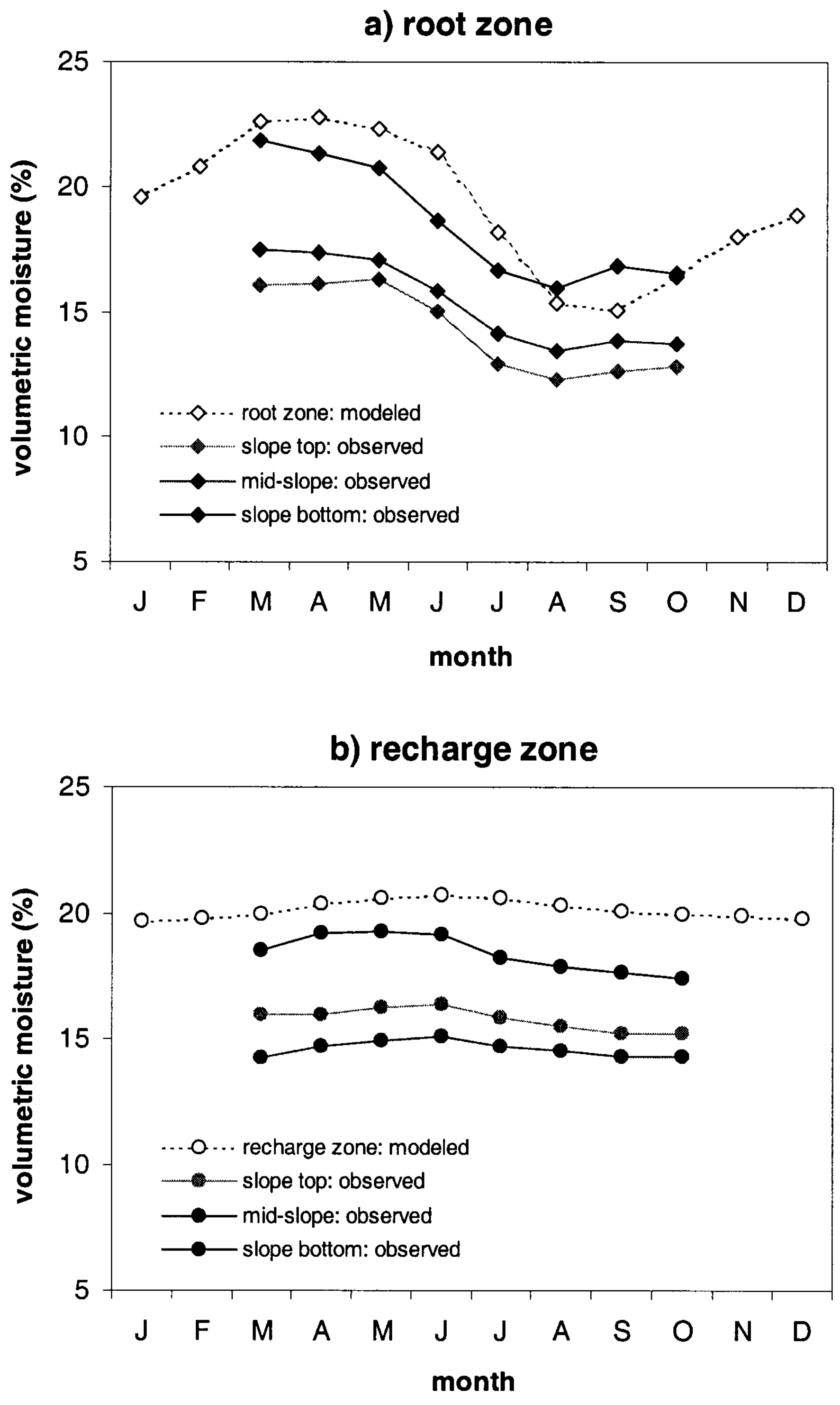

Figure 5.22. Comparison of modeled soil moisture with observed soil moisture at each of the positions on the clay loam slope at the CPER site: (a) root zone (b) recharge zone.

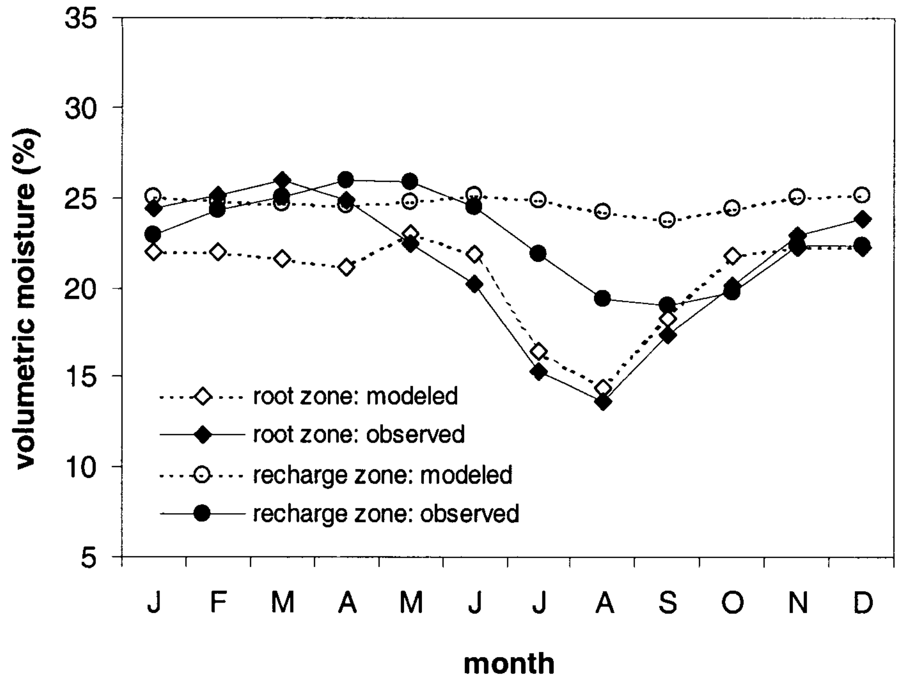

Figure 5.23. Comparison of observed soil moisture at the R-5 watershed with results from a model run using information on site-specific soil and green LAI.

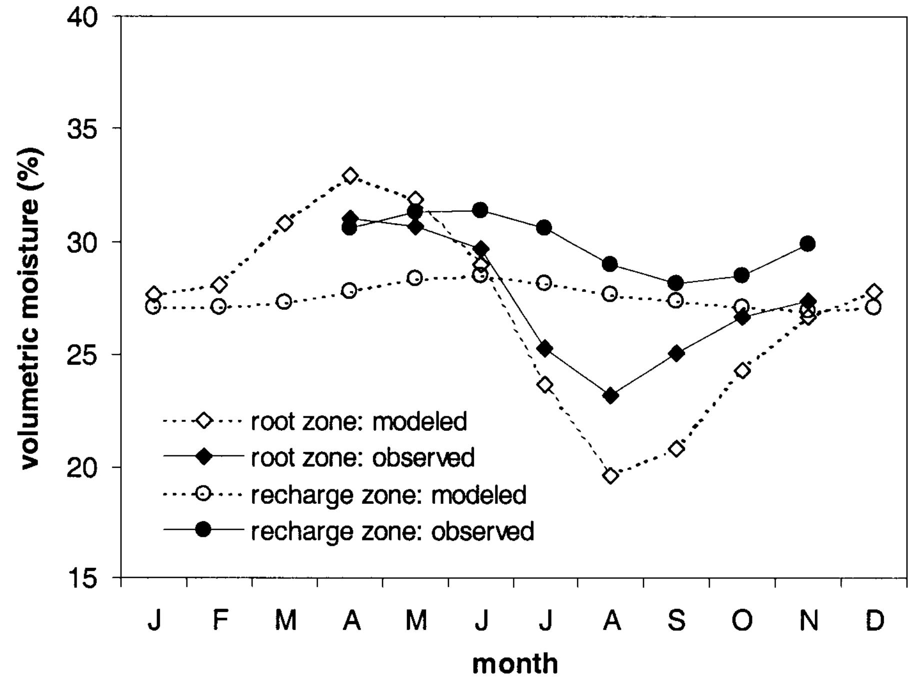

Figure 5.24. Comparison of observed soil moisture at the W-2 watershed with results from a model run using site-specific soil information.

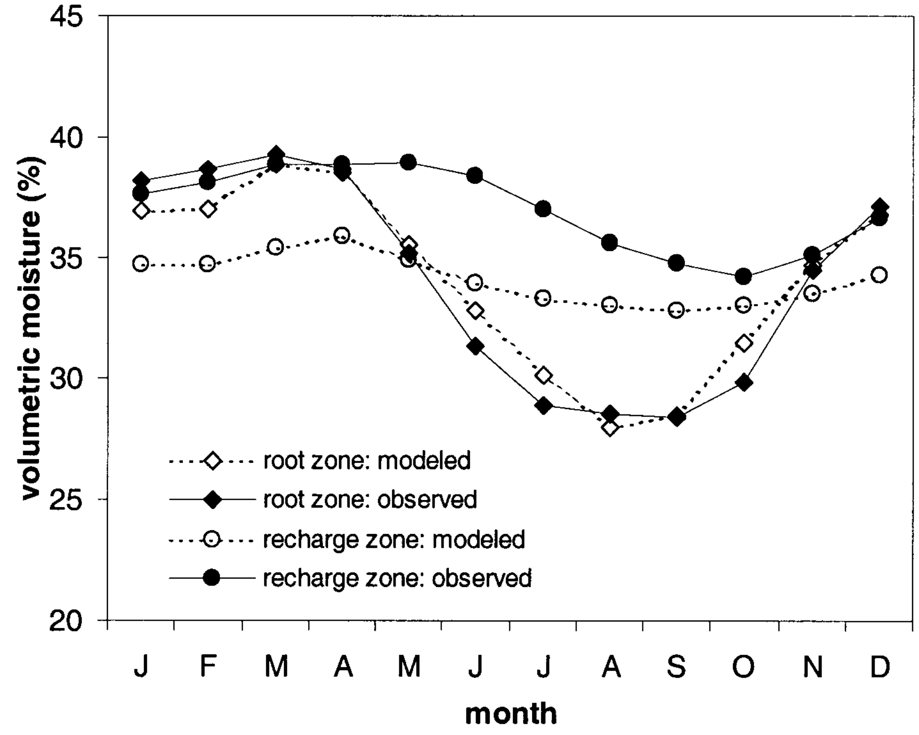

Figure 5.25. Modeled and observed soil moisture at the Bondville, Il site after capillary rise from a fixed water table was incorporated into the model.

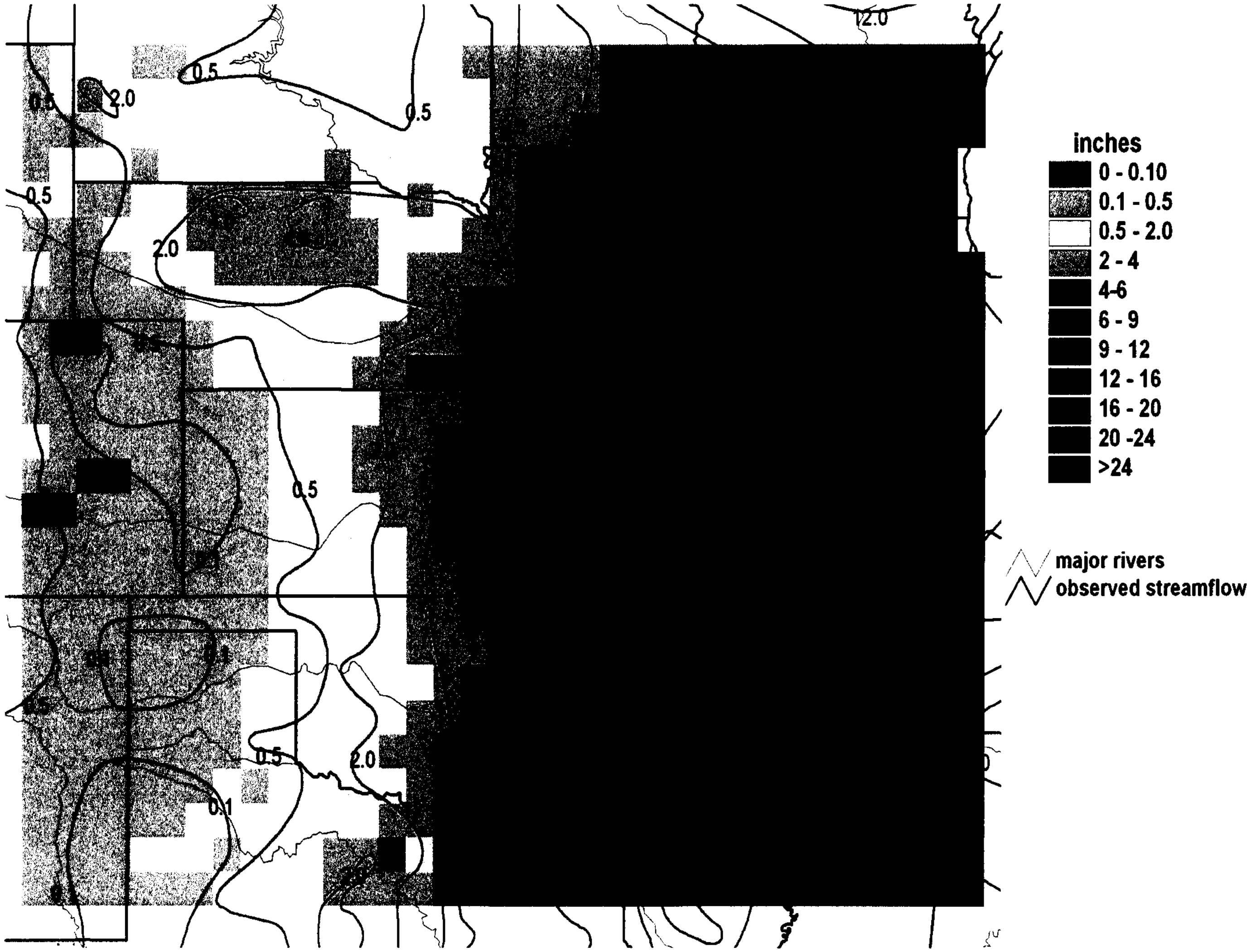

Figure 5.26. Comparison of modeled annual total runoff with observed streamflow (1951-1980). Contours are from Gebert et al. (1987).

Figure 5.27. Modeled average-annual values of: (a) surface runoff, and (b) groundwater recharge (1951-1980).

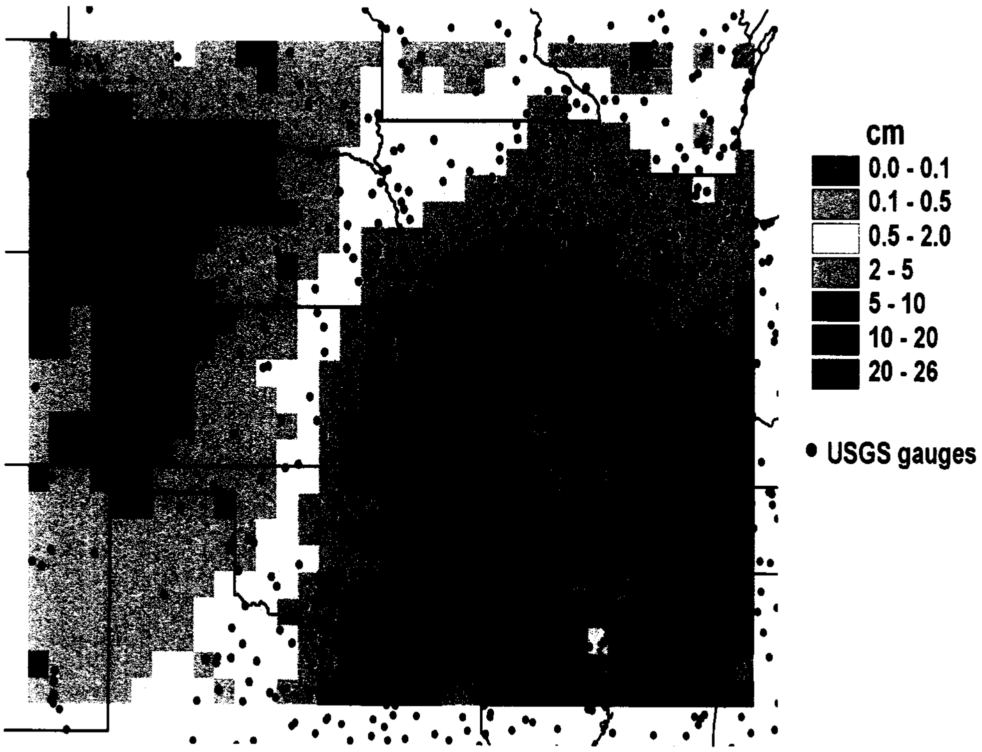

Figure 5.28. Interpolated annual average storm flow as estimated from USGS daily streamflow data using the hydrograph separation methodology of Woodruff and Hewlett (1970).

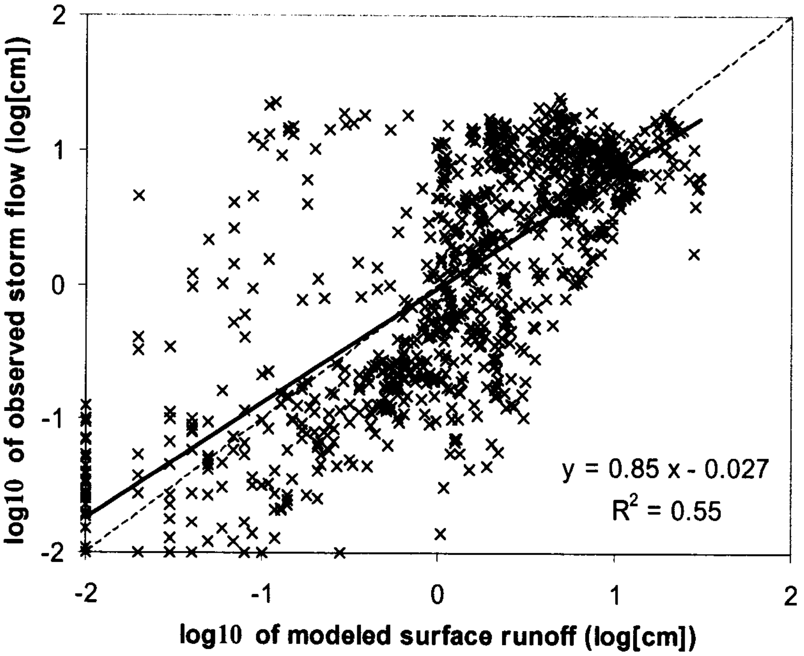

Figure 5.29. Log_{10} of modeled average-annual surface runoff (Fig. 5.27a) versus $\log_{10}$ of interpolated observed storm flow (Fig. 5.28) at each of the 872 grid cells. Values less than –2 are plotted at –2.

(a) modeled surface runoff ratios

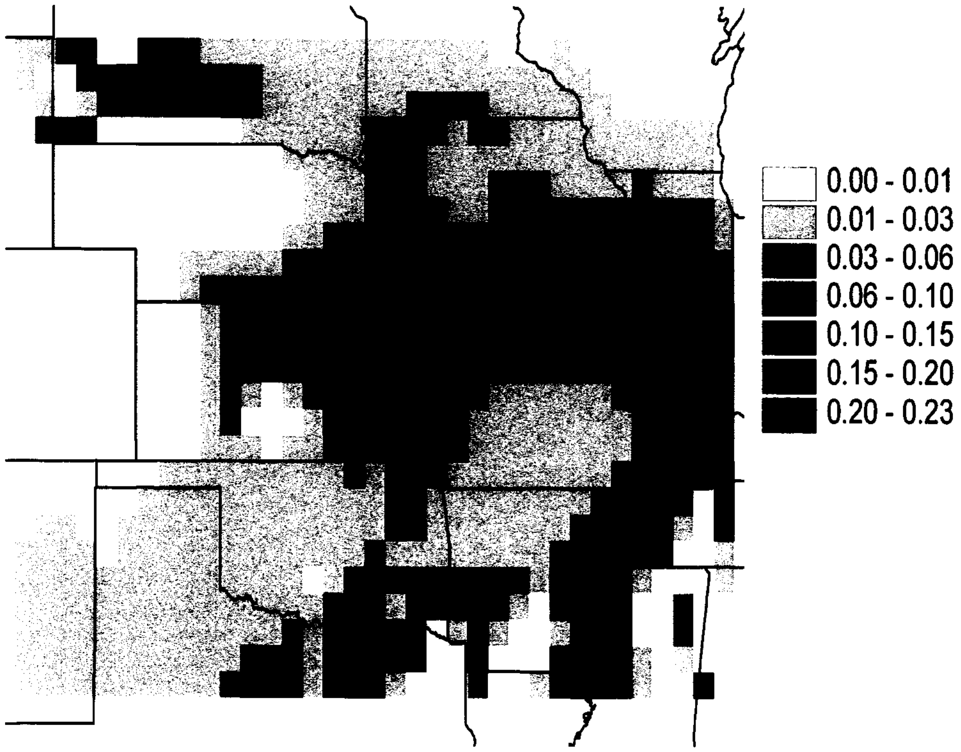

(b) difference with observed surface runoff ratios

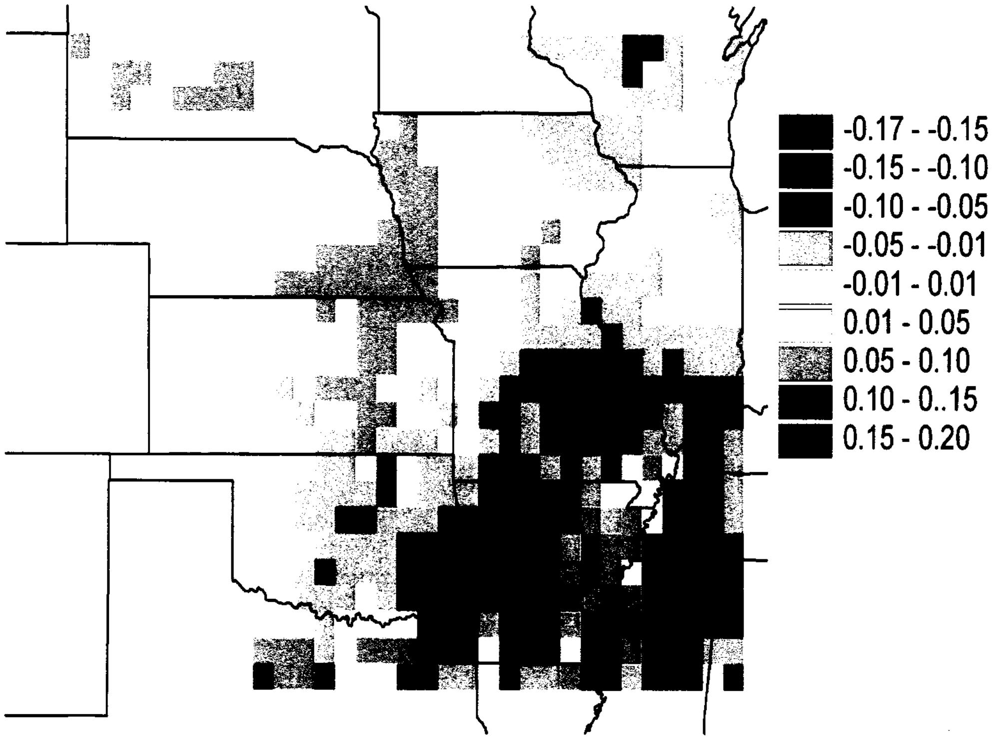

Figure 5.30. (a) Modeled average annual surface runoff ratios (1951-1980), and (b) their difference with observed surface runoff ratios based on interpolated storm flow.

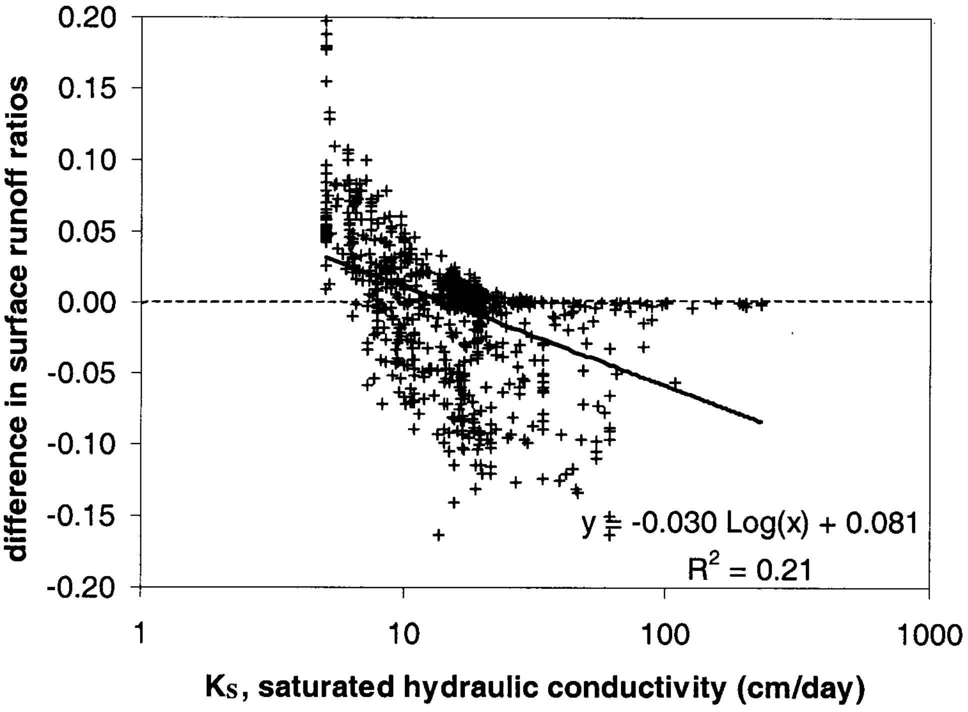

Figure 5.31. Saturated hydraulic conductivity in the root zone versus the difference in runoff ratios (Fig. 5.30).

Chapter 6: Results for the Interannual Variability of the Water Balance

6.1. Overview

The two components of the water balance for which there are the most widespread and longest-term measurements are precipitation and runoff. Precipitation is the main driver of the water balance, and so we begin this chapter by briefly examining the interannual variability in the VEMAP data. We compare it to the interannual variability predicted by the Poisson statistics and consider what the differences imply about the sources of the interannual variability of precipitation. We next examine how precipitation variability manifests itself in the model as interannual variability in growing-season soil moisture and green LAI. Model results are compared to the interannual variability of grassland productivity across the Great Plains. We also look at what the dataset of Buerman et al (2002) tells us about the interannual variability of LAI and its dependence on precipitation. The chapter concludes with a comparison of the interannual variability of modeled surface runoff and groundwater recharge with that of the observations of storm flow and base flow from Chapter 5. Because of the tendency of annual values of runoff to be highly skewed, we look at both the second and third moments in the form of coefficients of variation and skewness coefficients, respectively. Considerable analysis and discussion is devoted to ascertaining and understanding the structure in the data and the differences between the model results and observations.

In order to characterize the interannual variability of the water balance as completely as possible, we have extended the modeling period for this chapter an additional thirteen years (up to and including 1993, the last year in the VEMAP database) beyond the 30-yr period of Chapter 5. Inclusion of earlier years is restricted both by the lack of re-analysis data (from which wind speeds were derived) and the relative sparseness of the observations that form the basis of the VEMAP database.

6.2. Precipitation

Figure 6.1 depicts the coefficients of variation (CVs) in precipitation for January, July and the entire year in the VEMAP data over the 43-year period of analysis. While those precipitation data are what were used to drive the model, it is worthwhile for a number of reasons to compare the interannual variability in those data with the interannual variability implied by the Poisson stochastic model. Using the exponential distribution of the interarrival times of storms and the gamma distribution of storm depths, Eagleson (1978b) derives an analytical form for the cumulative distribution function (CDF) of annual precipitation. Eagleson (1978g) inputs precipitation sampled from such CDFs into his annual water balance equation to derive CDFs of annual runoff. Similarly, we could drive our monthly water balance model with monthly precipitation totals stochastically sampled from the corresponding CDFs. Such a process would be useful in the absence of long-term precipitation records or to investigate the impacts of climate change on the interannual variability of the water balance.

Using the results of Eagleson (1978b), the CV of precipitation in a given month can be written as

$$\mathrm{CV}[P] = \left(\frac{\left(1+\kappa^{-1}\right)}{m_v} \right)^{\frac{1}{2}} \tag{6.1}$$

where κ is a parameter of the gamma distribution of storm depth (see section 3.2), and m_v is the mean number of storms as given by (2.25). The CVs for January and July are shown in Figures 6.2a and 6.2b, respectively. Under the assumption of the Poisson model that the depths and interarrival times of storms are uncorrelated, precipitation totals should also be uncorrelated in time and the variance of annual precipitation is simply the sum of the variances of monthly precipitation. This gives for the CV of annual precipitation

$$\mathrm{CV}[P_A] = \left(\frac{\left(\sum_{i=1}^{12} \left(1+\kappa_i^{-1}\right) m_{v_i} m_{h_i}^{\,2} \right)^{\frac{1}{2}}}{\sum_{i=1}^{12} m_{v_i} m_{h_i}} \right) \tag{6.2}$$

where the index i represents months. Figure 6.2c depicts the results of the application of (6.2).

As illustrated by the ratios of the CVs calculated from the Poisson model to those from the VEMAP data (Figure 6.3), there are substantial differences between the two sets of numbers. Besides measurement and interpolation error, there are several other important potential sources for those differences. The first stems from the fact that the Poisson model is one of precipitation at a point, whereas the VEMAP data has been created as a spatial average over each grid cell. The interannual variability for a point within the cell should be higher than for the spatial average. Although this is seen to be the case for most cells in January and July, it is not for most cells at the annual level. Temporal correlation in monthly precipitation is one factor that increases the variability in annual precipitation. The Poisson model is essentially one of the high frequency, chaotic atmospheric dynamics that create precipitation, and therefore does not account for any long-term persistence. As long as precipitation from a single storm is assigned to a single month, any correlation in monthly precipitation must be attributed to low frequency dynamics. There are two principal sources for low frequency variability in precipitation: land-atmosphere feedbacks and ocean-atmosphere teleconnections. The GCM study of Koster et al. (2000) suggests that the former is more important for midlatitude, midcontinental regions. Land-atmosphere feedbacks might be accounted for by conditioning the statistics of the Poisson model on soil moisture, while ocean-atmosphere teleconnections might be accounted for by conditioning the statistics on indices of sea-surface temperature or atmospheric circulation (*e.g.*, Katz and Parlange 1993). Finally, one must recognize the potential for long-term climate trends to have increased the CVs of the VEMAP data. For example, Karl and Knight (1998) have shown that the increase in precipitation observed over most of the United States during the 20th century manifested itself mostly as increases in the size of large precipitation events. Such trends should translate to increases in both parameters of the gamma distribution of storm depth (*i.e.*, m_h and κ). The resulting impact on the CVs of monthly and annual precipitation is predicted by (6.1) and (6.2), respectively.

6.3. Growing-Season Soil Moisture

As both cause and consequence of each other, soil moisture and vegetation productivity are more tightly coupled than perhaps any two components of the water balance. The standard deviations in modeled soil moisture over three months of the growing season are plotted and compared to those in the observations in Figure 6.4 for the root zone, and in Figure 6.5 for the recharge zone. Overall, there is a tendency for the model to underestimate the variability in the observations. This is most directly the consequence of the observations being of a much smaller scale than the half-degree PRISM precipitation averages, which drive the model. There is also undoubtedly additional variance attributable to the low sampling frequencies and to measurement error. While we cannot make direct comparison of the magnitudes of the standard deviations in the observations and model results, we do see that, for the most part, the observations and model results share the same relative trends in space and time.

In the root zone, the growing season begins in April with the interannual variability in soil moisture looking very much like the interannual variability in winter and spring precipitation, particularly with regard to the "hotspot" over the south-central Great Plains. As soil moisture is depleted over the growing season, the hotspot disappears and the variability tends to increase in the humid half of the study area and decrease or stay the same in the dry half. In addition to low precipitation variability, the relatively low standard deviations in early spring in the humid regions are attributable to the fact that potential evapotranspiration is low and soil moisture is near field capacity (and, therefore, additional infiltration drains quickly.) The fact that the standard deviations decrease in the dry half shows that soil moisture there is typically drawn down to $\Psi_{uc.}$ In contrast, soil moisture in the humid half is more variable at the end of the growing season because productivity in typical years is not water limited.

Owing to the damping of climate variability with depth, the distribution of the standard deviations in recharge-zone soil moisture mirrors the distribution in the interannual variability of annual—more than winter-spring—precipitation. The damping with depth, along with the greater moisture holding capacity of the recharge zone, also explains the considerable lower standard deviations in that zone as compared to the root zone. Across the study area, the standard deviations in modeled recharge-zone soil moisture decrease with the means as the growing season progresses. This is likely due to the transitioning of the exchange between the root and recharge zone from relatively large flows from the root to recharge zone to relatively small flows from the recharge to root zone. With exception of most of the Illinois sites, the decreasing trend is also found in the observations. For the Illinois sites, the standard deviations initially decrease slightly from April to June, but then increase from June to August. This is suggestive of interactions with a groundwater table; in spring when the table is high, it helps damp the variability in soil moisture, while having less impact when it is lower at the end of summer.

6.4. Green Leaf Area Index

In Section 5.2 we saw that the annual maximization of green LAI by the model did a reasonable job of capturing large-scale patterns in observed mean LAI and ANPP. Here we consider the interannual variability of those quantities. Of the grassland studies incorporated into the NPP database of Zheng et al. (2003b), only Sala et al. (1988) take a look at interannual variability. In addition to estimates of average ANPP, the NRCS database contains estimates for "favorable" and "unfavorable" years, which are defined respectively as the wettest 10% and driest 10% of the precipitation record. For each of their MLRA units, Sala et al. (1988) calculate a measure of ANPP variability as the difference between the favorable- and unfavorable-year ANPPs divided by the average ANPP. Their plot of interpolated isopleths of that quantity is reproduced as Figure 6.6. The wedged-shaped area of high variability (as defined by the 0.9 isopleth) that extends into the central Great Plains corresponds exactly to the hotspot of interannual variability in modeled spring root-zone soil moisture (see Figure 6.4). Sala et al. (1988) identify this as a particularly drought prone region of the Great Plains. While the dependence of observed ANPP on the interannual availability of soil moisture is strong, there is another pattern evident: a trend (overlain on top of the hot spot) of decreasing variability with increasing mean ANPP. That trend could be explained by the fact that with greater average ANPP, light and nutrients become more limiting during wetter years.

For comparison to Figure 6.6, we approximated the 5th/95th percentiles of the model-maximized peak green LAI as the average of the smallest/largest four values in the 43-year model run. In Figure 6.7, the mean peak green LAI is plotted against the above variability calculation for each of the grid cells. Up to an average peak green LAI of four, the variability measure is almost exclusively between 0.9 and 1.0, indicating that the four highest and lowest values typically bump up against the bounds of +/-50% of the average. At and above an average of four, the upper bound becomes the absolute maximum of six, and that bound and the lower bound of –50% of the average effectively determine the variability measure. Thus, above an average peak green LAI of four, the model bounds very roughly reproduce the observed decreasing variability in ANPP with increasing mean. As a whole, though, Figure 6.7 suggests that the model bounds result in an overestimate of the interannual variability of vegetation density over most of the study area. We can get a better picture of the variability in the model from the CVs of maximized green LAI (Figure 6.8). The hotspot of summer and annual precipitation variability over Kansas (see Figure 6.1) has clearly been translated to an area of relatively high LAI variability. We can also see how the upper bound of six results in reduced variance in areas of average peak green LAI of four or more.

Because the NDVI-based LAI estimates of Buerman et al. (2002) are not long enough to make a meaningful comparison of their interannual variability to the interannual variability of LAI in the full 43-year model run, we isolated the ten years of overlap from the longer model run. Figure 6.9 depicts the CVs in model-maximized green LAI and in the observations for the month of July (*i.e.*, the average month in which the peak is reached) over the period of 1981 to 1990. Other than a similar range, the two plots show little in common. For example, the model results show the greatest variability in the humid half of the study area, whereas the observations show the least amount there. Given the uncertainties associated with the LAI observations discussed in Section 3.3.2, we cannot read too much into the lack of correspondence between to the two plots in Figure 6.9. Nonetheless, it is worth looking into how much the observations tell us of the dependence of LAI variability on precipitation variability. Figure 6.10 shows the CVs of the total of January-July precipitation from 1981 to 1990. The correlation coefficients between the January-July precipitation and the July LAI observations are depicted in Figure 6.11. With a sample size of only 10, the confidence limits are wide, and so only values outside the range of –0.4 to 0.4 are shown. Over most of the grasslands region the correlation coefficients are greater than 0.5. Over most of the rest of the study area, values are scattered both positive and negative. The exception is over the region of high crop density centered on west central Iowa (see Figure 3.18), where the correlation is significantly negative. In their discussion of the interannual variability of crop production in Iowa, Prince et al. (2001) note that two of the lowest levels of NPP occurred during a year with a very wet spring and one with summer flooding. Therefore, the negative correlation in that area may indeed be a real phenomenon. In general, the lack of significant positive correlation over cropped areas highlights the importance of management factors, such as fertilization and irrigation, and climatic factors other than the availability of soil moisture. The correlation results over the humid half of the study region—along with the related fact that the CVs of observed LAI are generally low—suggest that it may be more appropriate to hold LAI at fixed values for crops and other vegetation for which water limitation is relatively unimportant on an interannual basis. The effect of doing so for the entire study area is examined in Section 7.2.

6.5. Annual Runoff

Figure 6.12 depicts the CVs in modeled total runoff, surface runoff and groundwater recharge, along with the interpolated CVs in observed total streamflow, storm flow and base flow. In both the modeled and observed plots, the CVs for total runoff/streamflow and groundwater recharge/base flow follow a pattern similar to that for the standard deviations of recharge-zone soil moisture (see Figure 6.5)—namely, increasing variability heading west with local maximums midway across the Great Plains. That is not surprising given the direct dependence of groundwater recharge on recharge-zone soil moisture (see eqtn. 2.10) and the predominance of groundwater recharge in total runoff (see Figure 5.27).

The correlation between the variability in recharge-zone soil moisture and in annual precipitation leads to the question of how much of the interannual variation in runoff can be explained by the interannual variation in precipitation. The CVs of annual precipitation are plotted against the CVs of modeled total runoff in Figure 6.13a and for observed streamflow in Figure 6.13b. Interestingly, the former explains about the same amount of the latter for both the model results and observations. This then leads to the question of how does the variability in modeled runoff compare to the variability in the observations. The CVs of modeled annual total runoff are plotted against the interpolated CVs of observed streamflow in Figure 6.14a. Based on the linear regressions in Figures 6.13b and 6.14a, the CVs of modeled total runoff are a somewhat worse predictor (R^2=0.28) of the CVs of observed streamflow than are the CVs of annual precipitation

(R^2=0.38). Of course the advantage of the model is that it transforms the precipitation variability into runoff variability through a representation of the physics. From that standpoint, the mean of the CVs of modeled total runoff (=0.68) closely matches that for observed total streamflow (=0.71).

We can begin to understand the sources of the error in modeling the interannual variability of runoff through a comparison of the CVs of modeled surface runoff and groundwater recharge with those of observed storm flow and base flow (see Figures 6.14b and 6.14c). The CVs of modeled surface runoff almost universally underestimate the CVs in the observations of storm flow. This is most likely the consequence of the spatial and temporal lumping of the model. For one, the model leads to underestimating the variance because we are only calculating the expected value of surface runoff; the same amount of monthly precipitation falling on the same antecedent moisture conditions will generate varying amounts of surface runoff owing to differences in the temporal structure of the storms. Additional variance is lost because the precipitation values used are averages across a half-degree grid cell; because that precipitation is distributed unevenly within the grid cell, it generates a wide distribution of point values of precipitation. The subgrid variability in soil hydraulic properties and antecedent moisture conditions adds to the variability in the amount of surface runoff that a single value of grid-cell average precipitation can generate.

The underestimation of the CVs of storm flow is offset by a tendency to overestimate the CVs of base flow (see Figure 6.14c). Scale issues are certainly important here as well, although probably much less significant as groundwater recharge is not directly dependent on storm events and the recharge zone has longer memory than the root zone. Rather, the tendency of the model to overestimate the CVs of base flow is most likely the result of the model not accounting for the effect of groundwater storage, which has even longer memory. Groundwater storage reduces the interannual variability in base flow by increasing in wet years and decreasing in dry years. That this damping of variability can be significant is seen in the fact that for the cells over the Sand Hills, where much of the recharge is to the deep Ogallala Aquifer, the CVs of modeled recharge are about two to six times the CVs of observed base flow. Given the long memory of the recharge zone, the CVs of modeled groundwater recharge in most cases could be made to match the CVs of observed base flow through grid-cell-specific calibration of the depth of the recharge zone.

More general to issues of subgrid variability and groundwater storage, accurate modeling of the interannual variability of streamflow requires correctly partitioning total runoff between surface runoff and groundwater recharge, as the former tends to be much more variable than the latter. Furthermore, the standard deviations of each component are strongly correlated to the mean of the component. In Figure 6.15, the means of surface and groundwater runoff are plotted against the respective standard deviations for both the model results and observed streamflow. The superposition of the regressions for the model results on the observations indicates the tendency of the model to underestimate the variability of storm flow and to overestimate the variability of base flow while still preserving the structure in the observations. For both the model results and observations, there is a strong linear dependence of the standard deviation of surface runoff on the mean. Both plots possess similar slopes, which indicate a decreasing CV with increasing mean. Likewise, in the second two plots, we see that the model reproduces the tendency in the observations for the CV of groundwater runoff to decrease with increasing mean above an annual mean of about one cm. Below one cm, there are not enough observations to indicate whether the peak in the CV between one and ten cm in the model results is a real-world phenomenon. However, the interpolations of the observations in Figure 6.12f suggest that it is.

Because frequency distributions of runoff tend to be highly skewed at many scales, we are also interested in comparing the third moments in modeled and observed runoff. Figure 6.16 depicts the skewness coefficients (Gs) in modeled total runoff, surface runoff and groundwater recharge, along with the interpolated Gs in observed total streamflow, storm flow and base flow. Because the sample size is only 43 in the model results and an average of 44 in the observations, the 95% confidence limits on the population Gs average about +/-0.8 of the sample Gs. Nonetheless, somewhat similar large-scale patterns are evident in the model results as compared to the observations. The degree of grid-cell level correspondence between modeled and observed Gs is similar to that for the CVs, with the modeled values tending to be lower than the observations for total runoff and groundwater runoff, and higher for surface runoff (see Figure 6.17).

Likewise we see a strong dependence of the Gs on the CVs in both the model results and observations (Figure 6.18). Surprisingly the model appears to overestimate the G for a given CV for both storm flow and base flow. Thus, the overestimation of the Gs in storm flow in Figure 6.17b is offset by the tendency to underestimate the CVs, and the tendency to overestimate the Gs in base flow in Figure 6.17c is added to the tendency to overestimate the CVs.

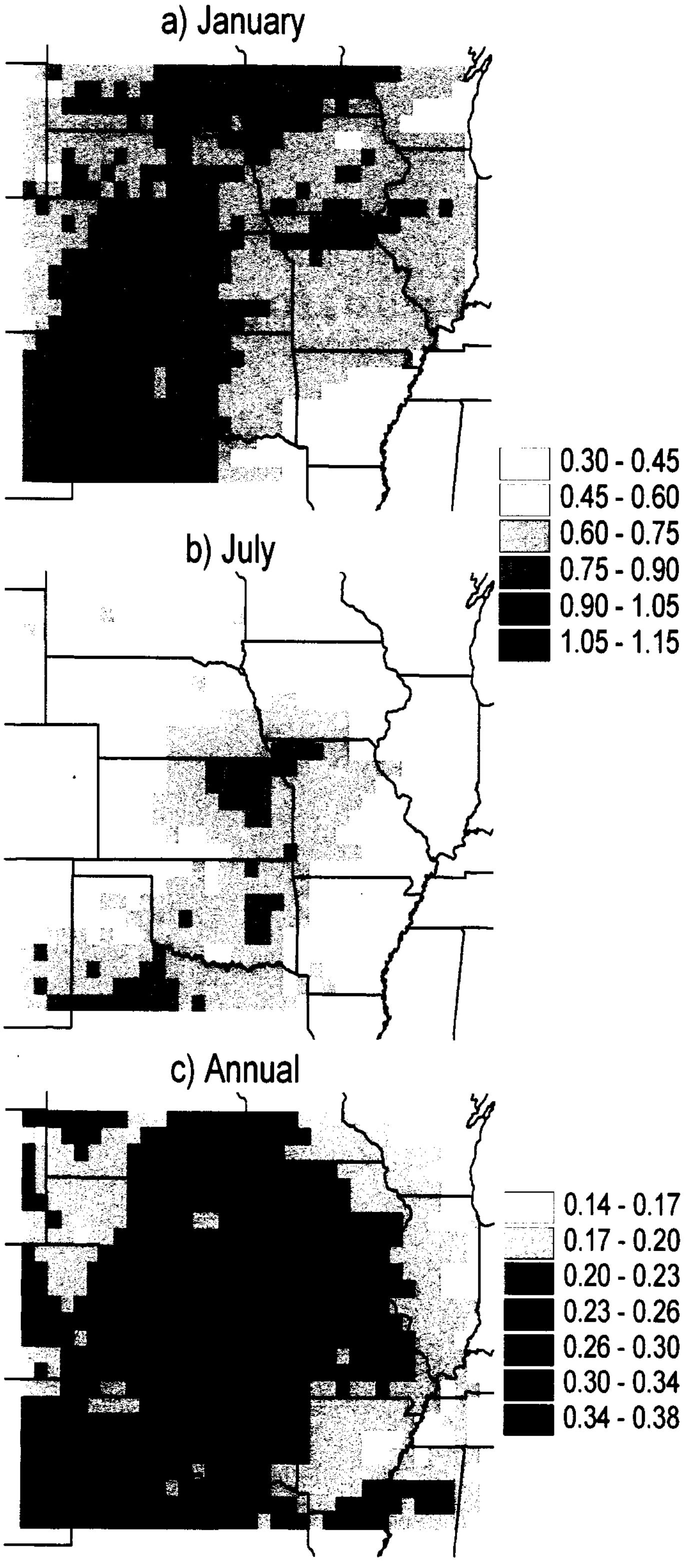

Figure 6.1. The coefficients of variation in the VEMAP precipitation data (1951-1993): (a) January, (b) July and (c) annual.

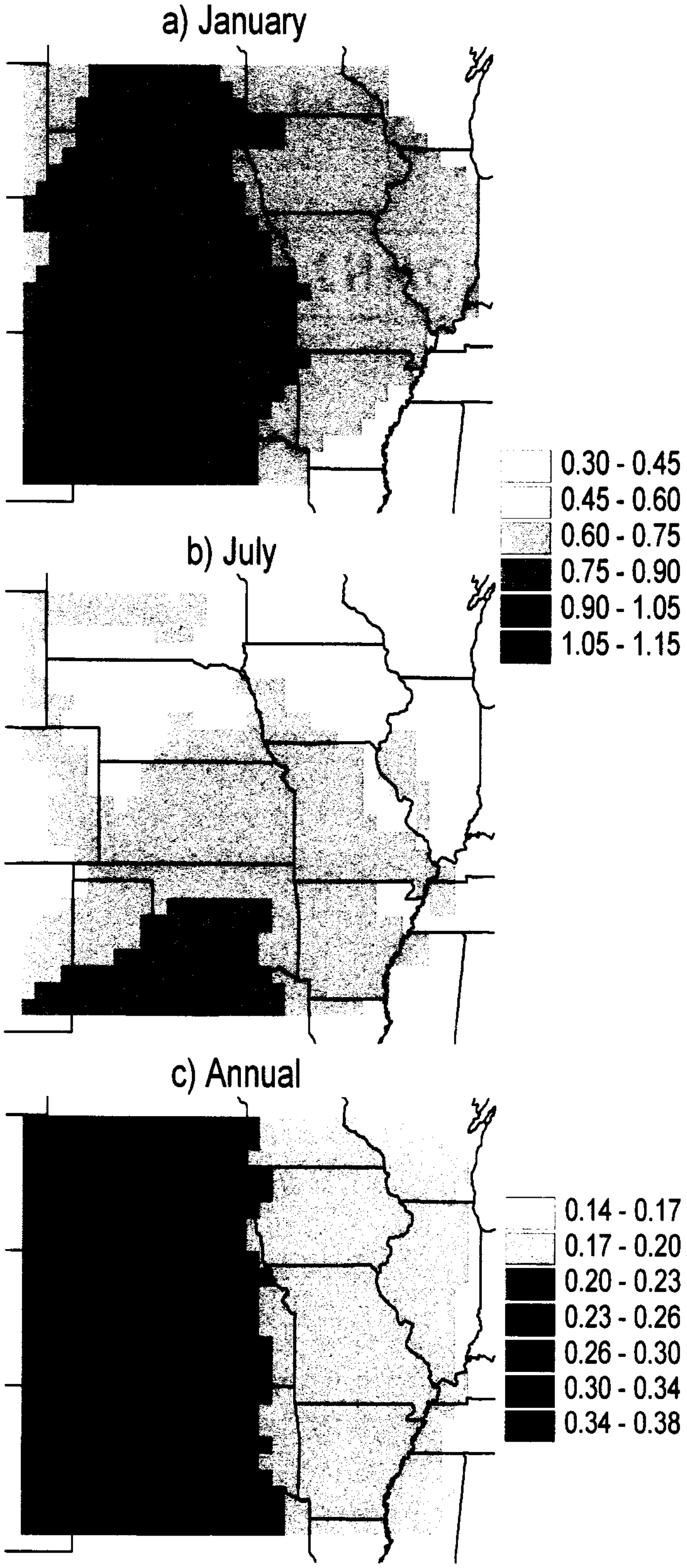

Figure 6.2. Coefficients of variation in point precipitation implied by the Poisson model: (a) January, (b) July and (c) annual.

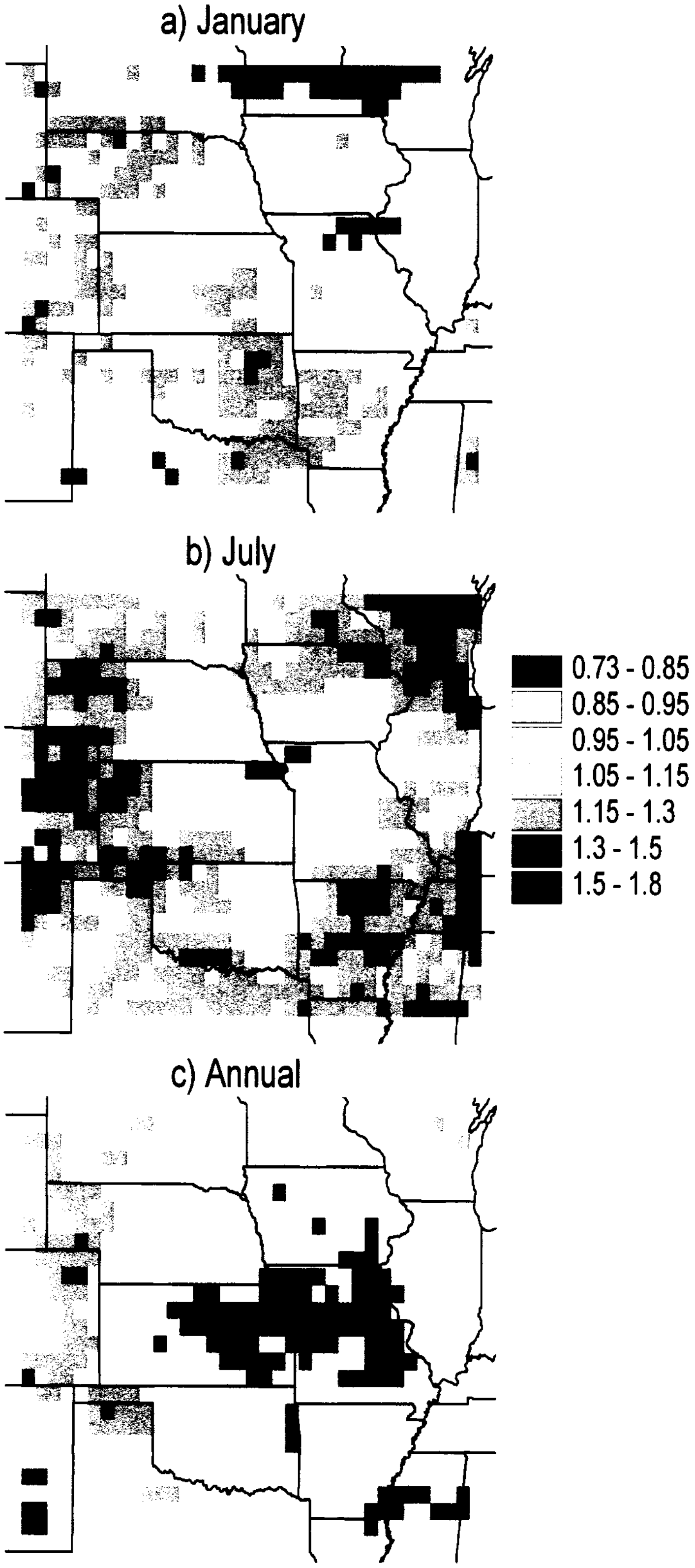

Figure 6.3. The ratio of the coefficients of variation from the Poisson model (Fig. 6.3) to those from the VEMAP data (Fig. 6.2): (a) January, (b) July and (c) annual.

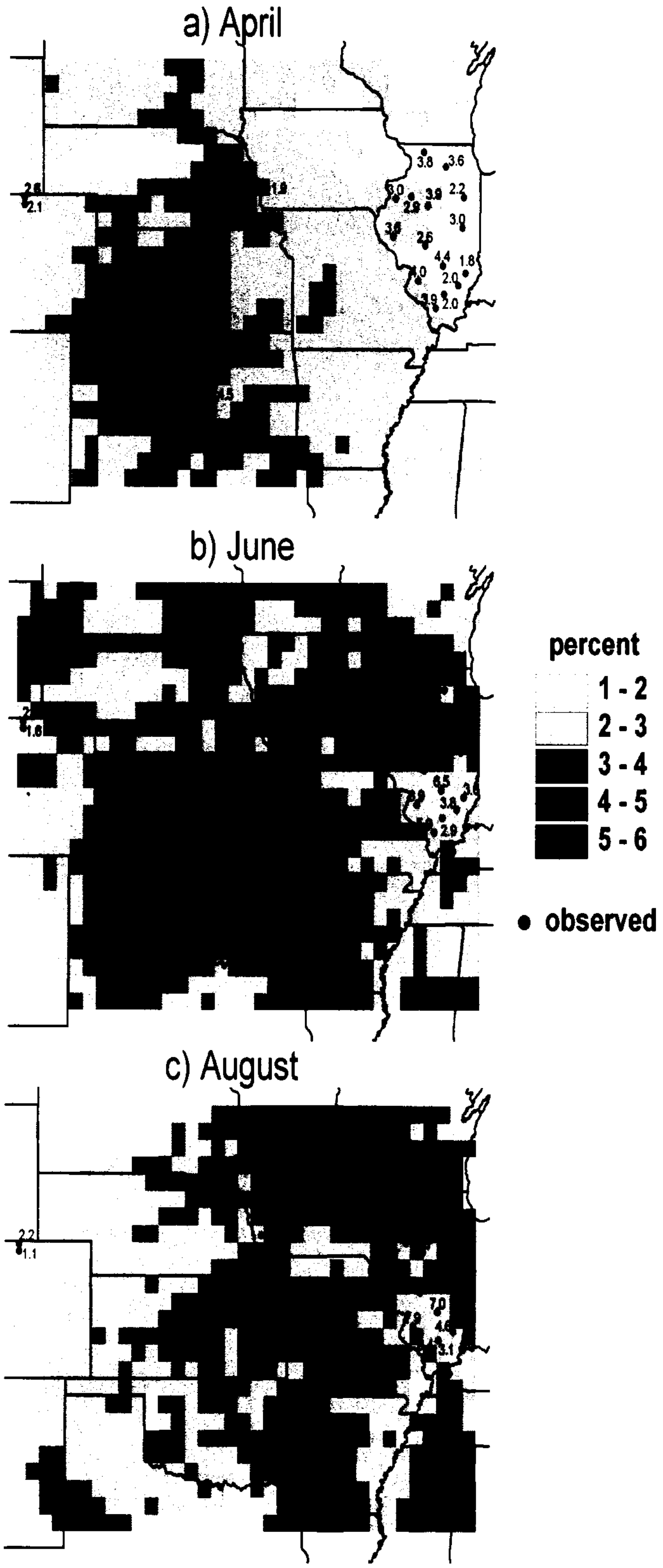

Figure 6.4. Standard deviations in modeled root-zone volumetric moisture content (1951-1993): (a) April, (b) June and (c) August. Because of small sample sizes, observations are averages of the given, previous and next month.

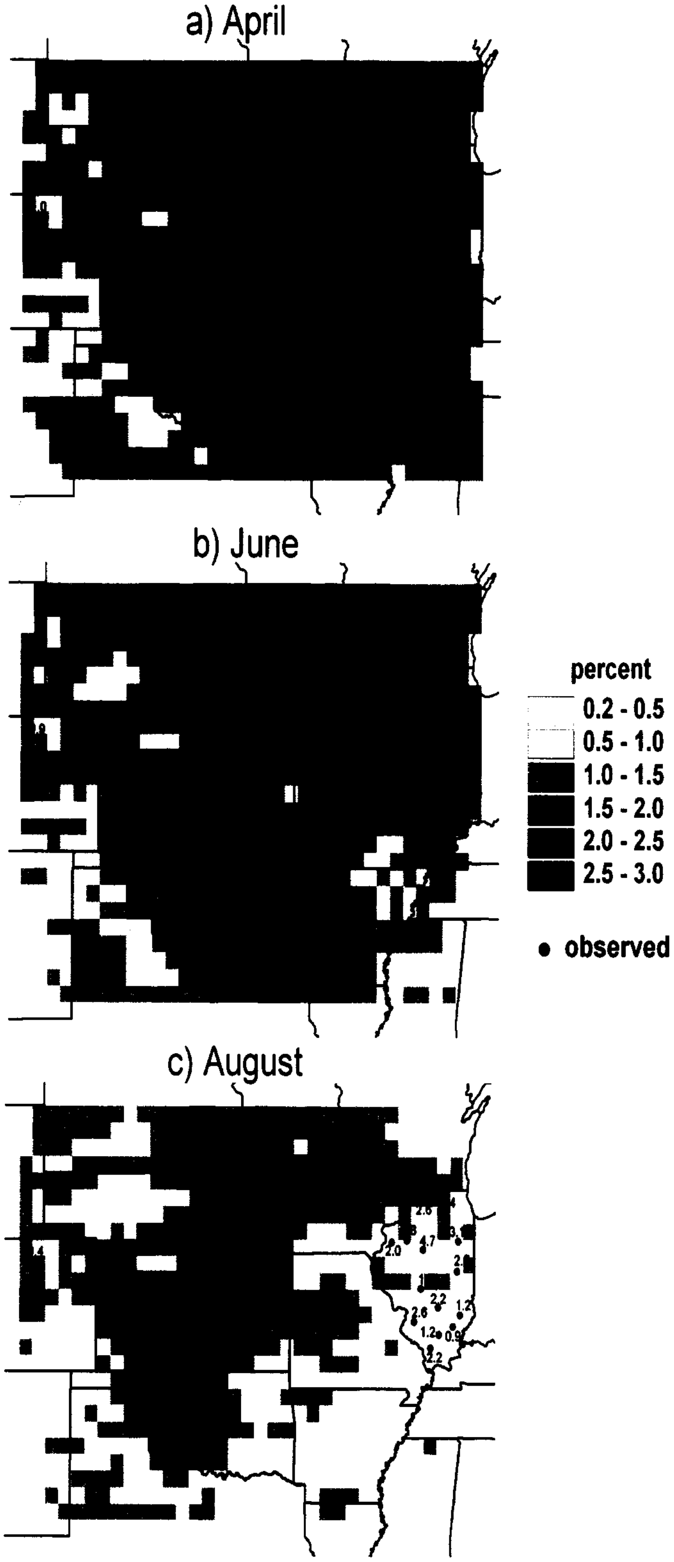

Figure 6.5. Standard deviations in modeled recharge-zone volumetric moisture content (1951-1993) for (a) April, (b) June and (c) August. Because of small sample sizes, observations are averages of the given, previous and next month.

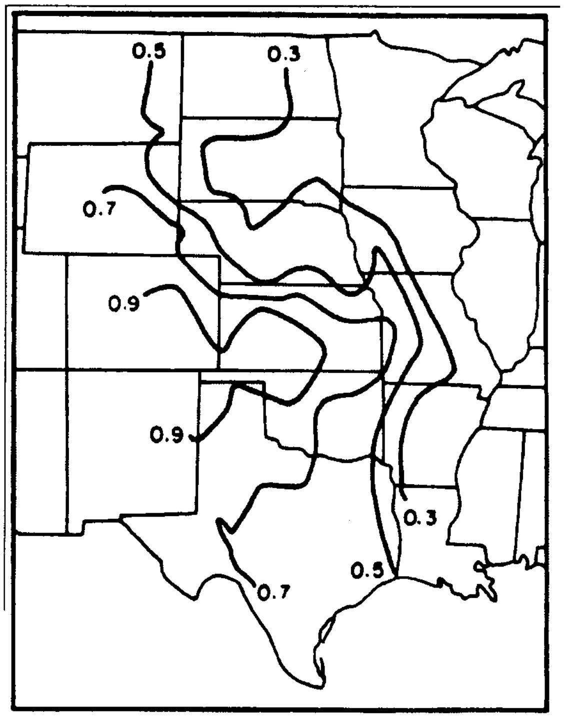

Figure 6.6. Variability of grassland ANPP over the Great Plains, as defined by: (ANNP during wettest 10% of years-ANPP during driest 10% of years)/average ANPP. Reproduced from Sala et al. (1988).

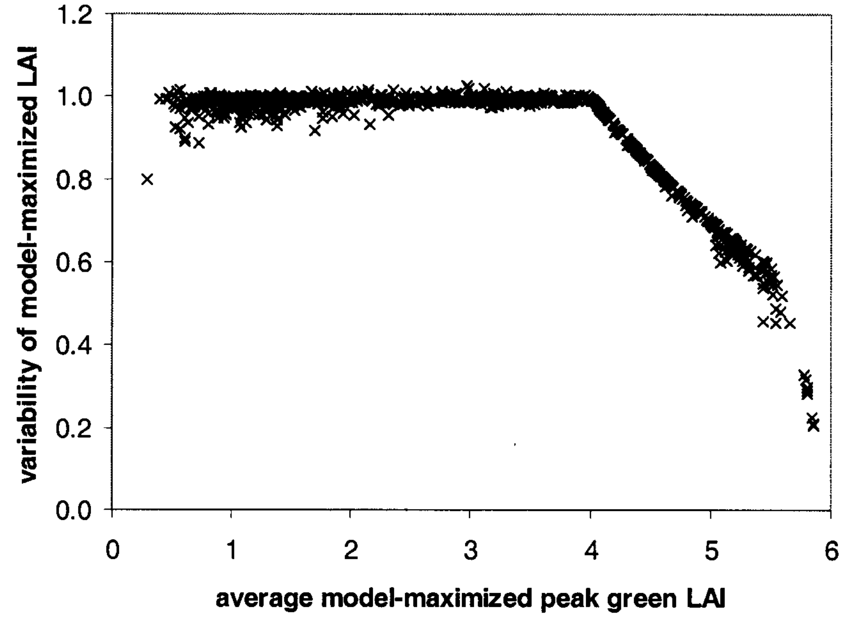

Figure 6.7. Variability of green LAI (as calculated in analogy to the definition of variability in Fig. 6.6) in model results as a function of average maximized peak green LAI (1951-1993).

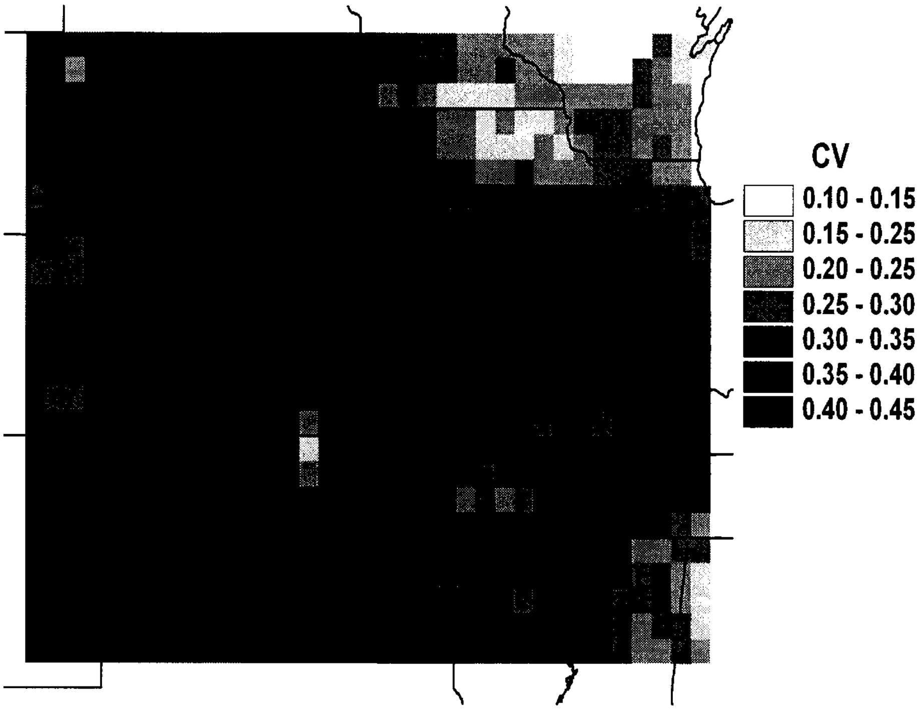

Figure 6.8. Coefficients of variation for model-maximized green LAI (1951-1993).

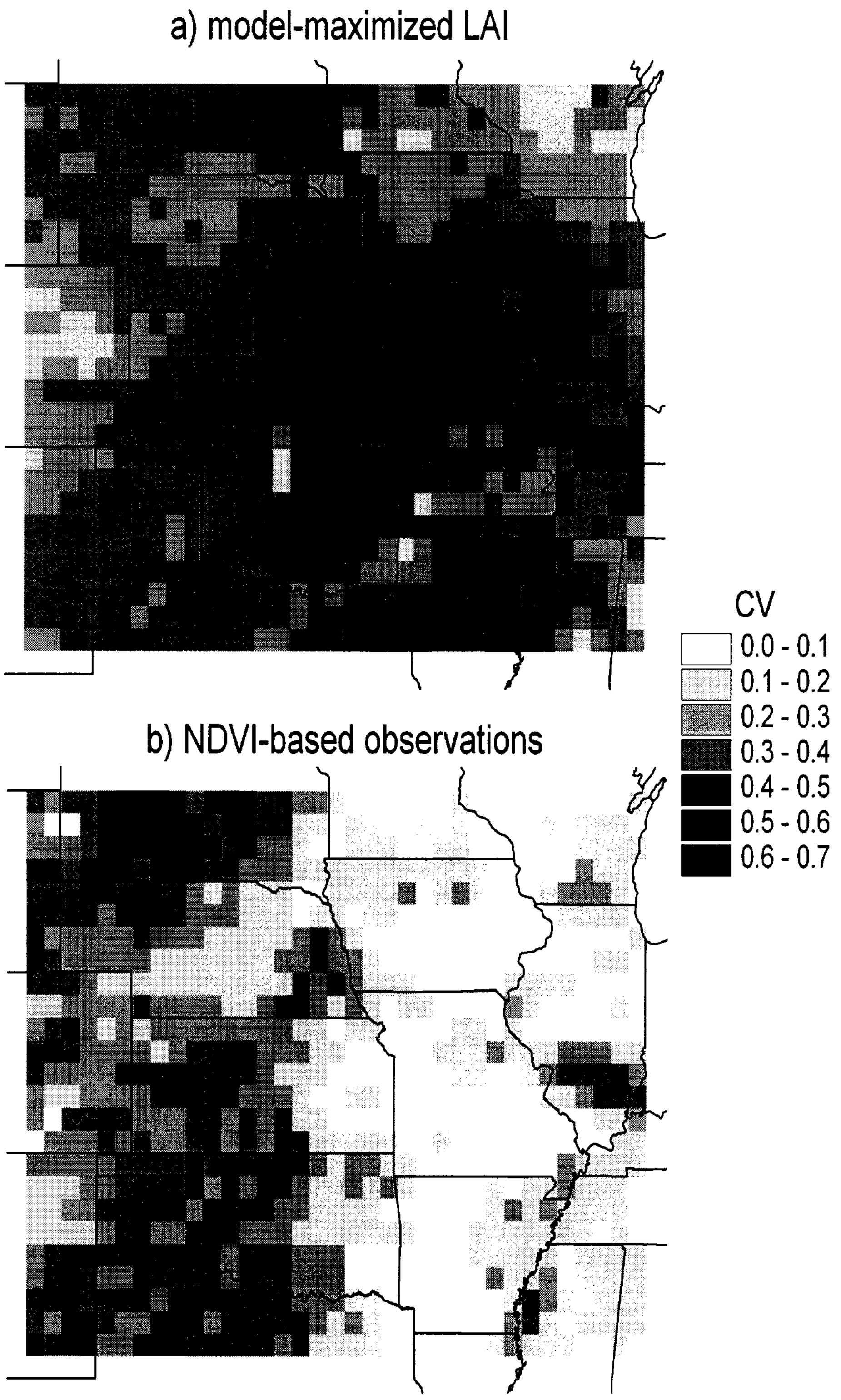

Figure 6.9. Coefficients of variation for: (a) model-maximized green LAI, and (b) the NDVI-based estimates of July green LAI from the dataset of Buerman et al. (2002), from 1981 to1990.

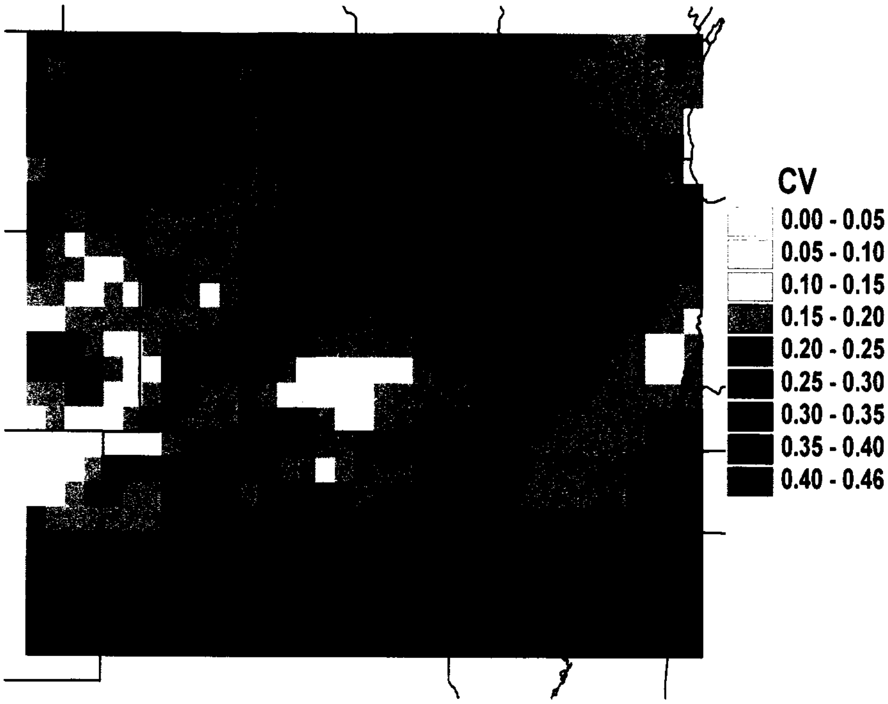

Figure 6.10. Coefficients of variation in January-July precipitation from 1981 to 1990.

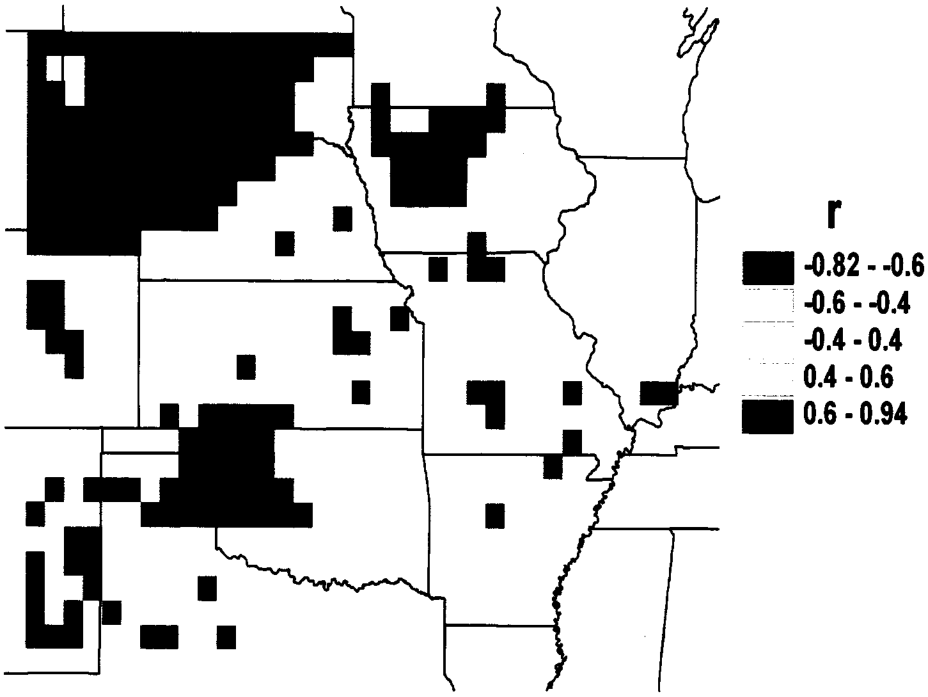

Figure 6.11. Correlation between January-July precipitation and July LAI from the dataset of Buerman et al. (2002) from 1981 to 1990.

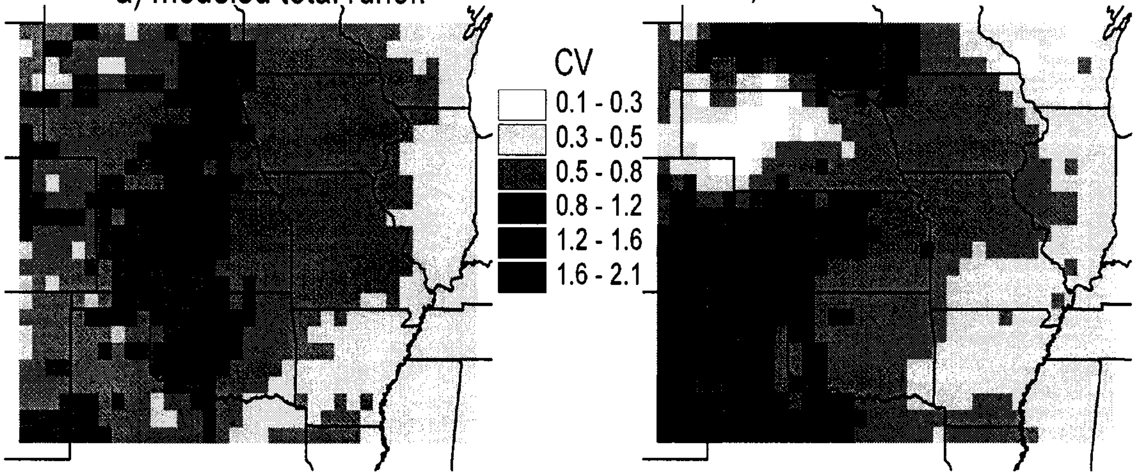
a) modeled total runoff

b) observed streamflow

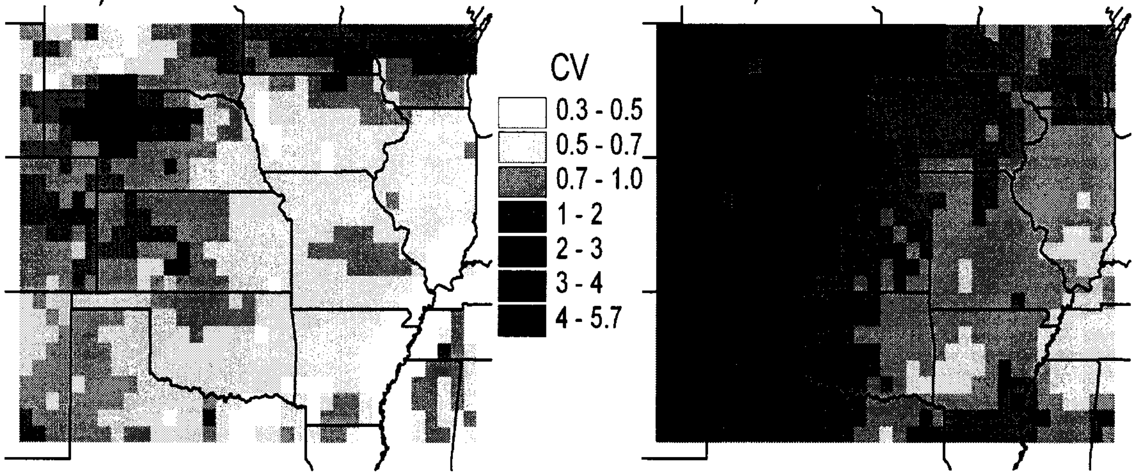
c) modeled surface runoff

d) observed storm flow

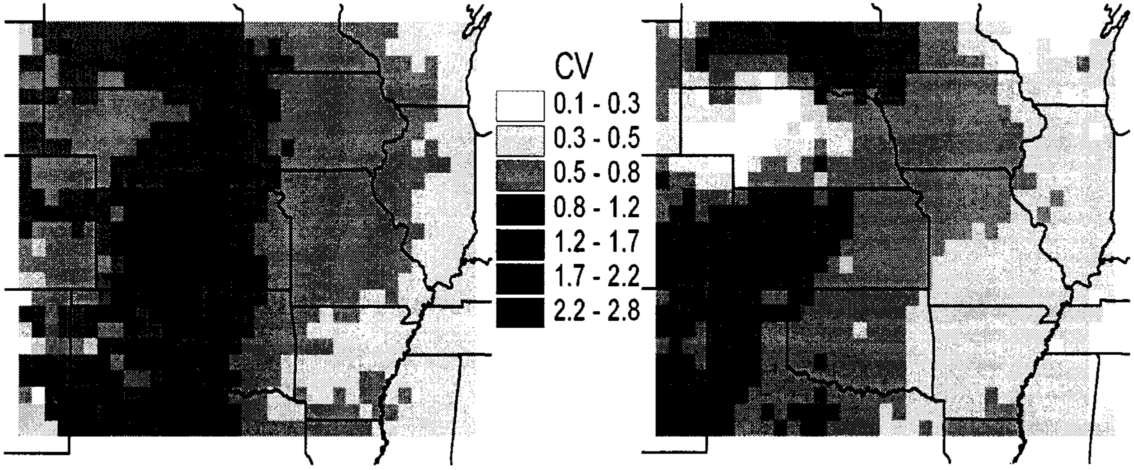
e) modeled groundwater recharge

f) observed base flow

Figure 6.12. Coefficients of variation for modeled runoff (1951-1993) and observed streamflow.

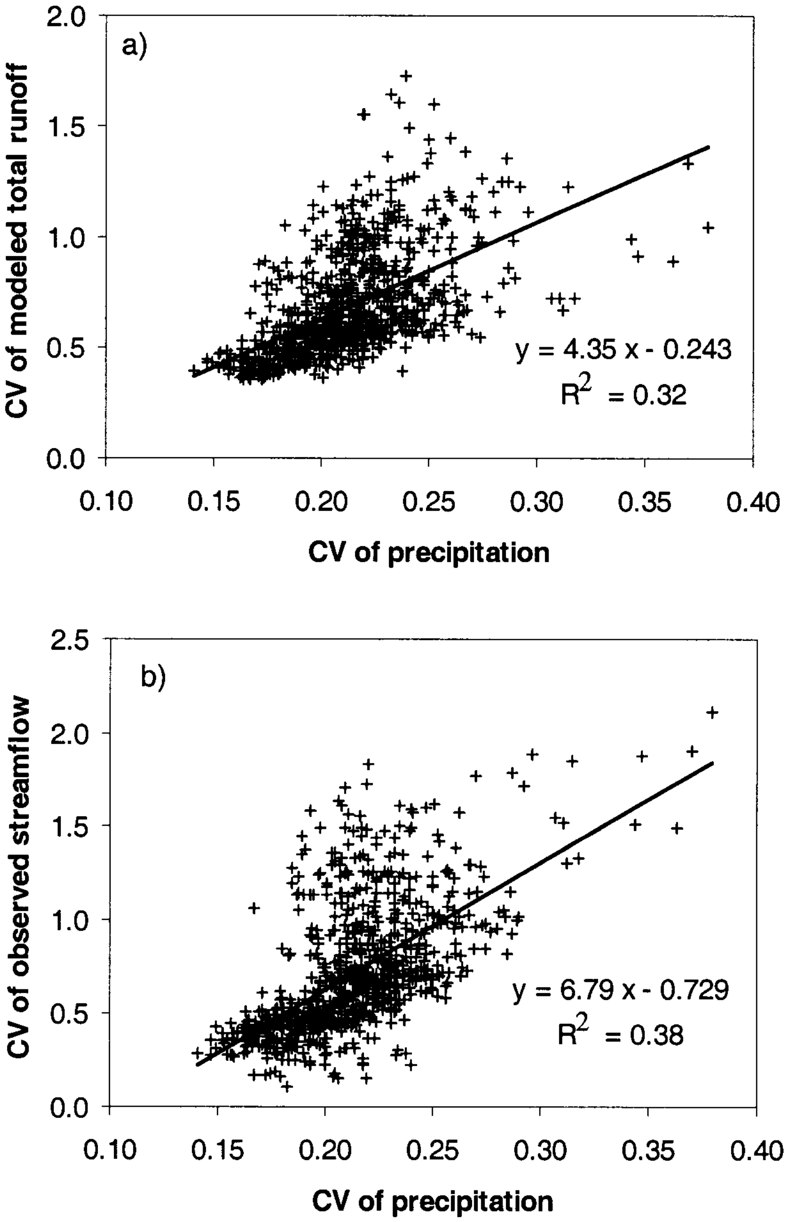

Figure 6.13. Coefficients of variation of annual precipitation (Fig. 6.1) versus the coefficients of variation: (a) modeled total runoff (Fig. 6.12a), and (b) observed streamflow (Fig. 6.12b).

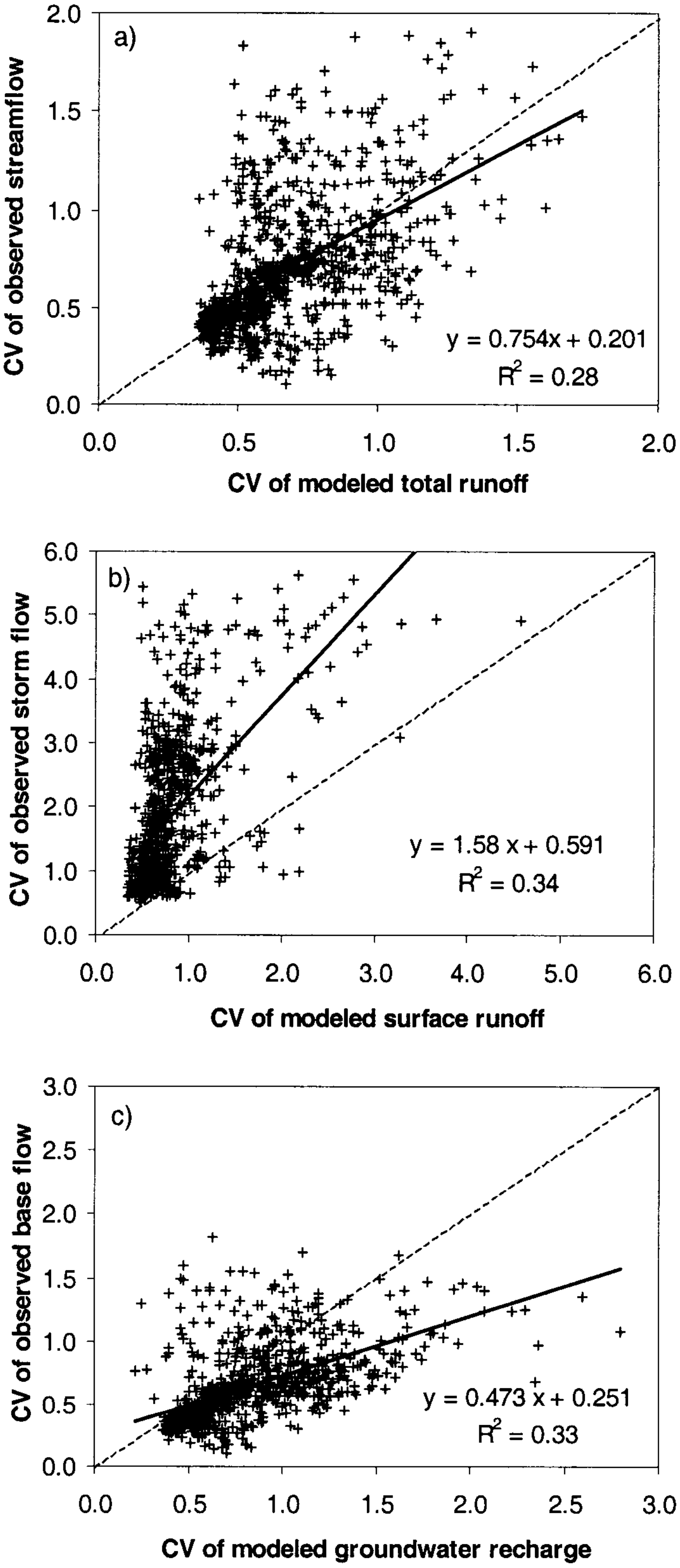

Figure 6.14. The coefficients of variation for modeled runoff versus those of observed streamflow (Fig. 6.12).

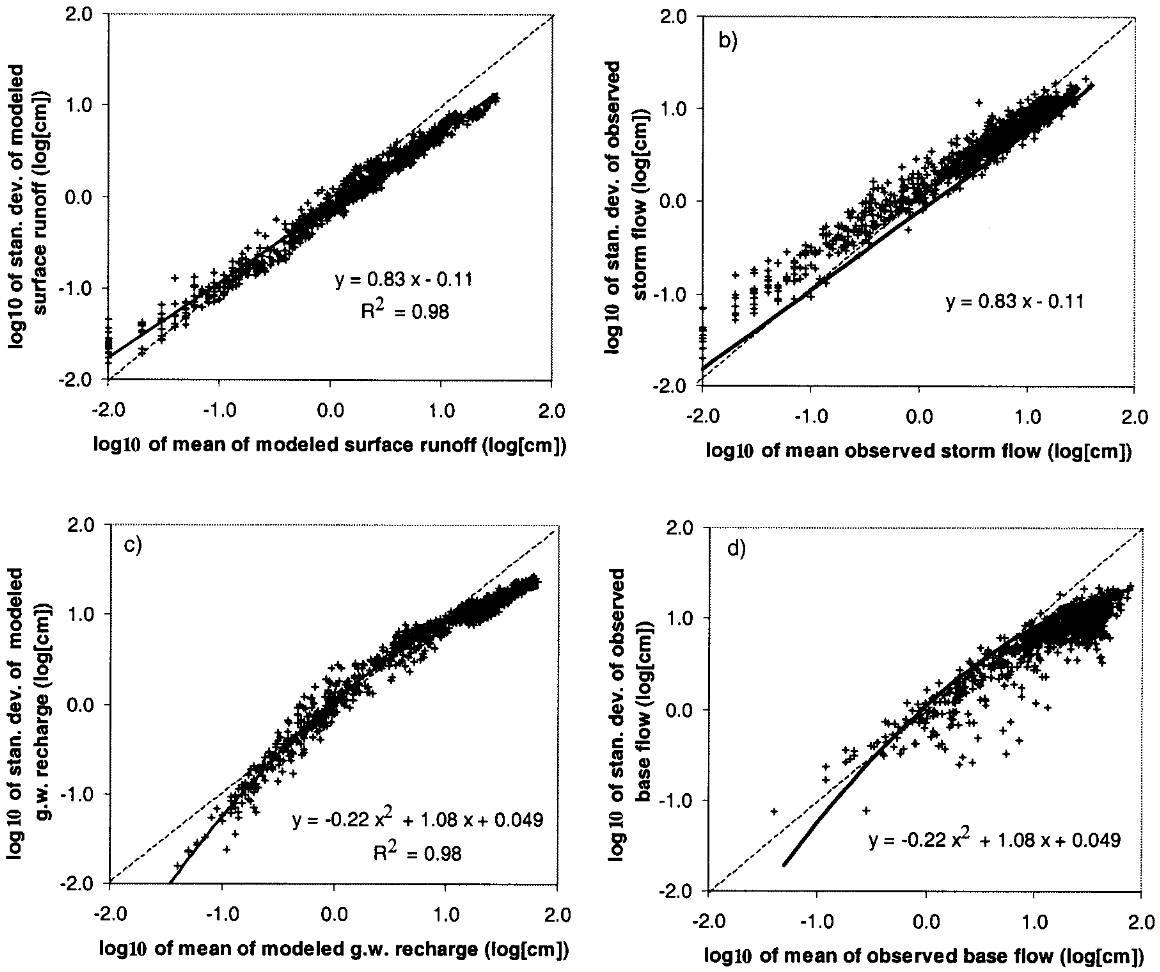

Figure 6.15. The relationships between the means and standard deviations: (a) modeled surface runoff, (b) observed storm flow, (c) modeled groundwater recharge, and (d) observed base flow. The modeled values are for 872 grid cells. The observed values are for 932 gauging stations (as opposed to the interpolated values). The regression results for the modeled values are superposed on top of the observed values. Dashed lines represent a coefficient of variation of one.

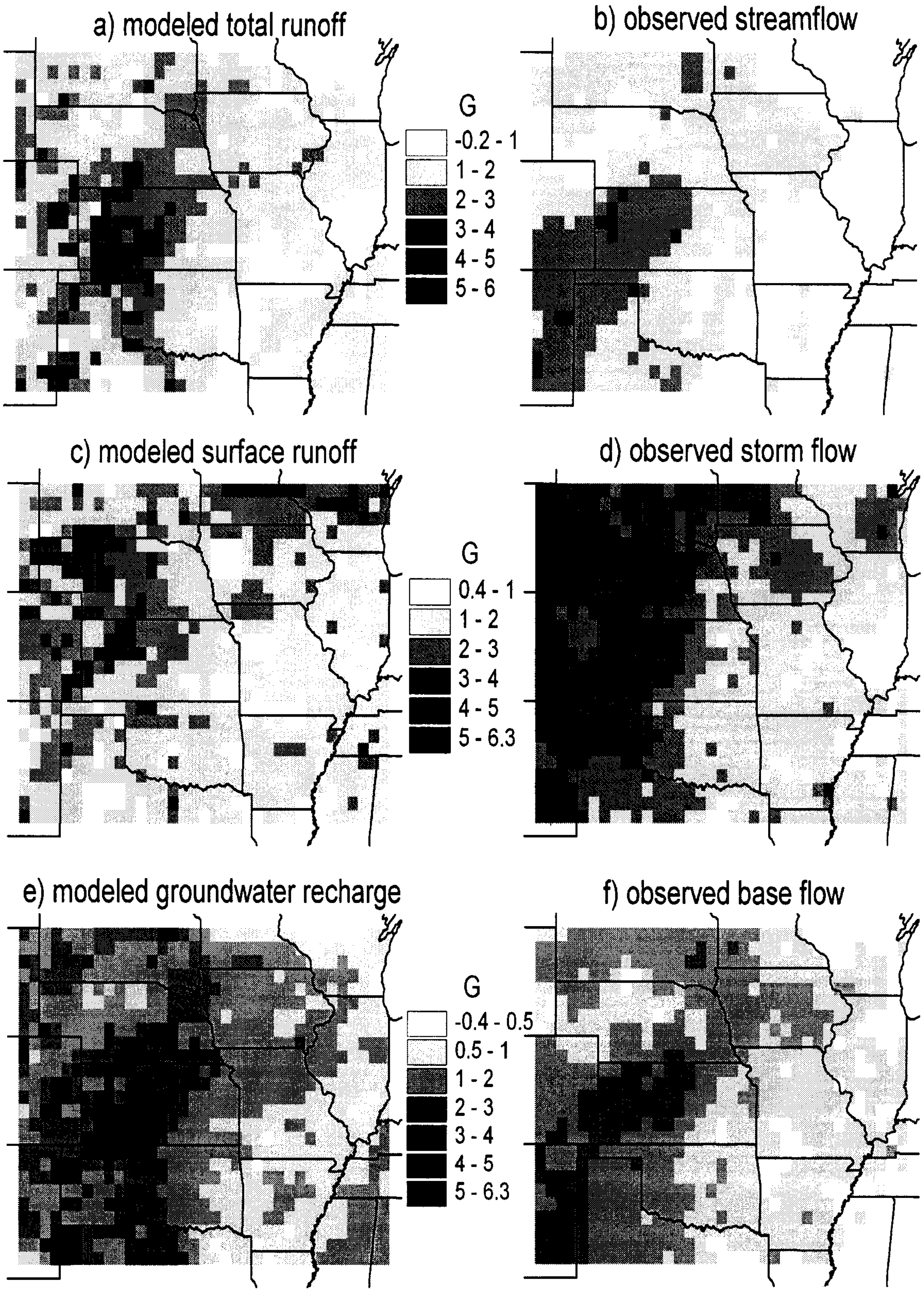

Figure 6.16. Skewness coefficients for modeled annual runoff (1951-1993) and observed annual streamflow.

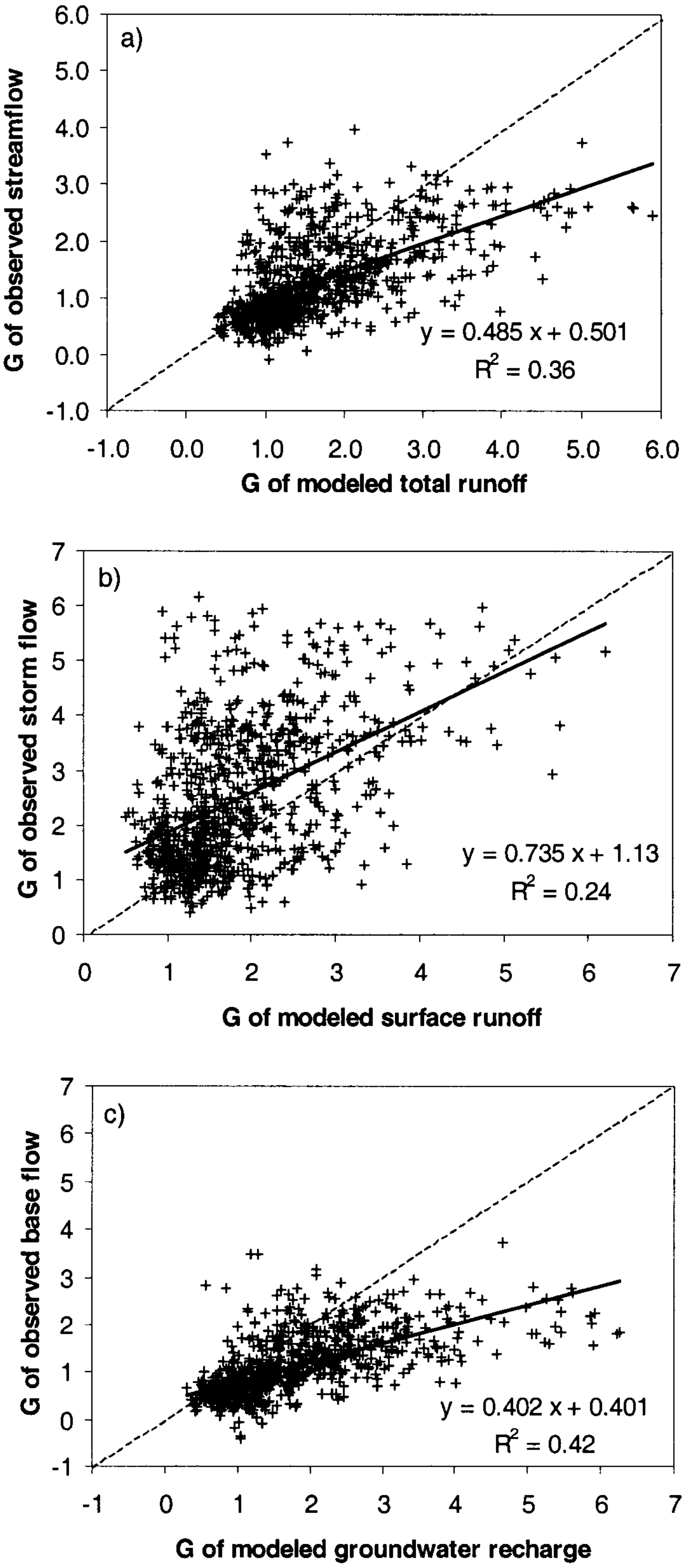

Figure 6.17. The skewness coefficients for modeled annual runoff versus those for observed annual streamflow (Fig. 6.16).

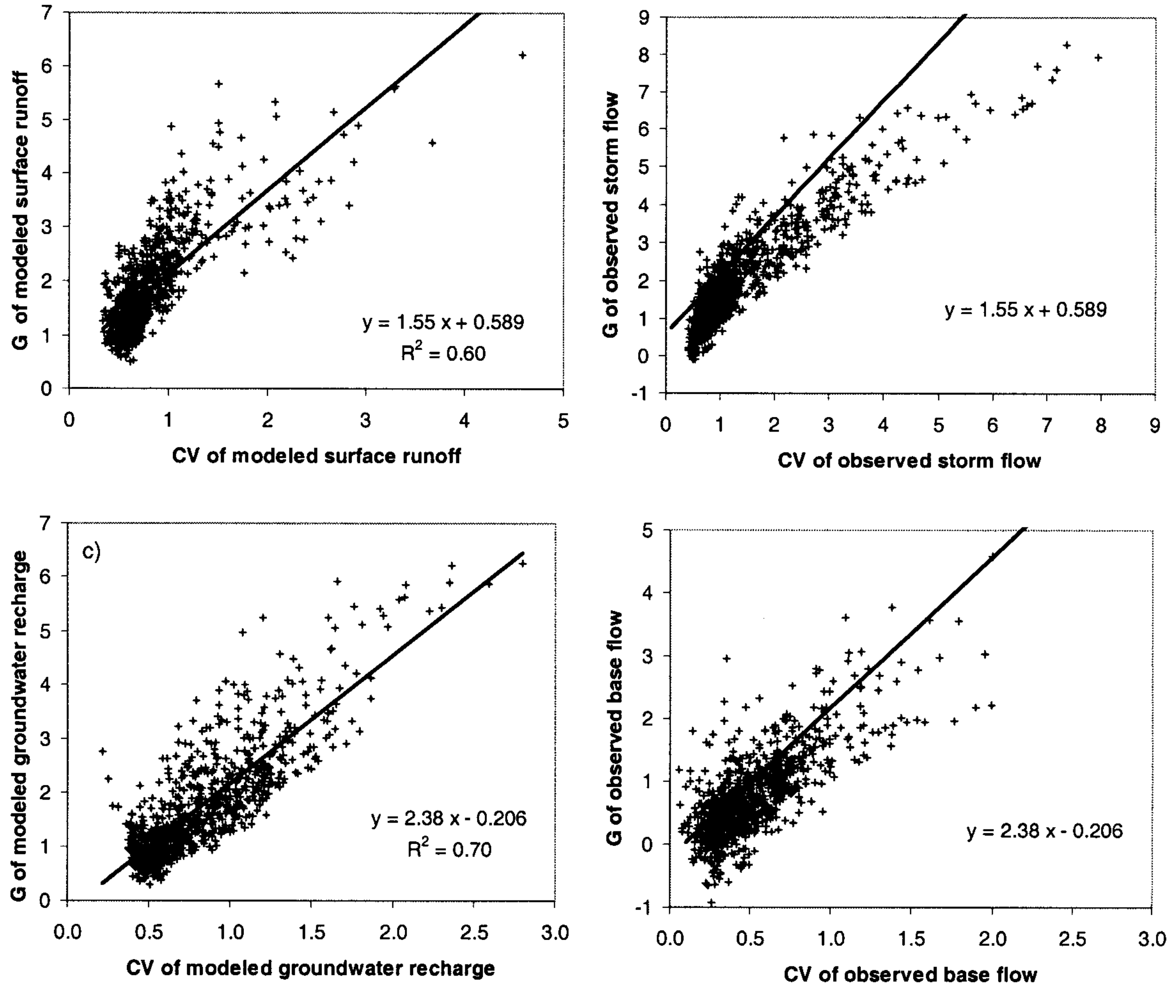

Figure 6.18. The relationships between the coefficients of variation (Fig. 6.12) and the skewness coefficients (Fig. 6.16): (a) modeled surface runoff, (b) observed storm flow, (c) modeled groundwater recharge, and (d) observed base flow. The regression results for the modeled values are superimposed on top of the observed values.

Chapter 7: Sensitivity Analyses

7.1. Overview

In this chapter we examine some of the issues regarding the variability and uncertainty of parameter values identified in previous chapters. In Section 7.2, we look at the significance of maximizing the LAI on an annual basis as compared to holding it fixed from year to year. In Section 7.3, the sensitivity of maximized LAI to soil texture is examined in the context of the inverse texture effect. In Section 7.4, scaling theory is applied in an analysis of the impact of the uncertainty and subgrid variability of soil hydraulic properties on the generation of surface runoff. In the final section, we investigate the sensitivity of runoff to changes in the Poisson storm statistics—ones that preserve the expected values of total monthly and annual precipitation but correspond to differences in the frequency, intensity and depth of storms.

7.2. Interannual Variability of Leaf Area Index and Evapotranspiration

In order to assess the significance of maximizing LAI on an annual basis, we conducted a 43-year run of the model in which the seasonal envelope of LAI was held fixed at the average maximized values. Figure 7.1a depicts the changes in average annual transpiration. Over most of the drier half of the study area, reductions in transpiration of up to 50% occur. This is explained by the fact that under a fixed LAI envelope the vegetation cannot take advantage of wetter years while being constrained by soil moisture in drier years. For most of the humid half and a few cells in the drier half, average transpiration is seen to increase, suggesting a more complex picture. Apparently in these cases the additional transpiration that is forced during dry years outweighs the transpiration lost during wet years. This makes the most sense where the average peak green LAI is above four and frequently tops out at the maximum of six. Beyond the humid/dry divide in transpiration changes, there appears to be no strong correlation to soil texture or vegetation class.

As a result of the accompanying soil-moisture changes, the transpiration changes tend to be offset by changes in bare-soil evaporation in the opposite direction (Figure 7.1b). The net effect on average total evapotranspiration as manifested by total runoff is depicted in Figure 7.2a. Almost universally, where transpiration decreases there is an increase in runoff. The interannual variability of runoff is also significantly affected (Figure 7.2b). Because holding LAI fixed drastically reduces the interannual variability of transpiration, the first order expectation is that it would increase the interannual variability of runoff. While this is the case over most of the study area, the CVs of total runoff actually decrease in the majority of the cells where transpiration decreases. Because a decrease in transpiration is generally associated with an increase in runoff, the decrease in the CVs of runoff is consistent with the overall trend of the CVs of runoff decreasing with increasing mean (see Figure 6.13). For the grid cells of decreased CVs of total runoff, the implication for the interannual variability of evapotranspiration is that increases in the variability in bare-soil evaporation outweigh the decreases in the variability in transpiration. Because those grid cells overwhelmingly lie in the dry half of the study area, the interannual variability in LAI appears to be a significant driver of the interannual variability of runoff there. On the other hand, it mostly provides a damping effect on the variability of runoff in the wet half of the study area. This makes sense from the standpoint that bare-soil evaporation is less sensitive there to variations in soil moisture—in other words, principally climate controlled. In terms of the correspondence of the modeled CVs to the observed CVs of streamflow as evaluated in Section 6.4, there are only minor differences between the variable- and fixed-LAI cases. This suggests that the issues of runoff partitioning, subgrid variability and groundwater storage discussed in that section are more important in reproducing the observations.

7.3. Dependence of Maximized LAI on Soil Texture

In order to assess the dependence of the water balance on soil texture in general and to determine specifically whether the model captures the inverse texture effect, we conducted 30-yr model runs wherein both soil layers in all grid cells were parameterized successively as five soil textures: sand, sandy loam, silt loam, clay loam and silty clay. The textures were selected so as to provide a wide range of self-consistent soil hydraulic properties. The Brooks-Corey parameter values used are those from Rawls et al. (1982) listed in Table 3.1, and the values of K_s are the geometric means from the two literature sources as listed in the same table. If we define available water capacity as the volumetric water content between 15 bars and 1/3 bars of matric potential, then that quantity (as determined by the Brooks-Corey parameter values) for the five soil textures is respectively: 0.038, 0.106, 0.145, 0.123 and 0.121.

We found that use of the silt loam texture minimized average annual runoff (and maximized evapotranspiration) over the entire study area with the exception of the far southwest corner (west of 99° W, south of 37° N), where the optimizing soil texture was about evenly divided between silt loam and sandy loam. Those results are consistent with the concept that runoff is minimized with soils of intermediate permeability as a compromise between high surface runoff at low permeability and high groundwater runoff at high permeability (Eagleson 1980). Maximum evapotranspiration, the correlate to minimum runoff, does not imply maximum transpiration, which in the model—with its fixed-shape LAI envelope—is virtually synonymous with maximized LAI. The soil textures that provide the largest average annually maximized LAI consist of the three most permeable soils: sand, sandy loam and silt loam (Figures 7.3 and 7.4). In the western third of the study area, the optimal soils are exclusively sand and sandy loam—with sandy loam dominating in the northwest corner, and sand in the southwest corner.

Using regression analysis of the relationship between water holding capacity, grass ANPP and average annual precipitation, Sala et al. (1988) determine that the inverse texture effect predominates in the Great Plains were annual precipitation is below 37 cm. Epstein et al. (1997b) use the same ANPP data at a higher resolution in a regression study with the independent variables as mean annual temperature, mean annual precipitation, and soil texture in the form of percentages of sand and clay. Holding precipitation constant in 5-cm intervals, they find that at 80 cm of precipitation ANPP switches from increasing with sand content and decreasing with clay content to the reverse dependencies. They propose that level of precipitation as the crossover point for the inverse texture effect. If we delineate the area where the inverse texture effect holds as that were the optimal soils are exclusively sand and sandy loam, our results suggest about 70 cm of annual precipitation (see Figure 3.16a) as the cutoff. In addition to the supply of moisture, we would expect that demand in the form of potential evapotranspiration also plays a role in the inverse texture effect. Comparison of Figures 5.10c and 5.50 indicates that a precipitation deficit of about 50 cm also provides a reasonable boundary. Furthermore, we can associate the area where sand predominates as the optimal soil with a precipitation deficit of greater than about 100 cm.

The hypothesized transition to the inverse texture effect in our results is hardly distinct, with silt loam (the texture with the highest available water capacity) as the optimal texture for only a minority of cells in the wettest two thirds of the study area. In that region, the distribution of optimal soil textures does not appear to have much dependence on either climate or vegetation type, with the exception perhaps of a bias of silt loam towards the shorter vegetation classes (*i.e.*, crops, wetlands and C_3 grasses). Figure 7.5 depicts the sensitivity of maximized LAI to the successive changes in soil texture. By comparison to Figure 7.4, we see that the greatest relative changes are most closely associated with the peak green LAI in the range of about 2 to 4.5. The relative lack of sensitivity at higher values implies that the climate is wet enough that water is not particularly limiting for any of the three textures. Even so, for LAI values in the intermediate range, we still do not see a preference for one of the three soil textures. At a minimum, our results emphasize the complexity of the role of the water balance in the relationship between climate, soil texture and plant productivity—a role that can be further elucidated only through more detailed sensitivity analyses and comparison to other observation-based studies.

7.4. Subgrid Variability and Uncertainty in Soil Hydraulic Properties

As a first step towards understanding the impact of the variability and uncertainty of the hydraulic properties of soil, we perform a sensitivity analysis using scaling theory based on the concept of similar media (Miller and Miller 1956; Warrick et al. 1979). The theory makes use of a dimensionless scaling factor, α_i, which is the ratio of the microscopic characteristic length of the i^{th} soil to that of a reference soil. The bubbling pressure and saturated hydraulic conductivity of the i^{th} soil is given by

$$\Psi_{si} = \Psi_{sr} / \alpha_i \tag{7.1}$$

$$K_{si} = K_{sr} \cdot \alpha_i^2 \tag{7.2}$$

where the subscript r refers to the reference soil. The mean of α is typically assumed to be one. Based on an analysis of the variation of saturated hydraulic conductivities within and across soil series conducted by Ahuja et al. (1989), one would be a reasonable assumption for the standard deviation of α in a large area (such as a model grid cell) with multiple soil series present. The results of Ahuja et al. (1989) also suggest that the frequency distribution of α may be reasonably approximated as lognormal. Under the above assumptions for α, it can be shown that Ψ_s and K_s will also be lognormally distributed with respective geometric means of $2^{1/2}\Psi_{sr}$ and $1/2 K_{sr}$.

In order to examine the sensitivity of surface runoff to variations in soil hydraulic properties, we performed 30-year model runs in which Ψ_s and K_s in both soil layers were scaled using α at the 10th, 30th, 50th, 70th and 90th percentiles of its assumed distribution. With the assumption of lognormal distributions, the 50th percentile of α (i.e., $2^{-1/2}$) produces the geometric means of Ψ_s and K_s, which are the base grid-cell parameter values, and thus the 50th percentiles of the distributions of surface runoff in each grid cell are the base-case values depicted in Figure 5.27a. Results for the other four percentiles are plotted in Figure 7.6. They clearly show the high degree of subgrid variability in surface runoff that is possible. Figure 7.7a depicts the arithmetic means of the five percentiles. In keeping with well-established theory and other modeling studies (*e.g.*, Sharma and Luxmoore 1979; Milly and Eagleson 1987), including spatial variability in soil hydraulic properties has increased grid-cell average surface runoff. Moreover the process has somewhat smoothed out the effects of soil texture, thereby resulting in a more climate dependent pattern similar to the observations. The smoothing can be explained in terms of the variability in the distributions (Figure 7.7b), which is greater the lower the mean. Because the positive skew in the distributions increases with the variability, the greater is the proportional difference between the 50th percentile and the arithmetic mean. In Figure 7.8, we see that where the 50th-percentile surface runoff is around 0.1 cm, the difference is about an order of magnitude and that at the highest levels of surface runoff, the difference is relatively negligible. In the range of 0.1 to 1 cm of 50th-percentile surface runoff, there are a number of cells where the increase is almost another order of magnitude on top of most of the other cells in that range. Those cells correspond to the ones in the southeast corner of the study area containing sandy loam soils (see Figure 3.2). Although the distribution average is still substantially lower than observed storm flow for most of those cells, the results demonstrate that including subgrid variability is particularly important for humid regions with soils of high permeability. For the study area as a whole, the inclusion of subgrid variability has increased the correlation between the interpolated observations and modeled values of annual surface runoff from $R^2 = 0.55$ to $R^2 = 0.69$ (Figure 7.9). However, there is now a clear tendency for the former to overestimate the latter, most significantly at lower values (with the exceptions being in humid regions). This brings into further relief the likely importance for dry regions of the issues of pre-stream-gauge infiltration and the negative correlation between storm duration and intensity noted in Section 5.7. A final effect of including subgrid variability is a strengthening of the correlation (from $R^2 = 0.21$ to $R^2 = 0.37$) between the difference in model and observed surface runoff ratios and the geometric mean saturated hydraulic conductivity (Figure 7.10), which arises from a worsening of the overestimate of observed storm flow at the lowest values of saturated hydraulic conductivity.

The above analysis of the potential affects of subgrid variability in soil hydraulic properties on the infiltration-excess runoff in the model should be viewed in the context of both the uncertainty in the geometric mean values of the parameters and the subgrid variability in the actual mechanisms of surface runoff. To wit, based on the discussion and analysis of Section 3.1, the actual grid-cell geometric means of K_s could easily fall anywhere between the 30th and 70th percentiles of the assumed distributions. For the majority of grid cells, the corresponding range in modeled surface runoff encompasses the interpolated observed storm flow. Most exceptions are found at the extremes of hydraulic conductivity and/or in the humid southeast area of the study region. As noted in Section 5.7, the underestimation of storm flow in the latter case suggests a significant amount of saturation-excess runoff. Given the absence of saturation-excess runoff in the model, the uncertainties in the geometric means of K_s and the observed dependency of modeling error on the geometric mean of K_s, it may be more beneficial simply to calibrate the relationship between soil texture and K_s using observations of storm flow (either on a regional basis or globally) than to try to incorporate subgrid variability in the parameter. Owing to the issues surrounding the sources and scales of storm flow noted throughout this dissertation, the values of K_s so obtained would represent effective values as opposed to actual geometric means.

7.5. Poisson Storm Statistics

In order to assess the significance of potential error in the Poisson storm statistics (as well as real changes as might be induced by climate change), we performed two sensitivity cases in which mean storm depths, intensities and interrarrival times were first increased and then decreased by 25%. With all the three parameters changed in proportion there is no net change in expected total monthly precipitation. In order to effect a 25% change in the mean interarrival times, we used the fact that the change is synonymous with a 25% change of the opposite sign in the mean number of storms. (2.25) then gives

$$m_{tb}^{*} = \frac{m_{tr} + m_{tb}}{1 \pm 0.25} - m_{tr} \tag{7.3}$$

where m_{tb}^{*} is the adjusted value of m_{tb}. Storm duration, m_{tr}, was left unchanged. Likewise, the shape parameter of the gamma distribution of storm depth, κ, was not changed. In short, we are examining the sensitivity of the model first to larger, more intense storms that arrive proportionally less frequently, and then to smaller, less intense storms that arrive proportionally more frequently.

Comparison of the surface runoff in the storm-statistic sensitivity cases (Figure 7.11) with that of the 30th and 70th percentiles of the subgrid distribution (Figure 7.6) shows the former to be somewhat narrower than the later. Based on the analysis and discussion of Section 3.2, the 25% change in storm statistics represents a worst-case scenario in the error of those statistics, and so we can conclude that the uncertainty in those parameters is of secondary concern to the error in soil hydraulic parameters —especially saturated hydraulic conductivity. As with the inclusion of subgrid variability in soil hydraulic properties, the relative magnitude of the changes in runoff exhibits a strong dependence on the base case values (Figure 7.12a). In grid cells producing surface runoff in the range of 0.1 cm/yr, a 25% increase in mean storm depths, intensities and interrarrival times increases surface runoff by an average of about 150 %. That percentage steadily decreases as the mean surface runoff increases until it reaches a value of 27% for a base-case surface runoff of 30 cm, the maximum amount produced in the study area. For a 25% decrease in the storm statistics, surface runoff decreases by an average of 75% for a base-case of 0.1 cm/yr and by 30% for a base-case of 30 cm/yr. Therefore, at the high end of surface runoff, we see a nearly proportional response to changes in storm depth and intensity, while at the low end there is considerable amplification of the changes.

Relative changes in total runoff are less significant (Figure 7.12b). From the perspective of evapotranspiration, increasing (decreasing) the time between storms increases (decreases) the likelihood that bare-soil evaporation will come under soil control, and therefore, will decrease (increase) the expected value of bare-soil evaporation—which then translates to an increase (decrease) in the expected value of total runoff. The degree to which this happens depends on the degree of soil control in the base case; at the highest levels of runoff, which are associated with the most humid part of the study area, soil control is minimal and the changes in storm statistics produce less than a 1% change in total runoff. At the low end of total runoff, values are associated with a range of climates, and so changes in total runoff range from minimal in humid regions to as much as 50% in the highly soil controlled region of the southwest corner of the study area.

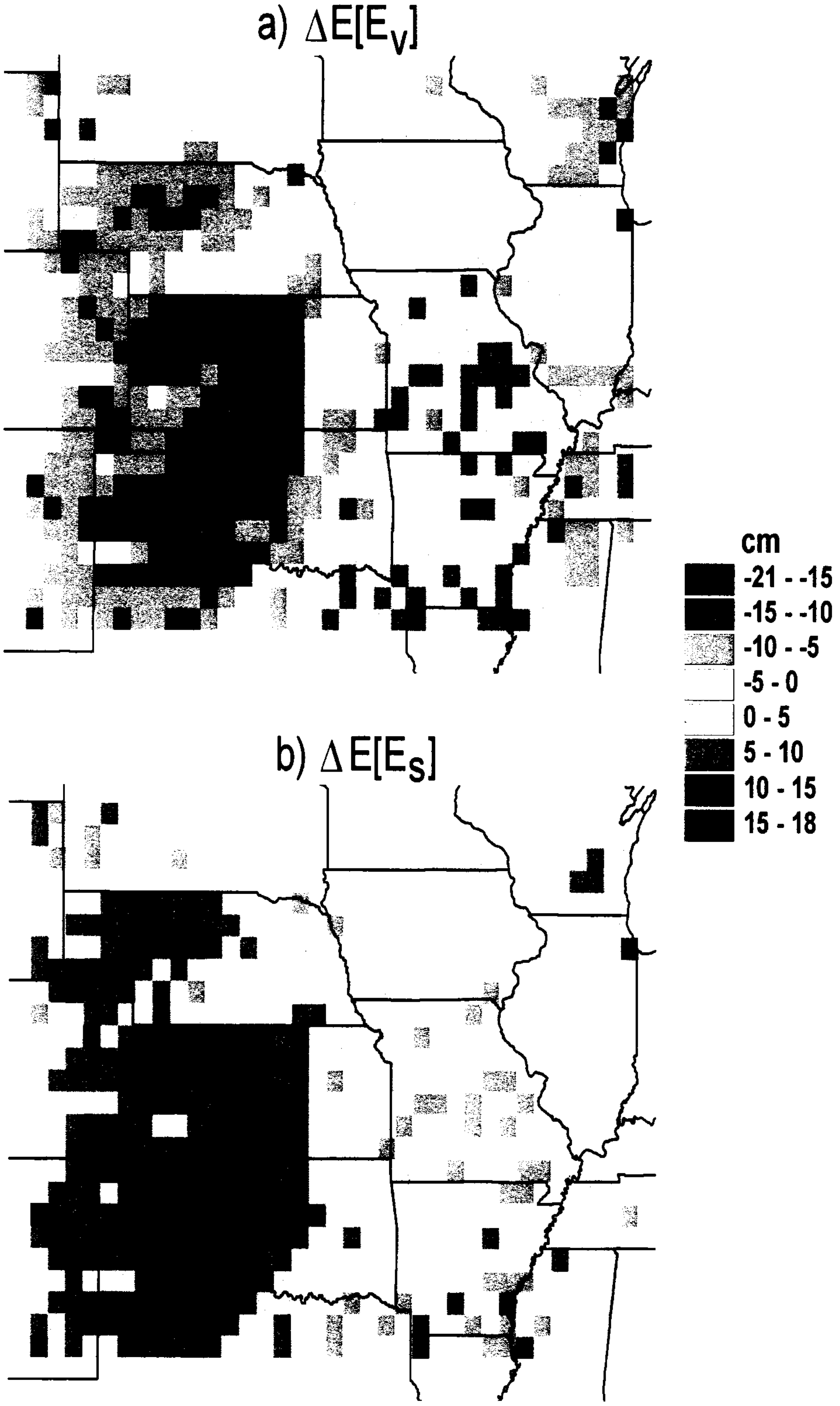

Figure 7.1. Changes in average annual (a) transpiration and (b) bare-soil evaporation (1951-1993) that occur as a result of holding LAI at the average maximized values (see Fig. 5.1a) versus maximization on a year-to-year basis.

a) $\Delta E[R_t]$

b) $\Delta CV[R_t]$

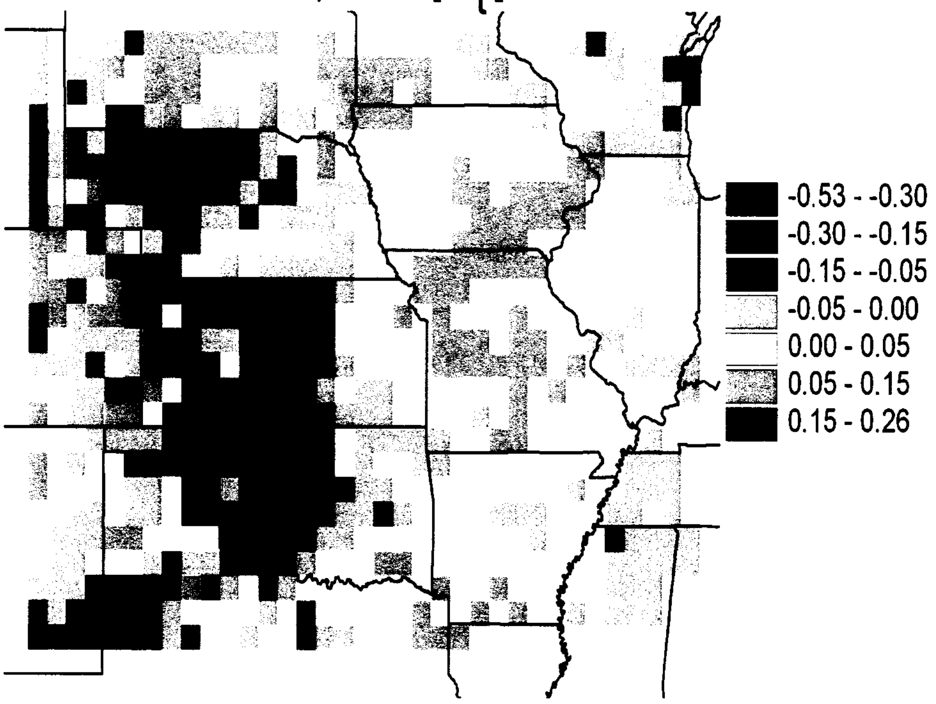

Figure 7.2. Changes in (a) average annual total runoff and (b) the CV of annual total runoff (1951-1993) from the annually maximized LAI case to the fixed-LAI case.

Figure 7.3. Soil textures amongst five which result in the largest average maximized LAI.

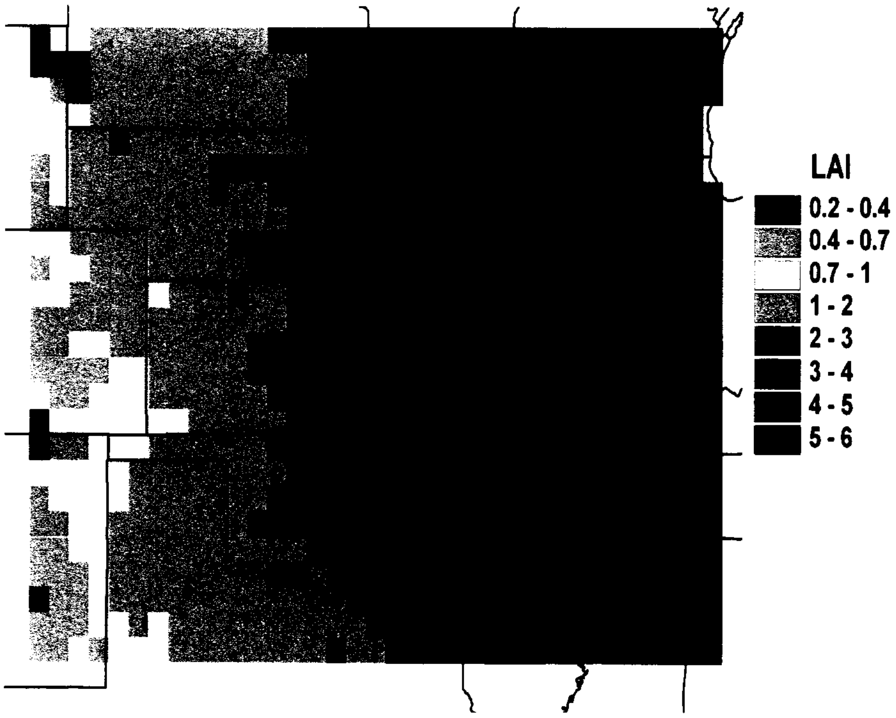

Figure 7.4. Maximized peak green LAI using the soil textures in Figure 7.3.

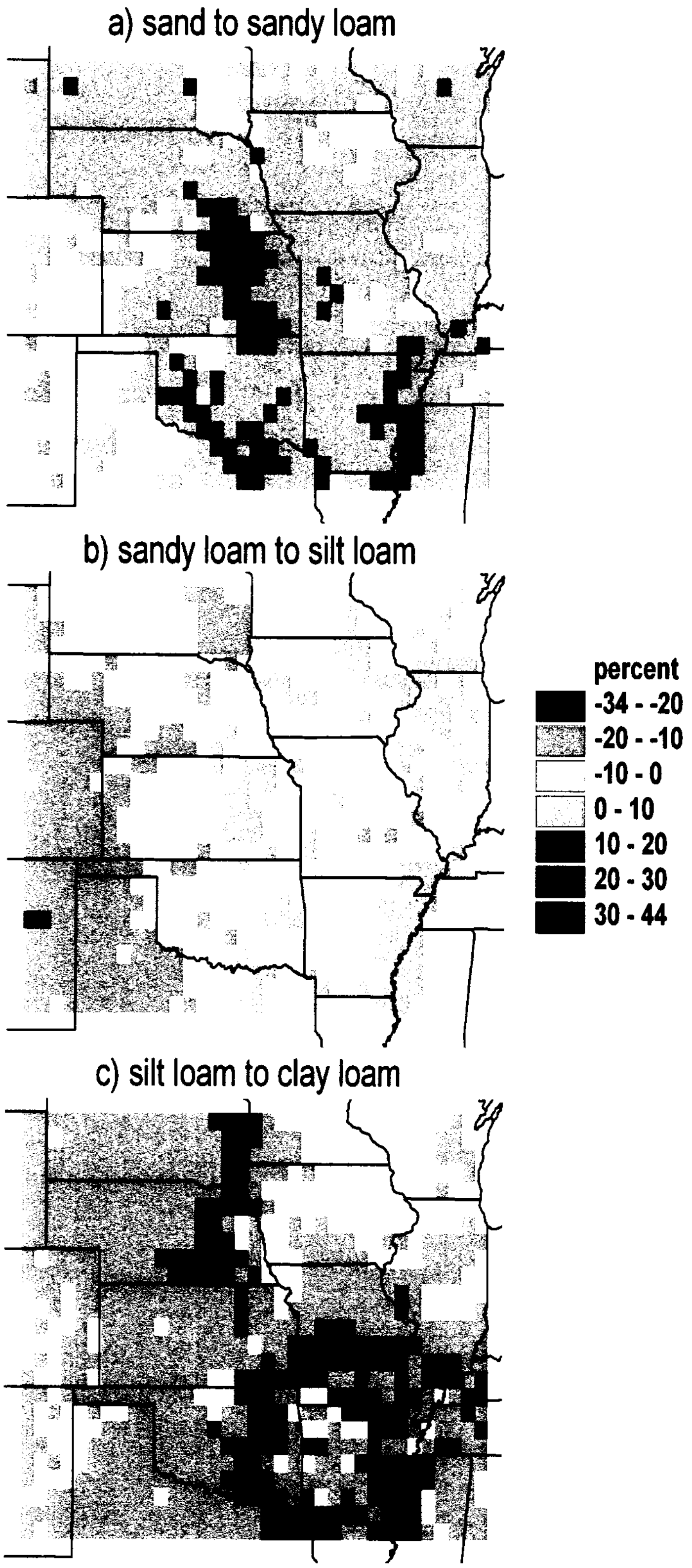
a) sand to sandy loam

b) sandy loam to silt loam

c) silt loam to clay loam

Figure 7.5. The percent changes in maximized LAI when the soil texture is changed from (a) sand to sandy loam, (b) sandy loam to silt loam, and (c) silt loam to clay loam.

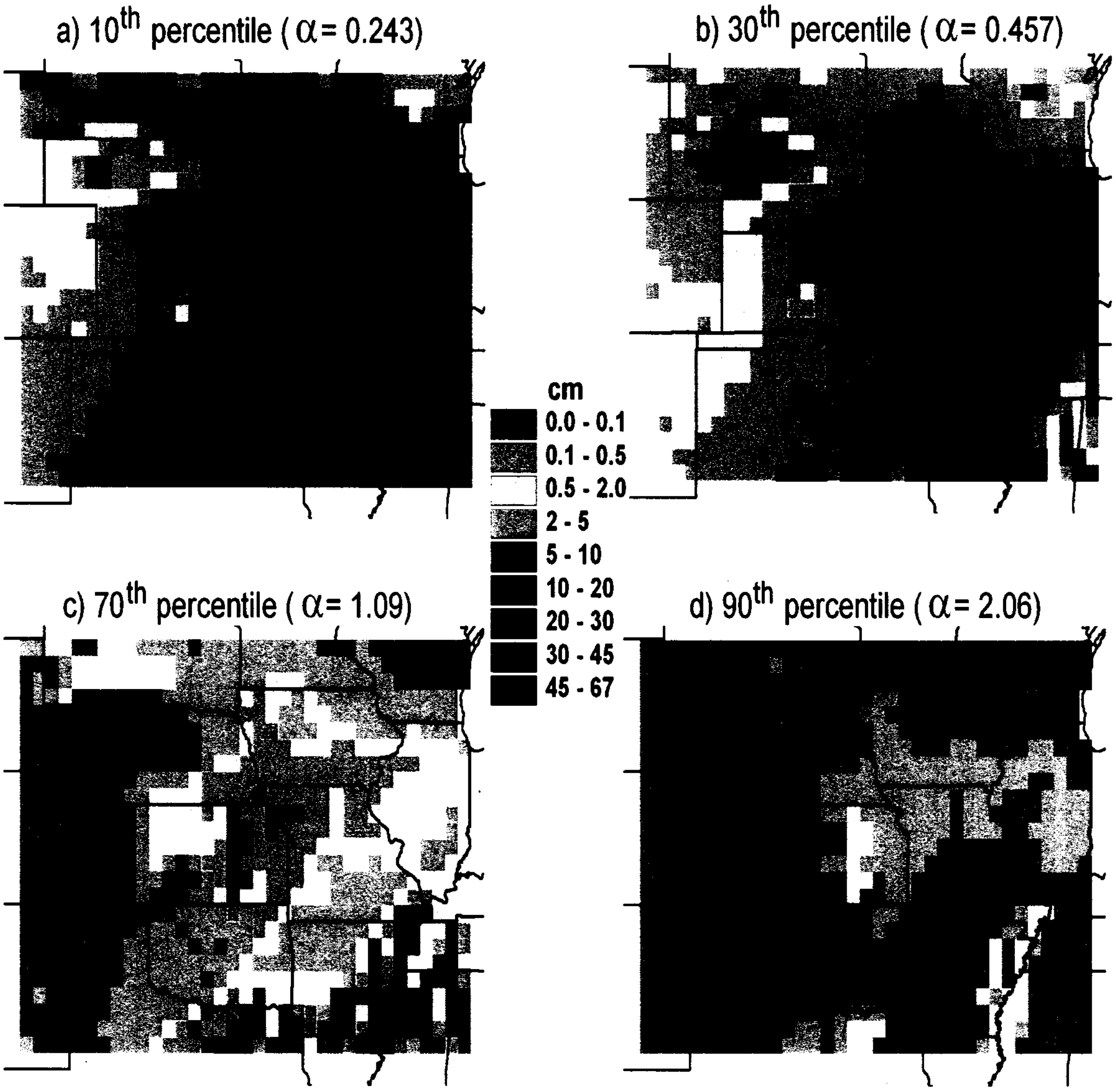

Figure 7.6. Modeled average annual surface runoff (1951-1980) for various percentiles of the assumed sub-grid distributions of saturated hydraulic conductivity, K_S, and bubbling pressure, Ψ_S. α is the scaling parameter.

a) mean

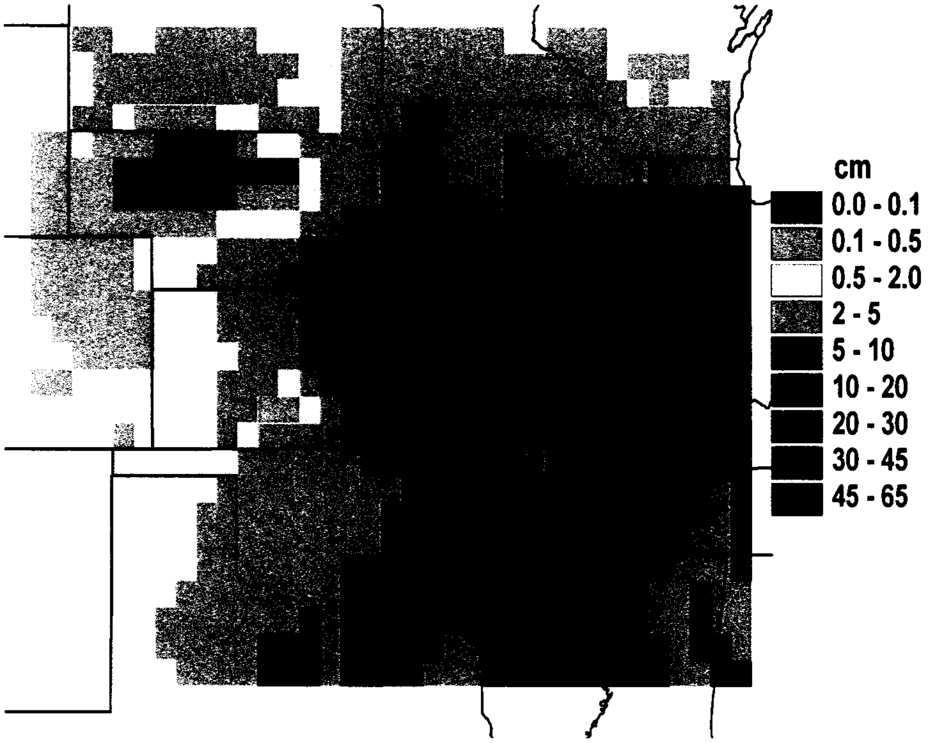

b) relative variability

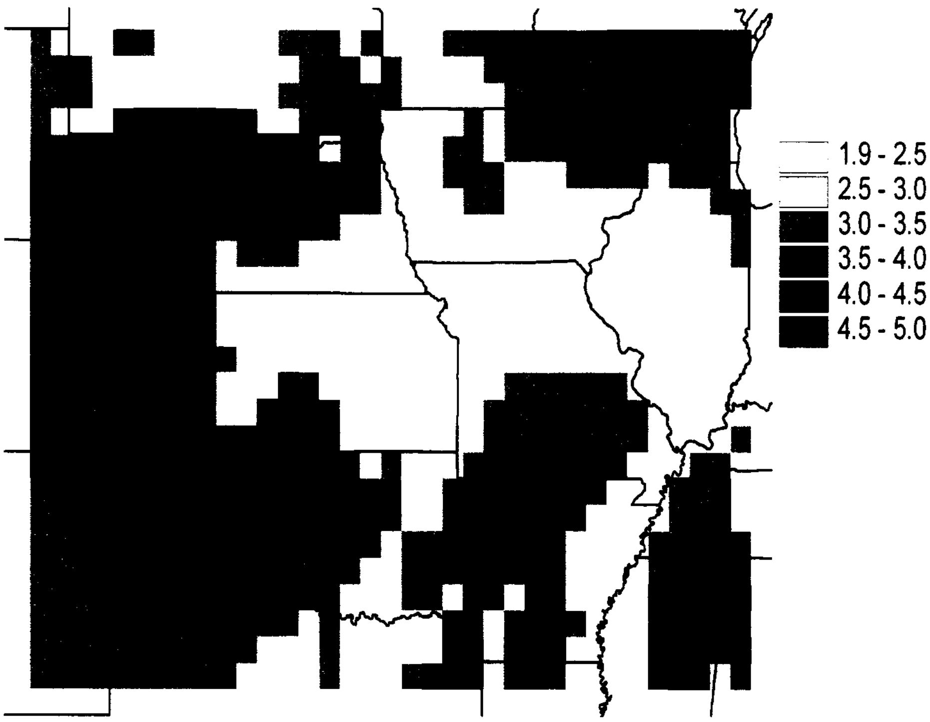

Figure 7.7. (a) the arithmetic means of the sub-grid distributions of surface runoff (see Figure 7.6), and (b) the relative variability in the distributions as defined by the difference between the 10th and 90th percentiles divided by the mean.

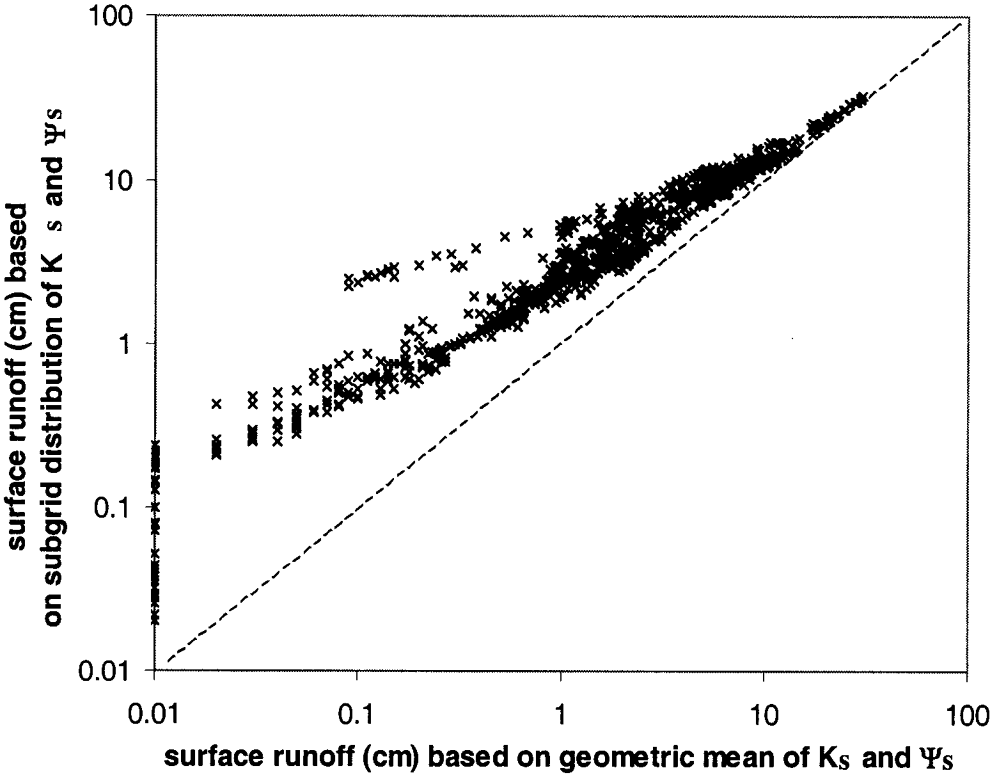

Figure 7.8. The 50th percentiles of the sub-grid distributions of surface runoff (*i.e.*, those values modeled using the geometric means of K_s and Ψ_s) versus the arithmetic means of the distributions (see Figures 5.27a and 7.7a). Values less than 0.01 cm are plotted at 0.01 cm.

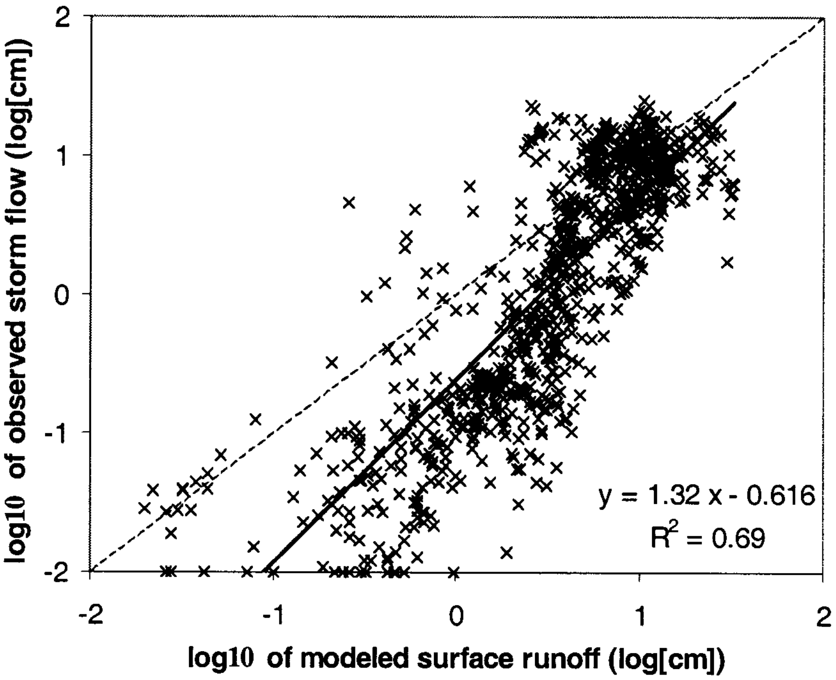

Figure 7.9. The arithmetic means of the sub-grid distributions of surface runoff versus interpolated observed storm flow. Values less than –2 are plotted at –2. Compare to base case in Figure 5.29.

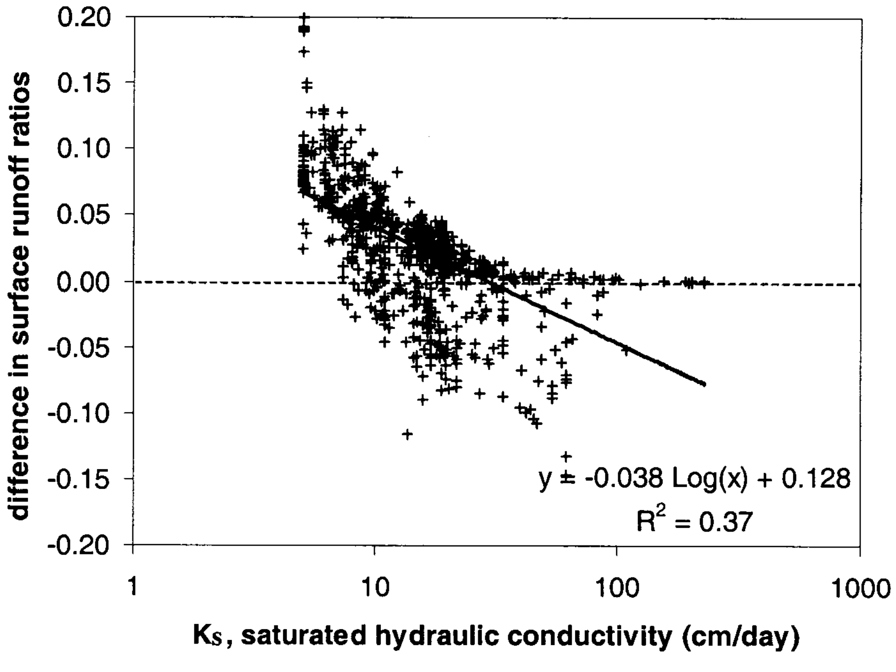

Figure 7.10. Comparison of the geometric mean saturated hydraulic conductivity in the root zone with the difference in runoff ratios between modeled arithmetic mean surface runoff and observed storm flow. Compare to base case in Figure 5.31.

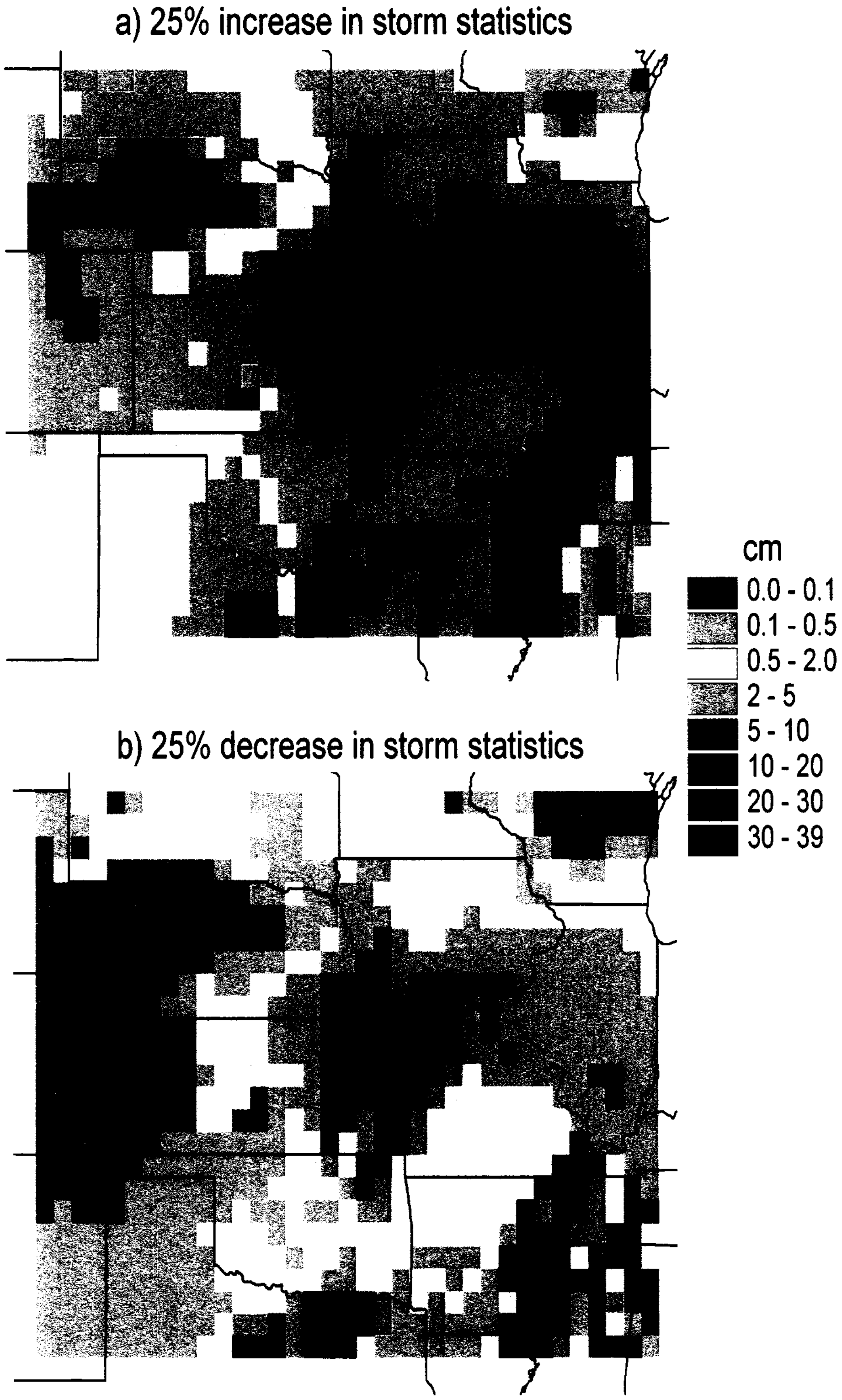

a) 25% increase in storm statistics

b) 25% decrease in storm statistics

Figure 7.11. Average annual surface runoff (1951-1980) for proportional changes in the Poisson storm statistics. The 25% increase (a) corresponds to larger and more intense, but less frequent storms. The 25% decrease (b) corresponds to smaller, less intense and more frequent storms. Compare to base case in Figure 5.27a.

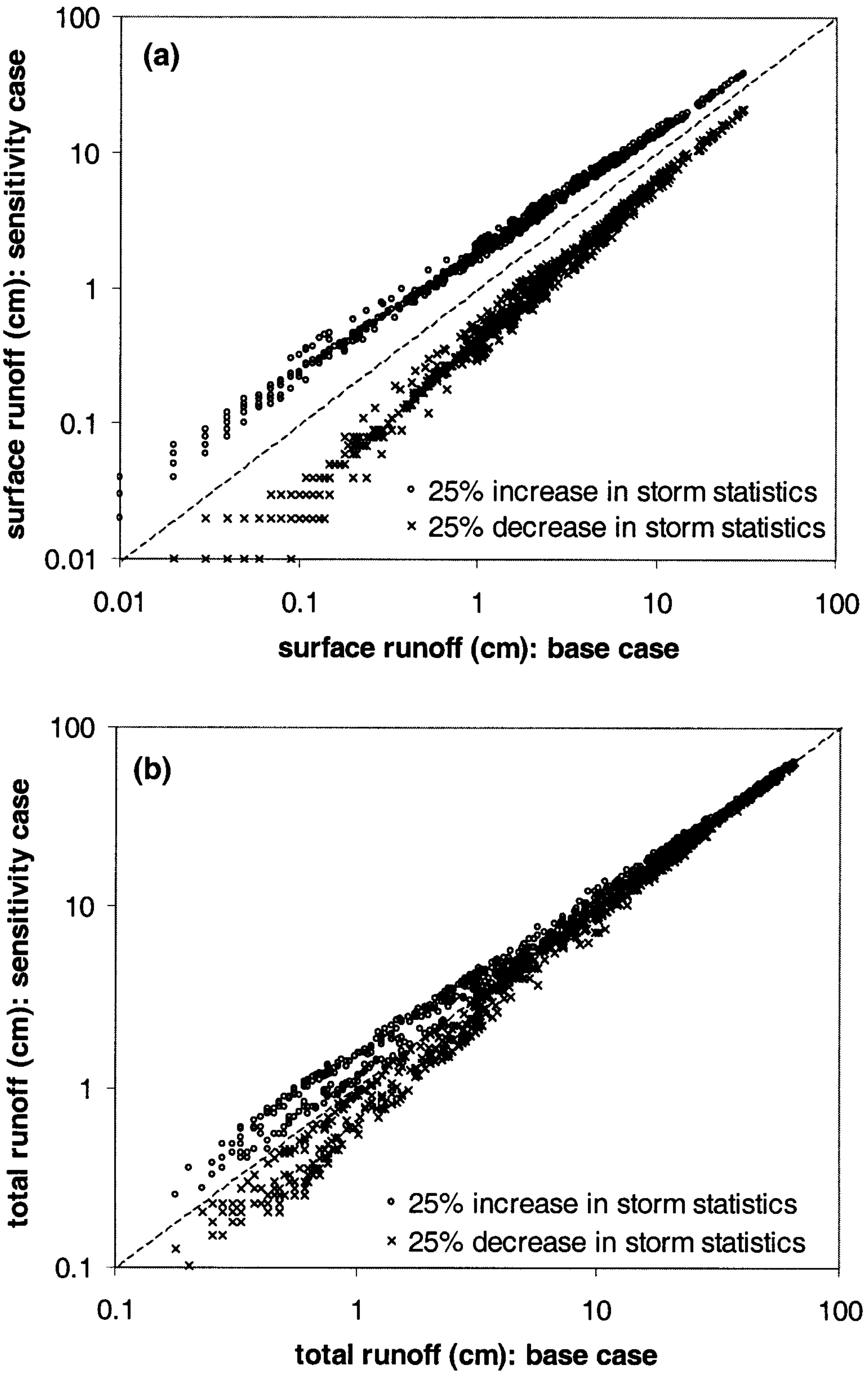

Figure 7.12. Base-case runoff versus that for changes in Poisson storm statistics for average annual (a) surface runoff (see Figure 7.11), and (b) total runoff (1951-1980).

Chapter 8: Conclusion

8.1. Summary of Results

An operational version of a statistical-dynamical water balance model has been developed which is applicable to regional-scale climate impact assessments. Major improvements to the model include implementation at a monthly scale, addition of snow and frozen soil, division of vadose-zone soil into two layers, and a more realistic representation of vegetation. The latter was achieved by coupling the water balance model to the Shuttleworth-Wallace (1985) evapotranspiration model. The coupled model has been applied to the central United States over a half-degree grid using vegetation, soil and climate data from the Vegetation/Ecosystem Modeling and Analysis Project (VEMAP). After detailed review of the literature, careful estimation of values for the parameters of the evapotranspiration, soil-hydraulic and stochastic-precipitation sub-models was performed. An excellent match of modeled mean annual runoff to contours of streamflow was achieved with only minimal calibration of two evapotranspiration parameters. Model validity was further established through comparison of results for the mean and interannual variability of the water balance with observations of leaf area index (LAI), vegetation productivity and soil moisture.

8.1.1. *Partitioning of Evapotranspiration*

Particular attention has been paid to capturing the differing dynamics of bare-soil evaporation and transpiration. The partitioning of evapotranspiration has been validated by comparison with observational data from the literature and calculation of water-use efficiencies from modeled transpiration and a gridded dataset of total net primary productivity. Surprising little dependence of the percentage of total evapotranspiration that is bare-soil evaporation on climate and vegetation type was found, with most of the variation across the study area attributable to soil texture and the resultant differences in vegetation density. The implication is that the higher (lower) soil moisture content in humid (dry) climates is more-or-less offset by the greater (lower) vegetation density. At the low end, with approximately 25-35% of annual average evapotranspiration being bare-soil evaporation, are mostly soils with high sand content. At the high end, with 60-

70% as bare-soil evaporation, are soils with high clay content. These results and their validation help to clarify the wide-ranging results in the partitioning of evapotranspiration that have been produced by other models of soil-vegetation-atmosphere transfer (SVAT) (*e.g.*, Mahfouf et al. 1996).

8.1.2. *Vegetation Density*

The partitioning of evapotranspiration in the model is highly dependent on vegetation density in the form of LAI. The spatial and interannual variation in LAI is captured in the model through application of the hypothesis that, in any year in which water is significantly limiting, vegetation will draw soil moisture down in the latter half of the growing season approximately to the point at which the vegetation just begins to experience water stress. This "LAI-maximization" hypothesis has been supported through the analysis of observations of soil moisture, soil-moisture retention data and water-relations studies in the plant physiology literature. The hypothesis is applied to maximize the annual peak in green LAI, with the shape of the seasonal LAI envelope held fixed. Grid-cell specific envelopes were determined from satellite-based estimates of green LAI developed by Buerman et al. (2002). Comparison of the means of modeled-maximized peak green LAI and those of the unaltered observations with ground-based observations of LAI and with a gridded datasets of above-ground net primary production indicated that the model-maximized values are at least as accurate as the unaltered observations. Analysis of the sensitivity of model-maximized LAI to soil texture showed that the model is able to reproduce the inverse texture effect (Noy-Meier 1973), which consists of the observation that natural vegetation in dry climates tends to be most productivity in sandy soils.

The interannual variability of peak green LAI was less successfully captured by the model, with the magnitude of that variability mostly dependent on the maximum and minimum bounds. Such bounds only roughly represent the influence of factors other than soil-moisture availability on the interannual variability of vegetation density. Nonetheless, analysis of the effects of holding LAI fixed in the model showed that, in terms of total evapotranspiration, it is probably sufficient that the model reproduces the sign and *approximate* magnitude of annual LAI anomalies.

8.1.3. *Partitioning of Precipitation into Surface Runoff and Infiltration*

A significant limitation of the model is its one-dimensional formulation and consequent estimation of only Hortonian (*i.e.*, infiltration excess) runoff. Nonetheless, comparison of model results to interpolated estimates of storm flow from USGS gauging stations showed that for most combinations of climate and soil that formulation does a reasonable job of approximating the spatially complex process of surface runoff generation at the regional scale. Overestimation biases that could easily be corrected by calibration of soil-hydraulic parameters include: (1) dry climates—likely due to an unaccounted-for negative correlation between storm intensity and duration, and (2) soils of low permeability—likely due to uncertainty in the relationship between soil texture and saturated hydraulic conductivity and additional infiltration mechanisms. The overestimation of surface runoff in dry climates is particularly severe if subgrid variability in soil hydraulic properties is included. This may be a scale issue in that much surface runoff in dry climates never reaches a gauged stream channel. In contrast, subgrid variability of soil hydraulic properties appears to be much less important in humid climates. Rather, the model tends to *underestimate* surface runoff in those climates owing to the unaccounted-for connection of the vadose zone to shallow groundwater and the resulting Dunne (*i.e.*, saturation excess) runoff and enhancement of Hortonian runoff. The discrepancy between modeled and observed surface runoff is worst for the most permeable soils in humid climates.

8.1.4. *The Interannual Variability of Runoff*

The coefficients of variation and skewness in modeled annual surface runoff and groundwater recharge were compared to the same statistics for observed storm flow and base flow. Although the model tends to underestimate the interannual variability in surface runoff and overestimate the interannual variability in base flow, it matches the overall structure in the observations. Specifically, it reproduces the linear decrease in the coefficients of variation of storm flow with the means, as well the peak in the coefficients of variation of base flow for means around one cm. The later was seen to be associated with a region of high interannual variability of precipitation over the central Great Plains. The model also reproduces the positive correlation between the skewness coefficients and the coefficients of variation in both storm flow and base flow. The tendency of the model to underestimate the interannual variability in storm flow was attributed to subgrid variability in precipitation and runoff processes, and to the spatiotemporal variability of antecedent soil moisture. The less severe overestimation of the interannual variability of base flow was attributed more to groundwater storage than to scale issues.

8.2. Directions for Future Research

The model in its present form demonstrates that the high-frequency variability in precipitation and its effects on the dynamics of infiltration and bare-soil evaporation can be adequately represented in the one-dimensional water balance at a monthly scale with a statistical-dynamical formulation. Yet to be addressed are the myriad issues of spatial variability. The desire is of course to incorporate spatial variability in the model while still maintaining the spirit of parsimonious parameterization inherent in the statistical-dynamical approach. Several researchers have in fact developed statistical-dynamical formulations of runoff processes that address various aspects of the spatial problem, particularly for implementation as the land-surface component of climate models (*e.g.*, Entekhabi and Eagleson 1989; Wood et al. 1992; Famiglietti and Wood 1994; and Stieglitz et al. 1996). The challenge for the water balance model of this dissertation is in combining spatial and temporal statistical-dynamical approaches.

Given that hard-coupling to a climate model is not the intent of the present model, the first step in investigating subgrid variability in the model should be its application at higher resolutions. In particular, application at a higher resolution would help clarify the significance of uncertainty and subgrid variability in soil hydraulic properties highlighted throughout this dissertation. As noted in Section 3.1, CONUS-SOIL (Miller and White 1998) provides the STATSGO textural information at a 1-km resolution. In addition, monthly precipitation has been generated using PRISM (Daly 1994) at a 10-km resolution, and the NDVI is produced from AVHRR data at a 10-km resolution.

In terms of capturing the mean and interannual variability of runoff, model results suggest that subgrid variability and uncertainty in soil hydraulic properties is the most important issue for the dry regions. In contrast, interaction with the water table and saturation-excess runoff appear to be the most important issue for humid regions.

Because groundwater has long memory, the location of the water table might be treated as static at the regional and monthly scales. Along those lines, Salvucci and Entekhabi (1995) have shown how the one-dimensional Eagleson model, modified to include a shallow water table and Dunne runoff, can be applied across a hillslope to define a so-called "climatic equilibrium" of the water table position. Levine and Salvucci (1999) coupled the modified model to a 3-dimensional finite-difference groundwater model. They applied the coupled model to a 16-km^2 watershed in the Canadian prairie and were able to reproduce the spatial pattern of groundwater recharge and discharge areas. As use of the same groundwater model would be computationally and parameterically prohibitive at the scale of the study area of this dissertation, it is of great interest as to whether the equilibrium approach can be incorporated with a statistical formulation of topography and groundwater, such as the topographic index of Beven and Kirkby (1978) and the topography-soil index of Sivapalan et al. (1987).

While the impacts of spatial variations in soils and topography on the regional-scale water balance have been extensively studied, the role of spatial variations in vegetation is not as well understood. One of the more interesting questions is how those variations act to either increase or smooth out spatial variations in soil moisture, as well as how variations in soil moisture control variations in vegetation. For the purposes of addressing such questions, there are several improvements to the vegetation component of the model that are worth investigating. First, the estimation of vegetation density and transpiration might be improved by actually "growing" the vegetation using energy and biogeochemical constraints, in addition to the soil moisture constraints. Second, the impact of water limitations might be better captured with inclusion of inter-storm water stress (*e.g.*, Levine and Salvucci 1999), in addition to the seasonal stress already captured by the model. Finally, inclusion of inter-species competition for light and energy (*e.g.*, Eagleson and Segarra 1985) might be useful in the prediction of the type of vegetation that will establish itself in a given location.

Any improvements to the model should be viewed in the context of the original purpose of the model, which is for use in integrated climate impact assessments. Key to the integration process is linking the model to climate and land-use information on the input end and socioeconomic and environmental impacts and decision-making on the output end. The paper in Appendix A outlines a framework for doing just that. It leaves out many details that can only be addressed with additional research. Of particular importance is the need to develop methods of perturbing the storm statistics and climate variables based on climate information, such as seasonal climate forecasts or scenarios of climate change. A particular challenge is quantifying uncertainty in that information, so that it can be propagated through the water balance model. The process requires understanding the sources of the interannual variability of climate, especially precipitation. That topic was touched on in Sections 4.3 and 6.2 in the context of the Poisson rectangular-pulse precipitation model. It warrants much more detailed thought and investigation. The large-scale statistical-dynamical water balance model developed in Appendix B is an additional tool that can be used to investigate the climatic sources of interannual variability in the water balance.

References

Ahuja, L. R., D. K. Cassel, R. R. Bruce, and B. B. Barnes, 1989: Evaluation of spatial distribution of hydraulic conductivity using effective porosity data. *Soil Science*, **148,** 404-411.

Asrar, G., M. Fuchs, E. T. Kanemasu, and J. L. Harfield, 1984: Estimating absorbed photosynthetic radiation and leaf area index from spectral reflectance in wheat. *Agronomy Journal*, **76,** 300-306.

Baldwin, J. L., 1973: *Climates of the United States*. US Department of Commerce, National Oceanic and Atmospheric Administration.

Beven, K. and M. J. Kirkby, 1979: A physically based, variable contributing area model of basin hydrology. *Hydrology Science Bulletin*, **24,** 43-69.

Bond, J. J. and W. O. Willis, 1969: Soil water evaporation: surface residue rate and placement effects. *Soil Science Society of America Proceedings*, **33,** 445-448.

Boyer, J. S., 1971: Resistances to water transport in soybean, bean, and sunflower. *Crop Sciences*, **11,** 403-407.

Brakensiek, D. L., W. J. Engleman, and W. J. Rawls, 1981: Variation within texture classes of soil water parameters. *Transactions of the ASAE*, 335-338.

Brooks, R. H. and A. T. Corey, 1966: Properties of porous media affecting fluid flow. *Journal of Irrigation Drainage Division of American Society of Civil Engineers*, **IR2,** 61-88.

Brutsaert, W., 1967: Some methods of calculating unsaturated permeability. *Transactions of the ASAE*, 400-404.

Brutsaert, W. and D. Chen, 1995: Desorption and the two stages of drying of natural tallgrass prairie. *Water Resources Research*, **31,** 1305-1313.

Buermann, W., Y. Wang, J. Dong, L. Zhou, X. Zeng, R. E. Dickinson, C. Potter, and R. Myneni, 2002: Analysis of a multiyear global vegetation leaf area index data set. *Journal of Geophysical Research*, **107,** 4646-4664.

Camillo, P. J. and R. J. Gurney, 1986: A resistance parameter for bare-soil evaporation models. *Soil Science*, **141,** 95-105.

Campbell, G. S., 1974: A simple method for determining unsaturated conductivity from moisture retention data. *Soil Science*, **117,** 311-314.

Carslaw, H. S. and J. C. Jaeger, 1959: *Conduction of Heat in Solids*. 2nd ed. Oxford University Press, 510 pp.

Childs, E. C. and N. Collis-George, 1950: The permeability of porous materials. *Proceedings of the Royal Society*, **A201,** 392-405.

Choudhury, B. J. and J. L. Monteith, 1988: A four-layer model for the heat budget of homogeneous land surfaces. *Quarterly Journal of the Royal Meteorological Society*, **114,** 373-398.

Chung, S. W., P. W. Gassman, and L. A. Kramer, 1999: Validation of EPIC for two watersheds in sourthwest Iowa. *Journal of Environmental Quality*, **28,** 971-979.

Cosby, B. J., G. M. Hornberger, R. B. Clapp, and T. R. Ginn, 1984: A statistical exploration of the relationships of soil moisture characteristics to the physical properties of soils. *Water Resources Research*, **20,** 682-690.

Cowan, I. R., 1965: Transport of water in the soil-plant-atmosphere system. *Journal of Applied Ecology*, **2,** 221-239.

Cowan, I. R. and F. L. Milthorpe, 1968: Plant factors influencing the water status of plant tissues. *Water Deficits and Plant Growth, Vol. I: Development, Control, and Measurement*, T. T. Kozlowski, Ed., Academic Press, 137-161.

Daly, C., R. P. Neilson, and D. L. Phillips, 1994: A statistical-topographic model for mapping climatological precipitation. *Journal of Applied Meteorology*, **33,** 140-158.

Denmead, O. T., 1976: Temperate cereals. *Vegetation and the Atmosphere*, J. L. Monteith, Ed., Academic Press, 1-31.

Denmead, O. T. and R. H. Shaw, 1962: Availability of soil water to plants as affected by soil moisture content and meteorological conditions. *Agronomy Journal*, **54,** 385-390.

Dickinson, R. E., A. Henderson-Sellers, and P. J. Kennedy, 1993: *Biosphere-Atmosphere Transfer Scheme (BATS) Version 1e as Coupled to the NCAR Community Climate Model.* University Corporation for Atmospheric Research, Boulder, CO.

Eagleson, P. S., 1970: *Dynamic Hydrology*. McGraw-Hill.
——, 1978a: Climate, soil, and vegetation: 1. Introduction to water balance dynamics. *Water Resources Research*, **14,** 705-712.

——, 1978b: Climate, soil, and vegetation: 2. The distribution of annual precipitation derived from observed sequences. *Water Resources Research*, **14,** 713-721.

——, 1978c: Climate, soil, and vegetation: 3. A simplified model of soil moisture movement in the liquid phase. *Water Resources Research*, **14,** 722-730.

——, 1978d: Climate, soil, and vegetation: 4. The expected value of annual evapotranspiration. *Water Resources Research*, **14,** 731-739.

——, 1978e: Climate, soil, and vegetation: 5. A derived distribution of storm surface runoff. *Water Resources Research*, **14,** 740-748.

——, 1978f: Climate, soil, and vegetation: 6. Dynamics of the annual water balance. *Water Resources Research*, **14,** 749-764.

——, 1978g: Climate, soil, and vegetation: 7. A derived distribution of annual water yield. *Water Resources Research*, **14,** 765-776.

——, 1982: Ecological Optimality in water-limited natural soil-vegetation systems 1. Theory and hypothesis. *Water Resources Research*, **18,** 325-340.

Eagleson, P. S. and T. E. Tellers, 1982: Ecological Optimality in water-limited natural soil-vegetation systems 2. Tests and applications. *Water Resources Research*, **18,** 341-354.

Eagleson, P. S. and R. I. Segarra, 1985: Water-limited equilibrium of savanna vegetation systems. *Water Resources Research*, **21,** 1483-1493.

EarthInfo. 1999: CDROM of National Climate Data Center Hourly Precipitation Records. Earthinfo, Inc, Boulder, CO.

Ehleringer, J. R. and T. E. Dawson, 1992: Water uptake by plants: perspectives from stable isotopes composition: commissioned review. *Plant, Cell and Environment*, **15,** 1073.

Entekhabi, D. and P. S. Eagleson, 1989a: *Landsurface Hydrology Parameterization for Atmospheric General Circulation Models: Inclusion of Subgrid Scale Spatial Variability and Screening with a Simple Climate Model.* Ralph M. Parsons Laboratory for Hydrology and Water Resource Systems Report Number 235, Massachusetts Institute of Technology, Cambridge, MA.

——, 1989b: Landsurface hydrology parameterization for atmospheric general circulation models including subgrid scale spatial variability. *Journal of Climate*, **2,** 816-831.

Entin, J. K., 1998: *Temporal and spatial scales of soil moisture variations*. Ph.D. Thesis, Department of Meteorology, University of Maryland, 143 pp.

Epstein, H. E., W. K. Lauenroth, I. C. Burke, and D. P. Coffin, 1997a: Productivity patterns of C_3 and C_4 functional types in the U.S. great plains. *Ecology*, **78,** 722-731.

Epstein, H. E., W. K. Lauenroth, and I. C. Burke, 1997b: Effects of temperature and soil texture on ANPP in the U.S. great plains. *Ecology*, **78,** 2628-2631.

Famiglietti, J. S. and E. F. Wood, 1994: Multiscale modeling of spatially variable water and energy balance processes. *Water Resources Research*, **30,** 3061-3078.

Federer, C. A., 1979: A soil-plant-atmosphere model for transpiration and availability of soil water. *Water Resources Research*, **15,** 555-562.

Fernandez-Illescas, C. P., A. Porporato, F. Laio, and I. Rodriquez-Iturbe, 2001: The ecohydrological role of soil texture in a water-limited ecosystem. *Water Resources Research*, **37,** 2863-2872.

Gale, M. R. and D. F. Grigal, 1987: Vertical root distributions of northern tree species in relation to successional status. *Canadian Journal of Forest Research*, **17,** 829-834.

Gardener, W. R., 1958: Some steady-state solutions of the unsaturated moisture flow equation with application to evaporation from a water table. *Soil Science*, **85,** 228-232.

Gardner, W. R., 1960: Dynamic aspects of water availability to plants. *Soil Science*, **89,** 63-73.

Gardner, W. R. and C. F. Ehlig, 1963: The influence of soil water on transpiration by plants. *Journal of Geophysical Research*, **68,** 5719-5725.

Gebert, W. A., D. J. Graczyk, and W. R. Krug, 1987: *Average annual runoff in the United States, 1951-80.* Online Linkage <http://water.usgs.gov/lookup/getspatial?runoff> and <ftp://nsdi.usgs.gov/pub/dsdl/runoff.sdts.tgz>, US Geological Survey.

Geraghty, J. J. and D. W. Miller, 1973: *Water Atlas of the United States.* Water Information Center, 122 pp.

Gill, R. A., R. H. Kelly, W. J. Parton, K. A. Day, R. B. Jackson, J. A. Morgan, J. M. O. Scurlock, L. L. Tieszen, J. V. Castle, D. S. Ojima, and X. S. Zhang, 2002: Using simple environmental variables to estimate below-ground productivity in grasslands. *Global Ecology & Biogeography*, **11,** 79-86.

Gollan, T., J. B. Passioura, and R. Munnus, 1986: Soil water status affects the stomatal conductance of fully turgid wheat and sunflower leaves. *Australian Journal of Plant Physiology*, **13,** 459-464.

Guswa, A. J., M. A. Celia, and I. Rodriguez-Iturbe, 2002: Models of soil moisture dynamics in ecohydrology: A comparative study. *Water Resources Research*, **38,** 1166-1181.

Gutman, G., 1988: A simple method for estimating monthly mean albedo from AVHRR data. *Journal of Applied Meteorology*, **27,** 973-988.

Havranek, W. M. and U. Benecke, 1978: Influence of soil moisture on water potential, transpiration and photosynthesis of conifer seedlings. *Plant and Soil*, **49,** 91-103.

Hawk, K. L. and P. S. Eagleson, 1992: *Climatology of Station Storm Rainfall, in the Continental United States: Parameters of the Bartlett-Lewis and Poisson Rectangular Pulses Models.* Ralph M. Parsons Laboratory for Hydrology and Water Resource Systems Report Number 336, Massachussets Institute of Technology, Cambridge, MA.

Hazlett, D., 1992: Leaf area development of four plant communities in the Colorado steppe. *The American Midland Naturalist*, **127,** 276-289.

Hellkvist, J., G. P. Richards, and P. G. Jarvis, 1973: Vertical gradients of water potential and tissue water relations in sitka spruce trees measured with the pressure chamber. *Journal of Applied Ecology*, **11,** 637-667.

Hirsch, R. M., T. A. Helsel, T. A. Cohn, and E. J. Gilroy, 1993: Statistical treatment of hydrologic data. *Handbook of Hydrology*, D. R. Maidment, Ed., McGraw-Hill, 17.1-17.55.

Hobbins, M., 2000: *Evaluating and enhancing two implementations of the complementary relationship in regional evapotranspiration.* M.Sc. Thesis, Department of Civil Engineering Colorado State University, Colorado State University.

Hobbins, M. T., J. A. Ramírez, T. C. Brown, and L. H. J. M. Claessens, 2001: The complementary relationship in estimation of regional evapotranspiration: The complementary relationship areal evapotranspiration and advection-aridity models. *Water Resources Research*, **37,** 1367-1387.

Holdridge, L. R., 1947: Determination of world plant formations from simple climatic data. *Science*, **105,** 367-368.

Hollinger, S. E. and S. A. Isard, 1994: A soil moisture climatology of Illinois. *Journal of Climate*, **7,** 822-833.

Jackson, R. B., J. Canadell, J. R. Ehleringer, H. A. Mooney, O. E. Sala, and E. D. Schulze, 1996: A global analysis of root distributions for terrestrial biomes. *Oecologia*, **108,** 389-411.

Jackson, R. B., H. J. Schenk, E. G. Jobbagy, J. Canadell, R. E. Colello, R. E. Dickinson, C. B. Field, P. Friedlingstein, M. Heimann, K. Hibbard, D. W. Kicklighter, A.

Kleidon, R. P. Neilson, W. J. Parton, O. E. Sala, and M. T. Sykes, 2000: Belowground consequences of vegetation change and their treatment in models. *Ecological Applications*, **10,** 470-483.

Jarvis, P. G., G. B. James, and J. J. Landsberg, 1976: Conifer forest. *Vegetation and the Atmosphere*, J. L. Monteith, Ed., Academic Press, 171-236.

Jury, W. A., W. R. Gardener, and W. H. Gardener, 1991: *Soil Physics*. 5th ed. John Wiley & Sons, Inc, 328 pp.

Kalnay, E. and co-authors, 1996: The NCEP/NCAR 40-year reanalysis project. *Bulletin of the American Meteorological Society*, **77,** 437-471.

Karl, T. R. and R. W. Knight, 1998: Secular trends of precipitation amount, frequency, and intensity of the United States. *Bulletin of the American Meteorological Society*, **79,** 231-241.

Katz, R. W. and M. B. Parlange, 1993: Effects of an index of atmospheric circulation on stochastic properties of precipitation. *Water Resources Research*, **29,** 2335-2344.

Kern, J. S., 1995: Geographic patterns of soil water-holding capacity in the contiguous United States. *Soil Science Society of America Journal*, **58,** 1126-1133.

Kitanidis, P. K., 1993: Geostatistics. *Handbook of Hydrology*, D. R. Maidment, Ed., McGraw-Hill, 20.1-20.39.

Kittel, T. G. F., N. A. Rosenbloom, T. H. Painter, D. S. Schimel, and V. M. Participants, 1995: The VEMAP integrated database for modeling United States ecosystem/vegetation sensitivity to climate change. *Journal of Biogeography*, **22,** 857-862.

Kittel, T. G. F., N. A. Rosenbloom, T. H. Painter, D. S. Schimel, H. H. Fisher, A. Grimsdell, V. Participants, C. Daly, and E. R. Hunt, 1996: *The VEMAP phase I database: an integrated input dataset for ecosystem and vegetation modeling for the conterminous United States*. University Corporation for Atmospheric Research, Boulder, CO.

Knight, D., 1973: Leaf area dynamics of a shortgrass prairie in Colorado. *Ecology*, **54,** 891-896.

Körner, C., J. A. Scheel, and H. Bauer, 1979: Maximum leaf diffusive conductance in vascular plants. *Photosynthetica*, **13,** 45-82.

Koster, R. D., M. J. Suarez, and M. D. Heiser, 2000: Variance and predictability of precipitation at seasonal-to-interannual timescales. *Journal of Hydrometeorology*, **1,** 26-46.

Kramer, P. J., 1983: *Water Relations of Plants.* Academic Press.

Lafleur, P. M. and W. R. Rouse, 1990: Application of an energy combination model for evaporation from sparse canopies. *Agricultural and Forest Meteorology*, **49,** 135-153.

Laio, F., A. Porporato, C. P. Fernandez-Illescas, and I. Rodriguez-Iturbe, 2001a: Plants in water-controlled ecosystems: active role in hydrologic processes and response to water stress IV. Discussion of real cases. *Advances in Water Resources*, **24,** 745-762.

Laio, F., A. Porporato, L. Ridolfi, and I. Rodriguez-Iturbe, 2001b: Plants in water-controlled ecosystems: active role in hydrologic processes and response to water stress II. Probabilistic soil moisture dynamics. *Advances in Water Resources*, **24,** 707-723.

Larcher, W., 1980: *Physiological Plant Ecology.* 2nd ed. Springer-Verlag, 297 pp.

Levine, J. B. and G. D. Salvucci, 1999a: Equilibrium analysis of groundwater-vadose zone interactions and the resulting spatial distribution of hydrologic fluxes across a Canadian prairie. *Water Resources Research*, **35,** 1369-1383.

——, 1999b: Characteristic rate scale and timescale of supply-limited transpiration under a Richards-Cowan framework. *Water Resources Research*, **35,** 3947-3954.

Loague, K., 1992: Soil water content a R-5. Part 1. Spatial and temporal variability. *Journal of Hydrology*, **139,** 233-251.

Los, S. O., G. J. Collatz, P. J. Sellers, C. M. Malstrom, N. H. Pollack, R. S. DeFries, L. Bounoua, M. T. Parris, C. J. Tucker, and D. A. Dazlich, 2000: A global 9-yr biophysical land surface dataset from NOAA AVHRR data. *Journal of Hydrometeorology*, **1,** 183-199.

Luxmoore, R. J. and M. L. Sharma, 1980: Runoff responses to soil heterogeneity: Experimental and simulation comparisons for two contrasting watersheds. *Water Resources Research*, **16,** 675-684.

Mahfouf, J.-F., C. Ciret, A. Ducharne, P. Irannejad, J. Noilhan, Y. Shao, P. Thornton, Y. Xue, and Z.-L. Yang, 1996: Analysis of transpiration results from the RICE and PILPS workshop. *Global and Planetary Change*, **13,** 73-88.

Marani, M., G. Grossi, F. Napolitano, M. Wallace, and D. Entekhabi, 1997: Forcing, intermittency, and land surface hydrologic partitioning. *Water Resources Research*, **33,** 167-175.

McCuen, R. H., W. J. Rawls, and D. L. Brakensiek, 1981: Statistical analysis of the Brooks-Corey and the Green-Ampt parameters across soil textures. *Water Resources Research*, **17,** 1005-1013.

Melillo, J. M., J. Borchers, J. Chaney, H. H. Fisher, and S. Fox, 1995: Vegetation/ecosystem modeling and analysis project: Comparing biogeography and biochemistry models in a continental-scale study of terrestrial ecosystem responses to climate change and CO_2 doubling. *Global Biogeochemical Cycles*, **9,** 407-437.

Miller, D. A. and R. A. White, 1998: A conterminous United States multi-layer soil characteristics data set for regional climate and hydrology modeling. *Earth Interactions*, **2**.

Miller, E. E. and R. D. Miller, 1956: Physical theory for capillary flow phenomena. *Journal of Applied Physics*, **27,** 324-332.

Milly, P. C. D., 1982: Moisture and heat transport in hysteretic, inhomogeneous porous media. *Water Resources Research*, **18,** 489-498.

Milly, P. C. D. and P. S. Eagleson, 1987: Effects of spatial variability on annual average water balance. *Water Resources Research*, **23,** 2135-2142.

Monteith, J. L., 1965: Evaporation and the environment. *Symposia of the Society for Experimental Biology*, **19,** 205-234.

Myneni, R. B., R. R. Nemani, and S. W. Running, 1997: Estimation of global leaf area index and absorbed par using radiative transfer models. *IEEE Transactions Geoscience Remote Sensing*, **35,** 1380-1393.

Myneni, R. B., C. J. Tucker, G. Asrar, and C. D. Keeling, 1998: Interannual variations in satellite-sensed vegetation index data from 1981 to 1991. *Journal of Geophysical Research*, **103,** 6145-6160.

Neilson, R. P., 1995: A model for predicting continental-scale vegetation distribution and water balance. *Ecological Applications*, **5,** 362-385.

Newman, E. I., 1969: Resistance to water flow in soil and plant: I. Soil resistance in relation to amounts of root: theoretical estimates. *Journal of Applied Ecology*, **6,** 1-112.

Noy-Meir, I., 1973: Desert ecosystems: Environment and producers. *Annual Review of Ecological Systems*, **4,** 25-51.

Parlange, J. Y., M. Vauclin, R. Haverkamp, and I. Lisle, 1985: The relation between desorptivity and soil-water diffusivity. *Soil Science*, **139,** 458-461.

Penman, H. L., 1948: Natural Evaporation from open water, bare soil and grass. *Proceedings of the Royal Society*, **A193,** 120-145.

——, 1956: Evaporation: An introduction survey. *Netherlands Journal of Agricultural Science*, **1,** 9-29, 87-97, 151-153.

Petrie, G., 1991: Modelling, interpolation and contouring procedures. *Terrain Modelling in Surveying and Civil Engineering*, G. Petrie and T. J. M. Kennie, Eds., McGraw-Hill, Chapter 8.

Philip, J. R., 1958: The theory of infiltration, 7. *Soil Science*, **85,** 333-337.

Phillips, J. R., 1969: Theory of infiltration. *Advances in Hydroscience, vol. 5*, 215-296.

Porporato, A., F. Laio, L. Ridolfi, and I. Rodriguez-Iturbe, 2001: Plants in water-controlled ecosystems: active role in hydrologic processes and response to water stress III. Vegetation water stress. *Advances in Water Resources*, **24,** 725-744.

Prince, S., J. Haskett, M. Steininger, H. Strand, and R. Wright, 2001: Net primary production of U.S. midwest croplands from agricultural harvest yield data. *Ecological Applications*, **11,** 1194-1205.

Rauner, J. L., 1976: Deciduous Forest. *Vegetation and the Atmosphere*, J. L. Monteith, Ed., Academic Press, 241-262.

Rawls, W. J. and D. L. Brakensiek, 1982: Estimating soil water retention from soil properties. *Journal of the Irrigation and Drainage Division, Proceedings of the American Society of Civil Engineers*, **108,** 166-171.

——, 1985: Prediction of soil water properties for hydrologic modeling. *Watershed Management in the Eighties*, 293-299.

Rawls, W. J., D. L. Brakensiek, and K. E. Saxton, 1982: Estimation of Soil Water Properties. *Transactions of the ASAE*, 1316-1320.

Rawls, W. J., D. L. Brakensiek, and B. Soni, 1983: Agricultural management effects on soil water processes, Part I: Soil water retention and Green and Ampt infiltration parameters. *Transactions of the ASAE*, 1747-1750.

Restrepo-Posada, P. J. and P. S. Eagleson, 1982: Identification of independent rainstorms. *Journal of Hydrometeorology*, **55,** 303-319.

Richter, H., 1976: The water status in the plant; experimental evidence. *Water and Plant Life, Problems and Modern Approaches*, O. L. Lange, L. Kappe, and E. D. Schulze, Eds., Springer-Verlag, 42-58.

Ridolfi, L., P. D'Odorico, A. Porporato, and I. Rodriguez-Iturbe, 2000: Duration and frequency of water stress in vegetation: An analytical model. *Water Resources Research*, **36,** 2297-2303.

Ripley, E. A. and R. E. Redmann, 1976: Grassland. *Vegetation and the Atmosphere*, J. L. Monteith, Ed., Academic Press, 351-396.

Ritchie, J. T., E. D. Rhoades, and C. W. Richardson, 1976: Calculating evaporation from native grassland watersheds. *Transactions of the ASAE*, 1098-1103.

Robock, A., K. Y. Vinnikov, G. Srinivasan, J. K. Entin, S. E. Hollinger, N. A. Speranskaya, S. Liu, and A. Namkhai, 2000: The global soil moisture data bank. *Bulletin of the American Meteorological Society*, **81,** 1281-1299.

Rodriguez-Iturbe, I., A. Porporato, L. Ridolfi, V. Isham, and D. R. Cox, 1999: Probabilistic modelling of water balance at a point: the role of climate, soil and vegetation. *Proceedings of the Royal Society*, **455,** 3789-3805.

Rodriquez-Iturbe, I., D. Entekhabi, and R. L. Bras, 1991: Nonlinear dynamics of soil moisture at climate scales, 1. Stochastic analysis. *Water Resources Research*, **27,** 1899-1906.

Rosenbloom, N. A. and T. G. F. Kittel, 1996: A User's Guide to the VEMAP Phase I Database.

Ross, J., 1975: Radiative transfer in plant communities. *Vegetation and the Atmosphere, Vol. 1: Principles*, J. L. Monteith, Ed., Academic Press, 13-55.

Running, S. W. and E. R. Hunt, 1993: Generalization of a forest ecosystem process model for other biomes, BIOME-BGC, and an application for global-scale models. *Scaling Physiological Processes: Leaf to Globe*, Academic Press, Inc, 141-158.

Rutter, A. J., 1975: The hydrological cycle in vegetation. *Vegetation and the Atmosphere, Vol. 1: Principles*, J. L. Monteith, Ed., Academic Press, 111-154.

Sala, O. E., W. K. Lauenroth, W. J. Parton, and M. J. Trlica, 1981: Water status of soil and vegetation in a shortgrass steppe. *Oecologia*, **48,** 327-331.

Sala, O. E., W. J. Parton, L. A. Joyce, and W. K. Lauenroth, 1988: Primary production of the central grassland region of the United States. *Ecology*, **69,** 40-45.

Salvucci, G. D. and D. Entekhabi, 1994a: Equivalent steady soil moisture profile and the time compression approximation in water balance modeling. *Water Resources Research*, **30,** 2737-2749.

——, 1994b: Comparison of the Eagleson statistical-dynamical water balance model with numerical simulations. *Water Resources Research*, **30,** 2751-2757.

——, 1995: Hillslope and climatic controls on hydrologic fluxes. *Water Resources Research*, **31,** 1725-1739.

Salvucci, G. D. and C. Song, 2000: Derived distributions of storm depth and frequency conditioned on monthly total precipitation: Adding value to historical and satellite-derived estimates of monthly precipitation. *Journal of Hydrometeorology*, **1,** 113-120.

Schenk, H. J. and R. B. Jackson, 2002: The global biogeography of roots. *Ecological Monographs*, **72,** 311-3228.

Scurlock, J. M. O., G. P. Asner, and S. T. Gower, 2001: Global leaf area index data from field measurements, 1938-2000. *Global leaf area index data from field measurements, 1938-2000*, Oak Ridge National Laboratory Distributed Active Archive Center.

Sellers, P. J., 1985: Canopy reflectance, photosynthesis and transpiration. *International Journal of Remote Sensing*, **6,** 1335-1372.

Sellers, P. J., M. D. Heiser, and F. G. Hall, 1992: Relation between surface conductance and spectral vegetation indices at intermediate (100 m^2 to 15 km^2) length scales. *Journal of Geophysical Research*, **97,** 19033-19059.

Sellers, P. J., O. L. Sietse, C. J. Tucker, C. O. Justice, D. A. Dazlich, G. J. Collatz, and D. A. Randall, 1996b: A revised land surface parameterization (SiB2) for atmospheric GCMs Part II: the generation of global fields of terrestrial parameters from satellite data. *Journal of Climate*, **9,** 706-737.

Sellers, P. J., G. J. Randall, G. J. Collatz, J. A. Berry, C. B. Field, D. A. Dazlich, C. Zhang, G. D. Collelo, and L. Bounoua, 1996a: A revised land surface parameterization (SiB2) for atmospheric GCMs, Part I: Model formulation. *Journal of Climate*, **9,** 676-705.

Sellers, W. D., 1965: *Physical Climatology*. The University of Chicago Press, 272 pp.

Sharma, M. L. and R. J. Luxmoore, 1979: Soil spatial variability and its consequences on simulated water balance. *Water Resources Research*, **15,** 1567-1573.

Shuttleworth, W. J., 1993: Evaporation. *Handbook of Hydrology*, D. R. Maidment, Ed., McGraw-Hill, 4.1-4.53.

Shuttleworth, W. J. and J. S. Wallace, 1985: Evaporation from sparse crops: an energy combination theory. *Quarterly Journal of the Royal Meteorological Society*, **111,** 839-855.

Singh, J. S., D. G. Milchunas, and W. K. Lauenroth, 1998: Soil water dynamics and vegtation patterns in a semiarid grasland. *Plant Ecology*, **134,** 77-89.

Sivapalan, M., K. Beven, and E. F. Wood, 1987: On hydrologic similarity 2. A scaled model of storm runoff production. *Water Resources Research*, **23,** 2266-2278.

Stannard, D. I., 1993: Comparison of Penman-Monteith, Shuttleworth-Wallace, and modified Priestley-Taylor evapotranspiration models for wildland vegetation in semiarid rangeland. *Water Resources Research*, **29,** 1379-1392.

Stephenson, N. L., 1990: Climatic control of vegetation distribution: The role of the water balance. *The American Naturalist*, **135,** 649-667.

Stieglitz, M., D. Rind, J. S. Famiglietti, and C. Rosenzweig, 1997: An efficient approach to modeling the topographic control of surface hydrology for regional and global climate modeling. *Journal of Climate*, **10**.

Tellers, T. E. and P. S. Eagleson, 1980: Estimation of Effective Hydrologic Properties of Soils from Observations of Vegetation DensityRalph M. Parsons Laboratory for Hydrology and Water Resource Systems Report Number 254.

Thornthwaite, C. W., 1948: An approach toward a rational classification of climate. *Geographical Review*, **38,** 55-94.

Tieszen, L. L., B. C. Reed, N. B. Bliss, B. K. Wylie, and D. D. DeJong, 1997: NDVI, C_3 and C_4 production, and distributions in great plains grassland land cover classes. *Ecological Applications*, **7,** 59-78.

USDA, 1994: State Soil Geographic (STATSGO) Data Base, miscellaneous publication number 1492. US Department of Agriculture Natural Resource Conservation Service.

USGS, 1993: Seasonal Land Cover Regions. Printed map, US Geological Survey, US Department of Interior.

Valdes, J. B., R. Seoane, and G. R. North, 1994: A methodology for the evaluation of global warming impact on soil moisture and runoff. *Journal of Hydrometeorology*, **161,** 389-413.

Van Bavel, C. H. M. and D. I. Hillel, 1976: Calculating potential and actual evaporation from a bare soil surface by simulation of concurrent flow of water and heat. *Agricultural Meteorology*, **17,** 453-476.

Van den Honert, T. H., 1948: Water transport in plants as a catenary process. *Discussions of the Faraday Society*, **3,** 146-153.

Van Haveren, B. P., 1974: Soil water phenomena of a shortgrass prairie site, Department of Range Science, Colorado State University, 172 pp.

Van Haveren, B. P. and W. D. Striffler, 1976: Snowmelt recharge on a shortgrass prairie site. *Western Snow Conference*, Calgary, Alberta, 56-62.

Villabalobos, F. J. and E. Fereres, 1990: Evaporation measurements beneath corn, cotton, and sunflower canopies. *Agronomy Journal*, **82,** 1153-1159.

Warrick, A. W., G. J. Mullen, and D. R. Nielson, 1977: Scaling field-measured soil hydraulic properties using similar media concept. *Water Resources Research*, **13,** 355-362.

Wood, E. F., D. P. Lettenmaier, and V. G. Zartarian, 1992: A land-surface hydrology parameterization with subgrid variability for general circulation models. *Journal of Geophysical Research*, **97,** 2717-27-28.

Woodruff, J. F. and J. D. Hewlett, 1970: Predicting and mapping the average hydrologic response for the eastern United States. *Water Resources Research*, **6,** 1312-1326.

Woodward, F. I., 1987: *Climate and Plant Distribution*. Cambridge University Press, 174 pp.

Woodward, F. I., T. M. Smith, and W. R. Emanuel, 1995: A global land primary productivity and phytogeography model. *Global Biogeochemical Cycles*, **9,** 471-490.

Yeh, P. J., M. Irizarry, and E. A. B. Eltahir, 1998: Hydroclimatology of Illinois: A comparison of monthly evaporation estimates based on atmospheric water balance and soil water balance. *Journal of Geophysical Research*, **103,** 19 823-19 837.

Zheng, D., S. Prince, and R. Wright, 2003: Terrestrial net primary production estimates for 0.5° grid cells from field observations: a contribution to global biogeochemical modeling. *Global Change Biology*, **9,** 46-64.

Appendix A:

Integrated Hydrological/Ecological/Economic Modeling for Examining the Vulnerability of Water Resources to Climate Change[1]

---

[1] KOCHENDORFER, J. P. AND J. A. RAMÍREZ, 1996: Hydrologic/Ecological Modeling for Examining Regional Hydrologic Vulnerability to Climate Variability. Proceedings of the North American Water and Environment Congress '96 - ASCE, Anaheim, CA, 22-28 June; pp 1-6.

Integrated Hydrological/Ecological/Economic Modeling for Examining the Vulnerability of Water Resources to Climate Change

John P. Kochendorfer and Jorge A. Ramírez
Water Resources, Hydrologic and Environmental Sciences Division,
Civil Engineering Department, Colorado State University

Abstract

A methodology for assessing regional-scale hydrologic vulnerability to climate variability that incorporates ecologic and economic factors is presented. A simple economic model of damages due to hydrologic drought and the decision to invest in "augmented" yield to mitigate these damages is coupled to a *statistical-dynamical*, soil-vegetation-climate model of the annual water balance (Eagleson, 1978). The coupling is through the cumulative distribution function (CDF) of annual basin yield as estimated by the Eagleson model. Using Bayesian concepts for optimal decision-making under uncertainty, uncertainty in the yield CDF is propagated through the drought damage model to the hypothetical investment decision.

A.1. Introduction

The concept of "vulnerability" has increasingly been a matter for discussion in the climate impact assessment literature. Despite the volume of papers written, there has yet to emerge a consensus as to how to define and quantify vulnerability to climate change. Part of the difficulty is due to the many dimensions of the problem; the vulnerability of a given geographic region is not just a function of climatic variables but also of the ecological and socioeconomic systems dependent on the climate of the region. Quantifying climatic vulnerability must therefore truly be an interdisciplinary effort. In this paper, we present a methodology for assessing regional-scale hydrologic vulnerability to climate variability that incorporates ecologic and economic factors. A simple economic model of damages due to hydrologic drought and the decision to undertake an investment to mitigate these damages is coupled to a statistical-dynamical, soil-vegetation-climate model of the annual water balance (Eagleson. 1978). The coupling is through the cumulative distribution function (CDF) of annual basin yield as estimated by the Eagleson model.

Thoroughly quantifying the impact of climate change on the variability (not just the mean) of a hydroclimatic variable is essential because the frequencies of extreme events such as droughts are more dependent on the dispersion about the mean of the variable than the mean itself (Katz and Brown, 1992). Uncertainty is related to variability and equally as important. An irreducible amount of uncertainty about the water yield from a basin in each of the coming years may exist because the drivers of the water balance in the basin (most particularly climate) are stochastic processes—as best as we can understand them. However, an additional, presumably reducible amount of uncertainty arises from our lacking the knowledge or resources to model perfectly the "deterministic" physical and biological processes involved. While the Eagleson model accounts for a portion of the former type of uncertainty with a CDF of basin yield derived from a stochastic model of precipitation, it does not directly account for the latter form. However, with statistical-dynamical models such as Eagleson's, uncertainty in at least model parameters can be evaluated using a variety of techniques such as Monte Carlo simulation with relatively low computational effort. In the following analysis we use Latin hypercube sampling (Morgan and Henrion, 1990) to examine the sensitivity of the CDF of annual yield of an experimental watershed in Oklahoma to uncertainties in several of the climate and vegetation parameters. The uncertainty in the yield CDF is propagated through the damage model to the investment decision using Bayesian concepts for optimal decision-making under uncertainty (Winkler and Murphy, 1985; Morgan and Henrion, 1990; Benjamin and Cornell, 1970).

A.2. The Water Balance Model and its Application to the Study Watershed

The Eagleson model is a statistical-dynamical representation of the annual-average water budget in the vertical dimension of a homogeneous soil column. The model is "driven" by a stochastic model of precipitation that assumes that storms are composed of rectangular pulses that arrive by a Poisson process and that individual storm depths follow a gamma probability distribution. The soil physics of infiltration and exfiltration are based on the Philip (1957) solution to the one-dimensional equation of concentration-dependent diffusion and the Brooks and Corey (1966) model of soil hydraulic properties. Extraction of soil moisture by plant roots is modeled as a homogeneously distributed sink and is calculated as a fraction of potential evapotranspiration. Percolation to and capillary rise from a groundwater table are assumed to be steady-state fluxes. All fluxes are linearly superimposed. A key assumption of the model is that of the "time compression" of soil moisture, which replaces the time variability of soil moisture with its long-term mean (Salvucci and Entekhabi, 1994). The advantage of these and several other assumptions is that they allow for an analytical solution to the annual water balance and the derivation of a functional relationship between annual precipitation and the other components of the water balance.

In this paper, the component of the water balance with which we are concerned is runoff. Unfortunately, a discussion of the strengths and weaknesses of the way in which the one-dimensional Eagleson model represents runoff processes is beyond the scope of the present paper. We are currently investigating methods of incorporating surface processes beyond the infiltration excess runoff already in the model (e.g., Salvucci and Entekhabi, 1995). As strong believers in problem- driven analysis, we feel that additional complexities brought to the model should be based on how the model is meant to be used. The economic and decision-analytic framework presented in this paper is one potential use of the Eagleson model. Improvements to the model can be measured against the extent to which they can help to assess vulnerabilities to climate change and variability and to maker better adaptation decisions in response to uncertainties about climate. One enhancement to the model which we have added and which clearly has shown merit is the division of the soil into two horizons: an upper zone, roughly corresponding to the root zone, which interacts dynamically with the atmosphere, and a lower zone in which steady-state percolation and capillary rise occur. Other than this addition to the model, the version we have used for this paper is identical to Eagleson's original formulation.

For the present study, we have applied the modified Eagleson model to the East Bitter Creek watershed, which is within a reach of the Washita River in central Oklahoma intensively studied by the USDA Agricultural Research Service (USDA-ARS, 1983) and others. The East Bitter Creek watershed is 92 km^2 in area and dominated by native mixed-grass rangeland with much smaller percentages of cultivated pasture, crops and timber. Runoff and precipitation were gauged by the ARS continuously at numerous

Notation	Description	Value		Units
	CLIMATE:			
m_τ	mean length of rainy season	365		days
m_{tb}	mean time between storms	6.08		days
m_i	mean storm intensity	12.5		cm/day
m_{tr}	mean storm duration	0.267		days
m_h	mean storm depth	1.37		cm
κ	parameter of gamma distribution of storm depth	0.55		
e_p	mean rate of potential evapotranspiration	0.40		cm/day
	SOIL:	Upper	Lower	
K(1)	saturated effective hydraulic conductivity	5	4	cm/day
Ψ(1)	saturated soil matrix potential	75	27	cm
n	effective porosity	0.35	0.25	
m	soil pore size distribution index	0.76	0.43	
c	soil pore disconnectedness index	5.6	7.7	
d	diffusivity index	3.3	4.3	
Z	depth to water table	N/A	∞	cm
	VEGETATION:			
h_o	surface retention capacity	0.2		cm
k_v	potential transpiration efficiency	0.8		
M	vegetation canopy density	variable		

Table 1: Parameters of the Modified Eagleson Model

points within the watershed from 1964 to 1977. Over this period, the average annual precipitation and instream runoff were respectively, 75.5 cm and 7.53 cm.

The climate, soil and vegetation parameters of the water balance model and their values applied to the study watershed are listed in Table 1. Soil parameters were initially estimated from soil moisture retention and hydraulic conductivity data reported by Luxmoore and Sharma (1980) for a small, upland subcatchment in the watershed. These parameters were then adjusted over realistic and self-consistent ranges for the silt-loam soils that predominate in the watershed until the modeled mean annual total runoff and surface runoff were approximately equal to, respectively, the measured and estimated mean values. The annual average water balance estimated by the model after the fairly crude calibration of the soil parameters is shown in Table 2.

As indicated in Table 2, an interesting feature of the model is its separate estimates of plant transpiration and bare soil evaporation. Transpiration is estimated in the model to occur at an areal and time-averaged rate equal to a fraction, Mk_v (canopy density x potential transpiration efficiency), of the potential rate of evapotranspiration. Eagleson has used the model to suggest that plants may adjust their value of M in response to soil-moisture stress in a way that maximizes long-term mean soil moisture

Water Balance Component	(cm)
precipitation	78.8
transpiration	52.2
evaporation from bare soil	9.4
evap. from surface retention	8.5
surface runoff	5.8
groundwater runoff	2.9
total runoff	8.7

Table 2: Modeled Average Annual Water Balance

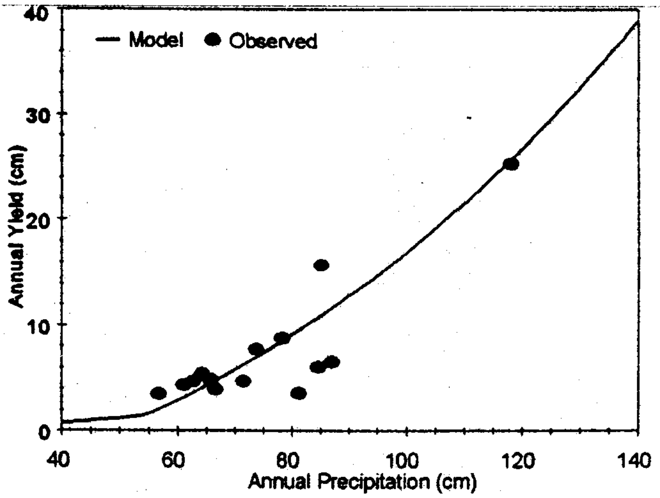

Figure 1: Precipitation vs. Yield

(Eagleson, 1978; Eagleson, 1982; Eagleson and Tellers, 1982). Despite the simplicity of this "ecological optimality" assumption, it is a way of estimating at least the direction of vegetation response to the interannual variability of precipitation. We have been examining modifications to the vegetation component of the model, including ones that reduce transpiration rates during drought stress.

The precipitation-water yield (*P-Y*) relationship estimated by the model for the parameterization in Table 1 is shown in Figure 1. Also shown in Figure 1 are the paired values of annual precipitation and yield measured over the period of record. It is quite evident from these data that the *P-Y* relationship is far from a true functional one. A variety of explanations are plausible for the amount of scatter about the monotonic function estimated by the model. The most intriguing involve issues of modeling scale and resolution. Along these lines, we have begun developing a distributed-parameter, monthly version of the model. Initial work with the data from East Bitter Creek and its sub-watersheds suggests that increasing temporal resolution is more important than increasing spatial resolution.

Despite the fact that the *P-Y* function of the lumped-parameter, annual version of the model is capable of explaining only some of the variance in annual runoff, it still may be useful to an economic analysis such as that carried out in the second part of this paper. The additional variance can be considered random noise that will be lost in the derived CDF of annual yield. The model also has an analytical form for the CDF of annual precipitation, making the derivation of the CDF of annual yield from the *P-Y* function

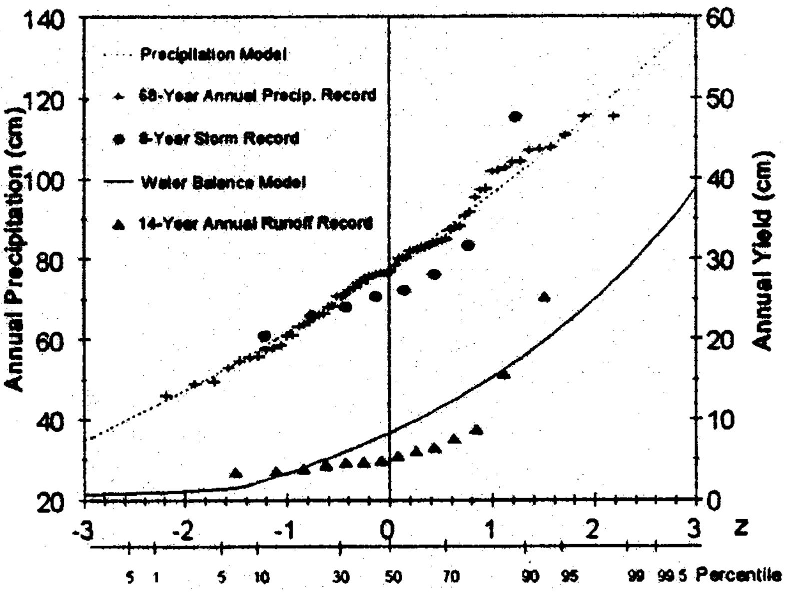

Figure 2: Precipitation and Yield CDFs

possible. Figure 2 compares the fit of the precipitation model to the empirical distribution of both a 68-year regionalized precipitation record and the eight years (1967-1974) of breakpoint precipitation data from which the storm parameters were derived. Whether or not the model actually accounts for all of the interannual variability of precipitation, it is clearly at least a better estimate than a fit to the eight annual values would provide. The derived CDF of yield produced by transforming the precipitation CDF with the *P-Y* function of the water balance model is shown in Figure 2, along with the empirical distribution for the 14 years of measured runoff from East Bitter Creek. As with the 8-year precipitation record, the short runoff record exaggerates the amount of variability. This is largely due to the one year of 115 cm of precipitation that both the longer precipitation record and the precipitation model indicate has about a 50-year return period.

In addition to providing a better estimate of the interannual variability of yield than would a short historical record, the water balance model also has the advantage of being a physically based model. As such it can be used to examine the sensitivity of the yield CDF to changes in the model parameters as might arise from climate or land-use changes. Figure 3 shows the sensitivity of the modeled yield CDF to changes in three of the climate parameters and one of the vegetation parameters. The magnitudes of these

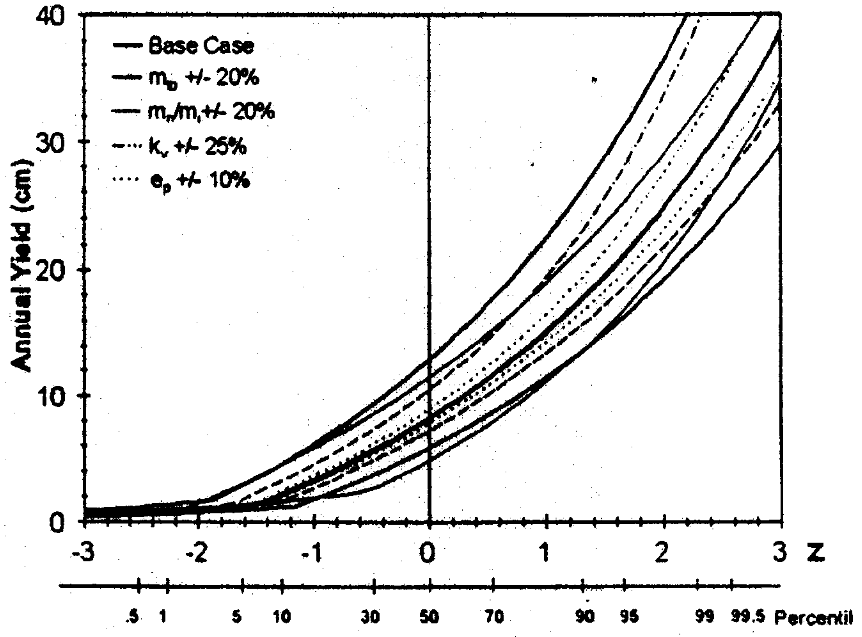

Figure 3: Sensitivity of the Yield CDF to Climate and Vegetation Changes

changes are based on the likely ranges of regional-scale climate changes and vegetation responses under a $2xCO_2$ global climate (Schaake, 1990; Allen, 1991). For example, k_v might increase as a result of greater water use efficiency of vegetation due to higher levels of CO_2. With regard to the climate parameters, it is worth noting that, although roughly the same percentage change in annual mean precipitation would result from the same percent change in the two storm parameters, very different shifts in the yield CDF occur. Specifically, surface runoff is much more sensitive to changes in mean storm depth/intensity than storm frequency.

A.3. An Economic Model of Drought Damages and Adaptation Decision-Making

Although the water balance model has obvious utility in quantifying the frequency of years of low basin yield and the sensitivity of this frequency to climate and vegetation changes, it still does not tell the whole story of hydrologic vulnerability. Vulnerability necessarily also has a socioeconomic dimension. Water in rivers has a derived demand. In other words, it is not the flows themselves that society values but the aesthetic pleasure, ecological integrity, electric power, irrigation water, transportation, recreation opportunities, etc., that they provide. To demonstrate how one might begin to

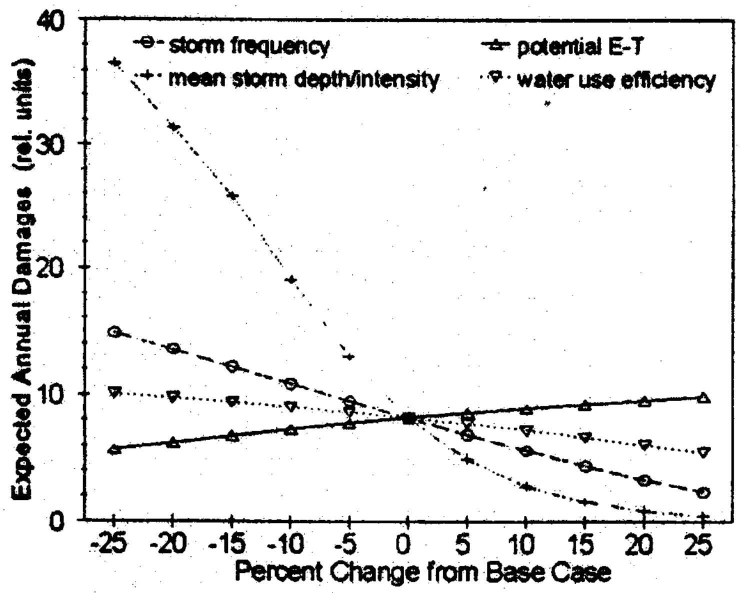

Figure 4: Sensitivity of Drought Damages to Climate and Vegetation Parameters

use the hydrologic information produced by the water balance model to assess the vulnerability of these economic and environmental goods and services to climate variability, we hypothesize a highly simplified world wherein one or a set of these goods or services are not adversely impacted as long as the yield of the basin of interest in any given year is above a "critical threshold". Below this threshold, damages are incurred which are an increasing function of the deficit below the threshold. Damages most typically would be measured in monetary terms, but in the otherworld of economics one is free to measure them in terms of, for example, fish killed or "utils" of lost enjoyment. Depending on the nature of the goods or services and associated damages, it could be argued that marginal damages increase, decrease or stay the same with the magnitude of the yield deficit. An exponential curve is a simple yet flexible equation which can be fit to any of the three types of marginal damage: $D = 0,\ Y>Y_c;\ D = a(Y_c - Y)^b,\ Y<Y_c$. The frequency of damages will increase with the critical threshold, Y_c, and the magnitude with the coefficient, *a*, and the exponent, *b*.

The probability of damages above a given value can be obtained from the CDF of damages that is derived with the damage function and the yield CDF. From the damages CDF, the expectation of annual damages can be calculated. For example, the expected annual damages are 8.2 for the base case yield CDF in Figure 3 and damage curve parameters: $Y_c = 8$ cm, $a=1$, $b=2$. Figure 4 shows the sensitivity of these annual expected damages to the same climate and vegetation parameters that were varied in Figure 3. Just as runoff is most sensitive to mean storm depth/intensity, drought damages are also most sensitive to these paired parameters.

Quantification of the frequency and magnitude of damages from drought still misses an additional aspect of vulnerability to climate change. Vulnerability is also a function of the ability of a society or an ecosystem to respond to climate change by adapting to the new climate in a way that mitigates damages. To examine this aspect of hydrologic vulnerability, we again turn to simplified economics. We suppose that it is possible through some type of investment to reduce the critical threshold, Y_c, of the damage function. The amount by which the threshold is reduced is termed the augmented yield, Y_a. The value of the parameters a and b of the damage function are assumed unaltered by the value of Y_a. Damages are now a function of the Yield CDF shifted by Y_a: $D=0$, $Y>Y_c-Y_a$; $D = a(Y_c-Y_a-Y)^b$, $Y<Y_c-Y_a$. The concept of augmented yield probably makes most sense for an investment consisting of the construction of a reservoir that is capable of providing a safe yield equal to Y_a. It also might make sense, though, for a project that protects or improves the habitat of an endangered species of fish susceptible to low flows. The shape of the function of annualized costs depends on the specific nature of the investment(s) considered. We again use a flexible exponential function to model the investment cost curve: $C = cY_a^d$. As good economic optimizers, and ignoring any tendency to risk aversion, we would choose to invest in a level of $Y_a=Y_a^*$ which minimizes the annual expected loss (equal to the annualized cost of the investment plus the annual expected damages given the reduced critical threshold). The optimal investment that minimizes expected loss is typically referred to as *Bayes' Decision*. For example sake, we use the water balance model parameters in Table 1 and economic parameters: $Y_c = 8$, $a = 1$, $b = 2$, $c = 3$, $d = 1$. The resulting value of $Y_a^* = 0.4$ cm corresponds to an expected annual loss of 8.1 (in comparison to the annual expected damages of 8.2 for no investment). For the given set of model parameters, one thus could conclude that the water resource system of the basin is for-the-most-part adapted as best as possible to the current climate.

Ideally, one could use the above economic model coupled to the regional-scale version of the water balance model to decide how to adapt to a potentially new climate. A few complexities should be added such as consideration of the likelihood and effects of multi-year droughts and the transience of climate change. One might argue that a fatal flaw of such an effort is that regional-scale estimates of climate change are at present highly uncertain, and therefore one would be at a loss to select values for the climate parameters. One of the advantages, though, of the water balance model is the relative ease with which uncertainty can be treated. Bayesian decision theory in fact recommends that uncertainty be included in the analysis. In order to investigate the importance of climate uncertainty for our hypothetical adaptation decision we ran the hydrological model 625 times, sampling each time by the Latin hypercube method from probability distributions of the four vegetation and climate parameters varied in Figures 3 and 4. In the absence of any sophisticated expert elicitation or uncertainty analysis of climate model output, uniform probability distributions were used for each of the four parameters, with ranges identical to those in Figure 3. With the assumption that the resulting 625 CDFs of annual yield were all equally as likely (*i.e.*, the input parameters are independent), we used the economic model to find the value, $Y_{aiu}^* = 1.5$ cm, the augmented yield which minimizes expected loss (equal to 11.1) given uncertainties in the parameters of the water balance model. This value can be compared to $Y_a^* = 0.4$ cm, which was selected when uncertainty in the model parameters was ignored. Given the assumed uncertainties, investment in Y_a^* would result in annual expected losses of 22.8, more than twice the amount associated with Y_{aiu}^*. Thus there is the potential for large benefits in including uncertainty in the analysis.

A.4. Acknowledgments

Partial support for this research was provided by the U.S. Department of Energy through a Graduate Fellowship for Global Change and the National Institute for Global Environmental Change under Project DEFCO3-90ER6 1010. The USDA-ARS Hydrology Laboratory provided precipitation and streamflow data.

A.5. References

Allen, L.H. 1991. Effects of Increasing Carbon Dioxide Levels and Climate Change on Plant Growth, Evapotranspiration, and Water Resources. In *Managing Water Resources in the West Under Conditions of Climate Uncertainty*. National Academy Press, Washington, D.C.

Benjamin, J.R. and C.A. Cornell. 1970. *Probability, Statistics and Decision for Civil Engineers*. McGraw- Hill, New York.

Brooks, R.R. and A.T. Corey. 1966. Properties of Porous Media Affecting Fluid Flow. *Journal of Irrigation and Drainage*, Vol. 1R2: 61-88.

Eagleson, P.S. 1978. Climate, Soil and Vegetation (7 parts). *Water Resources Research*, Vol. 14 No. 5: 705-776.

Eagleson, P.S. 1982. Ecological Optimality in Water Limited Natural Soil-Vegetation Systems: 1. Theory and Hypothesis. *Water Resources Research*, Vol. 18 No. 2: 325-340.

Eagleson, P.S. and T.E. Tellers 1982. Ecological Optimality in Water Limited Natural Soil-Vegetation Systems: 2. Tests and Applications. *Water Resources Research*, Vol. 18 No. 2: 341-354.

Katz, R.W. and B.G. Brown. 1992. Extreme Events in a Changing Climate: Variability is More Important than Averages. *Climatic Change*, July: 289-302.

Luxmoore, R.J. and M.L. Sharma. 1980. Runoff Responses to Soil Heterogeneity: Experimental and Simulation Comparisons for Two Contrasting Watersheds. *Water Resources Research*, Vol. 16 No. 4: 675-684.

Morgan, M.G. and M. Henrion. 1990. Uncertainty: A Guide to Dealing with Uncertainty in Quantitative Risk and Policy Analysis. Cambridge University Press.

Phillip, J.R. 1957. The Theory of Infiltration: 1. The Infiltration Equation and Its Solution. *Soil Science*, Vol. 83: 345-347.

Salvucci, G.D. and D. Entekhabi. 1994. Equivalent Steady Soil Moisture Profile and the Time Compression Approximation in Water Balance Modeling. *Water Resources Research*, Vol. 30, No. 10: 2737-2749.

Salvucci, G.D. and D. Entekhabi. 1995. Hillslope and Climatic Controls on Hydrological Fluxes. *Water Resources Research*, Vol. 31, No. 7: 1725-1739.

Schaake, J.C. 1990. From Climate to Flow. In *Climate Change and US. Water Resources*. John Wiley & Sons, New York.

Winkler, W.H. and A.R. Murphy. 1985. Decision Analysis. In A.H. Murphy and RW. Katz (eds), *Probability, Statistics and Decision Making in the Atmospheric Sciences*. Westview Press, Boulder, CO.

U.S. Department of Agriculture-Agricultural Research Service. 1983. *Hydrology, Erosion, and Water-Quality Studies in the Southern Great Plains Research Watershed, Southwestern Oklahoma, 1961 -1978*. USDA-ARS Water Quality and Watershed Research Laboratory, Chickasha, Oklahoma, ARM-S-29.

Appendix B:

The Impact of Land-Atmosphere Interactions on the Temporal Variability of Soil Moisture at the Regional Scale[1]

---

[1] KOCHENDORFER, J. P. AND J. A. RAMÍREZ, The Impact of Land Atmosphere Interactions in the Temporal Variability of Soil Moisture. *Journal of Hydrometeorology*. Vol 6. No. 1, 53-67.

The Impact of Land-Atmosphere Interactions on the Temporal Variability of Soil Moisture at the Regional Scale

John P. Kochendorfer and Jorge A. Ramírez

DEPARTMENT OF CIVIL ENGINEERING, COLORADO STATE UNIVERSITY,

FT. COLLINS, CO

Abstract

This study examines the impact of the nonlinear dynamics of soil-moisture feedbacks to precipitation on the temporal variability of soil moisture at the regional scale. Our approach first formulates the large-scale soil-water balance as an ordinary differential equation and then recasts it as a stochastic differential equation by incorporating colored noise representing the high-frequency temporal variability and correlation of precipitation. The underlying model couples the atmospheric and surface-water balances and accounts for both *precipitation recycling* and *precipitation-efficiency feedbacks,* which arise from the surface energy balance. Based on the governing Fokker-Planck equation, we derive three different analytical solutions (corresponding to differing forms and combinations of feedbacks) for the steady-state probability density function of soil moisture. Using NCEP/NCAR reanalysis data, estimates of potential evapotranspiration, and long-term observations of precipitation, streamflow and soil moisture, the model is parameterized for a 5°×5° region encompassing the State of Illinois. We show that *precipitation-efficiency feedbacks* can be significant contributors to the variability of soil moisture at the regional scale. *Precipitation recycling*, on the other hand, increases the variability by a negligible amount. For all feedback cases, the probability density function is unimodal and nearly symmetric. The analysis concludes with an examination of the dependence of the shape of the probability density functions on spatial scale. It is shown that the associated increases in either the correlation time scale or the variance of the noise will produce a bimodal distribution when *precipitation-efficiency* feedbacks are included. However, the magnitudes of the necessary increases are of an unrealistic magnitude.

B.1. Introduction

Since the seminal work of Charney et al. (1977), land-surface feedbacks have increasingly been recognized as significant sources of atmospheric variability. Soil moisture is perhaps the most important mediator of these feedbacks. In this paper, we examine the impact of land-atmosphere interactions on the temporal variability of regional-scale spatial averages of soil moisture. Our approach first formulates a large-scale, lumped-parameter water-balance model as an ordinary differential equation (ODE), with soil moisture as its state variable. In order to study the temporal variability in soil moisture in an analytical and probabilistic manner, we then recast the ODE as a stochastic differential equation (SDE) by adding colored noise that accounts for the high-frequency temporal variability and correlation of atmospheric moisture and precipitation efficiency. The underlying model of the coupled land-atmosphere water balance is formulated to capture both *precipitation recycling* and *precipitation-efficiency feedbacks*, which arise from the surface energy balance.

Our work here is based on that of Rodriguez-Iturbe et al. (1991), who used a lumped-parameter water-balance model formulated as an SDE to study continental-scale soil-moisture dynamics under the influence of land-atmosphere interactions. In their model, feedback from soil moisture to precipitation occurs through precipitation recycling only. In addition to including precipitation-efficiency feedbacks, our model also uses a fundamentally different relationship between atmospheric moisture and precipitation. A final important difference is that we use colored noise (rather than white noise, which is uncorrelated in time) to represent the high-frequency variability in advected atmospheric moisture. Wang et al. (1997) reformulated the original white-noise SDE of Rodriguez-Iturbe et al. (1991) to include colored noise. Our use of colored noise follows their general methodology. However, because our starting point is neither the same ODE nor a white-noise SDE, we arrive at necessarily and intrinsically different results.

For an example set of parameter values, Rodriguez-Iturbe et al. (1991) show that the probability density function (PDF) of soil moisture transitions from unimodal to bimodal as the variance of the noise increases. Using the same model, Entekhabi et al. (1992) demonstrate the bimodal phenomenon for a hypothetical set of parameter values representing both semiarid and semihumid climates. Relative to the semihumid case, the bimodality in the PDF of soil moisture for the semiarid case is much less pronounced and occurs with much greater variance in the noise. Using a correlation time scale of 0.2 years for the advected atmospheric moisture flux and the same parameter values in Rodriguez-Iturbe et al. (1991), Wang et al. (1997) find that their colored-noise solution enhances the bimodality in the PDF. As discussed in detail in Rodriguez-Iturbe et al. (1991) and Entekhabi et al. (1992), if a two-state dynamic exists in large-scale soil moisture, it would have profound implications for the persistence and variability of all components of the hydrological cycle. In particular, it may explain many of the multi-year droughts and pluvial periods observed over continental regions as oscillations within two distinct modes, with transitions between modes induced by ocean-controlled, low-frequency atmospheric variability.

Recycled precipitation has been shown to be a significant component of total precipitation at continental-scales (*e.g.*, Brubaker et al. 1993). Precipitation recycling, however, is somewhat of a misnomer in that moisture that re-falls as precipitation does so mostly downwind of the point from where it evaporated. Consequently, the ratio of atmospheric moisture recycled from within the region to that derived from outside the region increases downstream. A spatially lumped model may thus be inappropriate for studying this feedback process at continental scales. One useful improvement to the model would be to add a downwind dimension along the lines of Savenije (1995). However, because we are confining our analysis to the regional scale, the spatially lumped form of the model is justifiable.

While precipitation recycling may not be significant at the regional scale, there is the possibility that other important feedbacks exist through the surface energy balance. The potential for these feedbacks exists because the energy balance at the surface controls atmospheric convection, and the energy balance is in turn controlled by soil moisture (with vegetation as an intermediary) through the Bowen ratio and surface albedo. Our model incorporates the aggregate effect of all such feedback mechanisms as a precipitation efficiency factor (which determines the fraction of input moisture flux that falls as precipitation) that is a nonlinear function of soil moisture. We thus refer to them as both precipitation-efficiency feedbacks and energy-balance feedbacks, depending on the context.

Using NCEP/NCAR reanalysis data, estimates of potential evapotranspiration, and long-term observations of precipitation, streamflow and soil moisture, we parameterize our model for the region bounded by 37.5° N, 42.5° N, 87.5° W and 92.5° W (see Figure 1). This 5°×5° region encompasses all but the southern tip of Illinois. The Illinois State Water Survey (ISWS) has made observations of soil moisture using neutron probe techniques at 17 grass-covered sites across the state beginning as early as 1981

(Hollinger and Isard, 1994). To our knowledge, no other *in situ* soil-moisture observation network at such a scale for such a length of time has existed in the United States. Consequently, the ISWS data and Illinois have been the focus of several research efforts dealing with the large-scale water balance and land-atmosphere interactions (*e.g.*, Rodell and Famiglietti, 2001; Brown and Arnold, 1998; Eltahir and Yeh, 1999; Findell and Eltahir, 1997; and Yeh et al, 1998). It is fortuitous for the latter type of study that Illinois has a semihumid climate and is located in a midlatitude, midcontinental region. As demonstrated by the general circulation modeling study of Koster et al. (2000), it is generally semihumid to semiarid climates and midlatitude, midcontinental regions where land-surface feedbacks, relative to sea surface temperatures, have the greatest impact on the interannual variability of precipitation (and consequently soil moisture.) In midlatitudes, potential evapotranspiration is generally of such a magnitude that, where humidity is in an intermediate range, evapotranspiration is both significant and highly sensitive to soil moisture (*i.e.*, predominantly under soil control, as opposed to climate control.) Because evapotranspiration—in the form of latent heat—is a component of the energy balance in addition to the water balance, precipitation-efficiency feedbacks are expected to be highly sensitive to soil moisture in the same regions as is precipitation recycling.

Land-atmosphere feedbacks that act through the energy balance are often associated with changes in vertical gradients of temperature and moisture in the atmospheric boundary layer. For example, Eltahir (1998) theorizes that soil moisture has a positive feedback to precipitation through the effect of the surface energy balance on large-scale vertical gradients in moist static energy. His theory is supported with both an analysis of observations from Kansas (Zheng and Eltahir, 1998) and a modeling study of the drought of 1988 and the flooding of 1993 in the Midwestern United States (Pal and Eltahir, 2001), a domain that includes our study region. Through application of a regional climate model to several domains over Europe, Schär et al. (1999) show that significant differences in summertime convection result between uniformly dry and uniformly wet surface boundary conditions. In addition, there is a great deal of modeling and observational evidence for inhomogeneities in soil moisture and vegetation resulting in so-called "sea breeze" circulations through *horizontal* gradients in temperature and moisture in the atmospheric boundary layer, as for example created by irrigation (Pielke and Zeng, 1989) and other differences in land use and land cover. In our study region, there is a great deal of landscape patchiness created by agriculture fields and urbanization. In a study using satellite imagery, Brown and Arnold (1998) found a clustering of convective cloud cover along boundaries between differing land-cover types in Illinois during weak synoptic-scale flow. In addition, by comparison of that clustering with the ISWS soil-moisture data, they found that convective development occurred more often over the moister side of those boundaries. Although the mechanisms of feedbacks that act through the energy balance are undoubtedly multiple and complex, the evidence from the literature suggests that the net of all such feedbacks are positive over the entire observed range of soil moisture. Therefore, we assume that the mean precipitation efficiency is an increasing function of spatially averaged soil moisture.

B.2. Model Development and Analytical Solutions

B.2.1. Deterministic Differential Equation Governing the Water Balance

The differential equation governing the temporal evolution of soil moisture content in the root zone is

$$n_e Z_r \frac{ds}{dt} = P(s)\phi(s) - E(s) - R_g(s) \tag{1}$$

where s is the degree of soil saturation (dimensionless), n_e is the effective soil porosity (dimensionless), Z_r is the depth of the root zone (L), $P(s)$ is the rainfall rate (L/T), $\phi(s)$ is the fraction of precipitation which infiltrates (dimensionless), $E(s)$ is the evapotranspiration rate (L/T), and $R_g(s)$ is the net runoff to groundwater, i.e., percolation (L/T). Following Rodriguez-Iturbe et al. (1991), we write

$$E(s) = E_p s^{\varepsilon} \tag{2}$$

$$\phi(s) = 1 - r_s s^{\rho_s} \tag{3}$$

where E_p is the potential evapotranspiration rate (L/T), and ε, r_s, ρ_s are dimensionless constants. In parameterizing the model, it will be assumed that r_s takes on a value of either one or zero. When surface runoff is included, we want to ensure that the surface runoff ratio is unity for completely saturated soils (i.e., at $s=1$). As demonstrated in the appendix, this condition is necessary for bounding the solution of the SDE at $s=1$.

To the equation of Rodriguez-Iturbe et al. (1991) we have added a term for percolation to groundwater:

$$R_g(s) = Ks^{\rho_g} \tag{4}$$

where K is the effective large-scale saturated hydraulic conductivity (L/T), and ρ_g is a dimensionless constant. In contrast to surface runoff and evapotranspiration (which are highly dependent on the dynamics of storm and inter-storm periods), a power function for percolation to groundwater (by steady-state gravity drainage) is empirically and theoretically well established at a point scale (*e.g.*, Brooks and Corey 1966).

For the equation governing the rainfall rate, we assume that total precipitation is proportional to the total input to the atmospheric moisture flux over the region. The two sources of input are moisture advected to the region and evapotranspiration from within the region. Formulating the former quantity for a two-dimensional land surface, we write

$$P(s) = h(s)[\mathrm{A} + E(s)] \tag{5}$$

where A is the moisture flux advected to the region per unit area of land surface (L/T), and h is the precipitation efficiency, i.e., the fraction of input moisture flux which falls as precipitation. Schär et al. (1999) use the same equation, absent the explicit dependence on s, to determine precipitation efficiencies in the output of their regional climate model. We have included a dependence on s as a means of capturing energy-budget feedbacks as mediated by soil moisture. As is typical for a quantity defined as efficiency, h is theoretically limited to being no greater than one in the steady state. We use a power function for $h(s)$, as was done for $E(s)$, $R_g(s)$ and $\phi(s)$. Our equation for the precipitation rate as a function of soil moisture then becomes

$$P(s) = (\zeta + \eta s^{\theta})(\mathrm{A} + E_p s^{\varepsilon}) \tag{6}$$

where ζ, η and θ are nonnegative constants (assuming a net positive feedback). Notice that s appears in two terms of (6). These terms represent energy-budget feedbacks and precipitation recycling, respectively. A constant is added to the power law relationship in the precipitation efficiency function so that, in the case of completely dry soil (i.e., $s=0$), the precipitation efficiency is not zero. Setting η equal to zero will fix the precipitation efficiency at ζ, thereby removing the energy-budget feedbacks and leaving only precipitation recycling.

We substitute (2), (3), (4) and (6) into (1), divide by n_eZ_r, and normalize the atmospheric moisture flux by $\bar{A}$, the temporal mean of A, to arrive at a form of the differential equation for the water balance which involves only the time dimension:

$$ds/dt = a(\zeta + \eta s^{\theta})(\alpha + \beta s^{\varepsilon})(1 - r_s s^{\rho_s}) - e_p s^{\varepsilon} - k s^{\rho_g} \tag{7}$$

where $a = \bar{A}/n_eZ_r\,(T^{1})$, $\alpha = A/\bar{A}$, $\beta = E_p/\bar{A}$, $e_p = E_p/n_eZ_r\,(T^{1})$, and $k = K/n_eZ_r\,(T^{1})$. α is a dimensionless measure of advected moisture flux and is the external driver of the system.

B.2.2. Colored-Noise Formulation of the Stochastic Differential Equation

Conceptually, we can transform (7) from a deterministic to a stochastic differential equation by recognizing the existence of high frequency variability (*i.e.*, noise) in any of its three flux components. Precipitation undoubtedly contains the greatest amount of high frequency variability, and so we add noise to this component only. The precipitation efficiency, h, and the atmospheric moisture flux, α, are both rapidly varying quantities. The former contains noise internal to the system, while the latter contains noise external to the system. We treat both α and h as the sums of a mean and a stochastic noise term:

$$\alpha = 1 + \sigma_\alpha \gamma_\alpha \tag{8}$$

$$h(s) = \zeta + \eta s^\theta + \sigma_h(s)\gamma_h \tag{9}$$

where σ_α is the standard deviation of α, $\sigma_h(s)$ is the standard deviation of h, and γ_α and γ_h are stochastic noise (all dimensionless). The mean of the noise in both equations is zero, and the standard deviation is one. It is also typical to assume that the noise in an SDE is Gaussian. Wang et al. (1997) show that this assumption is unnecessary for the governing Fokker-Planck equation (FPE) to be valid. Non-Gaussian noise is particularly useful for applications, such as the present, in which the noisy quantities take on only nonnegative values.

As will be seen in Section 3.4, the coefficient of variation of h appears to be independent of soil moisture. Therefore we write

$$\sigma_h(s) = v_h(\zeta + \eta s^\theta) \tag{10}$$

where v_h is the coefficient of variation of h. Substituting (2), (8), (9) and (10) into (5), along with $A = \alpha \bar{A}$ and $E_p = \beta \bar{A}$, we have

$$P(s, \gamma_\alpha, \gamma_h) = \overline{A}(\zeta + \eta s^\theta)[v_h \sigma_\alpha \gamma_h \gamma_\alpha + (1 + \beta s^\varepsilon) v_h \gamma_h + \sigma_\alpha \gamma_\alpha + 1 + \beta s^\varepsilon] \tag{11}$$

For the purpose of analytical tractability, we would like to combine the two noise components, γ_α and γ_h, into a single, composite noise. A complicating factor is the product of $(1+\beta s^\varepsilon)$ and γ_h in (11). If the second term in the former is always small relative to one (which is equivalent to assuming that the evaporative flux is small relative to the mean of the input moisture flux), we can ignore its variability and replace s by $\bar{s}$, its temporal mean. Provided that the PDF of s is not heavily skewed, a reasonable *a priori* estimate of $\bar{s}$ is the deterministic steady state, which can be found by setting (7) equal to zero. In Section 3, we estimate a value for β of 0.087. Given that the maximum value of s is one, we can conclude that βs^{ε} will always be less than 0.087. Under the assumption that s is stationary in the second term in the brackets of (11), we define a new random variable,

$$\begin{aligned}\Gamma &= \nu_h \sigma_\alpha \gamma_h \gamma_\alpha + (1+\beta \bar{s}^{\varepsilon})\nu_h \gamma_h + \sigma_\alpha \gamma_\alpha \\ &= \mu + \sigma\gamma\end{aligned} \tag{12}$$

where γ is the composite noise (with zero mean and unit variance), and μ and σ are the mean and standard deviation of Γ. (11) can then be rewritten as

$$P(s,\gamma) = \bar{A}(\zeta + \eta s^{\theta})(\mu + \sigma\gamma + 1 + \beta s^{\varepsilon}) \tag{13}$$

Using basic principles for the addition and multiplication of random variables (Benjamin and Cornell, 1970), it can be shown that

$$\sigma \approx \left[(1+\nu_h^{\,2})\sigma_\alpha^{\,2} + (1+\beta\bar{s}^{\varepsilon})^2 \nu_h^{\,2} + 2(1+\beta\bar{s}^{\varepsilon})\nu_h \sigma_\alpha Cov[\gamma_\alpha, \gamma_h]\right]^{1/2} \tag{14}$$

$$\mu = \nu_h \sigma_\alpha Cov[\gamma_\alpha, \gamma_h] \tag{15}$$

where $Cov[\gamma_\alpha, \gamma_h]$ is the covariance of γ_α and γ_h. Including covariance between h and α captures a presumed dependence of precipitation efficiency on the external input of moisture (and associated latent heat).

Replacing the deterministic form of precipitation in (7) with the stochastic formulation, (13), allows us to write an SDE of the Langevin form (Gardiner 1985):

$$ds_t/dt = \Delta(s_t) + \sigma\delta(s_t)\,\gamma_t \tag{16a}$$

where $\Delta(s_t)$ is the drift function, and $\sigma\delta(s_t)$ is the diffusion function. These functions are defined in our model by

$$\Delta(s) = a(\mu + 1 + \beta s^{\varepsilon})(\zeta + \eta s^{\theta})(1 - r_s s^{\rho_s}) - e_p s^{\varepsilon} - ks^{\rho_g} \tag{16b}$$

$$\delta(s) = a(\zeta + \eta s^{\theta})(1 - r_s s^{\rho_s}) \tag{16c}$$

The use of the terms *drift* and *diffusion* dates from the original application of stochastic calculus to the study of Brownian motion and other diffusion processes. The subscript t is used in the usual sense to indicate the stochastic time-dependence of a quantity. As in (16b,c), we will frequently drop the subscript for the sake of notational parsimony, especially when time is not explicitly part of the equation.

Both α and h are temporally correlated, and so γ also possesses temporal correlation. In other words, we need to treat the noise in our SDE as colored, as opposed to more commonly used white noise, which is uncorrelated in time. One approach to coloring the noise in an SDE is to treat the noise as being generated by the Ornstein-Uhlenbeck process (*e.g.*, Wang et al. 1997, Høyrup 1996). The origin of the Ornstein-Uhlenbeck process is in Langevin's model of Brownian motion (Gardiner 1985) in which the velocity (rather than the position) of the particle is the principal stochastic variable subject to a white-noise forcing. The result is that the velocity is no longer non-differentiable in time and thus possesses temporal correlation. Conceptualizing γ as velocity in the Ornstein-Uhlenbeck process, we can write an SDE for γ of the form

$$d\gamma_t = -\frac{1}{\tau}\gamma_t dt + \sqrt{D}\, dW_t \tag{17}$$

where τ is the correlation time scale of γ, D is the diffusion coefficient, and dW_t is the derivative of the Weiner process (Gardiner 1985). The Weiner process is the stochastic integration of white noise. Gardiner (1985) shows that, in the steady state,

$$Var\,[\gamma_t] = \frac{D\tau}{2} \tag{18}$$

$$Cov[\gamma_{t_1}, \gamma_{t_2}] = \frac{D\tau}{2} e^{-|t_1 - t_2|/\tau} \tag{19}$$

In order that (18) and (19) both equal unity when $t_1 = t_2$,

$$D = \frac{2}{\tau} \tag{20}$$

The autocovariance functions of the three noise-containing terms in (11) can be aggregated in the same manner as the variances. If the correlation time scales of γ_α and γ_h are of the same order of magnitude, the autocovariance function of γ can be approximated well as exponential by equating the autocorrelation function of the composite noise with (19) at t_1-$t_2 = \tau$. This gives

$$\begin{aligned} \frac{\sigma^2}{e} &= (1 + \beta\bar{s}^{\varepsilon})^2 \nu_h{}^2 e^{-\tau/\tau_h} + \sigma_\alpha{}^2 e^{-\tau/\tau_\alpha} + \nu_h{}^2 \sigma_\alpha{}^2 e^{-\tau(\tau_\alpha + \tau_h)/\tau_\alpha \tau_h} \\ &\quad + (1 + \beta\bar{s}^{\varepsilon}) \nu_h \sigma_\alpha Cov[\gamma_\alpha, \gamma_h] \left(e^{-\tau/\tau_{\alpha,h}} + e^{-\tau/\tau_{h,\alpha}} \right) \end{aligned} \tag{21}$$

where τ_α and τ_h are the correlation time scales of γ_α and γ_h, respectively, and $\tau_{\alpha,h}$ and $\tau_{h,\alpha}$ are the cross-correlation time scales of γ_α and γ_h. τ can then be solved for numerically using (21).

Solving for γ in (16a) and substituting the result into (17) along with (20) yields

$$\frac{d}{dt}\left(\frac{1}{\sigma\delta(s)} \left[\frac{ds}{dt} - \Delta(s) \right] \right) = -\frac{1}{\tau} \left(\frac{1}{\sigma\delta(s)} \left[\frac{ds}{dt} - \Delta(s) \right] \right) + \sqrt{\frac{2}{\tau}} \frac{dW}{dt} \tag{22}$$

Differentiating the left-hand side (LHS) of (22) and rearranging gives

$$\frac{d^2 s}{dt^2} = \frac{1}{\delta(s)}\frac{\partial \delta(s)}{\partial s}\left(\frac{ds}{dt}\right)^2 + \left[\delta(s)\frac{\partial}{\partial s}\left(\frac{\Delta(s)}{\delta(s)}\right) - \frac{1}{\tau}\right]\frac{ds}{dt} + \frac{\Delta(s)}{\tau} + \sqrt{\frac{2}{\tau}}\sigma\,\delta(s)\frac{dW}{dt} \qquad (23)$$

As a simplifying approximation, we discard the squared and second-derivative terms (i.e., the higher order terms) to arrive at

$$ds = \frac{\Delta(s)dt + \sqrt{2\tau}\sigma\,\delta(s)dW}{1 - \tau\,\delta(s)\dfrac{d}{ds}\left(\dfrac{\Delta(s)}{\delta(s)}\right)} \qquad (24)$$

We define new drift and diffusion terms,

$$A(s) = \frac{\Delta(s)}{1 - \tau\,\delta(s)\dfrac{d}{ds}\left(\dfrac{\Delta(s)}{\delta(s)}\right)} \qquad (25a)$$

$$\sqrt{B(s)} = \frac{\sqrt{2\tau}\sigma\,\delta(s)}{1 - \tau\,\delta(s)\dfrac{d}{ds}\left(\dfrac{\Delta(s)}{\delta(s)}\right)} \qquad (25b)$$

in order to write (24) in another standard form of the Langevin equation (Gardiner 1985):

$$ds_t = A(s_t)dt + \sqrt{B(s_t)}dW_t \qquad (25c)$$

The time evolution of the PDF of s is governed by the Ito FPE (Gardiner, 1985),

$$\frac{\partial}{\partial t} f_S(s_t,t) = -\frac{\partial}{\partial s}[A(s_t) f_S(s_t,t)] + \frac{1}{2}\frac{\partial^2}{\partial s^2}[B(s_t) f_S(s_t,t)] \qquad (26)$$

where $f_S(s_t,t)$ is the PDF of s at time t.

B.2.3. Steady-State Solution of the Fokker-Planck Equation

Under steady-state conditions, the LHS of (26) equals zero, and $f_S(s_t,t)=f_{S_s}(s)$ (where the first subscript is the variable s, and the second subscript indicates the steady state), with the solution (Gardiner 1985),

$$f_{S_s}(s)=\frac{C}{B(s)}exp\left(2\int_0^s\frac{A(x)}{B(x)}dx\right) \tag{27a}$$

where C is a normalization constant such that

$$\int_0^1 f_{S_s}(s)ds=1 \tag{27b}$$

We now consider the existence and form of a general, analytical solution for (27a). None was found for the general forms of $\Delta(s)$ and $\delta(s)$. However, when the exponents θ, ε, ρ_s and ρ_g assume whole or half integer values, a particular solution usually can be found. In addition, when ζ is set equal to zero, a solution exists for all values of the exponents. Even with $\zeta=0$, the solution consists of a large number of infinite series sums. If we assume that τ is on the order of a few days or less, and that the surface runoff ratio is small—generally a reasonable assumption for all but the most humid climates and steep terrain—we can approximate the denominators in (25a,b) as one (see Appendix). With this approximation, (27a) becomes

$$f_{S_s}(s)=\frac{C}{2\tau\sigma^2\delta^2(s)}\exp\left(\frac{1}{\tau\sigma^2}\int_0^s\frac{\Delta(x)}{\delta^2(x)}dx\right) \tag{28}$$

If we assume all precipitation infiltrates by setting r_s equal to zero (see Appendix), (28) evaluates to

$$f_{s_s}(s)=\frac{C}{2\tau\sigma^2(\zeta+\eta\, s^{\theta})^2}$$

$$exp\left\{\frac{1}{\tau\sigma^2}\left[(1+\mu)\,s\sum_{n=0}^{\infty}\frac{\left(\dfrac{-\eta s^{\theta}}{\zeta}\right)^n}{\dfrac{1}{\theta}+n}+\sum_{i=1}^{3}\left(U_i s^{V_i}\left[\frac{\zeta}{\zeta+\eta\, s^{\theta}}+(\theta-V_i)\right]\sum_{n=0}^{\infty}\frac{\left(\dfrac{-\eta s^{\theta}}{\zeta}\right)^n}{\dfrac{V_i}{\theta}+n}\right)\right]\right\}$$

(29a)

where

$$\mathbf{U}_{\mathrm{T}}=\left[\frac{a\zeta\,\beta-e_p}{a\zeta},-\frac{k}{a\zeta},\frac{\eta\beta}{\zeta}\right] \qquad (29b)$$

$$\mathbf{V}_{\mathrm{T}}=\lfloor\varepsilon+1,\rho_g+1,\theta+\varepsilon+1\rfloor \qquad (29c)$$

If in addition $\zeta = 0$, the integration in (28) leads to:

$$f_{s_s}(s)=\frac{C}{2\tau\sigma^2\eta^2\, s^{2\theta}}$$

$$\exp\left\{\frac{s^{1-\theta}\left[\dfrac{(\mu+1)}{1-\theta}-\dfrac{ks^{\rho_g}}{a\eta s^{\theta}(1-2\theta+\rho_g)}+s^{\varepsilon}\left(\dfrac{\beta}{1-\theta+\varepsilon}-\dfrac{e_p}{a\eta s^{\theta}(1-2\theta+\varepsilon)}\right)\right]}{\tau\sigma^2 a\eta}\right\}$$

(30)

with the constraints $\theta \neq 1$, $\theta-\varepsilon \neq 1$, $2\theta-\varepsilon \neq 1$, and $2\theta-\rho_g \neq 1$. As a final case, if $\eta = 0$, (29) reduces to

$$f_{s_s}(s)=\frac{C}{2\tau\sigma^2\zeta^2}\quad\exp\left\{\frac{s\left[a\zeta\left(\mu+1+\dfrac{\beta s^{\varepsilon}}{1+\varepsilon}\right)-\dfrac{ks^{\rho_g}}{1+\rho_g}-\dfrac{e_p s^{\varepsilon}}{1+\varepsilon}\right]}{\tau\sigma^2 a^2\zeta^2}\right\} \qquad (31)$$

The first two cases (*i.e.*, equations 29 and 30) are those with precipitation-efficiency feedbacks and precipitation recycling, while the third (*i.e.*, equation 31) captures only the latter. A fourth case with no feedbacks at all can be had by setting β equal to zero in (31).

B.3. Estimation of Parameter Values for the Study Region

B.3.1. Soil Moisture

Monthly, spatial averages of s were calculated using data from the 14 ISWS stations (see Figure 1) that both began measurement in 1983 and are located in the dominant silt-loam soils. The data are currently available through November 2001 from the Global Soil Moisture Databank (Robock et al. 2000), making for a total of 227 months. An important aspect to vertically averaging the soil moisture data is selection of an averaging depth. We want to measure s over the depth that responds to high frequency atmospheric variability. This is often assumed to be the depth of the root zone, Z_r. Root density typically decreases exponentially with depth (Jackson et al. 1996), and so a single value for root depth is often difficult to determine. An alternative approach is to examine the coefficients of variation in soil moisture content as a function of depth. For the 14 ISWS sampling locations, the coefficients of variation generally decrease with depth in an exponential fashion with most of the variability damped out at about the 70-90 cm sampling interval. Therefore, a value of 90 cm was selected for Z_r. The mean effective soil porosity for the soils was estimated as 0.48, resulting in a value of $n_e Z_r$ of 43 cm. The vertically averaged values of s were then averaged within each month, followed by an averaging across stations to obtain a single statewide average for each month.

B.3.2. Precipitation

Monthly precipitation estimates for the study region were extracted from a monthly data set generated by the PRISM model (Daly et al. 1994) for the Vegetation/Ecosystem Modeling and Analysis Project (VEMAP) (http://www.cgd.ucar.edu/vemap/). These data cover the lower 48 states at a 0.5° resolution and span the period 1895-1993. In addition, daily precipitation data from the NOAA Climate Prediction Center (CPC) (Higgins et al. 2000) as made available by the NOAA-CIRES Center for the Diagnosis of Climate (http://www.cdc.noaa.gov/cdc/data.unified.html) were used in the calculation of daily values of *h* as described below in Section 3.4. These data cover the lower 48 states at a 0.25° resolution over the period 1948-1997. Aggregated to the monthly scale for the study region, they agreed extremely well with the PRISM data ($R^2 > 0.99$). The eleven-year overlap (1983-1993) of the VEMAP and ISWS data was selected as the parameterization period. Table 1 lists all parameter values, the derivation of which is further detailed below.

B.3.3. Surface Runoff, Groundwater Runoff, and Evapotranspiration

Daily data from US Geological Survey stream gauges (http://water.usgs.gov/nwis/discharge) were used to estimate monthly runoff over the parameterization period. In order to minimize routing times and to offset sampling bias in the soil moisture data, 14 small river basins were identified that contain, or are near, the soil-moisture sampling locations (see Figure 1 for locations of gauges). To divide total streamflow into storm flow and base flow, we used the hydrograph separation methodology of Woodruff and Hewlett (1970). The resulting average surface runoff ratio was found to be 0.13. Two sets of values for K and ρ_g, one under the assumption that all streamflow is groundwater runoff (r_s=0) and one with surface runoff included (r_s=1), were determined via a log-log regression of (4) (see Figures 2a,b). Likewise, a value for ρ_s in the case of r_s=1 was determined via a log-log regression of the surface runoff ratio versus soil moisture (see Figure 2c). As evidenced by the distinction made in Figure 2 between months of decreasing (March-August) and increasing (September-February) groundwater storage, estimates of groundwater runoff are subject to significant storage effects. It is assumed, however, that months of increasing storage will offset months of decreasing storage in the regression.

Annual values of evapotranspiration were estimated as the difference between precipitation and streamflow. Annual values were used because changes in vadose-zone and groundwater storage are too significant at the monthly scale. As long as ε in (2) does not deviate much from unity, the annual scale should provide a reasonable approximation of the exponent. As shown in Figure 3, a regression of $log(E/E_p)$ versus $log(s)$ produced a value for ε of 1.2, with an R^2 of 0.52. Estimates of annual potential evapotranspiration were aggregated from monthly estimates, which were calculated using the Penman equation (Penman 1948) as presented by Shuttleworth (1993). Inputs to the Penman equation where derived mainly from the VEMAP data set, with exception of surface windspeed, which was derived from NCEP/NCAR reanalysis data, and surface albedo, which was taken from a gridded, monthly climatology developed by Hobbins et al. (2001).

B.3.4. Atmospheric Moisture Flux and Precipitation Efficiency

Results from the NCEP/NCAR reanalysis project (Kalnay et al. 1996) as provided by NOAA-CIRES CDC (http://www.cdc.noaa.gov/cdc/reanalysis/) were the source of windspeed, specific-humidity and surface-pressure data. These data are at a six-hour time step and are resolved vertically by 14 pressure levels and horizontally at 2.5° latitude and longitude. Thus eight grid points bound the study region, with a single grid point at the center (see Figure 1). At each of these nine grid points, the meridional and zonal components of the horizontal moisture flux were vertically integrated via linear interpolation of wind and specific humidity and truncation at the surface pressure. The general form of this integration is

$$F_{u,v} = \frac{p_s}{g} \int_{p_s}^{0} w_{u,v}(p)\, q(p)\, dp \qquad (32)$$

where $F_{u,v}$ are the horizontal moisture flux components ($ML^{-1}T^{1}$), p_s is the surface pressure ($ML^{-1}T^{2}$), g is the acceleration due gravity (LT^{2}), p is the atmospheric pressure ($ML^{-1}T^{2}$), $w_{u,v}$ are the wind components (LT^{1}), and q is the specific humidity (dimensionless). Daily values of $F_{u,v}$ for the study region were obtained by taking the mean of the six-hour values at each grid point and then averaging across the nine grid points, weighting each by the fraction of the study region it represents. We divided the two flux components by the respective downwind length of the study region and the density of water to arrive at the desired dimensions of LT^{1}, where the length dimension represents water depth. The magnitude of the vector sum of the two components gives a single value, F_A, for the mean atmospheric moisture flux over the study region.

Using the analogy of a streamtube with uniform precipitation and evapotranspiration down its length (e.g., Entekhabi et al., 1992; Budyko, 1974), it can be shown that

$$A = F_A - \frac{(E - P)}{2} \tag{33}$$

Thus, to obtain daily values of A, we also need daily values of E. From an atmospheric water balance,

$$E = P + \nabla \bullet \mathbf{F} + dW_a / dt \tag{34}$$

where$\nabla \bullet \mathbf{F}$ is the divergence of atmospheric moisture from the region (LT^{1}) and dW_a/dt is the rate of change of moisture stored in the atmosphere above the region (LT^{1}). Via comparison to a surface water balance, Yeh at al. (1998) show that use of (34) with the NCEP/NCAR reanalysis data provides a reasonably accurate monthly climatology of E for the study region, but that there are significant errors to estimates for individual months (hence the reason such estimates were not used in the parameterization of (2)). Undoubtedly, daily estimates calculated with (34) will be even more inaccurate. Both the analysis of Yeh et al. and our own suggest that the accuracy of reanalysis-based evapotranspiration estimates decreases with decreasing size of the region. Fortunately, A —and thus its contribution to the moisture flux relative to E—is inversely proportional to the downwind length of the region. For the study region, maximum evapotranspiration occurs in July, for which we estimated a mean value of E of 4.2 mm/day, which is only about 10% of the July mean of A. Therefore, we can immediately conclude that evapotranspiration from within the region contributes minimally to the average atmospheric moisture flux over the study region. The impact this has on the variability of soil moisture is seen in Section 4.

Daily values of α were calculated by dividing the daily values of A by the annual harmonic in the means of A. As per (5), dividing daily precipitation by the daily estimates of $A + E$ provides daily values of h for the period 1983-1993. In this eleven-year period, there are only 70 days in the CPC precipitation data when all of the grid cells comprising the study region are assigned zero precipitation. The study region thus appears to be large enough that the spatial average of daily precipitation—and hence h—can be modeled as a continuous process. In order to investigate the dependence of the standard deviation of h on s, we averaged the standard deviation and mean within each month. Those values are plotted against each other in Figure 4 for the 132 months in the parameterization period. Based on the correlation between the two quantities, and assuming that s is relatively invariant within a given month, it appears that the standard deviation has the same dependence on s as does the mean, i.e., the coefficient of variation is independent of s. We use the slope of the regression line in Figure 4 as the coefficient of variation of h.

The next parameter values that we determine are the covariance and correlation time scales of γ_α and γ_h. Daily values of α vs. h are plotted in Figure 5. Only a small amount of positive correlation is evident in the plot, particularly at higher values. The correlation coefficient between α and h, which is approximately equal to the covariance of γ_α and γ_h, is 0.24. Autocorrelation and cross-correlation coefficients of the daily values of α and h are plotted in Figure 6. Fits to exponential autocorrelation functions were performed via least squares regression on a natural log transform of the values of the correlation coefficients up to an including the first value below 0.05. The cutoff was selected as a compromise between statistical significance and the need for an adequate number of points. The corresponding values of τ_α and τ_h are 1.79 and 0.86 days, respectively. Such correlation time scales are consistent with the passing of synoptic-scale fronts. With the parameters of α and h and their associated noise components determined, we apply (13), (15) and (21) to arrive at values for the mean, standard deviation and correlation time scale of the composite noise of 0.188, 1.83 and 0.89, respectively.

B.3.5. Precipitation Efficiency Function

For the purposes of estimating ζ, η and θ, the parameters of the precipitation efficiency function, the daily values of h were aggregated to monthly values. A log-log plot of s versus h is presented in Figure 7. The data have been divided into the five warmest months (May-September) and the seven coldest months (October-April). As one would expect for an energy-budget feedback, the correlation is strongest during the warm months, when precipitation is more often convectively generated. These months are also the core of growing season in Illinois, when vegetation draws moisture from the entire root zone, thereby increasing the dependency of the surface energy balance on the moisture throughout the root zone. The seasonality in the strength of the correlation between s and h is supported by the study of Findell and Eltahir (1997), which found a peak in correlation between soil moisture and lagged precipitation in Illinois during spring and summer months. The range of precipitation efficiency for the warm months in Figure 7 is also comparable to the approximately two- to four-fold increases in precipitation efficiency that Schär et al. (1999) found between their July dry-soil and wet-soil simulations over domains encompassing France and Central/Eastern Europe.

We could use the regression results in Figure 7 to parameterize the precipitation efficiency function with $\zeta=0$. However, because of the seasonality in both the magnitude of h and the strength of the correlation between s and h, an alternative was used. Specifically, an optimization routine was used to minimize the sum of the squared errors (SSE) between the observed monthly values of h and those predicted by the equation for h. Three parameterizations of the precipitation efficiency function were developed corresponding to (29), (30) and (31). In the first case, θ was set equal to 2, in order to increase the analytical tractability of (29). The SSEs of the first two cases—those with precipitation-efficiency feedbacks—are identical to two significant figures, while the SSE of the third case—that with a constant h—is 20% greater, lending further support for including a dependency of h on s.

B.4. Results: Temporal Variability of Soil Moisture

The analytical solutions for the steady-state PDFs of soil moisture corresponding to (29), (30) and (31) and their associated parameter values in Table 1 are plotted in Figure 8. Because the analytical solutions were derived under the assumption of no surface runoff, the values used for the runoff parameters are those in the left-hand column. The two solutions with precipitation-efficiency feedbacks ($\eta>0$) are nearly identical, indicating that the two versions of $h(s)$ have similar form over the realized range of s. The variance of s for these two cases is 0.0053 and 0.0055. In contrast, about

40% less variance (=0.0034) is observable in the precipitation-recycling-only case ($\eta=0$, $\beta>0$). Finally, the PDF with no feedbacks at all ($\eta=0$, $\beta=0$) is also plotted. With the resulting removal of precipitation recycling, there is only a slight shift to the left of the PDF and an insignificant reduction in variance, indicating that precipitation recycling is not a major source of soil moisture variability for the scale and climate of the study region. The variance in this case, i.e., that without either precipitation recycling or precipitation-efficiency feedbacks, is entirely derived from the high frequency variability in the input of atmospheric moisture and precipitation efficiency, as captured by the colored noise in the model.

For the purpose of comparison to the model results, we removed the seasonality in the observations of monthly average soil moisture by first standardizing them with the mean and standard deviation for the given month and then transforming them back with the overall mean and the average of the within-month standard deviations. The probability mass function (PMF) of the resulting values of s for all 227 months in the record is plotted in Figure 8.. While the variance of the precipitation-recycling-only case matches the variance of the observed PDF best, the model as a whole does a surprisingly good job of matching the observed variance, considering the physical simplicity of the model and the limits of the data. The lack of seasonality in the model and the difference in time scales are particularly significant limitations to comparing model results with observations. The longer averaging time of the observations is one reason to expect that their variance will be less than the model results. The connectivity of root-zone soil to the subsoil and ground water—which have longer memory—may also contribute to the lower variance in the observations. The model in its present form does not capture this connectivity. The model results in Figure 8 were also produced under the assumption of no surface runoff. As seen in the scaling analysis below, including surface runoff will further reduce the variance in the PDF.

For the purposes of confirmation of the approximate analytical solutions, PDFs for the first case (i.e., that with $\zeta=0.033$, $\eta=0.067$ and $\theta=2.0$) are arrived at by two additional methods. The first case was chosen because it uses the most nonlinear form of the precipitation efficiency function. The first method is numerical integration of (27). As can be seen in Figure 9, the anticipated shift to the left by the approximate analytical solution (see Appendix) is virtually imperceptible. The second method of validating the analytical solution—as well as the SDE itself—is a 5000-year simulation of (7) at a daily time step, with α and h generated stochastically according to (8), (9) and (10). γ_α and γ_h were simulated as a bivariate AR(1) process (*e.g.*, Bras and Rodriguez-Iturbe 1985). The PMF of the resulting values of s is plotted in Figure 9. Also plotted in Figure 9 is a PMF of 30-day averages of the simulation results. The reduction in variance is only slight, indicating that the persistence in soil moisture is large enough that the monthly averaging time of observed soil moisture explains only a small part of the difference in variance between the observed PMF and the modeled PDFs in Figure 8.

The final observation we make about the PDFs in Figures 8 is that they are nearly symmetric and unimodal and, hence, exhibit no propensity for bimodality. They do possess a slight leftward skew, which is also evident in the observed PMF. With the white-noise model of Rodriguez-Iturbe et al. (1991), the transition to bimodality takes place with increasing variance in the noise. By extension, bimodality may be induced in our colored-noise model by increasing not only the variance but also the correlation time scale of the composite noise. It is expected that both would be a function of spatial scale. As spatial scale is increased, moisture fronts would reside longer in the region and hence both τ_α and τ_h should increase. In contrast, we expect v_h and σ_α to decrease, as not only do moisture fronts reside longer in the region, but also the likelihood of multiple fronts being present at the same time within the region increases. Figure 10 shows the effect of proportional increases in τ_α, τ_h and β. The latter parameter is also scaled because increasing the downwind length of the region would proportionally increase the contribution of evapotranspiration from within the region to the overall moisture flux. The other parameters in the model remain the same with the exception that the runoff parameters are those for the case of $r_s=1$ (see Table 1) because, as discussed in the appendix, the inclusion of surface runoff is necessary for $s=1$ to be a *prescribed boundary*. The effect on the PDFs of adding surface runoff is a decrease of about 15% in the variance and enhancement of the skewness. A final difference with the PDFs of Figure 8 is that those of Figure 10 were generated by numerical integration of (27)—as further discussed in the appendix, we assumed that τ was on the order of a few days to arrive at (28) and its analytical solutions, (29)-(31).

In all three parameterizations, as the correlation time scales are increased, a heavy skew to the left develops at the same time the mode shifts to the right. Bimodality develops only in the parameterization with $\zeta=0$, which is the only one with a prescribed boundary at $s=0$. The second mode is at $s=0$, so it represents the unlikely case of precipitation ceasing. Furthermore, the mode develops between a scale factor of 10 and 15. Under the unlikely conditions of the correlation time scales increasing in proportion to the downwind length, and the variance of the noise remaining constant, the corresponding spatial scale is about 5000 to 7500 km—greater than the width of the United States at the latitude of Illinois and much greater than the scale at which the precipitation-efficiency feedback mechanisms are likely to operate. Therefore, soil moisture feedbacks to precipitation alone are unlikely to induce bimodality in soil moisture at large regional-to-continental scales for midlatitude, semihumid climates.

The alternative possibility is that bimodality might occur at spatial scales smaller than the study region. As spatial scale decreases, and larger scales of atmospheric motion are lost, the variance of the noise is expected to increase. Figure 11 shows the effect of proportional increases in both ν_h and σ_a. Because the other parameter values and solution methodology are the same as in Figure 10, the PDFs for a scale factor of one are the same. As the scale factor increases in Figures 11a-d, a leftward skew and shift of the primary, wet mode to the right occur as in Figure 10, although not as dramatically. In contrast to Figure 10, a second, dry mode develops for both parameterizations with precipitation-efficiency feedbacks. The dry mode in the parameterization with $\zeta=0$ is more pronounced and quickly shifts to $s=0$ as in Figure 10. The soil-moisture feedbacks, as well as our assumption in the model of continuous precipitation, require at least a small regional spatial scale. Thus, there are limits to how large ν_h and σ_a can be. We are also limited in parameterizing smaller scales by the resolution of NCEP/NCAR reanalysis. At minimum we can calculate the standard deviation of α at a single grid point. Doing that for the grid point at the center of the study region produces a value of 0.71, only slightly larger than that calculated for the study region using all nine grid points. Therefore, reducing the spatial scale is also highly unlikely to produce bimodality.

B.5. Concluding Remarks

Based on analysis with an SDE-based, large-scale water balance model, and detailed observations of relevant hydrologic and atmospheric variables, this study suggests that energy-budget feedbacks, as captured by a soil-moisture-dependent precipitation efficiency function, are a substantial source of the temporal variability of soil moisture in the semihumid regions of the U.S. Midwest. On the other hand, precipitation recycling within a regional-scale domain does not contribute to atmospheric moisture flux sufficiently to have a significant impact on soil moisture variability. Despite the significance of precipitation-efficiency feedbacks, they, along with precipitation recycling, are clearly not strong enough to induce a bimodal probability distribution in spatially averaged soil moisture, as other SDE-based studies (Rodriguez-Iturbe et al., 1991; Entekhabi et al, 1992 and Wang et al., 1997) have suggested. Because the study focuses on a specific region of the United States, we do not *prima facie* dismiss the possibility that a feedback-induced, two-state dynamic exists elsewhere. However, the work of Koster et al. (2000) and others suggests that midlatitude, semihumid climates are where the impact of land-surface feedbacks on the interannual variability of precipitation are the strongest relative to that of ocean-atmosphere teleconnections. We also do not dismiss the possibility that a two-state dynamic might exist in external drivers of the system with enough strength and persistence alone to produce bimodality in soil moisture.

In its present form, the model is a useful tool for examining the impact of the nonlinear dynamics of soil moisture feedbacks to precipitation on the variability of soil moisture at the regional scale. In estimating parameter values for the study region, we have demonstrated that hydrometeorological fluxes—most of which have high-frequency temporal variability and are dependent on smaller-scale spatial heterogeneities—can be captured at regional scales over long averaging periods by empirical power functions of spatially averaged soil moisture. A key feature of the simplified representation of those fluxes is the use of a soil-moisture-dependent precipitation efficiency factor. That a correlation exists between soil moisture and precipitation efficiency over the study region was shown in Section 3.5. While that correlation does not prove a causal mechanism, both the existence of positive precipitation-efficiency feedbacks and the assumed strength of those feedbacks are supported by observational and modeling studies of the region (Findell and Eltahir, 1997; Zheng and Eltahir, 1998; Brown and Arnold, 1998; Pal and Eltahir 2001) and similar climates of Europe (Schär et al., 1999). Greater confidence in the conclusions of this study depends on further elucidation of the mechanisms and magnitudes of precipitation-efficiency feedbacks, especially with regards the extent to which they are dependent on regional-scale averages of soil moisture.

In a forthcoming paper, it will be shown that the model also does a good job of reproducing the persistence and interannual variability in the soil-moisture observations for Illinois. We will also examine the persistence and interannual variability of precipitation, as well as use of the model to resolve the relative contributions of land-surface feedbacks, ocean-atmosphere teleconnections and chaotic atmospheric dynamics to the interannual variability of the water balance.

B.6. Acknowledgements

This work was partially supported by the National Institute for Global Environmental Change through the U.S. Department of Energy (Cooperative Agreement No. DE-FC03-90ER61010).

B.7. Appendix: Analysis of Boundary Conditions

While soil moisture is physically limited to the interval $s \in [0,1]$ in the real world, it may not be mathematically in the model. Both the drift and diffusion terms determine the boundaries of the solution of the FPE. We first consider the significance of the drift term. If the soil were ever to become either completely saturated (*i.e.*, $s=1$) or dry to its residual moisture limit (*i.e.*, $s=0$), it should move back to the interior of the interval. $s=0$ and $s=1$ would then be *entrance boundaries*, and it would be necessary that $A(0)>0$ and $A(1)<0$ (Gardiner 1985). In the denominators of (25a,b),

$$\delta(s)\frac{d}{ds}\left(\frac{\Delta(s)}{\delta(s)}\right) = s^{-1}\Big[a\beta s^{\varepsilon}(\zeta+\eta s^{\theta})(1-s^{\rho_s}) - \varepsilon e_p s^{\varepsilon} - \rho_g k s^{\rho_g} + \frac{\eta\theta s^{\theta}\left(e_p s^{\varepsilon} + k s^{\rho_g}\right)}{\zeta+\eta s^{\theta}} - \frac{\rho_s s^{\rho_s}\left(e_p s^{\varepsilon} + k s^{\rho_g}\right)}{1-s^{\rho_s}}\Big] \tag{A1}$$

where r_s has been set equal to one. Thus, for any set of nonnegative parameter values with ε and ρ_g greater than one,

$$\lim_{s \to 0} \delta(s) \frac{d}{ds}\left(\frac{\Delta(s)}{\delta(s)}\right) = 0 \tag{A2}$$

and $A(0)=\Delta(0)$, which is greater than zero as long as ζ is greater than zero. On the other hand,

$$\lim_{s \to 1} \delta(s) \frac{d}{ds}\left(\frac{\Delta(s)}{\delta(s)}\right) = -\infty \tag{A3}$$

Consequently $A(1)=0$, and therefore $s=1$ is actually a *natural boundary* at which s would tend to remain. (A3) comes about only because we set r_s to unity in (A1). However, if the diffusion term goes to zero near $s=1$, the boundary cannot be reached and is also termed a *prescribed boundary* (Gardiner 1985). The drift and diffusion terms share the same denominator and $\delta(1)=0$, so (25b) does in fact go to zero near $s=1$. From the standpoint of a physically realistic PDF, a prescribed boundary is desirable because it ensures that the PDF will be zero at that boundary. From (16c), we see that $s=0$ is a prescribed boundary only when $\zeta=0$. With $\zeta=0$, the drift term also goes to zero, and thus $s=0$ also becomes a natural, prescribed boundary. The physical implication for $s=0$ is the cessation of all fluxes to and from the soil. This would be expected of evapotranspiration and groundwater runoff, but unlikely to happen to precipitation. However, the precipitation efficiency may still be well approximated over the realized range of s with $\zeta=0$ (see Section 3.5).

In order to argue for a simpler, but approximate solution of (27a,b), we examine the form of (A1). We have already established that (A1) ranges from 0 to $-\infty$; plotting it with example parameter sets reveals that the asymptote becomes sharper as ρ_s increases. This behavior is such that, if we assume that τ is on the order of a few days or less, and that the surface runoff ratio is small—generally, a reasonable assumption for all but the most humid climates and steep terrain—we can approximate the denominators in (25a,b) as one. Because the overestimation in the drift term created by this approximation worsens as s approaches one, we expect that the overall effect will be to shift probability mass to the left—an effect almost imperceptible in the analytical solution as compared to the exact numerical integration in Figure 9. The approximation also necessitates re-evaluation of the boundary conditions. The nature of the boundary at $s=0$ remains unchanged. On the other hand, $\Delta(1)<1$, and so $s=1$ becomes an *entrance boundary*. The prescribed status of $s=1$ still depends on $r_s=1$. However, setting r_s equal to zero is also desirable for simplifying the evaluation of the integral in (28). Based on a comparison between the PMF for the numerical simulation and the PDFs in Figure 9, a consequence of the absence of a prescribed boundary at $s=1$ may be a slight shift of the PDF to the right. Otherwise, it does not appear to be a problem for the given parameter values. However, the much larger values of the correlation time scales and noise variances used in the scaling analysis do create unrealistic behavior at $s=1$ in the approximate analytical solutions—hence the reason they were not used in that analysis.

B.8. References

Benjamin, J.R. and C.A. Cornell, 1970: *Probability, Statistics, and Decision for Civil Engineers*. McGraw-Hill, 684 pp.

Bras, R.L., and I. Rodriguez-Iturbe, 1984: *Random Functions and Hydrology*. Dover Publications, 559 pp.

Brooks, R.H., and A.T. Corey, 1966: Properties of porous media affecting flow. *Journal of the Irrigation and Drainage*, IR2, 61-88.

Brown, M.E. and D.L. Arnold, 1998: Land-surface–atmosphere interactions associated with deep convection Illinois. *International Journal of Climatology*, 18, 1637-1653.

Brubaker, K.L., D. Entekhabi, and P.S. Eagleson, 1993: Estimation of Continental Precipitation Recycling. *Journal of Climate*, 6, 1077-1089.

Budyko, M.I., 1974: *Climate and Life*. Academic Press, 508 pp.

Charney, J., J.Q. Quirk, S-H. Chow and J. Kornfield, 1977: A comparative study of effects of albedo change on drought in semi-arid regions. *Journal of the Atmospheric Sciences*, 34, 1366-1385.

Daly, C., R.P. Neilson and D.L. Phillips, 1994: A statistical-topographic model for mapping climatological precipitation over mountainous terrain. *Journal of Applied Meteorology*, 33,140-158.

Eltahir, E.A.B., 1998: A soil moisture-rainfall feedback mechanism, 1. Theory and Observations. *Water Resources Research*, 34(4), 765-776.

Eltahir, E.A.B., and P. Yeh, 1999: On the asymmetric response of aquifer water level to floods and droughts in Illinois. *Water Resources Research*, 35(4), 1199-1217.

Entekhabi, D., I. Rodriguez-Iturbe, and RL. Bras, 1992: Variability in large-scale water balance with land surface-atmosphere interaction. *Journal of Climate*, 5, 798-813.

Findell, K.L. and E.A.B. Eltahir, E.A.B., 1997: An analysis of the soil moisture-rainfall feedback mechanism, based on direct observations from Illinois. *Water Resources Research*, 33(4), 725-735.

Gardiner, C.W., 1985: *Handbook of Stochastic Methods for Physics, Chemistry and the Natural Sciences*. Springer-Verlag, Berlin, 2nd edition, pp. 442.

Higgins. R.W., W. Shi, E. Yarosh and R. Joyce, 2000: *Improved Unites States Precipitation Quality Control System and Analysis,* NCEP/Climate Prediction Center ATLAS No. 7. U.S. Department of Commerce,
National Oceanic and Atmospheric Administration, National Weather Service.

Hobbins, M. T., Ramírez, J. A., Brown, T. C., and L. H. J. M. Claessens, 2001: The complementary relationship in estimation of regional evapotranspiration: The Complementary Relationship Areal Evapotranspiration and Advection-Aridity models. *Water Resources Research*, 37(5), 1367-1388.

Hollinger, S.E. and S.A. Isard, 1994: A soil moisture climatology of Illinois. *Journal of Climate*, 7, 822-833.

Høyrup, M., 1996: *The influence of passed-diffused laser light on three-level atoms*, master's thesis, Institute of Physics and Astronomy, Aarhus University, Denmark, pp. 121.

Jackson, R.B., J. Canadell, J.R. Ehleringer, H.A. Mooney, O.E. Sala, and E.D. Schulze, 1996: A global analysis of root distributions fro terrestrial biomes. *Oecologia*, 108, 389-411.

Kalnay, E. and co-authors, 1996: The NCEP/NCAR 40-year reanalysis project. *Bulletin of the American Meteorological Society*, 77(3), 437-471.

Koster, R.D., M.J. Suarez, and M. Heiser, 2000: Variance and predictability of precipitation at seasonal-to-interannual timescales. *Journal of Hydrometeorology*, 1, 26-46.

Pal, J.S. and E.A.B. Eltahir, 2001: Pathways relating soil moisture conditions to future summer rainfall within a model of the land-atmosphere system. *Journal of Climate*, 14, 1227-1242.

Penman, H.L., 1948: Natural evaporation from open water, bare soil and grass. *Proceedings of the Royal Society of London*, A193, 120-145.

Pielke, R.A. and X. Zeng, 1989: Influence on severe storm development of irrigated land. *National Weather Digest*, 14, 16-17.

Robock, A., K. Y. Vinnikov, G. Srinivasan, J. K. Entin, S. E. Hollinger, N. A. Speranskaya, S. Liu, and A. Namkhai, 2000: The Global Soil Moisture Data Bank. *Bull. Amer. Meteorol. Soc.*, 81, 1281-1299.

Rodell, M. and J.S. Famiglietti, 2001: An analysis of terrestrial water storage variations in Illinois with implications for the Gravity Recovery and Climate Experiment (GRACE). *Water Resources Research*, 37(5), 1327-1339.

Rodriguez-Iturbe, I., D. Entekhabi and R.L. Bras, 1991: Nonlinear dynamics of soil moisture at climate scales, 1. stochastic analysis. *Water Resources Research*, 27(8), 1899-1906.

Savenije, H.H.G, 1995: New definitions for moisture recycling and the relationship with land-use changes in the Sahel. *Journal of Hydrology*, 167, 57-78.

Schär, C., D., D. Luthi and U. Beyerle, 1999: The soil-precipitation feedback: a process study with a regional climate model. *Journal of Climate*, 12, 722-741.

Shuttleworth, W.J., 1993: Evaporation, Chapter 4 of *Handbook of Hydrology*, D.R. Maidment, ed., McGraw-Hill, Inc.

Wang, J., R.L. Bras and D. Entekhabi, 1997: Structure in fluctuations of large-scale soil moisture climate due to external random forcing and internal feedbacks. *Stochastic Hydrology and Hydraulics*, 11, 95-114.

Woodruff, J.F. and J.D. Hewlett, 1970: Predicting and mapping the average hydrologic response for the eastern United States. *Water Resources Research*, 6(5), 1312-1326.

Yeh, J.Y., M. Irizarry and E.A.B. Eltahir, 1998: Hydroclimatology of Illinois: a comparison of monthly evaporation estimates based on atmospheric water balance and soil water balance. *Journal of Geophysical Research*, 34(D16), 19,823-19,837.

Zheng, X and E.A.B. Eltahir, 1998: A soil moisture-rainfall feedback mechanism, 2. Numerical Experiments. *Water Resources Research*, 34(4), 777-785.

Table 1. Parameter values for the study region

<table>
<tr><th>*Parameter*</th><th colspan="4">*Value*</th></tr>
<tr><td>Storage capacity of root zone, n_eZ_r (mm)</td><td colspan="4">430</td></tr>
<tr><td>Temporal mean of s, $\bar{s}$</td><td colspan="4">0.68</td></tr>
<tr><td>Mean advected moisture flux, $\bar{A}$ (mm/day)</td><td colspan="4">34.1</td></tr>
<tr><td>Standard deviation of α, σ_α</td><td colspan="4">0.697</td></tr>
<tr><td>Coefficient of variation of h, v_h</td><td colspan="4">1.24</td></tr>
<tr><td>Covariance of γ_α and γ_h, $Cov[\gamma_\alpha, \gamma_h]$</td><td colspan="4">0.24</td></tr>
<tr><td>Correlation time scale of γ_α, τ_α(days)</td><td colspan="4">1.77</td></tr>
<tr><td>Correlation time scale of γ_h, τ_h (days)</td><td colspan="4">0.87</td></tr>
<tr><td>Cross-correlation time scale of $\gamma_\alpha$and γ_h $\tau_{\alpha h}$ (days)</td><td colspan="4">2.1</td></tr>
<tr><td>Cross-correlation time scale of γ_h and γ_α, $\tau_{h,\alpha}$ (days)</td><td colspan="4">0.50</td></tr>
<tr><td>Mean of composite noise, μ</td><td colspan="4">0.207</td></tr>
<tr><td>Standard deviation of composite noise, σ</td><td colspan="4">1.84</td></tr>
<tr><td>Correlation time scale of composite noise, τ</td><td colspan="4">0.89</td></tr>
<tr><td>Precipitation efficiency constant, ζ</td><td>0.064</td><td colspan="2">0</td><td>0.033</td></tr>
<tr><td>Precipitation efficiency coefficient, η</td><td>0</td><td colspan="2">0.091</td><td>0.067</td></tr>
<tr><td>Precipitation efficiency exponent, θ</td><td>NA</td><td colspan="2">0.9</td><td>2</td></tr>
<tr><td>Infiltration function coefficient, r_s</td><td colspan="2">0</td><td colspan="2">1</td></tr>
<tr><td>Infiltration function exponent, ρ_s</td><td colspan="2">NA</td><td colspan="2">7.9</td></tr>
<tr><td>Effective saturated hydraulic conductivity, K (mm/day)</td><td colspan="2">7.1</td><td colspan="2">4.2</td></tr>
<tr><td>Groundwater runoff function exponent, ρ_g</td><td colspan="2">6.2</td><td colspan="2">5.7</td></tr>
<tr><td>Potential evapotranspiration rate, E_p (mm/day)</td><td colspan="4">2.96</td></tr>
<tr><td>Ratio of E_p to $\bar{A}$, β</td><td colspan="4">0.087</td></tr>
<tr><td>Evapotranspiration function exponent, ε</td><td colspan="4">1.2</td></tr>
</table>

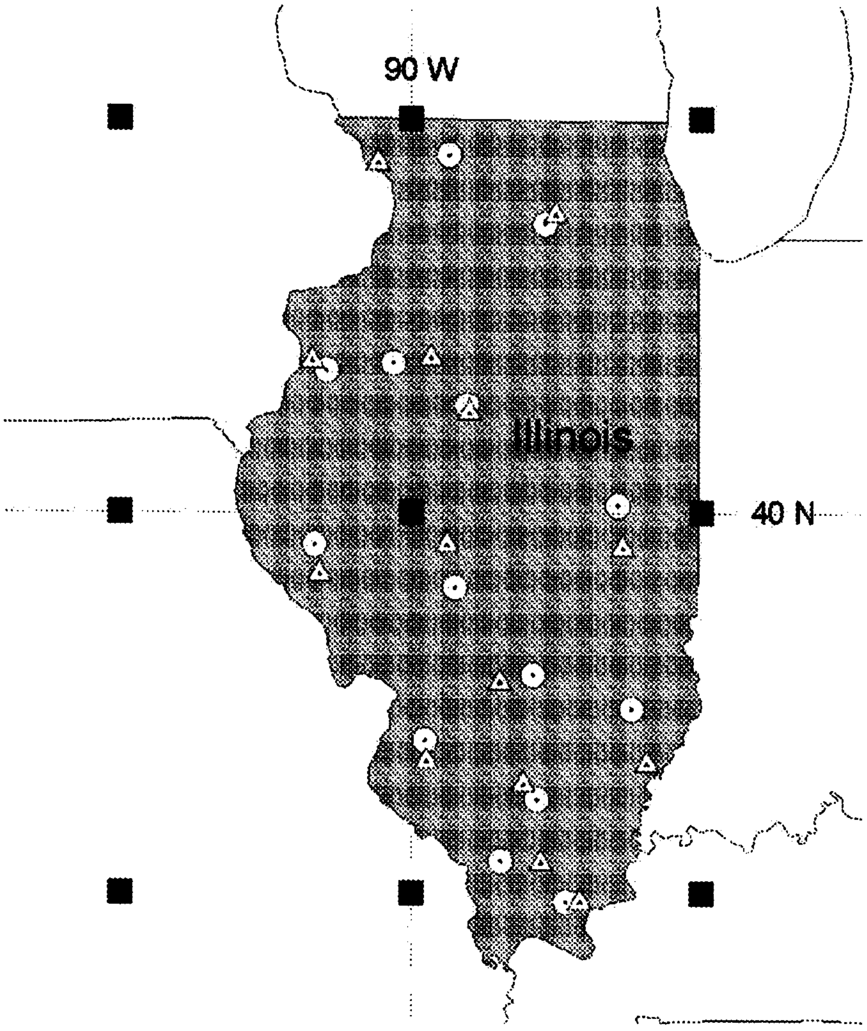

Figure 1. Study region and data locations: NCEP/NCAR reanalysis grid points (black squares), ISWS soil moisture stations (white circles), USGS streamflow gauges (white triangles).

a) total streamflow

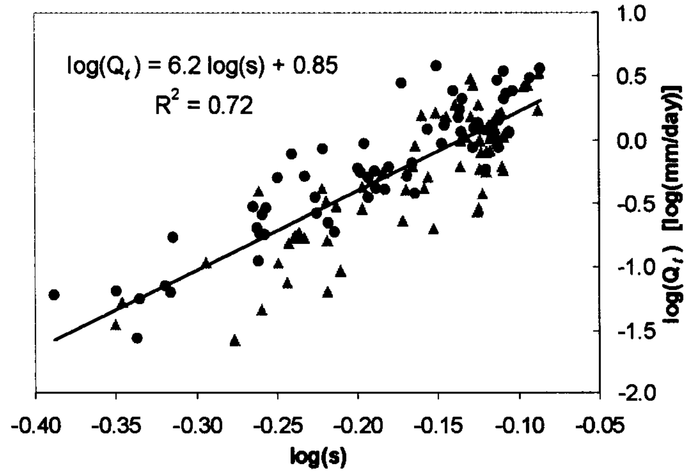

b) base flow

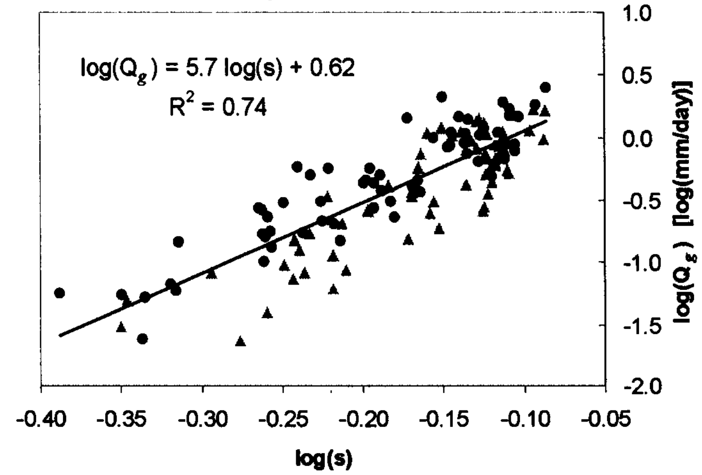

c) surface runoff ratio

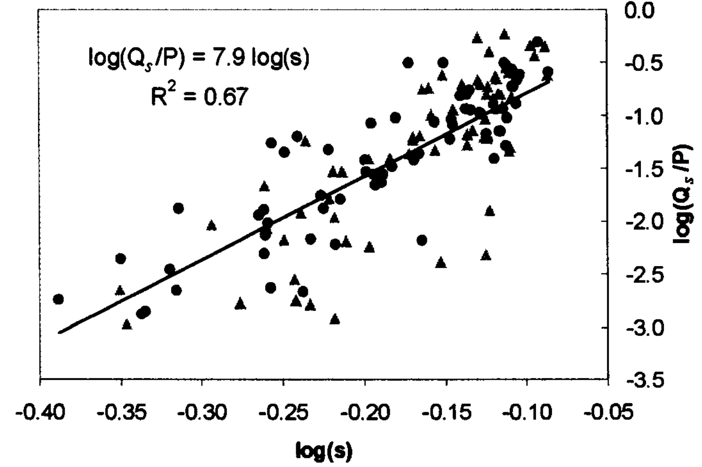

Figure 2. Log-log regressions of monthly streamflow vs. soil moisture (1983-1993): (a) total streamflow, (b) base flow; and (c) surface runoff ratio. Black circles are months of decreasing soil and groundwater storage (March-August). Grey triangles are months of increasing storage (September-February). The regressions are for all months.

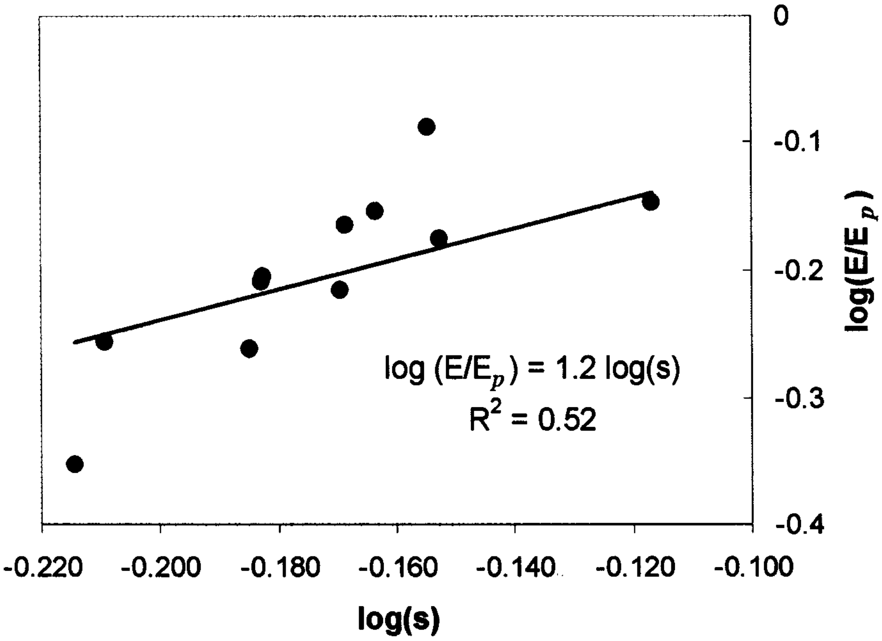

Figure 3. Log-log regression of the ratio of annual evapotranspiration to potential evapotranspiration vs. annual mean soil moisture (1983-1993).

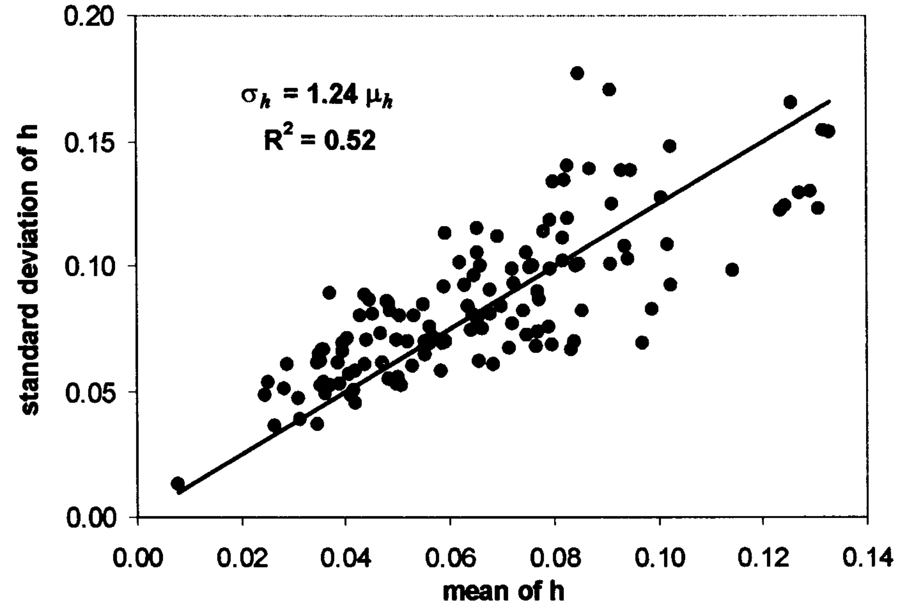

Figure 4. Mean vs. standard deviation of daily precipitation efficiencies within each month (1983-1993). Line and equation are results of zero-intercept least-squares regression.

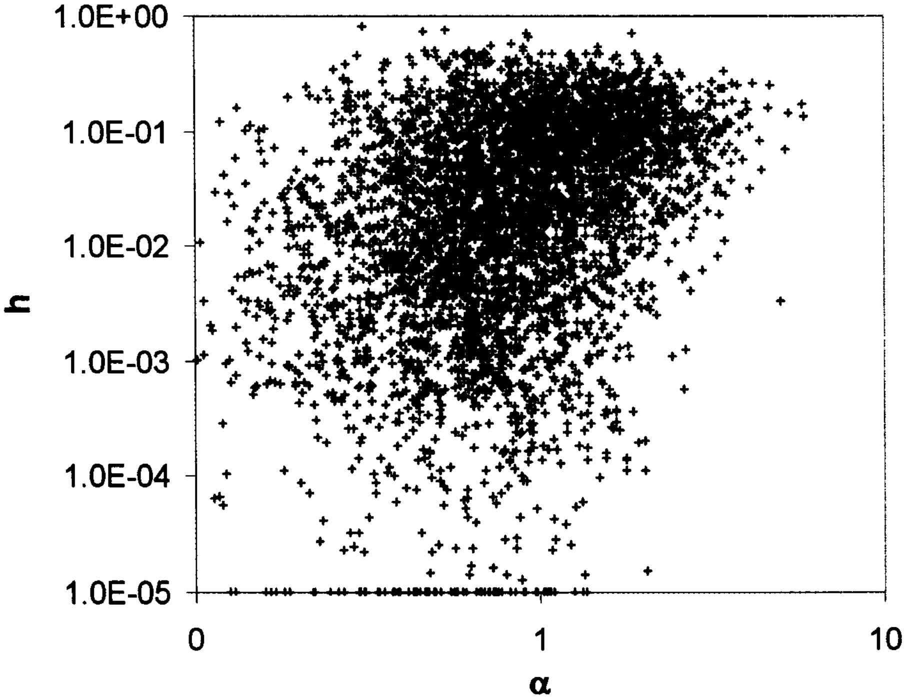

Figure 5. Normalized daily advected moisture flux vs. precipitation efficiency (1983-1993). Values of *h* less than 10^{-5} are plotted at 10^{-5}.

a) advected moisture flux

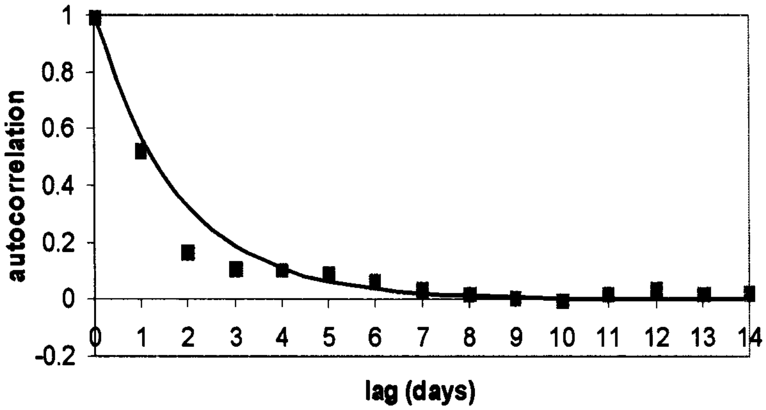

b) precipitation efficiency

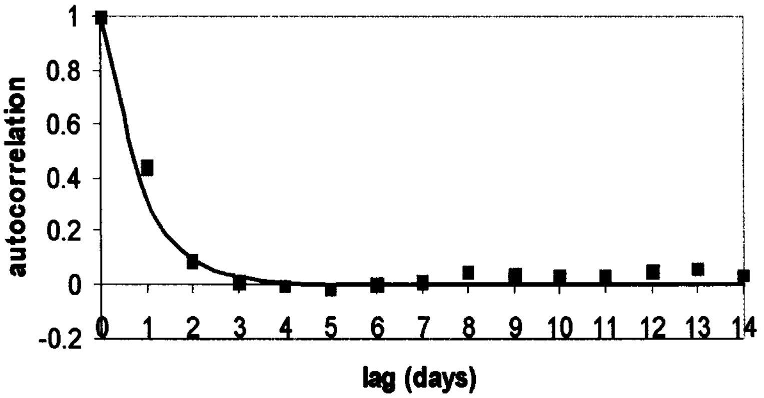

c) advected moisture flux and precipitation efficiency

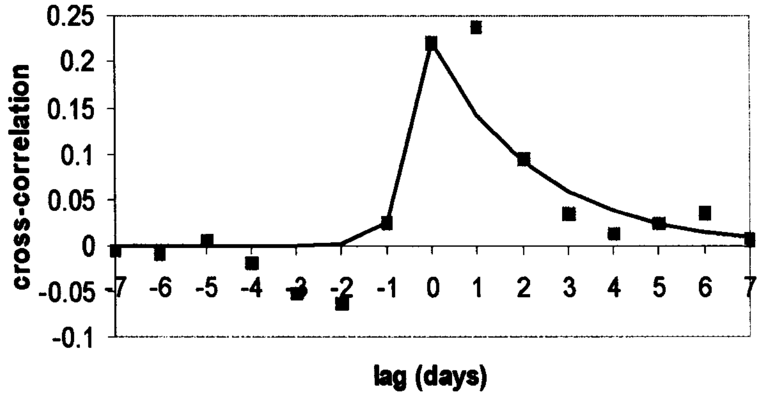

Figure 6. Autocorrelation of daily (a) normalized advected moisture flux, α, (b) precipitation efficiency, h, and (c) cross-correlation of α and h: (1983-1993). Grey squares are observed values, and black curves are exponential fits.

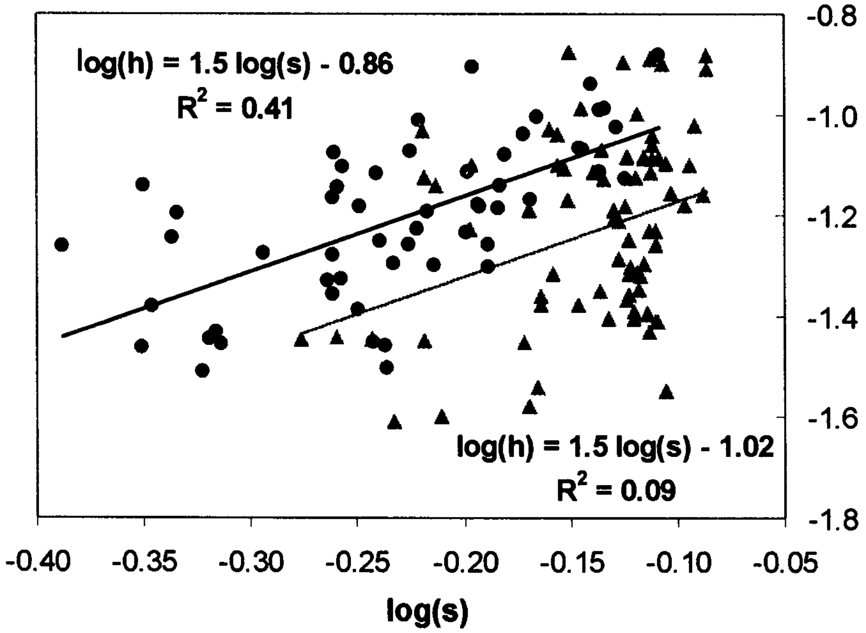

Figure 7. Monthly average soil moisture vs. precipitation efficiency (1983-1993). Black circles are warm months/growing season (May-September). Grey triangles are cold months (October-April). Correspondingly colored lines and equations are regression results.

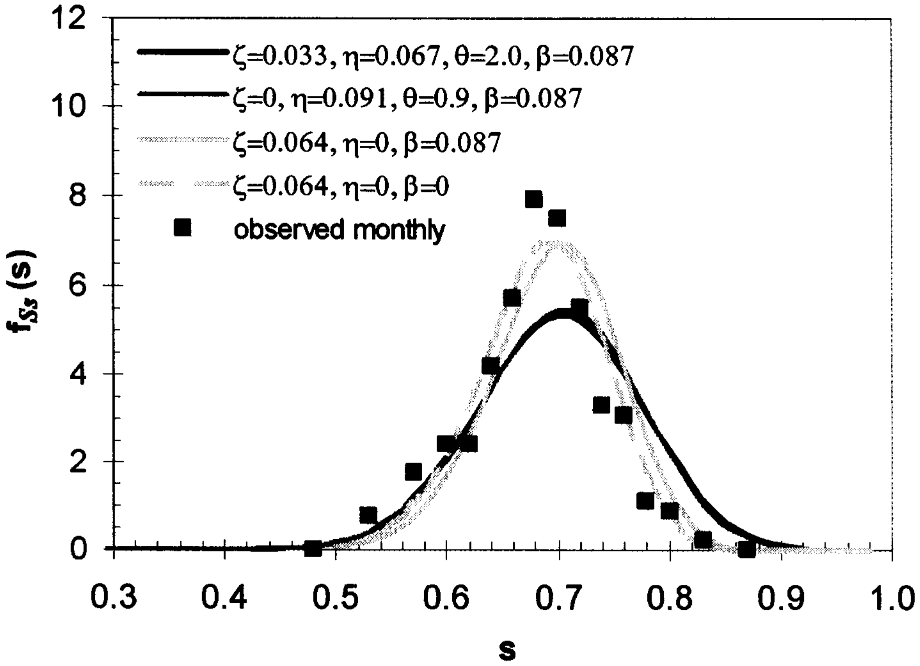

Figure 8. Approximate analytical solutions of the Fokker-Plank equation for three parameterizations of the precipitation efficiency function. The third parameterization is plotted both with and without precipitation recycling. Black squares are the PMF of "season-less" observed monthly values (1983-2001).

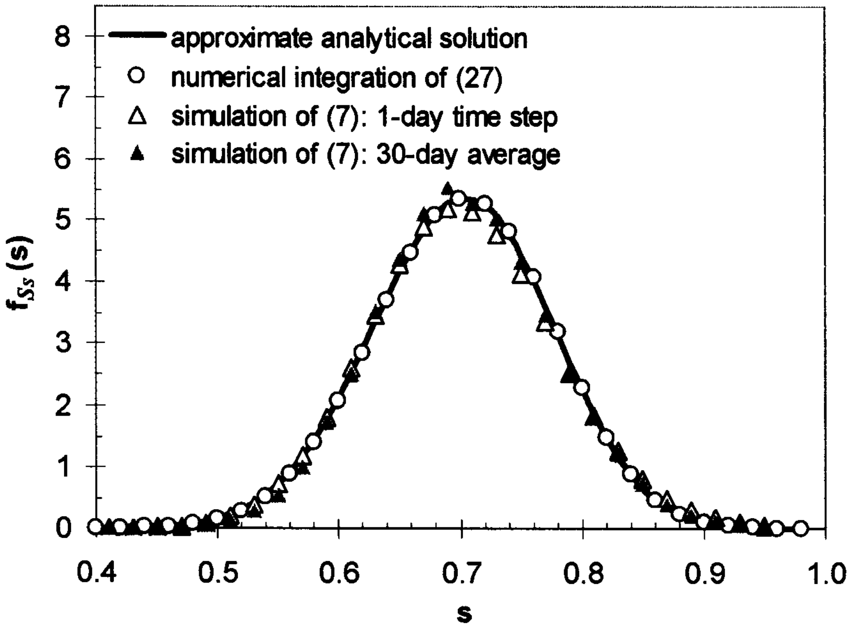

Figure 9. Comparison of the approximate analytical solution of the PDF (Eq. 30) with numerical integration of (27) and a stochastic simulation of (7). Parameter values for the precipitation efficiency function are: ζ=0.033, η=0.067 and θ=2.0.

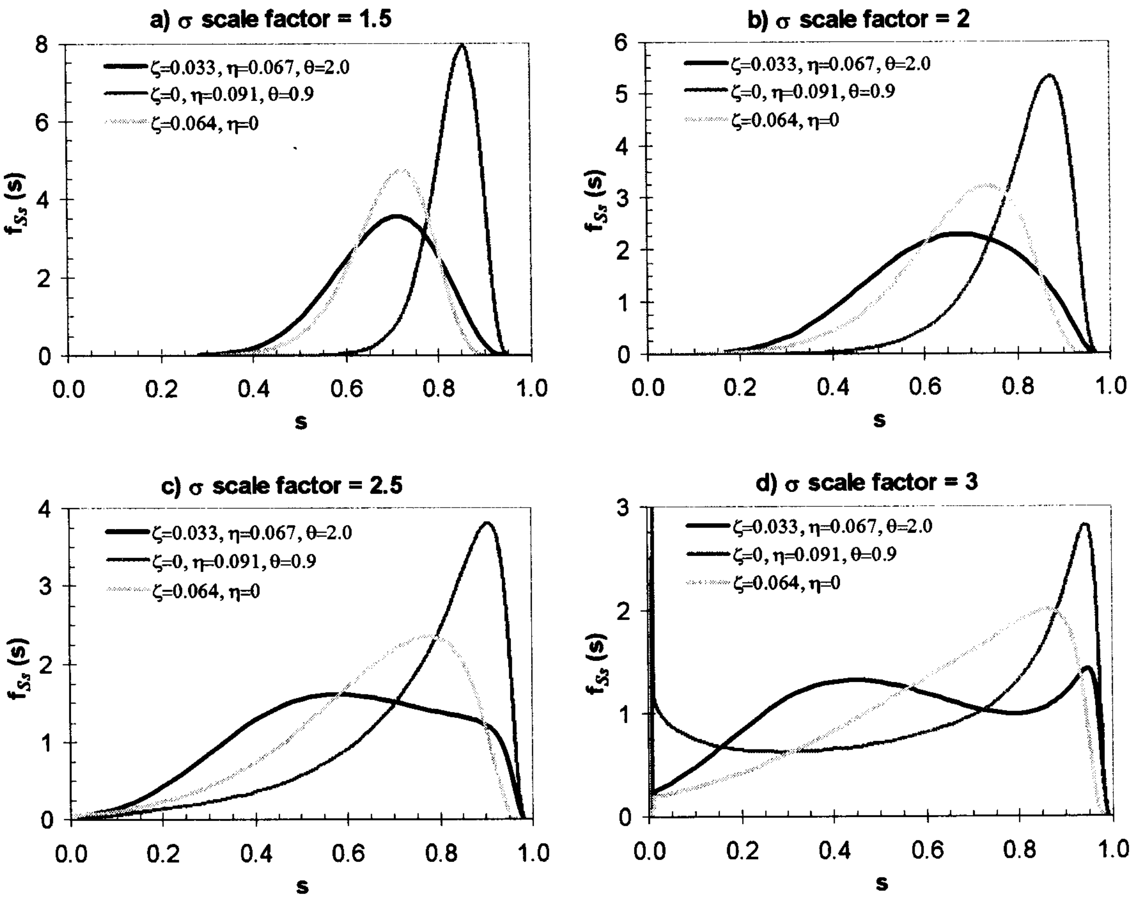

Figure 11. The effect of increasing variance in the noise on the PDFs of soil moisture as might be manifested by decreasing spatial scale.